



**HAL**  
open science

# Photonic crystal-based emissive microstructures in III-V semiconductor thin films: light extraction and directivity control applied to micro-LED color conversion

Amade Ndiaye

## ► To cite this version:

Amade Ndiaye. Photonic crystal-based emissive microstructures in III-V semiconductor thin films: light extraction and directivity control applied to micro-LED color conversion. Other. Ecole Centrale de Lyon, 2023. English. NNT : 2023ECDL0001 . tel-04473707

**HAL Id: tel-04473707**

**<https://theses.hal.science/tel-04473707>**

Submitted on 22 Feb 2024

**HAL** is a multi-disciplinary open access archive for the deposit and dissemination of scientific research documents, whether they are published or not. The documents may come from teaching and research institutions in France or abroad, or from public or private research centers.

L'archive ouverte pluridisciplinaire **HAL**, est destinée au dépôt et à la diffusion de documents scientifiques de niveau recherche, publiés ou non, émanant des établissements d'enseignement et de recherche français ou étrangers, des laboratoires publics ou privés.



N°d'ordre NNT : 2023ECDL0001

THESE DE DOCTORAT DE L'ÉCOLE CENTRALE DE LYON  
membre de l'Université de Lyon

**Ecole Doctorale N°160**  
**Électronique, Électrotechnique et Automatique**

Spécialité / discipline de doctorat :  
**Électronique, micro et nano-électronique, optique et laser**

Soutenue publiquement le 10/01/2023, par :  
**Amade NDIAYE**

---

# **Photonic crystal-based emissive microstructures in III-V semiconductor thin films: light extraction and directivity control applied to micro-LED color conversion**

---

Devant le jury composé de :

**SAGNES, Isabelle** CNRS-C2N, Paris-Saclay

*Directrice de recherche CNRS*

**BENISTY, Henri** IOGS, Palaiseau

*Professeur des Universités*

**VAN THOURHOUT, Dries** IMEC, Louvain

*Professeur Université de Gand*

**WIRTH, Ralph** ams-Osram, Regensburg

*Directeur de groupe de recherche et de pré-développement*

**SEASSAL, Christian** INL, Lyon

*Directeur de recherche CNRS*

**BEN BAKIR, Badhise** CEA-LETI, Grenoble

*Ingénieur chercheur*

**DROUARD, Emmanuel** Ecole Centrale de Lyon, INL

*Maître de Conférences*

Examinatrice

Rapporteur et président du jury

Rapporteur

Examineur

Directeur de thèse

Co-directeur de thèse

Membre invité

Thèse préparée au sein de l'INL UMR 5270 et du CEA-LETI



## Résumé en français

**Mots-clés en français :** extraction de lumière, directionnalité, force de couplage, intégration, 200nm, émission spontanée, FDTD, modes de Bloch, puits quantiques, conversion de couleur, microled, microécran.

Les lunettes à réalité augmentée emplissent de plus en plus notre quotidien au travers de diverses applications à la fois militaires, médicales, éducatives, etc. Pour réaliser des microécrans couleurs pour lesdites lunettes la stratégie la plus viable reste pour le moment la conversion de couleur, suivant laquelle on part de matrices de  $\mu$ -LEDs bleues sur lesquelles on dépose (ou colle) des convertisseurs de couleur vert et rouge. Les convertisseurs de couleurs à l'état de l'art sont à base de boîtes quantiques, souffrant de problème de photostabilité à haute luminance ainsi que d'une faible absorption dans le bleu. L'objectif de cette thèse est la conception, l'intégration & fabrication ainsi que le test de nouvelles couches de conversions à base de puits quantiques offrant plus de photostabilité à haute luminance et une très forte absorption dans le bleu. Il s'agira en particulier de lever les verrous liés à leur faible extraction de lumière (~3%), leur diagramme d'émission pas directionnel (émission quasi-Lambertienne) ainsi que leur intégration sur les matrices de  $\mu$ -LEDs bleues sur silicium (transfert sur des matrices bleues, process and pixellisation).

Durant cette thèse nous avons d'abord conçu, fabriqué et testé les premières couches de conversions à base de multi-puits quantiques InGaP/AlGaInP et de cristaux photoniques complètement optimisées pour la conversion du bleu vers le rouge dans les lunettes à réalité augmentée. Avec lesdites couches de conversion, nous avons obtenu des exacerbations de l'extraction pouvant aller jusqu'à des facteurs 9 sur des longueurs d'extraction très faibles (~2 $\mu$ m).

Nous avons ensuite développé un nouveau formalisme matriciel 3x3 pour la modélisation de la modification de l'émission spontanée dipolaire dans des milieux stratifiés. Ledit modèle a été appliqué à des structures en géométrie de couche mince émettant de la lumière incohérente. Avec ce modèle, nous avons pu réaliser (design et démonstration expérimentale) des couches de conversions rouges avec des émissions ultra-directionnelles (~5 fois plus directionnelles qu'une émission Lambertienne).

Avec cette démonstration, nous avons aussi proposé une nouvelle méthodologie pour la conception de structures multimodes à émission très directionnelle en se basant à la fois sur le contrôle de l'émission spontanée et le mécanisme de repliement de bande en 2D.

Comme l'efficacité d'extraction de lumière augmente avec la longueur du cristal photonique, les pixels avec des longueurs faibles ont toujours des efficacités d'extraction faibles. Pour pallier ce problème, nous avons développé une nouvelle approche basée sur la réplique des modes de Bloch permettant d'augmenter virtuellement l'extension latérale des pixels pour laisser aux photons la possibilité de faire plusieurs allers-retours dans la cavité avant d'être extraits. Ce principe a été modélisé et démontré expérimentalement sur des pixels rouges montrant qu'on pouvait atteindre des efficacités d'environ

40% (sachant qu'on parlait de ~3%) tant que les tailles de pixels sont maintenues au-dessus de  $2\mu\text{m}$ , ce qui correspond aux exigences pour les applications visées. De plus, un process flow robuste et compatible à la fabrication en salle blanche 200mm a été développé pour la fabrication de tels composants.

Ces travaux sont en train d'être utilisés au LETI pour faire les premiers microécrans microled couleur à bases de couches de conversion en multi-puits quantiques.

## English summary

**Keywords in English:** light extraction, directionality, coupling strength, integration, 200mm, spontaneous emission, FDTD, Bloch-modes, quantum wells, color conversion, microLED, microdisplay.

Augmented reality glasses are expanding in various applications of our daily lives such as military, medical, educational, etc. As of now, the most viable strategy for realizing full-color microdisplays for these glasses is color conversion, which starts with blue  $\mu$ -LED arrays on which green and red color converters are deposited (or bonded). The state-of-the-art color converters are based on quantum dots, suffering from photostability issues at high luminance as well as a low absorption in the blue spectral range. The aim of this thesis is the design, integration & fabrication as well as testing of new quantum-well based conversion layers offering more photostability at high luminance and a very high absorption efficiency in the blue spectral range. In particular, we tackle the issues related to their low light extraction ( $\sim 3\%$ ), their non-directional emission pattern (Lambertian-like emission) and their integration on blue  $\mu$ -LED arrays on silicon (transfer onto blue arrays, process and pixelization).

During this thesis, we have designed, fabricated and tested the first color conversion layers based on InGaP/AlGaInP multi quantum wells and photonic crystals, fully optimized for blue-to-red color conversion in augmented reality glasses. With said conversion layers, we have obtained extraction enhancement that can go up to factors of  $\sim 9$  within very short extraction lengths ( $\sim 2\mu\text{m}$ ).

We have then developed a new  $3 \times 3$ -matrix formalism for modeling the modification of the dipolar spontaneous emission in layered media. This model has been applied to structures in thin-film geometry emitting incoherent light. With this model, we have been able to realize (design and experimental demonstration) red conversion layers with ultra-directional emission ( $\sim 5$  times more directional than Lambertian emission).

Along with this demonstration, we have also proposed a new methodology for the design of multimode structures with directional emission based on both spontaneous emission control and 2D band-folding mechanism.

In addition, as the light extraction increases with the length of the photonic crystal, pixels with short lengths still have low extraction efficiencies. To overcome this problem, we have developed a new approach based on Bloch-mode replication in order to virtually increase the lateral extension of the pixels to allow non-extracted photons to make several round trips in the cavity before being extracted. This principle has been modeled and experimentally demonstrated on red pixels showing that efficiencies of  $\sim 40\%$  (we recall that we have started from  $\sim 3\%$ ) can be achieved as long as the pixel sizes are kept above  $2\mu\text{m}$ , which corresponds to the requirements for the targeted applications. In addition, a robust and 200mm-compatible process flow has been proposed for the fabrication of such devices.

This work is currently being used at CEA-LETI to achieve the first full-color microdisplays based on multiple quantum well conversion layers.

# Author list of publications

## Articles

**Paper I :** A. Ndiaye, A. Ghazouani, C. Seassal, E. Drouard, N. Olivier, and B. B. Bakir, "Enhanced light-extraction efficiency and emission directivity in compact photonic-crystal based AlGaInP thin-films for color conversion applications," *Opt. Express*, OE 29, 35965–35979 (2021).

**Paper II :** A. Ndiaye, H. S. Nguyen, C. Seassal, E. Drouard, and B. Ben Bakir, "Farfield pattern and guided-mode extraction analysis for highly directional emission from photonic-crystal based AlGaInP/InGaP MQW color-converters in thin-film geometry," *AIP Advances* **12**, 045122 (2022).

**Paper III:** A. Ndiaye, H. S. Nguyen, A. Ghazouani, C. Seassal, E. Drouard, N. Olivier, and B. Ben Bakir, "Enhanced conversion efficiency and tailored radiation patterns assisted by photonic-crystal light-extractors in compact MQW based color-converters for  $\mu$ LED applications," in *Light-Emitting Devices, Materials, and Applications XXVI*, M. Strassburg, J. K. Kim, and M. R. Krames, eds. (SPIE, 2022), p. 37.

**Paper IV:** A. Ndiaye, C. Seassal, E. Drouard, and B. Ben Bakir, "Generalized transfer matrix model for dipole radiation-dynamics modification in layered media: application to incoherent light-emitting structures in thin film geometry," *Opt. Continuum*, OPTCON 2(1), 31–53 (2023).

**Paper V:** P. Gaillard, A. Ndiaye, B. Ben Bakir, P. Le Maitre, J. Da Fonseca, J. M. Hartmann, M. Martin, J. Moeyaert, H. Mehdi, T. Baron, and C. Jany, "III-V Heterostructure Grown on 300mm Ge/Si Wafer for Large-Scale Fabrication of Red  $\mu$ -LEDs," *IEEE Photonics Technology Letters* 35(2), 101–104 (2023).

**Paper VI:** A. Ndiaye, A. Ghazouani, R. Sommer, E. Vermande, C. Di Nardo, C. Seassal, E. Drouard, and B. Ben Bakir, " Quasi-3D harnessing of visible light in emissive III-V on Si microstructures: Application to multiple-quantum-well color conversion layers," *Micro and Nanostructures*, Volume 185, 2024, 207721, ISSN 2773-0123,

## Conferences

Oral presentation at SPIE Photonics West 2022 (San Francisco, California)

Poster presentation at SPIE Photonics West 2022 (San Francisco, California)

Poster presentation at SPIE Photonics West 2023 (San Francisco, California)

Oral presentation at SPIE Photonics West 2024 (San Francisco, California)

## Patents

A. Ndiaye, B. Ben Bakir, " Optoelectronic device with sub-wavelength antireflective structure, associated screen and manufacturing method," worldwide patent (FR, EP, US, CN) (2023).





# Acknowledgements / Remerciements

*Wa al laisa lil insaani illaa maa sa'aa.* On obtient que le fruit de nos efforts. Un travail de presque quatre années, pour lesquelles de simples remerciements semblent peu de choses devant le nombre et la qualité des personnes qui m'ont permis de mener à bien ma thèse. Je me prête cependant volontiers à l'exercice, en espérant que ces lignes suffiront à exprimer ma profonde gratitude.

Je tiens tout d'abord à remercier chaleureusement tous les membres du jury : Pr. Henri Benisty en tant que président du jury, Pr. Henri Benisty et Pr. Dries Van Thourhout en tant que rapporteurs ainsi de Dr. Ralph Wirth et Dr. Isabelle Sagnes en tant qu'examineurs. Vous avez pris le temps d'évaluer ma thèse, vous avez su la questionner en jouant le jeu de pluri-technicité, et ce avec beaucoup de bienveillance. Pour tout cela, vous avez toute ma reconnaissance.

Au sein de mon laboratoire d'accueil, CEA-LETI/DOPT/SNAP/LCEM, qui est plus tard devenu LITE et LISE, mes remerciements vont tout d'abord à Badhise Ben Bakir, mon encadrant de thèse. Il m'a d'abord formé à tous les aspects de la photonique comprenant la conception et modélisation (théorie et phénoménologie), la fabrication et les tests. De plus son ambition et son dynamisme m'ont guidé et inspiré tout au long de ces années de thèse, sans lesquelles je ne serai pas la personne que je suis aujourd'hui. Je remercie ensuite Stéphanie Gaugiran (chef de labo à mon arrivée) et à Roch Espiau de Lamaestre (qui a pris la suite), pour m'avoir accueilli au sein de leur laboratoire. Une mention spéciale à Ahlem Ghazouani dans l'équipe filière du labo qui m'a accompagné durant toute la thèse (et même au-delà), sans qui la thèse n'en serait encore qu'au stade de « théorie ». Elle a été ma lumière pendant certaines heures sombres et m'a inspiré « in so many different ways ». Je remercie aussi particulièrement Pascale Pham et Julia Simon, qui m'ont permis de réaliser ce travail aussi indirectement, en me redirigeant vers ce sujet et mon encadrant. Merci aussi à Etienne Quesnel, Fabien Rol, Nicolas Michit, Stéphane Altazin, etc. pour toutes les discussions très fructueuses qu'on a eues durant la thèse. Et aussi merci à toute l'équipe filière du LCEM pour leur aide en me fournissant un badge d'accès à la salle, en m'indiquant une solution « éclair » ou en me débloquent un lot en salle blanche, en particulier Olivier Haon, Marion Douma, Clément Ballot, Manon Arch (merci pour tous les FIBs.). Enfin merci à Stéphanie Huet pour sa gentillesse et ses questions. Merci à toutes et tous.

Au sein de la plateforme de fabrication du LETI, je tiens aussi à remercier l'équipe du LITP, Christophe Jany, Nicolas Olivier (bonne chance pour la suite) et Romain Thibon pour leur soutien dans la fabrication, malgré que je les ai harcelés avec beaucoup de demandes de retrait de substrat après collage. Aussi merci à l'équipe choc Romain-Elisa (Romain Sommer et Elisa Vermande) qui m'ont accompagné dans chaque étape de développement des procédés qui m'ont permis d'avoir la dernière génération de composants et les efficacités attendues. Sans eux, la thèse en serait aussi et toujours au stade de théorie. Merci aussi à Christine Di Nardo pour tous les collages métal-métal et pour son enthousiasme. Un grand

merci à Fabien Laulagnet, spécialiste de l'e-beam avec qui on a pu développer de superbe litho et de tout petit motif (things are not always as they seem indeed). Merci à tous ces gens aussi qui sont en salle et font avancer les lots, les gens dont on ne parle pas, les gens qui font une grosse partie du boulot, les gens de l'ombre. Vous vous connaissez et merci à toutes et à tous.

Au sein de la plateforme caractérisation, je souhaite aussi remercier Christophe Licitra de la PFNC pour m'avoir formé à l'utilisation de son banc de photoluminescence. Il m'a aussi accompagné dans le montage de pas mal de choses, merci pour ta disponibilité. Quand il n'était pas, je m'en remettait à Younes Boussadi, maître des tests, qui m'a aidé dans mes mesures et au-delà et est devenu plus qu'un ami. Merci pour les mesures, pour le foot, pour ton aide, tes valeurs et stay whom you are.

Je remercie aussi toute l'équipe de l'INL. En commençant par mon directeur de thèse Christian Seassal, qui malgré l'éloignement géographique a été là depuis le début de la thèse et m'a accompagné dans tout ce que je faisais. Il m'a permis d'avoir du recul en apportant toujours cette vision extérieure (pas si extérieure que ça ☺). Merci Christian. Merci aussi à Emmanuel Drouard qui nous a aussi accompagné durant toute la thèse. Contrairement à ce qu'il paraît, tes questions et interrogations nous ont apporté plus de réponses que de questions. Merci pour ton aide et ton temps. Aussi, merci à Hai Son Nguyen, pour m'avoir formé à l'imagerie de Fourier et rappelé la beauté de la physique.

Daumen hoch à tous mes fellows thésards aussi, les anciens et les nouveaux. Sans les citer (je vais les citer quand-même), je parle bien sûr de Corentin Lemaoult (le foot c'est bien quand on le regarde avec un footeux !), Younes Boussadi, Eirini Sarelli, Pauline Gaillard et nos aventures aux états unis, Sultan El Badawi (chokran Jazzilan my friend), Simon Litschgi (merci pour ta gentillesse), Beatrice Wannous (avec ses onnnnn, ses welllll, sa bonne humeur et sa joie de vivre). Merci à Diego Alvaro Robayo aussi (je l'ai écrit sans checker) qui n'était pas un thésard mais en est un, avec qui j'ai pu partager ma passion du foot, des voyages et bien au-delà.

Merci à tous mes amis de Grenoble (Solemn, Céline, Elisa, Lucas Laplanche, Corentin, Younes, la team), Paris (team 07 les chocs ! et Louis Tomczyk), de Lille (Ufuk, Oussama, etc.), Senegal, Allemagne, France et finalement de partout dans le monde. Mention Spéciale à Amadou Sall Dia et Mapenda Seye qui m'ont permis de me retrouver ou de me trouver (ils sauront de quoi je parle). Stay who you are ! Vous avez tous participé à cette belle aventure qui a commencé bien plus tôt qu'au début de cette thèse

On dit que « family is power » et c'est vrai. Je voulais donc terminer en remerciant ma famille. D'abord mon père Cheikh Ndiaye, qui m'a inspiré à faire de la science et à vouloir devenir physicien à tout prix. Je ne sais pas si j'en suis un mais je te dédie cette thèse Vati et j'espère que tu en es fier. Dieuredieuf sama Yaya Boye, ma maman, mon âme, Diodio tall. Tu as été pour moi ma source de motivation, depuis le lycée jusqu'ici et j'espère aussi que tu es fier de moi. Mon frère Birama Junior Ndiaye et surtout ma sœur Awa Cheikh Ndiaye m'ont toujours permis de rester sur mon chemin ou d'y revenir quand j'ai pu oublier. Merci à ton fils Awa (le petit Mansour), mon premier neveu, qui sans le savoir m'a permis de

relativiser beaucoup de choses. Merci à vous tous d'exister. Merci aussi à ma cousine Diouma Faye et ses enfants Kyllian Mbappé (non je veux dire Camille) et Anaïs, pour m'avoir rappelé qu'il fait aussi bon vivre de l'autre côté du Rhin. Merci aussi à toute ma famille étendue. Je parle de mes oncles, tantes, cousins, cousines, tallène, ndiayène, etc. Je dédie aussi cette thèse aux membres de la famille avec qui j'ai commencé cette aventure et qui nous ont quitté au cours. Mon oncle Boubou Tall et mon grand-père Aliou Kane (je n'oublie pas les derniers conseils que tu m'as donnés). Aussi à ma grand-mère Nguada Ndoye, ton Diayli pense à toi et prie pour toi.

Veillez toutes et tous trouver dans ce travail l'expression de mon immense gratitude et affection.

Dieuredieuf

Merci

Danke Schön

Chokran

Thanks



*To my family, Diodio Tall, Cheikh Ndiaye, Awa Cheikh Ndiaye, Birama Junior Ndiaye and Mansour Samba.*

*“It is far more beautiful to know something about everything than to know everything about something; this universality is the most beautiful”,  
Blaise Pascal*

*“Il est bien plus beau de connaître peu de choses de tout que de connaître tout d’une seule chose; cette universalité est la plus belle”, Blaise Pascal*



# Table of contents

## Introduction

### Chapter I: Context and research objectives

I.1	Introduction .....	6
I.2	Microdisplay requirements for augmented reality applications .....	6
I.3	Available display technologies: LCD vs OLED vs $\mu$ -LED.....	8
I.3.1	Liquid-Crystal Display (LCD) .....	8
I.3.2	Organic Light-emitting Diodes (OLED) .....	9
I.3.3	Micro-size inorganic Light-Emitting Diodes (micro-LED or $\mu$ -LED).....	10
I.4	Strategies for full-color realization.....	11
I.4.1	Optical lens synthesis .....	12
I.4.2	White light + color filters .....	13
I.4.3	Direct color generation .....	14
I.4.4	Color conversion: benchmark comparison of mainstream color converters .....	15
I.5	Overall integration strategy and challenges.....	17
I.6	Research methodology and objectives .....	19
I.7	Conclusion.....	21
I.8	References .....	21

### Chapter II: Spontaneous emission modeling and basics of photonic-crystals for light extraction and farfield-pattern engineering

II.1	Introduction .....	27
II.2	Modeling light emission processes in planar MQW color converters.....	27
II.2.1	Spontaneous emission in an unbounded medium.....	27
II.2.2	Generalized transfer-matrix formulation in an unbounded medium .....	28
II.2.2.a	Without light source .....	28
II.2.2.b	With light source .....	29
II.2.3	Dipole emission modification in stratified media.....	30
II.2.3.a	Determination of the external fields .....	31

II.2.3.b	Derivation of the internal fields and power .....	32
II.2.3.c	Radiation patterns and extraction efficiency .....	33
II.2.4	Incoherent combination for extension to complex emitter regions .....	33
II.2.4.a	Spatially-distributed incoherent dipoles .....	34
II.2.4.b	Emitters with spectral distribution.....	34
II.2.4.c	Completely isotropic emitter's distribution .....	35
II.2.5	Flow chart summary of the implementation procedure .....	35
II.2.6	Application examples: high-index slabs to mimic MQW color-converters .....	36
II.2.6.a	MQW color-converters in vacuum .....	37
1)	Convergence study and accuracy .....	37
2)	Physical origins of spontaneous emission distribution: antinode factor, Airy function ....	39
3)	Monochromatic distributed dipole source planes .....	40
4)	Spectrally-broadened single-plane emitters.....	42
II.2.6.b	On a substrate .....	44
II.2.6.c	With a distributed Bragg reflector: LEE vs directionality .....	45
II.2.7	Conclusion on the SpE modeling framework and planar strategies .....	46
II.3	Principle of operation of photonic-crystals for light diffraction.....	47
II.3.1	Starting point: extraction issue in a single-mode waveguide .....	47
II.3.2	General overview of photonic-crystals.....	48
II.3.2.a	Foreword .....	48
II.3.2.b	Photonic crystal parameters.....	49
II.3.2.c	Different photonic-crystal integration for increasing light extraction.....	50
II.3.3	Bragg's law in a basic 2D problem: case of a single-mode waveguide .....	51
II.3.4	First-order Bragg lattice: reflection of the guided mode .....	52
II.3.5	Second-order grating: total extraction and vertical beaming to free space .....	53
II.3.6	Higher order Bragg gratings.....	55
II.3.7	Incoherent multiple-dipoles emission in a second-order grating.....	55
II.3.8	Conclusion on the analytical and numerical analysis .....	57
II.4	Conclusion.....	57

II.5	References .....	57
Chapter III: Photonic crystals for light extraction from MQW III-V membrane on transparent substrate: modeling and experimental study		
III.1	Introduction .....	61
III.2	Device fabrication .....	61
III.3	Characterization procedures .....	65
III.3.1	Micro-photoluminescence .....	65
III.3.2	Back focal plane imaging for radiation-pattern measurements .....	66
III.4	Extraction lengths.....	67
III.5	Light extraction efficiency enhancement .....	70
III.6	Directionality.....	71
III.6.1	Azimuthal radiation patterns and directionality .....	71
III.6.2	Spectrally-resolved farfield emission profiles.....	74
III.6.3	Novel design approach for highly directional emission from MQW CCL .....	78
III.6.3.a	Tailoring spontaneous emission distribution.....	78
III.6.3.b	Fine tuning the lattice period.....	80
III.6.3.c	Analysis of a measured photonic band-structure.....	82
III.6.4	Additional levers to control the directionality of the farfield patterns .....	84
III.6.4.a	Air-filling factor .....	85
III.6.4.b	Lattice symmetry .....	86
III.6.5	Conclusion.....	87
III.7	Identification of the different contributions in the experimental LEE enhancement .....	88
III.8	Coupling to an optical system with limited numerical aperture ( $NA < 1$ ) .....	90
III.8.1	Extraction length vs acceptance angle.....	91
III.8.2	Directional light extraction efficiency enhancement.....	93
III.9	Preliminary design guidelines .....	94
III.10	Conclusion.....	94
III.11	References .....	95

Chapter IV: Pixelated photonic-crystal MQW III-V membrane with back- and lateral reflectors: design and experimental demonstration.

IV.1	Introduction .....	100
IV.2	Design principles .....	100
IV.2.1	Preliminary investigations with 2D-FDTD .....	101
IV.2.1.a	Influence of a back-reflector (LOT II) .....	101
IV.2.1.b	Red color converters with vertical and lateral mirrors: Bloch-mode replication. ....	104
IV.2.2	Full 3D-FDTD simulations.....	106
IV.2.2.a	Phase-matching layer.....	107
IV.2.2.b	Gap between the MQW CCL and the bottom reflector .....	109
IV.2.3	Conclusion.....	109
IV.3	Device fabrication .....	110
IV.4	Harnessing the bottom emitted light using back reflectors: LOT II.....	115
IV.4.1	Extraction lengths, LEE enhancement and directionality.....	116
IV.4.2	Towards polarized light emission with 1D lattices .....	119
IV.4.3	Experimental evaluation of light extraction efficiency .....	120
IV.4.4	Conclusion.....	121
IV.5	Enhancing light extraction efficiency using Bloch-mode replication: LOT III.....	122
IV.5.1	Proof-of-principle experimental demonstration of Bloch-mode replication .....	122
IV.5.2	Modeling the impact of lateral-mirror losses .....	124
IV.5.3	Conclusion on the Bloch-mode replication principle .....	127
IV.6	Conclusion.....	127
IV.7	References .....	128
Chapter V: Conclusions and outlook		
V.1	Work overview.....	131
V.2	Perspectives towards the integration of MQW CCL on blue $\mu$ -LED arrays .....	134
V.2.1	Near-field coupling between the color converters and the blue pump for mode-to-mode absorption: proof of concept.....	134
V.2.2	Does further thinning the MQW epilayer help? .....	136

V.3	References .....	137
Appendix A: Description of the rigorous electromagnetic simulation techniques utilized in this work.		
A.1	Incoherent light emission with the Finite-Difference Time-Domain technique.....	140
	Incoherent and isotropic light emission.....	140
	Creating a single ‘unpolarized’ light dipole with FDTD.....	140
	Creating a spatially incoherent unpolarized LED.....	141
	Decay rates .....	142
	Light extraction efficiency and farfields .....	142
Appendix B: Photonic crystals for light extraction from MQW III-V membrane on transparent substrate: additional information		
B.1	Excitation-power dependent photoluminescence measurements .....	145
B.2	Measured vs simulated azimuthal farfield emission patterns .....	146
B.3	Vertical vs tapered profiles of the PhC patterns: simulation study .....	147
B.4	Impact of the PhC patterns on the absorption efficiency: simulation study .....	148
B.5	LEE and farfield emission patterns vs etch depth: simulation study.....	149
Appendix C: Pixelated photonic-crystal MQW III-V membrane with back- and lateral reflectors: supplemental information.		
C.1	Reflectance measurements for the back- and lateral reflectors .....	152



# Introduction

The early twentieth century has surely been the birth period of modern physics, with a plethora of major emerging scientific breakthroughs that helped us sharpen our grasp of the world around us. Among them, there was Einstein's quantum theory of radiation<sup>1</sup> in 1916 commonly known as the "mother of modern quantum electrodynamics and optics". This theory later paved the way for the first prediction of the spontaneous emission (SpE) process, which was then known to occur when an excited quantum mechanical system transitioned from a high-energy state to a lower one by emitting quanta of the electric field called photons. Subsequently, using all the advances made in quantum mechanics by Heisenberg and Schrödinger, Dirac provided a more precise description of the rates associated with this SpE mechanism in his famous quantum theory of radiation. This has marked a crucial cornerstone in the history of physics, because SpE is the ubiquitous phenomenon responsible for most of the light emission we perceive around us, ranging from light emitted by fireflies to candles.

Thereafter, it was not until the 1960s that Texas Instruments<sup>2</sup>, later followed by the SERL<sup>3</sup>, manufactured the first practical semiconductor light-emitting devices in SpE regime (GaAsP-based), commonly referred to as light-emitting diodes (LEDs). However, those devices, emitting a low power infrared or red light at the time, were labelled as "nice but useless" and only dedicated to indicators on circuit boards. This appeared to be a hasty denomination later on, considering the so-called "Haitz's law" (similar to Moore's law for microelectronics) established by Roland Haitz in 2000. This law forecasted<sup>4</sup> that every decade the amount of light emitted by an LED would increase by a factor of 20, while the cost per lumen (unit of useful light emitted) decreases by a factor of 10. Due to a wealth of continuous research efforts, the efficiency of LEDs has greatly been improved, over-fulfilling the former prediction. These endeavors have even culminated to the invention of a new energy-efficient and environment-friendly blue LED, which was awarded the 2014 Physics Nobel prize and then labelled as "an invention of greatest benefit to mankind". Indeed, those blue-LEDs combined with yellow phosphors enabled white LEDs with efficiencies over 70%, outmatching the so-far used incandescent light bulbs that converted only 5% of the electrical energy they used into light. Modern LED-based lighting was then born. Therefore, LEDs became present in almost every aspect of our lives being involved in various types of applications, ranging from UV light for water purification to solid-state lighting and display.

---

<sup>1</sup> A. Einstein, "Zur Quantentheorie der Strahlung," *Physikalische Zeitschrift*, 18, 121 (1917).

<sup>2</sup> Texas Instrument Incorporated is an American Technology Company that manufactures semiconductor devices.

<sup>3</sup> The Services Electronics Research Laboratory (SERL) is a British research and development establishment working in the military electronics.

<sup>4</sup> *Nature Photon* **1**, 23 (2007).

Particularly, the display market has rapidly evolved. Initially, it was mainly about large-panel displays such as home TVs and projectors, seeing various display technologies arising one after another. Traditional ones used to feature a cathode-ray tube (CRT), before being replaced in the 2000s by liquid-crystal display (LCD) and plasma display panels afterwards, which enabled better portability. With rapid advancements in cost-reduction and performance improvements in LCD technology, the plasma display technology became rapidly uncompetitive. Thus, despite the necessity of using color filters for colored images (see Chapter I), their slow response time and very low contrast due to their non-self-emissive nature, LCD technology has dominated the display market for several years now, at least for large-size displays.

However, the future of the display market might be mainly driven by an increasing demand of augmented-reality (AR) headsets (head-mounted or head-up) for various applications ranging from industry to healthcare including education. Indeed, human interaction with both physical and digital worlds is now to be changed in those aforementioned areas. This technology is based upon the overlay between computer-generated information (CGI) from a  $\text{cm}^2$ -size display (referred to as microdisplay), magnified afterwards, and the physical world. Large-panel displays are now miniaturized. In order to keep resolutions as high as those of large-size displays, the light emitters also needed to be miniaturized into micro-sized light-emitters (with lateral sizes less than  $5\mu\text{m}$ ). As we will see in Chapter I, AR headsets additionally require very bright microdisplays to keep the image readable with a good contrast. From all the display technologies available at the time, only micro-sized inorganic light-emitting diodes ( $\mu$ -LEDs) seem to be the next promising candidates being able to undergo the required level of luminances with a long lifetime as well as a high dynamic range and a quasi-infinite contrast<sup>5</sup>. Now, what about color?

Having a colored image from those microdisplays can be tricky. Indeed, one needs the three primary colors (Red, Blue and Green). In the beginning of this PhD thesis in November 2019, the most efficient blue and green  $\mu$ -LEDs were relying on InGaN/GaN grown on sapphire substrates while the most efficient red  $\mu$ -LEDs were made up of AlGaInP/GaInP grown on GaAs substrates. Since those material systems stem from different native substrates and have different properties, then it is not a simple task to achieve full-color microdisplays by integrating those three primary colors directly on a single wafer. In this regard, color conversion was gaining a lot of ground as a credible alternative to native RGB emission, particularly for the red spectral range.

In a standard color conversion process, an incoming pump light (often blue) is absorbed by a color conversion layer (CCL), converted into the color light (say red for blue-to-red color conversion) and extracted out of the CCL. Following that, state-of-the-art full-color microdisplays are mainly dominated by quantum-dot (Q-dot) color converters (see Chapter I), which are failing to meet the demands for

---

<sup>5</sup> Due to their self-emissive nature, the contrast values of  $\mu$ -LEDs could theoretically be infinite.

photostability (lifetime issues) and blue-light absorption (requirements for compactness and resolution) in AR headsets. Therefore, the next generation of very bright and high-resolution AR microdisplays could rely on multiple quantum well (MQW) color converters due to their better photostability and higher blue-light absorption. However, until now and to the best of our knowledge, there has not been any practical implementation of these MQW color converters in real-life RGB microdisplays yet, whether in academia or in released industrial products. Focusing on blue-to-red color conversion, we can see that this is due to the various challenges related to their low light-extraction efficiency (LEE) inherent to their high refractive indices, which drastically limits their conversion efficiencies to ~3%. Additionally, their Lambertian-like emission patterns as well as the challenges related to their integration on on-Silicon blue  $\mu$ LED arrays make the matter trickier. Due to their unique ability to diffract guided light out of high refractive-index materials and provide a simultaneous control of their radiation patterns, photonic-crystals (PhCs), periodic dielectric modulations, are used as light-extractors to solve the two former issues.

In that context, this work overall aims at investigating all the issues related to the design, integration & fabrication, as well as the testing of novel blue-to-red MQW based CCL to pave the way for their use to achieve full-color microdisplays on a single wafer. This work was achieved at CEA-LETI (DOPT/SNAP/LITE) in collaboration with INL (i-lum team). I was in charge of all the design aspects from initial modeling to final ready-to-fab tapeouts. For that purpose, I employed rigorous electromagnetic-simulation methods, herein-developed model- and simulation-frameworks as well as commercially available layout tools. Next, I defined all process flows used in this work, with the help of Ahlem Ghazouani (process integration engineer at CEA-LETI) and in collaboration with process engineers. As for the fabrication, all the devices (on transparent and silicon substrates) utilized here have been fabricated during this work in CEA-LETI's 200mm cleanroom facilities, where I monitored every step of the flow by performing in-line metrology. I finally performed all the device-testing procedures: measurements in real-space for evaluating the photoluminescence enhancement factors by the PhCs (at CEA-LETI) and Fourier imaging (at INL) for farfield-pattern measurements.

# **Chapter I**

## *Context and research objectives*

## Table of contents

I.1	Introduction .....	6
I.2	Microdisplay requirements for augmented reality applications .....	6
I.3	Available display technologies: LCD vs OLED vs $\mu$ -LED.....	8
I.3.1	Liquid-Crystal Display (LCD) .....	8
I.3.2	Organic Light-emitting Diodes (OLED) .....	9
I.3.3	Micro-size inorganic Light-Emitting Diodes (micro-LED or $\mu$ -LED).....	10
I.4	Strategies for full-color realization.....	11
I.4.1	Optical lens synthesis .....	12
I.4.2	White light + color filters .....	13
I.4.3	Direct color generation .....	14
I.4.4	Color conversion: benchmark comparison of mainstream color converters .....	15
I.5	Overall integration strategy and challenges.....	17
I.6	Research methodology and objectives .....	19
I.7	Conclusion.....	21
I.8	References .....	21

## I.1 Introduction

This chapter describes the technological context of this work while highlighting its research objectives. First, we present the specific requirements of augmented reality (AR) headsets and the available display technologies to achieve them. Then, we focus on the different strategies that are currently being investigated to realize full-color emission on a single wafer with a special focus on color conversion. Afterwards, the challenges related to multiple quantum well (MQW) color converters follow. To finish with this chapter, the overall integration strategy and research objectives of this work are specified.

## I.2 Microdisplay requirements for augmented reality applications

The future of the display market might be dominated by head-mounted displays such as AR headsets, which have been attracting significant endeavors and attention [1]. Indeed, this technology has gained a great momentum in various types of applications, ranging from military purposes [2] (to help pilots in cockpits display additional information on their windshields) to medical [3], industrial [4] and even educational applications [5]. In **Figure I-1-a**, a typical scene is depicted where the user displays additional information from Google Maps related to the time, temperature, geographic location, etc. on glasses for navigation purposes.

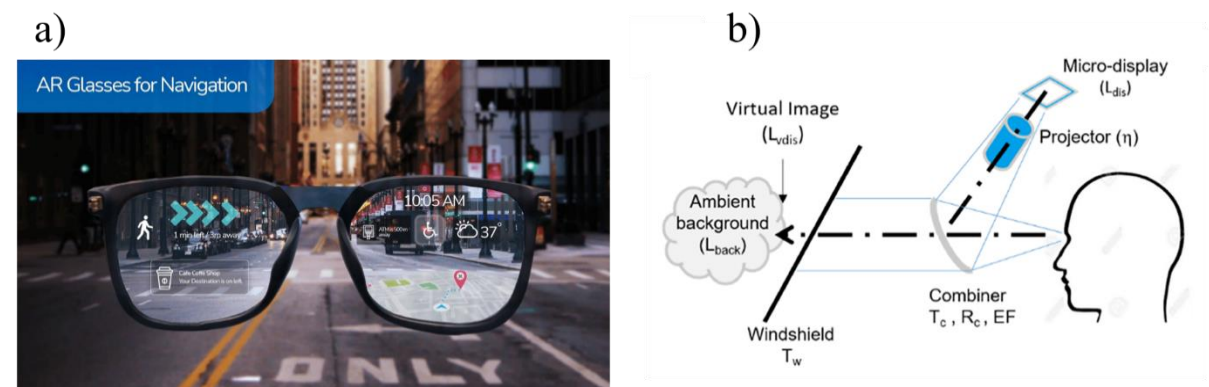


**Figure I-1** : a) Use-case example of AR glasses for navigation purposes<sup>1</sup>. b) Basic elements embedded in a typical AR headset [1].

The specificity of this technology relies on its ability to enrich human interaction with both the physical and digital worlds by overlaying a computer-generated information (CGI) displayed on a transparent surface and the physical environment. In this see-through configuration, a schematics of the basic elements embedded in a typical AR glass is provided in **Figure I-1-b**. The digital information is encoded into light emitted by the microdisplay, which is only a few cm<sup>2</sup>-size. This image needs then to propagate through a dedicated optical system represented here by the projector and combiner before being reflected back to the viewer's eyes. The roles of the optics are to magnify and shape the digital image for it to be

<sup>1</sup> <https://www.queppelin.com/ar-glasses-for-navigation/>

adequately perceived by the user. Thus, to provide an acceptable user-experience, one needs to make sure that these so-formed images are readable enough with bare human eyes.

A standard feature to assess this readability is the ambient contrast ratio (ACR), which is the ratio of the luminance of the CGI relative to the real-world background. It reads as [1]:

$$ACR = \frac{L_{vdis} + T_c L_{back}}{T_c L_{back}} \quad \text{with} \quad L_{vdis} = \frac{\eta R_c}{EF} \cdot L_{dis}. \quad (\text{I-1})$$

Here,  $L_{vdis}$  and  $L_{back}$  are the luminances of the CGI collimated to infinity and perceived by the observer and the one of the real-world background, respectively.  $T_c$ ,  $R_c$  and  $\eta$  account for the optical transmittance and reflectance of the combiner, as well as the efficiency of the projection optics, respectively.  $EF$  is the expansion factor of the exit pupil of the combiner, which can range from one for classical combiners to 10 for combiners including optical waveguides.  $L_{dis}$  is then the luminance of the light emitted by the microdisplay before it goes through the optical system. Under typical illumination conditions, ACRs of 3:1, 5:1 and 10:1 are required for recognizable images, adequate readability and appealing qualities, respectively [6]. Following those considerations, one can find that values of  $L_{vdis}$  of  $\sim 20,000$  cd/m<sup>2</sup> are a good compromise under 34,000 cd/m<sup>2</sup> of background luminance (very bright sunlight) to ensure adequate readability. Taking into account standard values for the overall throughput of the optics [1], this translates into values of  $L_{dis}$  as high as 1,000,000 cd/m<sup>2</sup>. This ultimate luminance requirement at the display level is technologically very demanding, since it sets some constraints on the technology control and the material quality.

Therefore, the ultimate light sources able to meet those requirements would need to be efficient enough to reach those high luminances and stable enough to undergo those conditions for a long lifetime ( $>10,000$  hours at their operating points [7]). Nevertheless, it is not quite all! Indeed, in addition to those luminance requirements, the microdisplay also needs to have very high resolutions (sometimes  $>2000$  pixel per inch) for the devices to be compact and portable, as well as high color purity which translates into narrow emission peaks [1].

Finally, as we have seen in **Figure I-1-b**, light generated at the microdisplay level propagates through optical elements, each of them having a limited numerical aperture (NA). As a result, only a part of the light emitted at the display level will go into the optical systems. Standard implementation of AR headsets often include additional collimating refractive lenses to reshape the output beams and thereby help alleviate this issue, but they tend to be very bulky and heavy [8]. Hence, light emitted by the microdisplay also needs to be as directional as possible to avoid using additional optics.

It thus appears that the display technology embedded in AR glasses needs to be efficient enough, stable under constraining conditions, highly resolved for better compactness and image quality, directional enough to avoid using additional external optics and with high color purity. In the following, a brief

benchmark study of the available display technologies for AR headsets is performed, based on the aforementioned considerations.

### I.3 Available display technologies: LCD vs OLED vs $\mu$ -LED

State-of-the-art microdisplays rely on three main technologies: liquid-crystal display (LCD), organic light-emitting diode (OLED) and micro-size inorganic light emitting diodes ( $\mu$ -LEDs) [9]. In this section, we benchmark all the three different technologies regarding the aforementioned requirements for AR headsets. In **Table I-1**, basis of this study, we report on the main characteristics of those technologies.

**Table I-1** : Benchmark study of the existing display technologies [9].

Display technology	LCD	OLED	$\mu$ -LED
Emission mechanism	Backlight + color filters	Self-emissive	Self-emissive
Luminance	$< 3 \times 10^4$ cd/m <sup>2</sup>	$< 2 \times 10^4$ cd/m <sup>2</sup>	$\sim 10^6$
Lifetime	Medium	Short	Long
Contrast	$5 \times 10^3 : 1$	$10^5 : 1$	$10^6 : 1$
Resolution (pixel per inch)	$< 8 \times 10^2$ PPI	$< 10^3$ PPI	$\sim 6 \times 10^3$ PPI
Response time	ms	$\mu$ s	ns
Operating temperature	$\sim 20$ to $80^\circ\text{C}$	$\sim 30$ to $70^\circ\text{C}$	$\sim 100$ to $120^\circ\text{C}$
Color gamut	Medium	Excellent	Excellent
Technological maturity	High	High	Low
Cost	Low	Low	High

#### I.3.1 Liquid-Crystal Display (LCD)

Currently utilized in a wide range of applications (mostly large-panel displays) such as LCD televisions, computers, etc., LCD is a flat-panel display that relies on the light-modulating characteristics of liquid crystals. Schematics of the basic elements comprised in a LCD are provided in **Figure I-2**.

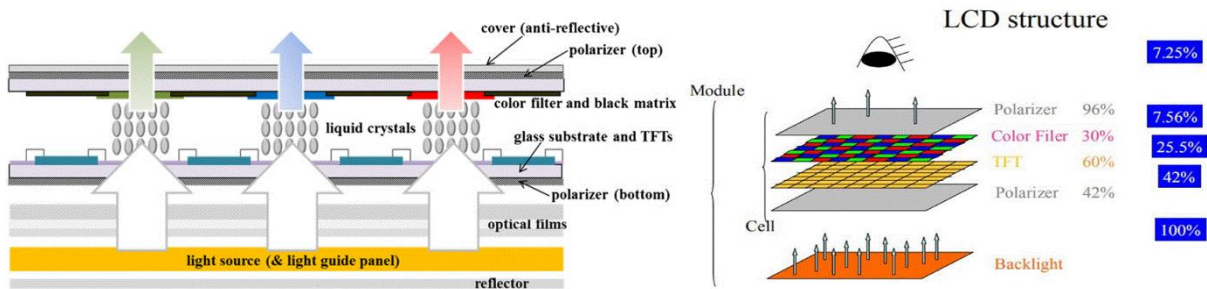


**Figure I-2** : Overall architecture of a TFT-LCD display. The transmission coefficient values of each of the embedded layers are provided [10].

There are generally four main elements embedded in this type of technology: the backlight panel, the polarizers, liquid crystals with the thin-film transistor (TFT) layers and color filters. Liquid crystals do not emit light; rather depending on the polarization of the incoming light, they are either transparent or dark. Light is generated by a backplane standardly composed of blue LEDs covered with yellow phosphors, which act as color-converting materials. The resulting white light propagates through a

polarizer allowing often only ~42% of the light to be transmitted. This polarized light then goes through the TFT layer, which controls the orientation of the liquid crystals by applying a voltage difference. Depending on the matching between the polarization of the incoming light and the orientation of those molecules, the pixel state is either dark (no transmission) or white (transparency). Subsequently, in order to obtain a colored image, the resulting light needs then to go through color filters. Despite its indisputable advantage related to its technological maturity, the implementation of this technology for AR glasses is hindered by lots of drawbacks. First, because the molecule orientation is electronically controlled, their contrast is limited to 5,000:1 considering their poor black level. Besides, every layer embedded in this technology has a limited transmittance, which usually leads to an overall throughput of ~7% (see **Figure I-2**), clearly limiting the reachable luminances to ~30,000 cd/m<sup>2</sup> in most advanced implementation schemes. Moreover, their low resolution and response time clearly do not match the requirements of AR glasses (see **Table I-1**). All these performances can hold for head-mounted display applications such as virtual reality (VR), but they are clearly not enough for the aforementioned requirements of AR applications.

### I.3.2 Organic Light-emitting Diodes (OLED)

Contrary to LCD-based technology, OLED microdisplays are self-emissive technologies that do not rely on a backlight for light emission. The standard architecture of mainstream OLED stacks is displayed in **Figure I-3-a**.

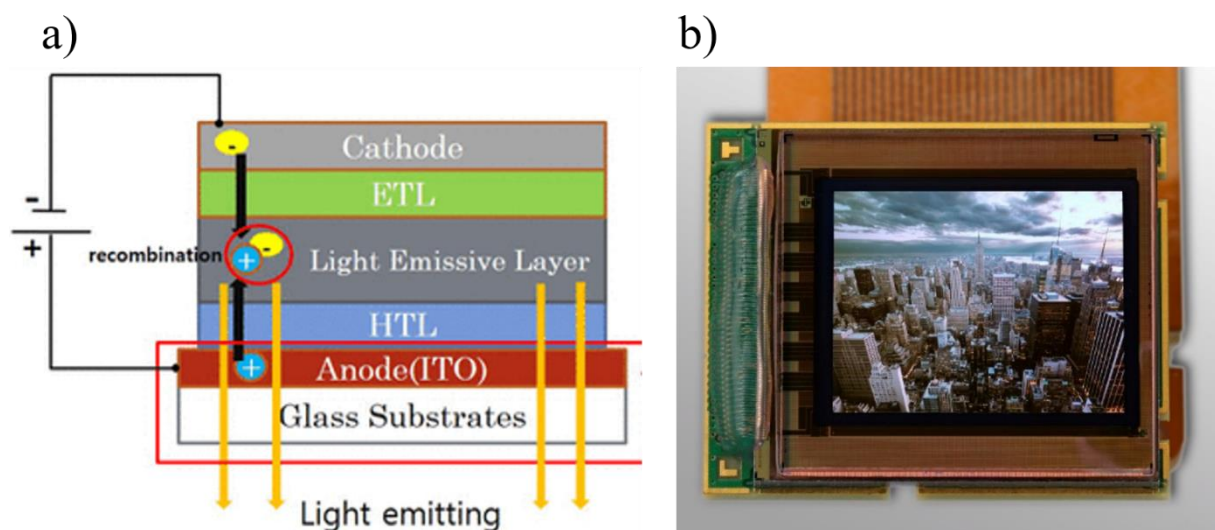


**Figure I-3**: a) Schematics of the basic elements composing mainstream OLED displays [11]. b) Example of an OLED microdisplay from the company Microoled<sup>2</sup>.

Carriers (holes and electrons) are injected into the structures through electrical contacts (anode and cathode). They are subsequently transported by electron- and hole-transport layers (ETL and EHL, respectively) to the active region where they can recombine radiatively while emitting photons. The so-

<sup>2</sup> <https://www.dpreview.com/articles/1543086327/microoled>

generated light is generally emitted outside through the backside of the structure (bottom emitting OLED) by using the cathode as a top reflector [12]. Due to this self-emissive nature, OLEDs (initially developed in the early 90s) now seem to overcome many challenges of LCD-based technologies. Indeed, they have a far better contrast approaching the requirements of AR headsets. In addition, they exhibit a faster response time, a higher resolution, a larger color gamut and a very good technological maturity (see **Table I-1**). Hence, they have rapidly become the mainstream technologies for smartwatches, smartphones and some head-mounted displays (see **Figure I-3-b**, already commercialized by the company Microoled through their AR division ActiveLook).

Nonetheless, despite all those advantages, their utilization in AR headsets is hindered by issues inherent to their organic nature. Indeed, since they are made up of organic materials, they cannot undergo the high luminances required for outdoor usage for so long [13]. In fact, they experience a rapid decrease of their efficiencies under high-luminance conditions with maxima of 20,000 cd/m<sup>2</sup> and 3,000 cd/m<sup>2</sup> for best performing commercial monochrome and bicolor OLED-based microdisplays [14], respectively, which does not meet the lifetime requirements of AR applications. In addition to those lifetime issues, they also need very advanced encapsulation schemes for long-term environmental stability, which generally also limits their brightness [13].

Those stability and lifetime issues do not make them suitable candidates for AR microdisplays.

### I.3.3 Micro-size inorganic Light-Emitting Diodes (micro-LED or $\mu$ -LED)

Like OLED-based technology,  $\mu$ -LED displays are also self-emissive with a similar architecture to those of OLED displays. As a result, they also dispose of a very high contrast and a very high resolution, which are paired with a nanosecond response time and a very wide color gamut (see **Table I-1**). In addition, due to a wealth of research efforts, they have rapidly evolved from “nice but useless” to the “ultimate lamp”, capable of delivering very high luminances within a very long lifetime. Indeed, for instance at CEA-LETI, gallium nitride (GaN) based  $\mu$ LED arrays exhibiting luminances as high as 10<sup>6</sup> and 10<sup>7</sup> cd/m<sup>2</sup> have been demonstrated for blue and green arrays, respectively, operating within a reasonable number of hours [15].

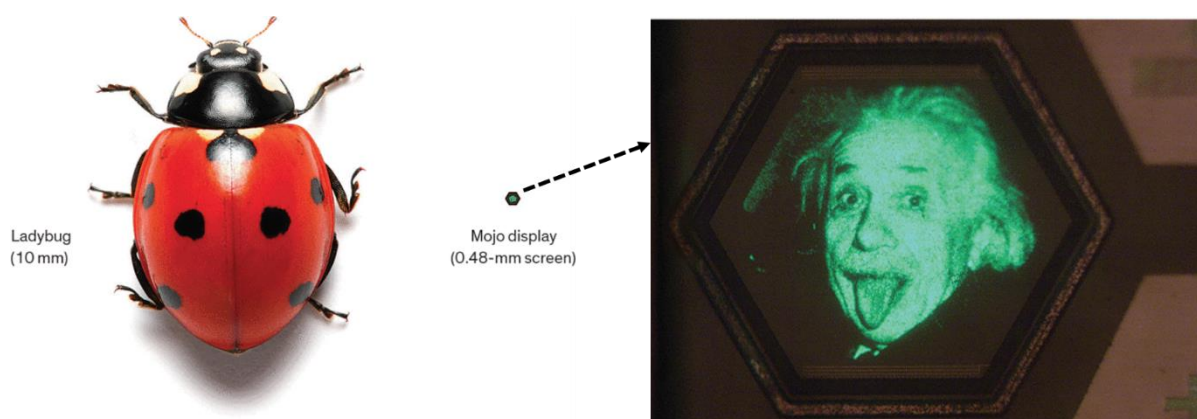


**Figure I-4:** “Bright and tiny”  $\mu$ -LED display from the company Mojo Vision with a resolution of 14000 PPI [15].

Other technological developments of such “bright and tiny”  $\mu$ -LED display have continued and more recently, the company Mojo vision has unveiled its monochrome green  $\mu$ -LED display with a resolution of 14000 PPI as displayed in **Figure I-4**. With a size of only half a millimeter across, the whole microdisplay is only barely bigger than a single pixel from the  $\mu$ -LED large-panel display prototyped by Samsung in 2018<sup>3</sup>!

In summary, notwithstanding their still low maturity<sup>4</sup> compared to OLED- and LCD-based technologies, the rapid expansion of  $\mu$ -LEDs seems to make them the only technology that could help meet all the constraining requirements of AR applications as of now. The AR headset that we aim at developing in this work will then be based on this approach.

The next question that arises is the following: how does one efficiently realize full-color emission from  $\mu$ -LED arrays?

#### **I.4 Strategies for full-color realization**

To develop a full-color  $\mu$ -LED display for AR glasses, one needs to integrate at least the three primary colors per pixel (R for red, B for blue and G for green) on a single wafer. This monolithic integration is a bit tricky.

Indeed, one of key parameters to control the color of the light emitted by a  $\mu$ -LED is its bandgap, which partly depends on the concentration of the different atoms composing the layers of its epitaxial stack. For red  $\mu$ -LED, the initial choices could be epitaxial structures based on the  $\text{Al}_x\text{Ga}_{1-x}\text{As}$  material system. These ternary alloys have the advantages of being grown lattice-matched on GaAs across the entire possible Aluminum (Al) molar fraction and could span wavelengths from infrared (GaAs, 870nm) to red ( $\text{Al}_{0.45}\text{Ga}_{0.55}\text{As}$ , 621nm). However, below the latter wavelength ( $x > 0.45$ ), their bandgap becomes indirect and their radiative rates rapidly decrease. Those drawbacks, paired with the large Al concentration required to reach red emission (~45%), lead to the increasing use of quaternary alloys based on the AlGaInP material system [17,18]. Those alloys can also be grown lattice-matched on GaAs substrates ( $(\text{Al}_x\text{Ga}_{1-x})_{0.52}\text{In}_{0.48}\text{P}$ ) with lower Al fraction and cover a large part of the visible spectrum ranging from red ( $\text{G}_{0.52}\text{In}_{0.48}\text{P}$ , 650nm) to yellow ( $(\text{Al}_{0.53}\text{Ga}_{0.47})_{0.52}\text{In}_{0.48}\text{P}$ ). Therefore, there have been extensive studies on AlGaInP based red  $\mu$ -LEDs and AlGaInP is being foreseen as the material of choice for devices emitting at the long wavelength range [18]. However, due to the still-present direct-to-indirect bandgap transition, their external quantum efficiencies (EQE) abruptly decrease as we approach the green and blue spectral ranges.

---

<sup>3</sup> <https://displaysolutions.samsung.com/led-signage/the-wall>

<sup>4</sup> Since the  $\mu$ -LED epilayer comprises materials that are scarcer and whose fabrication is still an issue,  $\mu$ -LEDs are not yet widespread in many applications. On the contrary, OLEDs, which are easier to fabricate, are mainly employed in all the current applications. However, for high-luminance AR applications such as in this PhD work, only  $\mu$ -LEDs seem to be promising.

For blue and green emission on the other hand, state-of-the-art  $\mu$ -LEDs mostly rely on  $\text{In}_x\text{Ga}_{1-x}\text{N}$  alloys. Theoretically, the entire visible spectrum could be spanned from infrared (0.69 eV) to ultraviolet (3.42 eV) by varying their Indium (In) composition. Following that consideration and thanks to a wealth of research efforts, quite efficient blue and green InGaN/GaN based  $\mu$ -LEDs have been demonstrated [15,19,20]. However, in the red spectral range ( $x \geq 40\%$ ), the EQE of those  $\mu$ -LEDs start to rapidly decrease. This decrease has mainly been attributed to two phenomena. On the one hand, the high indium content in the active region increases the lattice mismatch between the different epitaxial layers, which leads to a poor crystal quality: this phenomenon actually starts to become compelling in the green spectral range [7]. On the other hand, a high indium content increases the so-called quantum-confined Stark effect (QCSE) resulting in a decrease of the overlap integral of the electron and hole wave-functions and, therefore, a decrease of the radiative recombination efficiency [21].

Hence, InGaN/GaN material systems are used for blue and green  $\mu$ -LEDs, while AlGaInP/InGaP material system is dedicated to the red emission. Since those material systems stem from different native substrates and have different properties, it is not an easy task to achieve a full-color  $\mu$ LED-based microdisplay. There are four main technological routes for that purpose: optical lens synthesis, white light combined with color filters, direct color generation and color conversion. In **Figure I-5**, we provide a summary of those four strategies, which will serve as a basis for the analyses of the following subsections.

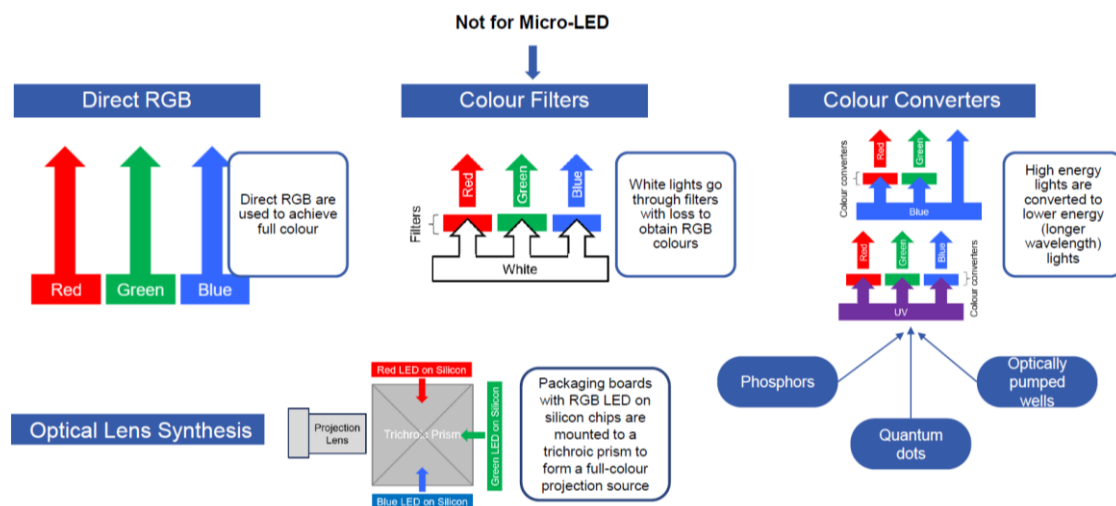


**Figure I-5:** Summary of the main strategies for full-color emission with  $\mu$ LED-based microdisplays<sup>5</sup>.

#### I.4.1 Optical lens synthesis

The first and most straightforward way to obtain full-color emission is to fabricate three different  $\mu$ -LED chips for each primary color and to combine those colors using optical systems.

<sup>5</sup> <https://www.idtechex.com/en/research-report/micro-led-displays-2020-2030-technology-commercialization-opportunity-market-and-players/738>

To the best of our knowledge, the most advanced prototype-implementation of this scheme was realized in 2013 by Chong et al. [22] from the Hong Kong University of Science and Technology (HKUST), where blue, green and red  $\mu$ -LED chips were separately fabricated and attached to signal boards. Those signal boards were then mounted on a trichroic prism, which combines the three primary colors (see **Figure I-6-a**). Although a 15'' full-color HKUST logo has been successfully projected on a wall (see **Figure I-6-b**), this approach is not a viable solution for  $\mu$ -LED displays, due to its bulkiness and its low technological maturity. There is thus a need for more monolithic approaches where RGB emission is achieved on a single wafer.

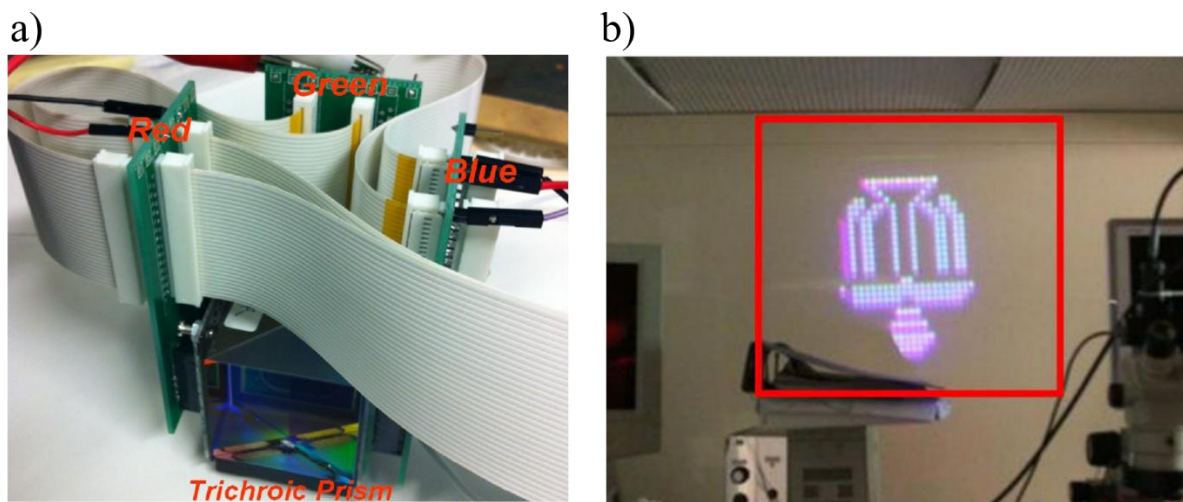


**Figure I-6:** a) “3LED system” with a trichroic mirror for optical lens synthesis and signal boards with RGB  $\mu$ -LED chips. b) Demonstration of the world first full-color “3LED” projection system (the logo of the Hong Kong University of Science and Technology is displayed) [22].

#### I.4.2 White light + color filters

Another route to develop full-color  $\mu$ -LED display within a monolithic integration scheme is to start with white light and use color filters. This strategy is inspired by what used to be done in LCD-based technologies as mentioned before. A very recent realization of this strategy has been achieved by Gou et al. in 2019 [23] and is depicted in **Figure I-7**. The architecture consists of a GaN-based blue  $\mu$ -LED array, which pumps red and green phosphor downconverters to obtain white light first. Next, color filters are fabricated on top along with a black matrix to obtain RGB subpixels. One of the main issues inherent to this strategy was the crosstalk between two subpixels due to the diffusive nature of phosphors [24]. However and very surprisingly, Gou et al. managed to eliminate this crosstalk by incorporating their phosphor-based converters in an array of tapered funnel tubes, whose inner sides have been covered with a reflective coating (see **Figure I-7**). The implementation of this strategy in AR glasses would however be hindered by some technological challenges. First, due to the use of color filters, roughly two thirds of the incoming light is lost per subpixel, which would increase the energy consumption of the resulting device. Besides, phosphors (similarly to OLEDs) cannot undergo very high luminances within a reasonable lifetime. Indeed, they can experience a rapid luminescence quenching (decrease of the emitted intensity) under high-luminance conditions. Finally yet importantly, phosphors and particularly

red ones suffer from a very low absorption efficiency in the UV/blue spectral range [25]. One way to overcome this challenge would simply be to increase the thickness of the color-converting layer. However, roughly more than  $100\mu\text{m}$  would be needed for complete blue light absorption, which would definitely lead to aspect ratio issues for pixel lateral sizes below  $5\mu\text{m}$  (target in AR glasses). Other research groups even tried to include distributed feedback reflectors (DBR) to recycle the non-absorbed blue light, but this would definitely degrade the brightness of the overall device as shown in [26].

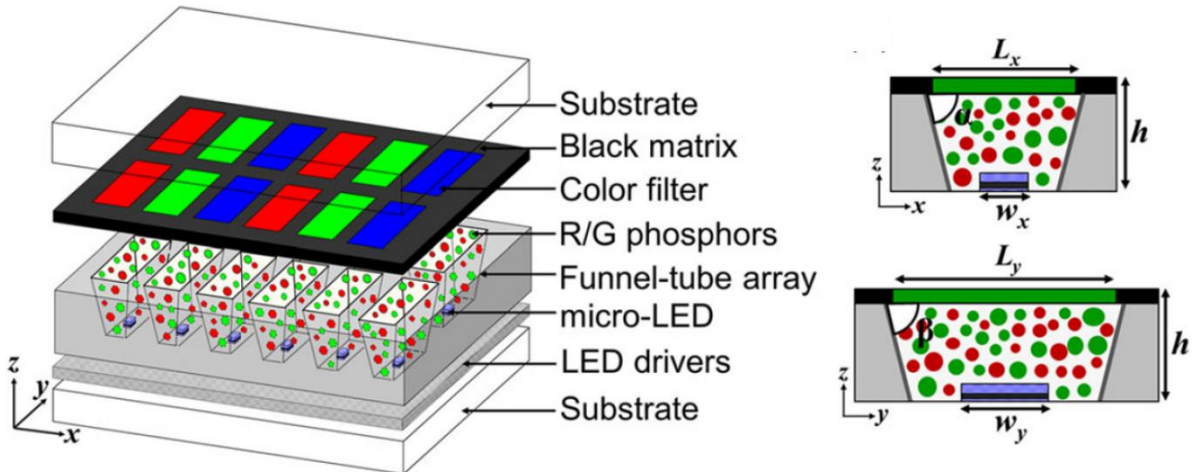


**Figure I-7:** Schematics of a full-color  $\mu$ -LED display based upon white light + color converters. Funnel tube arrays are filled with R/G phosphors to generate white light from a blue incoming pump and suppress the crosstalk between subpixels [23].

Thus, albeit an improved conversion efficiency and vivid colors with this novel approach, this strategy would not be viable for AR applications.

### I.4.3 Direct color generation

Instead of converting the blue incoming light into white light first, recent technological developments have been focused on straightforward approaches based on mass transfer methods [27,28]. Direct color generation (DCG) gathers all the techniques that consist of having three native color emitters as subpixels on a single wafer. A description of the standard way to realize that is provided in **Figure I-8**.

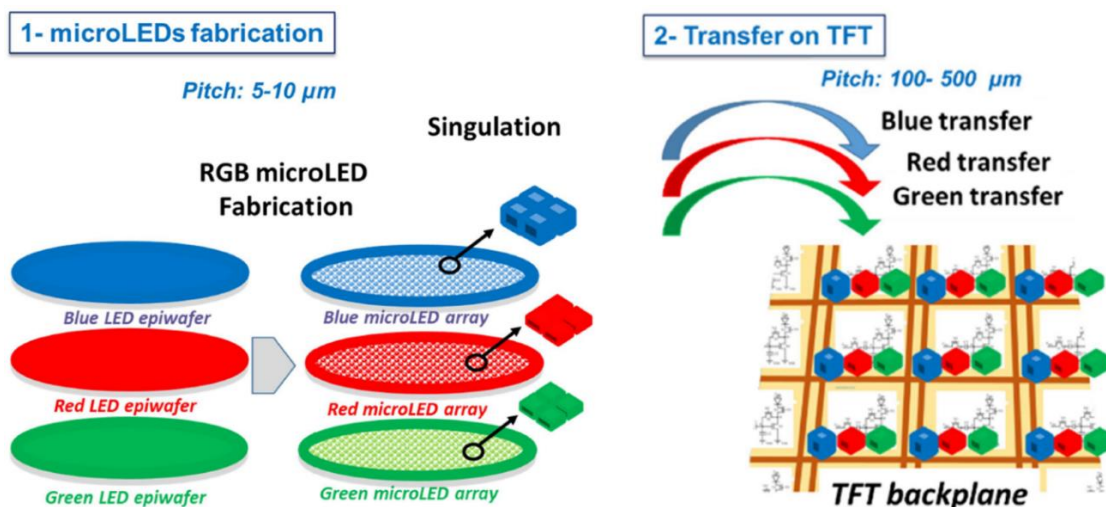


**Figure I-8:** Standard mass-transfer approach for fabricating full-color microdisplays [27].

It can be roughly seen as a three-step process. Blue, green and red  $\mu$ -LED chips are initially fabricated separately. They are then diced either into individual pixels or into a group of them and afterwards transferred onto a backplane driving circuit. The driving circuit can be based on either TFT technologies or novel CMOS electronics depending on the level of brightness needed [27].  $\mu$ -LEDs can be fabricated separately on different chips with quite reasonable efficiencies but one the main bottlenecks of this approach is to obtain an efficient transfer-method. For a transfer-method to be actually technologically viable, there are three important factors: yield (number of pixels transferrable without defects), speed of the transfer (which determines its costs) and easiness to repair when a pixel is “dead”. The ideal technique has been evaluated<sup>6</sup> to need a speed of a least 100 million units of pixel per hours, a yield over 99.9999% and a placement accuracy of  $\pm 1\mu\text{m}$ .

Different transfer techniques are currently being investigated but the most standard one is based on the massive parallel pick-and-place approach. In this approach, a transfer head is used to pick over thousands of pixels from the native chips and transfer them to the backplane driving circuits. As a result, its resolution is for now limited to 100-400 PPI level display applications such as smart watches, TVs, etc., but their use for high-resolution displays such as AR displays is still under investigation [27]. Further improvements are also needed in terms of its speed and transfer yields. Let us however note that even if all those challenges were overcome, one main issue would remain which is that AlGaInP and InGaN material systems have different properties. Although they work separately quite efficiently for blue-green and for red, once on the same chip their driving conditions would be very challenging due to the mismatch between their threshold voltages as show in [7].

Despite the various efforts many companies such as Ostendo [29] as well as a plethora of research groups [30,31] are currently putting into finding new approaches for DCG, these techniques are still failing to comply with the requirements of AR glasses in terms of feasibility.

#### I.4.4 Color conversion: benchmark comparison of mainstream color converters

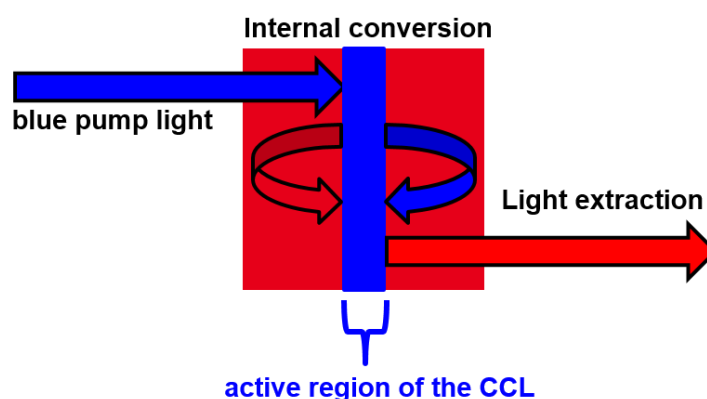


**Figure I-9:** Schematics depicting the color conversion process from blue to red.

<sup>6</sup> <https://www.idtechex.com/en/research-report/micro-led-displays-2020-2030-technology-commercialization-opportunity-market-and-players/738>

Due to all the aforementioned issues, color conversion is gaining a lot of ground as a credible alternative to mass-transfer techniques and optical lens synthesis. We use this technology in this PhD thesis, particularly focusing on blue-to-red color conversion.

Color conversion has already been a key-technology strategy in many applications in the field of optoelectronics, e.g., solid-state lighting [32], optical communication [33] and more recently information display [34]. Particularly in microdisplays, its core mechanism is quite clear-cut as portrayed in **Figure I-9**. The incoming pump light comes from a blue  $\mu$ -LED array. This pump light needs to be efficiently absorbed by the color-converting layer (CCL), converted into red light in the active region and then extracted out of the CCL. The efficiency of this conversion process is often assessed by the external photoluminescence quantum yield (EPLQY) which is the ratio between the number of down-converted photons extracted out of the CCL and the number of blue incoming pumping-photons [34]. It can thus read as:

$$EPLQY = \eta_{abs} \times IQE \times LEE. \quad (I-2)$$

Here  $\eta_{abs}$ ,  $IQE$  and  $LEE$  account for absorption efficiency, internal quantum efficiency and light extraction efficiency, respectively. Hence, an ideal CCL would maximize those three factors.

Various types of CCL have already been implemented in the literature, particularly in the red spectral range. Phosphor-based color conversion is the first route at hand, since it has already been widely applied in LED-based solid-state lighting [32]. However, due to their very low absorption efficiency in the blue spectral range, they need to be thicker than 100 $\mu$ m to maximize the absorption of the pump and thus the EPLQY [25]. This would clearly be challenging and lead to aspect ratio issues for AR glasses, since pixel lateral sizes can be less than 5 $\mu$ m. Thereupon, state-of-the-art RGB microdisplays mainly rely on colloidal quantum dots (Q-dots) pumped by blue  $\mu$ -LEDs. Q-dots are nanosized semiconductor crystals whose most compelling characteristic is the tuneability of their bandgap as a function of their size. Due to their narrow emission linewidth and low fabrication costs, various prototypes and even commercialized products exist [35,36]. However, they have not been extended to AR glasses yet for various reasons. To begin with, like phosphors Q-dots also suffer from a low absorption efficiency in the blue spectral range, which drastically limits their EPLQY. This could also lead to aspect ratio issues since they need to be thicker than 10 $\mu$ m for complete blue light absorption [37]. Moreover, one of the most serious concerns related to their implementation is their lack of photostability, meaning that they cannot undergo the high luminances required by AR glasses without experiencing a photoluminescence quenching (large intensity decrease) [1]. Additionally, they raise serious questions as far as their toxicity is concerned. In fact, despite the emerging InP-based Q-dots, their CdSe-based counterparts [7], which remain the most efficient ones, contain heavy metals that can be toxic to living beings [38]. All these considerations are summarized in **Table I-2**.

**Table I-2:** Benchmark study of the different blue-to-red conversion strategies and challenges.

<b>Color conversion route</b>	<b>Blue absorption (absorption coefficient <math>\alpha</math>)</b>	<b>Conversion efficiency limitation factor</b>	<b>Photostability</b>
Phosphors	Poor ( $\alpha < 0.01 \mu\text{m}^{-1}$ )	$\eta_{abs}$	Photoluminescence quenching under high incident flux
QDs	Moderate ( $\alpha \sim 0.1 \mu\text{m}^{-1}$ )	$\eta_{abs}$	Photoluminescence quenching under high incident flux
MQW (InGaP/AlGaInP)	High ( $\alpha > 1 \mu\text{m}^{-1}$ )	$LEE$	Stable by nature (epilayer)

In this regard, inorganic multiple quantum well (MQW) CCL could therefore gain a great momentum as an alternative to Q-dots for AR microdisplays. Within this approach, the CCL would comprise an epitaxial structure with an active region composed of quantum wells and able to efficiently in-couple all the incoming blue light. InGaP/AlGaInP material system would thus be a great choice for these blue-to-red color converters. They have already been implemented in several applications in optoelectronics ranging from solar cells [39] to electrically pumped LEDs [40], because they offer a very high blue light absorption (thus they could be made thinner than  $1\mu\text{m}$  and exhibit no transmission of the incoming blue light) and exciting performances. Besides, due to their epitaxial nature, they can undergo very harsh conditions without degrading and in this way have a far better photostability than Q-dots [1]. Due to all these considerations, MQW color converters might be the only alternative to Q-dots in AR applications involving very high luminances (need for photostability) and compact integration schemes (need for CCL thinner than  $1\mu\text{m}$ ). However, until now and to the best of our knowledge, there has not been any practical implementation or investigation of these MQW color converters for real-life RGB microdisplays yet, whether in academia or released industrial products due to some challenges they are facing.

That is the reason why in this work, we investigate the possibility of implementing this novel approach for blue-to-red color conversion in AR microdisplays.

### **I.5 Overall integration strategy and challenges**

As mentioned before, MQW color conversion layers (CCL) could be the next “big thing” in AR microdisplays, since they could substitute state-of-the-art Q-dot color converters when the required luminances are too high (photostability issues) and when high resolutions are at stake (need for compact integration schemes). However, their implementation is still hindered by some challenges that we are going to tackle in this PhD thesis, particularly for blue-to-red color conversion. The first one is related to their low LEE inherent to their high refractive indices. Indeed AlGaInP has refractive indices over three in the red spectral range, so most of the emitted red light will couple to the available guided modes inside the so-formed membrane and drastically limit their maximum reachable EPLQY to  $\sim 3\%$ . It has

recently been evaluated that for a CCL to be able to reach the targeted luminances in AR microdisplays, its efficiency must reach values between 40 and 50% [34]. These light-extraction issues need then to be dealt with and there is still a large gap to bridge.

A schematic side view of a possible integration strategy of those MQW color converters on on-Silicon blue  $\mu$ -LED array is displayed in **Figure I-10**.

A GaN-based blue  $\mu$ -LED array is used to pump blue-to-green and blue-to-red MQW CCL. In this work, we focus on blue-to-red color conversion. As we can see in this integration strategy, not only must light extraction issues be solved, but also additional application-driven requirements need to be taken into consideration.

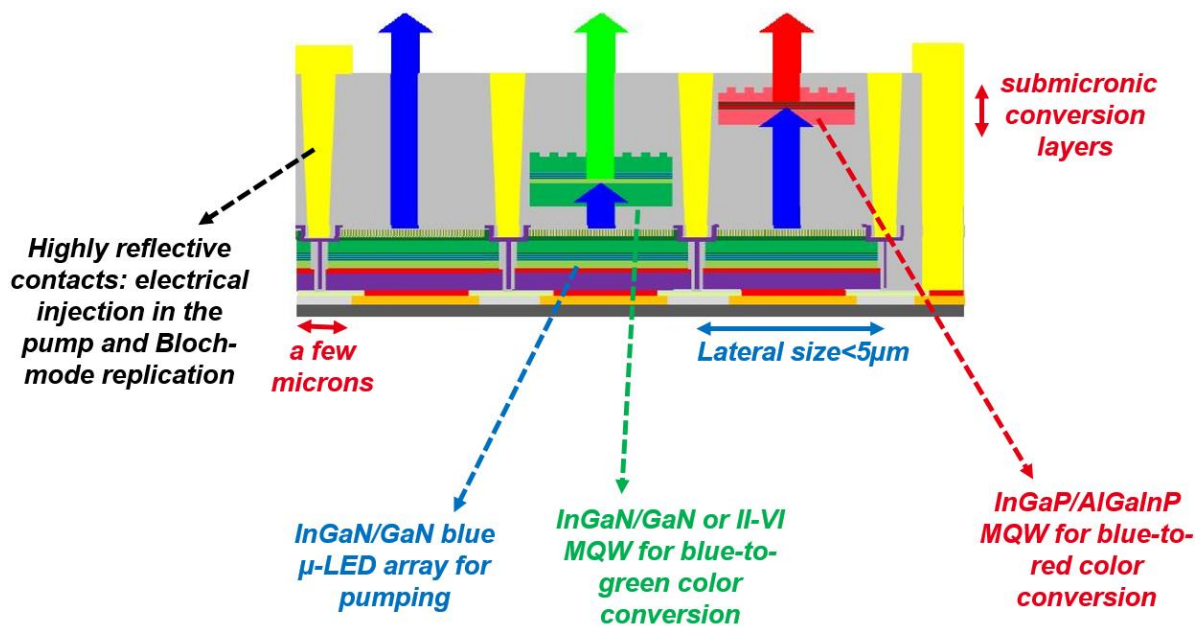


**Figure I-10:** Schematic side view of a possible integration strategy for monolithic RGB emission using MQW color converters (not at scale).

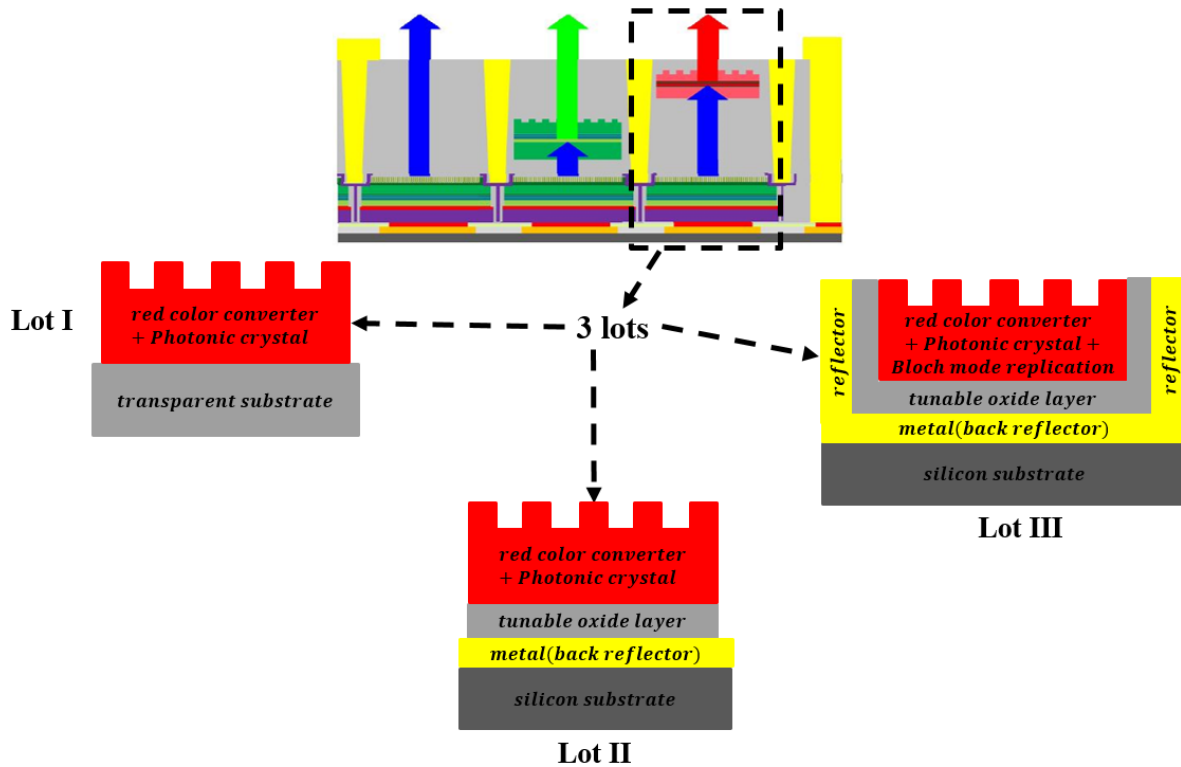
To begin with, the resolution is a key-element in the product development for AR microdisplays. Indeed, in this application, pixel lateral sizes denoted  $L_{\text{pixel}}$  can be less than  $5 \mu\text{m}$ . This means that not only must most of the emitted light be extracted, but also the extraction length  $L_{\text{ext}}$  (the lateral extent needed to extract most of the guided light) needs to be shorter than  $L_{\text{pixel}}$ . Besides, as we have mentioned in **section I.2**, the light source needs to be as directional as possible in an AR headset to avoid the use of additional optics such as collimating refractive lenses. This is not met yet due to the Lambertian-like farfield emission patterns of AlGaInP MQW CCL. Finally but yet importantly, the technological integration of those red CCL on on-silicon blue  $\mu$ -LED arrays in 200mm cleanroom facilities can be tricky, since those epitaxial structures are initially on 3-inch diameter GaAs substrates and need then to be efficiently transferred onto the receiving substrates as well as pixelated. All the above-mentioned issues are summarized in **Table I-3** and need to be circumvented to ensure that this strategy becomes a credible alternative to Q-dots in AR microdisplays for outdoor usage.

**Table I-3:** From display requirements to challenges for blue-to-red MQW color converters.

	<b>Luminance</b>	<b>Resolution</b>	<b>Compactness</b>	<b>Integration technology</b>
Pixels for AR microdisplays	Between $10^5$ and $10^6$ cd/m <sup>2</sup>	$L_{\text{pixel}} < 5\mu\text{m}$	Avoid additional external optics	Feasibility
Challenges to overcome for AlGaInP/InGaP CCL	LEE between 40 and 50%	$L_{\text{ext}} < L_{\text{pixel}}$	Directional emission through control of the emission pattern	Transfer of epilayers + pixelization

Photonic-crystals (PhCs), which are periodic dielectric modulations at wavelength-scale, have already been widely applied to reach high LEE in high refractive-index materials [41]. Due to the coherent nature of their diffraction process, they also have the unique ability to outcouple guided modes and provide a superior control of the farfield emission patterns all at once [42]. In addition, with a proper design and associated with thin-film devices, they could exhibit a strong interaction with guided Bloch-modes, which has been suggested to lead to short extraction lengths [43]. They could thus be an interesting route to mitigate the issues in **Table I-3** related to light extraction, extraction length and directionality. Therefore, in this PhD work we implement them as light-extractors for our AlGaInP blue-to-red CCL as depicted in **Figure I-10**.

## I.6 Research methodology and objectives

**Figure I-11:** Schematics depicting the research methodology.

The main goal of this PhD work is thus to develop those novel photonic-crystal-based InGaP/AlGaInP MQW color converters for blue-to-red color conversion in AR glasses by alleviating all the aforementioned issues in **Table I-3**. As we have seen, the overall integration scheme can be very intricate. To properly grasp and decorrelate all the physical phenomena at play here, we have divided our study into three major parts that will eventually represent three sets of fabrication lots in CEA-LETI 200mm cleanroom facilities (Lots I, II and III) and define the different parts of this PhD work. The architectures of these devices are displayed in **Figure I-11**. In that regard, the investigations carried out herein are organized in five main chapters.

In the second chapter, all the basic physics required to understand light emission processes in a planar high-index MQW color-converting layer (CCL) is provided. Since the spontaneous emission process (SpE) is the mechanism underlying light emission in those incoherent light-emitting structures, we propose a novel full-matrix algebraic framework for modeling dipole radiation-dynamics modification in layered media. This formulation generalizes the standard 2x2 transfer-matrices into a compact 3x3 framework, which allows us to treat dipole radiation directly into the matrix formulation as a source matrix. Its accuracy has been confirmed by incoherent 3D-Finite-Difference-Time-Domain (FDTD) simulations and its applicability demonstrated through various configurations of MQW CCL, while highlighting the fact that light extraction and directionality cannot be optimized all at once using standard planar strategies and thus pointing out the need for photonic-crystals (PhCs). Subsequently, all the material required to understand how light diffraction by PhCs works is detailed.

The third chapter deals with a preliminary investigation of the opto-geometrical properties of the bare PhCs (lattice symmetry, pattern type, lattice period, filling factor, lateral extent, etch depth) and the challenges related to the transfer of the MQW CCL on receiving substrates as well as the fabrication of those PhCs (Lot I). For these studies, AlGaInP CCL were first bonded on transparent substrates but not pixelated, and then various PhCs were designed and fabricated. The blue-to-red color conversion was demonstrated using room-temperature photoluminescence measurements along with innovative ways to circumvent the issues related to light extraction and extraction lengths as well as radiation-pattern control. All the obtained experimental results are coupled to analyses based on a herein-developed model derived from coupled-mode theory, the preceding SpE model, modal analyses and rigorous electromagnetic simulations to set novel design guidelines that could pave the way for the use of inorganic MQW CCL for full-color AR microdisplays.

The fourth chapter is dedicated to the “fully integrated” pixels. It starts with the investigation of the possibility of harnessing the light that is diffracted towards the transparent substrate by studying the interplay between light diffraction and a metallic back-reflector (Lot II). In the full integration scheme (see **Figure I-10**), this back reflector and the tunable oxide layer mimic the electrical contact at the bottom of the blue  $\mu$ -LEDs and all the layers embedded between the contact and the CCL, respectively.

We will subsequently go on with the process to singularize the pixels representing AlGaInP MQW CCL (LOT III). The overall objective of this part is threefold. First, it aims at understanding the impact of the electromagnetic environment of the pixel on the previous performances we obtained on transparent substrates. Secondly, since AR microdisplays can involve pixels whose lateral sizes are short and still need to be larger than the extraction lengths, we will investigate the possibility of virtually extending the lateral size of pixels using a principle we refer to as Bloch-mode replication. Finally yet importantly, the whole process flow of these devices will be given, while highlighting all the challenges we have encountered during the integration of those PhC-based MQW CCL in 200mm cleanroom facilities on Silicon.

In the fifth and final chapter of this manuscript, we conclude this PhD work by summarizing all the results and opening some perspectives for full color microdisplays based on MQW CCL.

## **I.7 Conclusion**

$\mu$ -LED-based display is a promising technology that enables AR glasses, which could be utilized in a plethora of applications ranging from healthcare to industry, including education. However, color is still an issue. In this regard, this thesis aims at investigating a novel strategy based on MQW color converters for monolithic full-color realization. The challenges related to the design, integration & fabrication as well as testing of those MQW color converters are studied for efficient, compact, directional and technologically-feasible blue-to-red color conversion. We believe that this work could pave the way for the use of those color converters in the next generation of very bright and high-resolution AR microdisplays.

## **I.8 References**

1. E. Quesnel, A. Lagrange, M. Vigier, M. Consonni, M. Tournaire, V. Le Marchand, A. Suhm, P. Demars, J.-C. Pillet, B. Ben Bakir, N. Olivier, E. Feltin, J. M. Lamy, M. D'Amico, E. Cao, G. Haas, L. Charrier, and P. Coni, "Dimensioning a full color LED microdisplay for augmented reality headset in a very bright environment," *J. Soc. Inf. Disp.* **29**, 3–16 (2021).
2. M. A. Livingston, L. J. Rosenblum, D. G. Brown, G. S. Schmidt, S. J. Julier, Y. Baillot, J. E. Swan, Z. Ai, and P. Maassel, "Military Applications of Augmented Reality," in *Handbook of Augmented Reality*, B. Furht, ed. (Springer, 2011), pp. 671–706.
3. N. Cui, P. Kharel, and V. Gruev, "Augmented reality with Microsoft HoloLens holograms for near infrared fluorescence based image guided surgery," in *Molecular-Guided Surgery: Molecules, Devices, and Applications III* (SPIE, 2017), Vol. 10049, pp. 32–37.
4. S. K. Ong, M. L. Yuan, and A. Y. C. Nee, "Augmented reality applications in manufacturing: a survey," *Int. J. Prod. Res.* **46**, 2707–2742 (2008).
5. M. E. C. Santos, A. Chen, T. Taketomi, G. Yamamoto, J. Miyazaki, and H. Kato, "Augmented Reality Learning Experiences: Survey of Prototype Design and Evaluation," *IEEE Trans. Learn. Technol.* **7**, 38–56 (2014).
6. Y.-H. Lee, T. Zhan, and S.-T. Wu, "Prospects and challenges in augmented reality displays," *Virtual Real. Intell. Hardw.* **1**, 10–20 (2019).

7. Z. Liu, C.-H. Lin, B.-R. Hyun, C.-W. Sher, Z. Lv, B. Luo, F. Jiang, T. Wu, C.-H. Ho, H.-C. Kuo, and J.-H. He, "Micro-light-emitting diodes with quantum dots in display technology," *Light Sci. Appl.* **9**, 83 (2020).
8. X. Fu, Y. Mehta, Y.-A. Chen, L. Lei, L. Zhu, N. Barange, Q. Dong, S. Yin, J. Mendes, S. He, R. Gogusetti, C.-H. Chang, and F. So, "Directional Polarized Light Emission from Thin-Film Light-Emitting Diodes," *Adv. Mater.* **33**, 2006801 (2021).
9. Z. Chen, S. Yan, and C. Danesh, "MicroLED technologies and applications: characteristics, fabrication, progress, and challenges," *J. Phys. Appl. Phys.* **54**, 123001 (2021).
10. W. Y. Park, A. Phadke, and N. Shah, "Efficiency improvement opportunities for personal computer monitors: implications for market transformation programs," *Energy Effic.* **6**, 545–569 (2013).
11. Y. Boussadi, "Corrélation de mesures électro-optiques en température dans les micro-structures LED à puits quantiques pour applications micro-écrans," phdthesis, Université de Lyon (2022).
12. A. Gasonoo, Y.-S. Lee, J.-H. Yoon, B.-S. Sung, Y. Choi, J. Lee, and J.-H. Lee, "Outcoupling efficiency enhancement of a bottom-emitting OLED with a visible parylene film," *Opt. Express* **28**, 26724–26732 (2020).
13. S. Kim, H. J. Bae, S. Park, W. Kim, J. Kim, J. S. Kim, Y. Jung, S. Sul, S.-G. Ihn, C. Noh, S. Kim, and Y. You, "Degradation of blue-phosphorescent organic light-emitting devices involves exciton-induced generation of polaron pair within emitting layers," *Nat. Commun.* **9**, 1211 (2018).
14. G. Haas, "40-2: Invited Paper: Microdisplays for Augmented and Virtual Reality," *SID Symp. Dig. Tech. Pap.* **49**, 506–509 (2018).
15. F. Templier, "GaN-based emissive microdisplays: A very promising technology for compact, ultra-high brightness display systems," *J. Soc. Inf. Disp.* **24**, 669–675 (2016).
16. S. K. Moore, "Microled displays expected in 2020: The last remaining hurdle is mastering mass production - [News]," *IEEE Spectr.* **56**, 8–9 (2019).
17. K. Streubel, N. Linder, R. Wirth, and A. Jaeger, "High brightness AlGaInP light-emitting diodes," *IEEE J. Sel. Top. Quantum Electron.* **8**, 321–332 (2002).
18. Th. Gessmann and E. F. Schubert, "High-efficiency AlGaInP light-emitting diodes for solid-state lighting applications," *J. Appl. Phys.* **95**, 2203–2216 (2004).
19. M. S. Wong, C. Lee, D. J. Myers, D. Hwang, J. A. Kearns, T. Li, J. S. Speck, S. Nakamura, and S. P. DenBaars, "Size-independent peak efficiency of III-nitride micro-light-emitting-diodes using chemical treatment and sidewall passivation," *Appl. Phys. Express* **12**, 097004 (2019).
20. D. Hwang, A. Mughal, C. D. Pynn, S. Nakamura, and S. P. DenBaars, "Sustained high external quantum efficiency in ultrasmall blue III-nitride micro-LEDs," *Appl. Phys. Express* **10**, 032101 (2017).
21. J. M. Smith, R. Ley, M. S. Wong, Y. H. Baek, J. H. Kang, C. H. Kim, M. J. Gordon, S. Nakamura, J. S. Speck, and S. P. DenBaars, "Comparison of size-dependent characteristics of blue and green InGaN microLEDs down to 1  $\mu\text{m}$  in diameter," *Appl. Phys. Lett.* **116**, 071102 (2020).
22. W. C. Chong, K. M. Wong, Z. J. Liu, and K. M. Lau, "60.4: A Novel Full-Color 3LED Projection System using R-G-B Light Emitting Diodes on Silicon (LEDoS) Micro-displays," *SID Symp. Dig. Tech. Pap.* **44**, 838–841 (2013).
23. F. Gou, E.-L. Hsiang, G. Tan, Y.-F. Lan, C.-Y. Tsai, and S.-T. Wu, "High performance color-converted micro-LED displays," *J. Soc. Inf. Disp.* **27**, 199–206 (2019).
24. F. Gou, E.-L. Hsiang, G. Tan, Y.-F. Lan, C.-Y. Tsai, and S.-T. Wu, "Tripling the Optical Efficiency of Color-Converted Micro-LED Displays with Funnel-Tube Array," *Crystals* **9**, 39 (2019).
25. C. C. Lin and R.-S. Liu, "Advances in Phosphors for Light-emitting Diodes," *J. Phys. Chem. Lett.* **2**, 1268–1277 (2011).
26. H.-Y. Lee, Y.-C. Lin, I.-H. Chen, and C.-H. Chao, "Effective Color Conversion of GaN-Based LEDs via Coated Phosphor Layers," *IEEE Photonics Technol. Lett.* **25**, 764–767 (2013).
27. F. Templier and J. Bernard, "18-3: A New Approach for Fabricating High-Performance MicroLED Displays," *SID Symp. Dig. Tech. Pap.* **50**, 240–243 (2019).
28. A. R. Anwar, M. T. Sajjad, M. A. Johar, C. A. Hernández-Gutiérrez, M. Usman, and S. P. Łepkowski, "Recent Progress in Micro-LED-Based Display Technologies," *Laser Photonics Rev.* **16**, 2100427 (2022).

29. H. S. El-Ghoroury, M. Yeh, J. C. Chen, X. Li, and C.-L. Chuang, "Growth of monolithic full-color GaN-based LED with intermediate carrier blocking layers," *AIP Adv.* **6**, 075316 (2016).
30. M. Funato, K. Hayashi, M. Ueda, Y. Kawakami, Y. Narukawa, and T. Mukai, "Emission color tunable light-emitting diodes composed of InGaN multifacet quantum wells," *Appl. Phys. Lett.* **93**, 021126 (2008).
31. X. Liu, Y. Wu, Y. Malhotra, Y. Sun, Y.-H. Ra, R. Wang, M. Stevenson, S. Coe-Sullivan, and Z. Mi, "Submicron full-color LED pixels for microdisplays and micro-LED main displays," *J. Soc. Inf. Disp.* **28**, 410–417 (2020).
32. S. Li, L. Wang, N. Hirotsuki, and R.-J. Xie, "Color Conversion Materials for High-Brightness Laser-Driven Solid-State Lighting," *Laser Photonics Rev.* **12**, 1800173 (2018).
33. J. M. M. Santos, B. E. Jones, P. J. Schlosser, S. Watson, J. Herrnsdorf, B. Guilhabert, J. J. D. McKendry, J. D. Jesus, T. A. Garcia, M. C. Tamargo, A. E. Kelly, J. E. Hastie, N. Laurand, and M. D. Dawson, "Hybrid GaN LED with capillary-bonded II–VI MQW color-converting membrane for visible light communications," *Semicond. Sci. Technol.* **30**, 035012 (2015).
34. E. Quesnel, A. Suhm, M. Consonni, M. Reymermier, G. Lorin, C. Laugier, M. Tournaire, P. L. Maitre, A. Lagrange, B. Racine, M. D'Amico, and E. Cao, "Experimental and theoretical investigation of 2D nanoplatelet-based conversion layers for color LED microdisplays," *Opt. Express* **29**, 20498–20513 (2021).
35. R. Tangirala, E. Lee, C. Sunderland, W. Guo, A. Mamuye, K. Wang, E. Hwang, N. Kim, and C. Hotz, "62-7: Invited Paper: Quantum Dot Color Conversion for OLED and microLED Displays," *SID Symp. Dig. Tech. Pap.* **52**, 906–908 (2021).
36. H.-M. Kim, M. Ryu, J. H. J. Cha, H. S. Kim, T. Jeong, and J. Jang, "Ten micrometer pixel, quantum dots color conversion layer for high resolution and full color active matrix micro-LED display," *J. Soc. Inf. Disp.* **27**, 347–353 (2019).
37. J. Osinski and P. Palomaki, "4-5: Quantum Dot Design Criteria for Color Conversion in MicroLED Displays," *SID Symp. Dig. Tech. Pap.* **50**, 34–37 (2019).
38. M. Bottrill and M. Green, "Some aspects of quantum dot toxicity," *Chem. Commun.* **47**, 7039–7050 (2011).
39. J. S. Cheong, A. N. A. P. Baharuddin, J. S. Ng, A. B. Krysa, and J. P. R. David, "Absorption coefficients in AlGaInP lattice-matched to GaAs," *Sol. Energy Mater. Sol. Cells* **164**, 28–31 (2017).
40. Y. Wang, B. Wang, W. A. Sasangka, S. Bao, Y. Zhang, H. V. Demir, J. Michel, K. E. K. Lee, S. F. Yoon, E. A. Fitzgerald, C. S. Tan, and K. H. Lee, "High-performance AlGaInP light-emitting diodes integrated on silicon through a superior quality germanium-on-insulator," *Photonics Res.* **6**, 290–295 (2018).
41. X. Tang, X. Tang, X. Tang, L. Han, L. Han, L. Han, Z. Ma, Z. Ma, Z. Ma, Z. Deng, Z. Deng, Z. Deng, Y. Jiang, Y. Jiang, W. Wang, W. Wang, W. Wang, H. Chen, H. Chen, H. Chen, C. Du, C. Du, C. Du, C. Du, H. Jia, H. Jia, H. Jia, and H. Jia, "Enhanced light extraction from AlGaInP-based red light-emitting diodes with photonic crystals," *Opt. Express* **29**, 5993–5999 (2021).
42. J. J. Wierer, A. David, and M. M. Megens, "III-nitride photonic-crystal light-emitting diodes with high extraction efficiency," *Nat. Photonics* **3**, 163–169 (2009).
43. A. David, T. Fujii, B. Moran, S. Nakamura, S. P. DenBaars, C. Weisbuch, and H. Benisty, "Photonic crystal laser lift-off GaN light-emitting diodes," *Appl. Phys. Lett.* **88**, 133514 (2006).

## **Chapter II**

*Spontaneous emission modeling and basics of  
photonic-crystals for light extraction and  
farfield-pattern engineering*

## Table of contents

II.1	Introduction .....	27
II.2	Modeling light emission processes in planar MQW color converters.....	27
II.2.1	Spontaneous emission in an unbounded medium.....	27
II.2.2	Generalized transfer-matrix formulation in an unbounded medium .....	28
II.2.2.a	Without light source .....	28
II.2.2.b	With light source .....	29
II.2.3	Dipole emission modification in stratified media.....	30
II.2.3.a	Determination of the external fields .....	31
II.2.3.b	Derivation of the internal fields and power .....	32
II.2.3.c	Radiation patterns and extraction efficiency .....	33
II.2.4	Incoherent combination for extension to complex emitter regions .....	33
II.2.4.a	Spatially-distributed incoherent dipoles .....	34
II.2.4.b	Emitters with spectral distribution.....	34
II.2.4.c	Completely isotropic emitter's distribution .....	35
II.2.5	Flow chart summary of the implementation procedure.....	35
II.2.6	Application examples: high-index slabs to mimic MQW color-converters .....	36
II.2.6.a	MQW color-converters in vacuum.....	37
1)	Convergence study and accuracy .....	37
2)	Physical origins of spontaneous emission distribution: antinode factor, Airy function ....	39
3)	Monochromatic distributed dipole source planes .....	40
4)	Spectrally-broadened single-plane emitters.....	42
II.2.6.b	On a substrate .....	44
II.2.6.c	With a distributed Bragg reflector: LEE vs directionality.....	45
II.2.7	Conclusion on the SpE modeling framework and planar strategies .....	46
II.3	Principle of operation of photonic-crystals for light diffraction.....	47
II.3.1	Starting point: extraction issue in a single-mode waveguide .....	47
II.3.2	General overview of photonic-crystals.....	48
II.3.2.a	Foreword .....	48

II.3.2.b	Photonic crystal parameters.....	49
II.3.2.c	Different photonic-crystal integration for increasing light extraction.....	50
II.3.3	Bragg's law in a basic 2D problem: case of a single-mode waveguide .....	51
II.3.4	First-order Bragg lattice: reflection of the guided mode .....	52
II.3.5	Second-order grating: total extraction and vertical beaming to free space .....	53
II.3.6	Higher order Bragg gratings.....	55
II.3.7	Incoherent multiple-dipoles emission in a second-order grating.....	55
II.3.8	Conclusion on the analytical and numerical analysis.....	57
II.4	Conclusion.....	57
II.5	References .....	57

## II.1 Introduction

Multiple quantum well (MQW) color-converting layers (CCL) are thin epitaxial films, whose light emission is ruled by spontaneous emission (SpE) from radiating electric dipoles, stemming from radiative electron-hole recombinations inside the quantum wells [1]. Understanding the behavior of SpE in those layered media is thus of crucial interest to optimize the key figures of merits (FoM) of those devices such as light extraction efficiency (LEE), directionality, brightness, etc. The main modeling frameworks have so far relied on 2x2 transfer-matrices with dipole source terms [2], which requires to treat dipole emission separately as a discontinuity of the field across the source plane. This often leads to complex analytical calculations and could require additional computation efforts [3]. In this chapter, we first propose a novel SpE modeling framework where 2x2 transfer-matrices are generalized into 3x3 ones enabling a more convenient treatment of dipole emission, which makes it easier to implement numerically. The model is then thoroughly developed and its accuracy as well as its validity have been demonstrated, highlighting the need for photonic-crystals (PhCs). Eventually, the basic physics required to understand light diffraction by PhCs is presented.

## II.2 Modeling light emission processes in planar MQW color converters

In this section, we start by introducing SpE in unbounded media, before coming back to our 3x3 modeling framework. Next, the model is thoroughly developed and applied to various configurations of MQW CCL.

### II.2.1 Spontaneous emission in an unbounded medium

Our modeling framework is based upon generalized 3x3 transfer-matrices with source terms, so the starting point is to write the emission patterns of the radiating electric dipoles representing the electron-hole recombinations. As shown by Lukosz [4], a suitable way to represent those patterns is to consider a basis of horizontal and vertical dipoles emitting  $s$ - and  $p$ -polarized plane and evanescent waves. This basis as well as the corresponding radiation shapes are depicted in **Figure II-1**. In that framework, the powers per unit solid angle emitted by vertical (denoted  $v$ ) and horizontal (denoted  $h$ ) dipoles in an unbounded medium express as [5,6]:

$$\Pi_{\infty}^{v,p} = \frac{3}{8\pi} \sin^2(\theta_e) \quad (\text{II-1})$$

$$\Pi_{\infty}^{h,s} = \frac{3}{16\pi}, \quad \Pi_{\infty}^{h,p} = \frac{3}{16\pi} \cos^2(\theta_e). \quad (\text{II-2})$$

Here  $\theta_e$  is the off-normal emission angle and  $e$  refers to the emission's medium. Those emission patterns are normalized using the factors  $3/8\pi$  and  $3/16\pi$  so that the total power emitted by vertical dipoles in  $p$ -polarization through  $4\pi$  sr as well as the one emitted by horizontal dipoles in  $(s+p)$  equal unity. In the next section, the 3x3 modeling framework will be introduced for the simple case of dipoles in an

unbounded medium using normalized source terms, which are the square roots of the above-given radiation patterns.

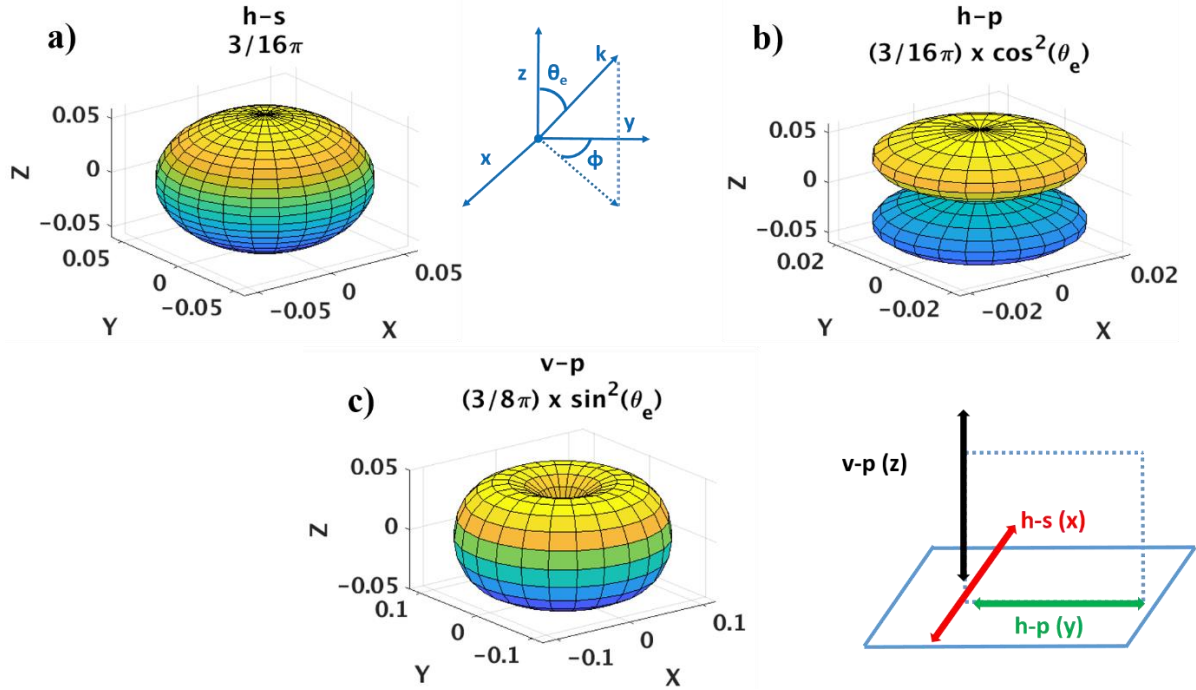


**Figure II-1:** Normalized emission patterns of horizontal dipoles in a)  $s$ - and b)  $p$ - polarizations and of c) vertical dipoles in  $p$ -polarization, all lying in an unbounded medium.

## II.2.2 Generalized transfer-matrix formulation in an unbounded medium

In this section, we establish our modeling framework in the basic case of an emitter in an unbounded medium. In that regard, let us consider two arbitrary positions  $z_1$  and  $z_2$  where the electric fields are denoted  $E_1$  and  $E_2$ , respectively, as described in **Figure II-2-a**. The superscripts + (-) denote the forward- (backward-) propagating electric fields.

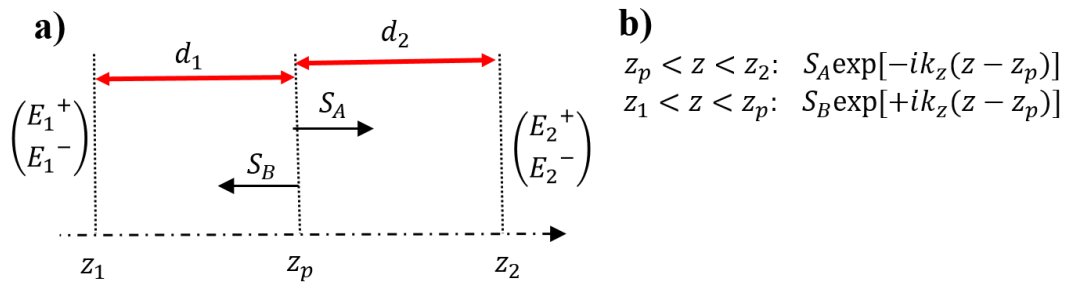


**Figure II-2:** a) Schematics diagram of a dipole placed at a position  $z_p$  in an unbounded medium.  $z_1$  and  $z_2$  are 2 positions at distances of  $d_1$  and  $d_2$  from the source, respectively.  $S_A$  and  $S_B$  are the amplitudes of the forward- and backward-propagating source terms. b) Expressions of the electric-field amplitudes on both sides of the dipole.

### II.2.2.a Without light source

When there are no light sources, we can write the following relationships between the electric fields at those two arbitrary positions and a position  $z_p$  in-between using the standard  $2 \times 2$  transfer-matrices:

$$\begin{pmatrix} E_1^+ \\ E_1^- \end{pmatrix} = \begin{pmatrix} \exp(ik_z d_1) & 0 \\ 0 & \exp(-ik_z d_1) \end{pmatrix} \begin{pmatrix} E_p^+ \\ E_p^- \end{pmatrix}. \quad (\text{II-3})$$

$$\begin{pmatrix} E_p^+ \\ E_p^- \end{pmatrix} = \begin{pmatrix} \exp(ik_z d_2) & 0 \\ 0 & \exp(-ik_z d_2) \end{pmatrix} \begin{pmatrix} E_2^+ \\ E_2^- \end{pmatrix}. \quad (\text{II-4})$$

### II.2.2.b With light source

The presence of a light source changes the previous expressions. Let us consider an emitter positioned at  $z_p$  and whose electric-field amplitudes are  $S_A$  and  $S_B$  as displayed in **Figure II-2-a**. The fields at any position on the left and right sides of the emitter are now set by the source terms (electric fields emitted from the source) and are expressed in **Figure II-2-b**. Particularly, at  $z_1$  and  $z_2$  the electric fields  $E_{1(2)}^{+(-)}$  become  $E'_{1(2)}^{+(-)}$ , which read as:

$$\begin{aligned} E_1^+ &\rightarrow E'_{1^+} = E_1^+ & E_2^+ &\rightarrow E'_{2^+} = E_2^+ + S_A \exp(-ik_z d_2) \\ E_1^- &\rightarrow E'_{1^-} = E_1^- + S_B \exp(ik_z d_1) & E_2^- &\rightarrow E'_{2^-} = E_2^- \end{aligned} \quad (\text{II-5})$$

Those previous analytical formulas can be rewritten in a 2x2-matrix formulation as follows:

$$\begin{pmatrix} E'_{1^+} \\ E'_{1^-} \end{pmatrix} = \begin{pmatrix} \exp(ik_z d_1) & 0 \\ 0 & \exp(-ik_z d_1) \end{pmatrix} \begin{pmatrix} E_p^+ - S_A \\ E_p^- \end{pmatrix}, \quad (\text{II-6})$$

$$\begin{pmatrix} E'_p{}^+ \\ E'_p{}^- \end{pmatrix} = \begin{pmatrix} \exp(ik_z d_2) & 0 \\ 0 & \exp(-ik_z d_2) \end{pmatrix} \begin{pmatrix} E_2^+ \\ E_2^- + S_B \exp(ik_z d_2) \end{pmatrix}, \quad (\text{II-7})$$

By combining **Eq. (II-6)** and **Eq. (II-7)**, we can obtain a direct relationship between the electric fields across the dipole source in a single 3x3 framework, which reads as<sup>1</sup>:

$$\begin{pmatrix} E'_{1^+} \\ E'_{1^-} \\ 1 \end{pmatrix} = P^e(d_1) S P^e(d_2) \begin{pmatrix} E'_{2^+} \\ E'_{2^-} \\ 1 \end{pmatrix}, \quad (\text{II-8})$$

Here  $P^j(d_j)$  and  $S$  designate the propagation matrix in the layer (or medium in this case) denoted  $j$  over a distance  $d_j$  and the source matrix, respectively. They are expressed as:

$$P^e(d_j) = \begin{pmatrix} \exp(ik_z d_j) & 0 & 0 \\ 0 & \exp(-ik_z d_j) & 0 \\ 0 & 0 & 1 \end{pmatrix}, \quad (\text{II-9})$$

$$S = \begin{pmatrix} 1 & 0 & -S_A \\ 0 & 1 & +S_B \\ 0 & 0 & 1 \end{pmatrix}. \quad (\text{II-10})$$

For the three basic dipole configurations described in the beginning of this section, the normalized source terms are provided in **Table II-1** where  $k_{z,e}$  ( $k_{//,e}$ ) accounts for the z- (in-plane) -wave-vector component inside the emission layer.

In the next section, we are going to use the framework of **Eq. (II-8)** in the case of dipole emission in layered media, which depicts our MQW CCL.

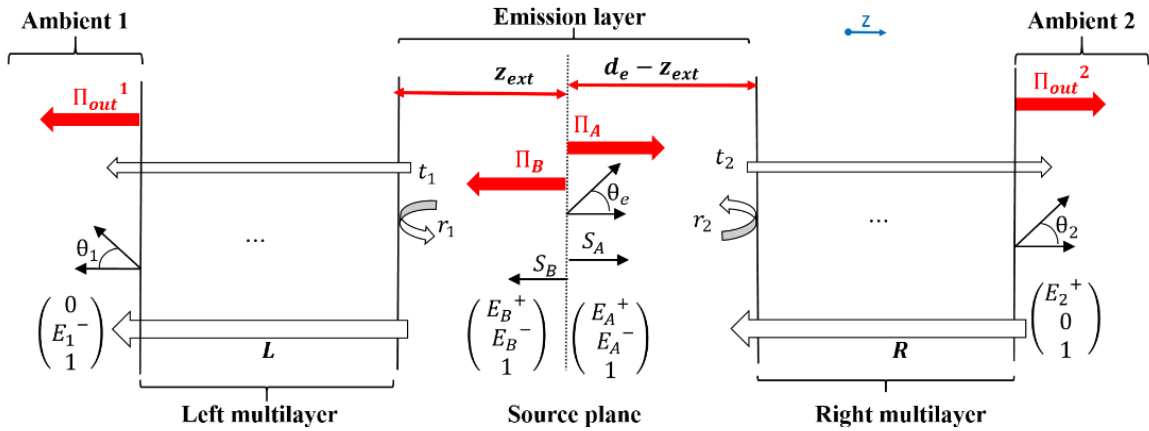
<sup>1</sup> The third component of the electric field vector 1 is merely a mathematical trick to enable the generalization.

**Table II-1:** Normalized source terms for horizontal and vertical dipoles.

Dipole orientation	<i>s</i> -polarized light	<i>p</i> -polarized light
Horizontal	$S_A^{h,s} = S_B^{h,s} = \sqrt{\frac{3}{16\pi}}$	$S_A^{h,p} = S_B^{h,p} = \sqrt{\frac{3}{16\pi}} \cos(\theta_e) = \sqrt{\frac{3}{16\pi}} \frac{k_{z,e}}{k_e}$
Vertical	$S_A^{v,s} = S_B^{v,s} = 0$	$S_A^{h,p} = S_B^{h,p} = \sqrt{\frac{3}{8\pi}} \sin(\theta_e) = \sqrt{\frac{3}{8\pi}} \frac{k_{//,e}}{k_e}$

### II.2.3 Dipole emission modification in stratified media

As mentioned above, MQW CCL are epitaxial layers whose light emission processes rely on SpE. In this section, those devices are modelled as multilayer structures comprising a stack of layers supposed homogeneous, infinite along the  $xy$  plane and with finite thickness along  $z$ . The emitters representing quantum wells are embedded into a single region named emission layer, where the dipoles are modelled as source planes<sup>2</sup>. The electric fields  $E_{A(B)}$  designate the source terms modified by the optical environment on the right (left) side of the source plane. The multilayer structure is enclosed with two semi-infinite ambient media (denoted 1 and 2) that can be either air, substrates or superstrates. The matrices  $R$  and  $L$  depict the propagation from the ambient medium 2 up to the right interface of the emission layer and from the left interface of the emission layer to the ambient medium 1, respectively. In this configuration, the boundary conditions read as  $E_1^+ = E_2^- = 0$ .


**Figure II-3:** Schematics depicting a multilayer structure enclosed with two semi-infinite ambient layer.

**Figure II-3** reports the multilayer structure as well as all the necessary parameters. Using the considerations of the previous subsection in **Eq. (II-8)**, we can now write a compact link between the electric field vectors in the ambient media as follows:

$$\begin{pmatrix} 0 \\ E_1^- \\ 1 \end{pmatrix} = M \begin{pmatrix} E_2^+ \\ 0 \\ 1 \end{pmatrix} = \begin{pmatrix} M_{11} & M_{12} & M_{13} \\ M_{21} & M_{22} & M_{23} \\ 0 & 0 & 1 \end{pmatrix} \begin{pmatrix} E_2^+ \\ 0 \\ 1 \end{pmatrix}, \quad (\text{II-11})$$

<sup>2</sup> In the planar case (unpatterned), a dipole source plane at a position  $z$  is equivalent to a single dipole placed at  $z$  for symmetry reasons. In the last sections of this manuscript, we will see that for devices with photonic-crystals, we need many dipoles in the same source plane along one period of the device for FDTD simulations.

Here  $M$  is the equivalent matrix of the MQW CCL and reads as:

$$M = LP^e(z_{ext})SP^e(d_e - z_{ext})R. \quad (\text{II-12})$$

In the next sections, we are going to calculate the electric fields outside and inside the multilayer for determining key figure of merits (FoM) of MQW CCL such as LEE, directionality through the farfield radiation patterns, Purcell factor, etc.

### II.2.3.a Determination of the external fields

The electric fields in the ambient media are the starting points of this model development. For a given external angle  $\theta_{l(2)}$  corresponding to an internal angle  $\theta_e$ , one can easily infer using **Eq. (II-11)** that they can be written as:

$$E_2^+ = -\frac{M_{13}}{M_{11}}, \quad E_1^+ = \frac{M_{23}M_{11} - M_{21}M_{13}}{M_{11}}. \quad (\text{II-13})$$

Although these expressions are easy to implement, they do not portray the physics inside the multilayer structures. Another way to express the outside fields is to consider the Fresnel reflection and transmission coefficients, which by definition (see **Figure II-3**) and using  $L$  and  $R$  read as:

$$\begin{aligned} r_1 &= -\frac{L_{12}}{L_{11}}, & r_2 &= \frac{R_{21}}{R_{11}}, \\ t_1 &= \frac{L_{22}L_{11} - L_{12}L_{21}}{L_{11}}, & t_2 &= \frac{1}{R_{11}}. \end{aligned} \quad (\text{II-14})$$

After some calculations by combining the two previous equations, we obtain new formula for the external fields:

$$\begin{aligned} E_2^+ &= \frac{t_2(S_A e^{-ik_{z,e}(d_e - z_{ext})} + r_2 S_B e^{-ik_{z,e}(d_e + z_{ext})})}{1 - r_1 r_2 e^{-ik_{z,e}2d_e}}, \\ E_1^- &= \frac{t_1(r_2 S_A e^{-ik_{z,e}(2d_e - z_{ext})} + S_B e^{-ik_{z,e}z_{ext}})}{1 - r_1 r_2 e^{-ik_{z,e}2d_e}}. \end{aligned} \quad (\text{II-15})$$

The physical meaning of these fields can now be easily captured. For instance, the outgoing field on the left ( $E_l^-$ ) stems from the left-going source term propagated into the left side the emission layer, added to the right-going source term reflected off the right side of the structure, which are both transmitted through the left side of the structure.

Furthermore, the common denominator of the fields in **Eq. (II-15)**, generally noted  $\Delta$  carries the modal properties of the multilayer structure. Particularly for some discrete angles where the unity round-trip condition is satisfied,  $\Delta$  equals zero and all those fields diverge. To properly evaluate the fields at those angles (corresponding to guided modes), the trick is to introduce ultrathin absorbing layers called damping layers at each side of the source plane as suggested in [2]. More details about this point will be provided in **Subsection II.2.6.a.1**.

### II.2.3.b Derivation of the internal fields and power

From the previous external electric fields, one can deduce the internal fields at each side of the source plane. They express as follows:

$$\begin{pmatrix} E_A^+ \\ E_A^- \\ 1 \end{pmatrix} = P^e(d_e - z_{ext})R \begin{pmatrix} E_2^+ \\ 0 \\ 1 \end{pmatrix}, \quad (\text{II-16})$$

$$\begin{pmatrix} E_B^+ \\ E_B^- \\ 1 \end{pmatrix} = (P^e(z_{ext}))^{-1}L^{-1} \begin{pmatrix} 0 \\ E_1^- \\ 1 \end{pmatrix}. \quad (\text{II-17})$$

Those fields are key elements to grasp the physics of light emission inside our MQW CCL. Indeed, by calculating the fluxes of the corresponding Poynting vectors, one can obtain the angular distribution of the internal emission on each side of the source plane as:

$$\Pi_A = \frac{dP_{in}^A}{d\Omega_{in}^A} = |E_A^+|^2 - |E_A^-|^2, \quad (\text{II-18})$$

$$\Pi_B = \frac{dP_{in}^B}{d\Omega_{in}^B} = |E_B^+|^2 - |E_B^-|^2. \quad (\text{II-19})$$

As we will see in the next chapter dedicated to the design, fabrication and test of real-life MQW CCL, those angular distributions are key elements in designing directional light emission. Particularly, they can be rewritten as follows<sup>3</sup> (see [7]):

$$\Pi_B = \xi_B \times \mathcal{A}_B \times \Pi_\infty, \quad (\text{II-20})$$

Here  $\xi_B$  is the antinode factor, which governs how dipole emission couples to the available cavity modes. It is given in **Eq. (II-21)**.  $\mathcal{A}_B$  is the Airy function, which on the other hand accounts for the resonant behavior of the bare Fabry-Perot (FP) cavity and is expressed in **Eq. (II-22)**. Its denominator is  $\Delta$  whose zeros provide the discrete angular positions of the guided modes inside the membrane. The last factor is the emission pattern in an unbounded medium.

$$\xi_B = |1 + r_2 \exp(-ik_{z,e}2(d_e - z_{ext}))|^2 = |1 + r_2 \exp(-i\varphi_c)|^2. \quad (\text{II-21})$$

$$\mathcal{A}_B = \frac{1 - |r_1|^2}{|1 - r_1 r_2 \exp(-ik_{z,e}2d_e)|^2} = \frac{1 - |r_1|^2}{\Delta^2}. \quad (\text{II-22})$$

More details about the roles of these factors will be provided in **Subsection II.2.6.a.2)**.

Finally, it is well known that in some structures SpE can be strongly impacted by the optical environment leading to the so-called Purcell effect [8]. The associated Purcell factor (modification of total SpE rates of a structure as compared to SpE rates of dipoles in unbounded media) can be written as:

$$F_P = \int_{\theta_e=0}^{\theta_e=\frac{\pi}{2}} \int_{\varphi=0}^{\varphi=2\pi} (\Pi_A + \Pi_B) \sin(\theta_e) d\theta_e d\varphi. \quad (\text{II-23})$$

We can note that there is no need to divide by values in unbounded media because all the electric fields are already normalized.

<sup>3</sup> A similar expression can of course be provided for  $\Pi_A$ .

### II.2.3.c Radiation patterns and extraction efficiency

The main objectives of this PhD work are to circumvent light extraction issues in planar MQW CCL and to reshape their farfield patterns from Lambertian-like shapes to directional ones. It is therefore of key interest to evaluate the radiation patterns as well as the LEE in our modeling framework. By definition, the emission shape in the ambient medium  $I$  can be expressed as:

$$\Pi_{out}^1 = \frac{dP_{out}^1}{d\Omega_{out}^1} = \frac{dP_{out}^1}{dP_{in}^B} \times \frac{d\Omega_{in}^B}{d\Omega_{out}^1} \times \frac{dP_{in}^B}{d\Omega_{in}^B}, \quad (\text{II-24})$$

The power transmission efficiency between the emission layer and the outside medium  $I$  is the first factor and reads as:

$$\frac{dP_{out}^1}{dP_{in}^B} = \frac{\vec{S}_{out}^1 \cdot \vec{A}_{out}^1}{\vec{S}_{in}^B \cdot \vec{A}_{in}^B} = \frac{n_1 |E_1^-|^2 \cos(\theta_1)}{n_e (|E_B^+|^2 - |E_B^-|^2) \cos(\theta_e)}, \quad (\text{II-25})$$

Here  $\vec{S}_{in}^B$  ( $\vec{A}_{in}^B$ ) and  $\vec{S}_{out}^1$  ( $\vec{A}_{out}^1$ ) designate the Poynting vectors (unit vectors normal to the surface) in the emission layer and the outer ambient medium  $I$ , respectively. Then, one also needs to account for the change in solid angles when light goes out of the emission layer to the ambient medium. After an angular differential of the Snell-Descartes' law  $n_e \sin(\theta_e) = n_1 \sin(\theta_1)$ , one can get:

$$d\Omega_{in}^B = \sin(\theta_e) d\theta_e d\varphi_e = \frac{n_1^2 \cos(\theta_1)}{n_e^2 \cos(\theta_e)} d\Omega_{out}^1, \quad (\text{II-26})$$

The last factor is provided in **Eq. (II-19)**. The farfield radiation patterns can subsequently be obtained in either ambient medium by combining the three previous equations<sup>4</sup>:

$$\Pi_{out}^{1(2)} = \frac{dP_{out}^{1(2)}}{d\Omega_{out}^{1(2)}} = |E_{1(2)}^-|^2 \frac{n_{1(2)}^3 \cos^2(\theta_{1(2)})}{n_e^3 \cos^2(\theta_e)}. \quad (\text{II-27})$$

LEE will then naturally express as:

$$LEE_{1(2)} = \frac{\int_{\theta_{1(2)}=0}^{\theta_{1(2)}=\frac{\pi}{2}} \int_{\varphi=0}^{\varphi=2\pi} \Pi_{out}^{1(2)} \sin(\theta_{1(2)}) d\theta_{1(2)} d\varphi}{F_p}. \quad (\text{II-28})$$

### II.2.4 Incoherent combination for extension to complex emitter regions

We now have the formulas for the internal emission distribution, the radiation patterns and LEE but only for the monochromatic single-emitter case. Real-life devices such as MQW CCL can often include polychromatic light emitters, multiple quantum wells (spatially distributed source planes along  $z$ ) and many emitter's orientations. Since the SpE process is by nature incoherent, we propose post-processing formula for incoherent combination to treat these cases.

<sup>4</sup> If the external fields have been calculated within complex angles (evanescent waves) as well, then one needs to drop those evanescent waves and only consider outside angles  $\theta_{1(2)}$  ranging from 0 to  $\pi/2$  for the farfield patterns.

### II.2.4.a Spatially-distributed incoherent dipoles

This is the case when the emitters or equivalently source planes lie within a layer whose thickness (along  $z$ , see **Figure II-3**) is non-negligible compared to the emission wavelength. One needs then to consider light emission from each of those dipoles. For the simplest case of a uniform carrier distribution<sup>5</sup>, the combined values of the angular internal emission and LEE (over all dipoles) express as follows using simple arithmetic averages<sup>6</sup>:

$$\begin{aligned}\Pi_{int(out)}^{combined} &= \frac{\sum_{z_{ext}=z_{ext,1}}^{z_{ext}=z_{ext,N}} \Pi_{int(out)}(z_{ext})}{N}, \\ LEE^{combined} &= \frac{\sum_{z_{ext}=z_{ext,1}}^{z_{ext}=z_{ext,N}} LEE(z_{ext})}{N}.\end{aligned}\tag{II-29}$$

Here,  $N$  is the number of dipole emitters along  $z$  and  $z_{ext,j}$  designates the spatial position of the dipole labelled  $j$ .

### II.2.4.b Emitters with spectral distribution

For most of the incoherent light-emitting devices, the emission linewidth is not negligible and needs to be accounted for in our model. Considering the source intrinsic spectrum  $I_{in}$  and an emission between  $\lambda_{min}$  and  $\lambda_{max}$ , we only need to perform the weighted averages of the internal emission, farfield and LEE to obtain their combined values over the whole emission spectrum:

$$\begin{aligned}\Pi_{int}^{combined}(\theta_e) &= \frac{\int_{\lambda=\lambda_{min}}^{\lambda=\lambda_{max}} I_{in}(\lambda) \Pi_{int}(\lambda, \theta_e) d\lambda}{\int_{\lambda=\lambda_{min}}^{\lambda=\lambda_{max}} I_{in}(\lambda) d\lambda}, \\ \Pi_{out}^{combined}(\theta_{1(2)}) &= \frac{\int_{\lambda=\lambda_{min}}^{\lambda=\lambda_{max}} I_{in}(\lambda) \Pi_{out}(\lambda, \theta_{1(2)}) d\lambda}{\int_{\lambda=\lambda_{min}}^{\lambda=\lambda_{max}} I_{in}(\lambda) d\lambda}, \\ LEE^{combined} &= \frac{\int_{\lambda=\lambda_{min}}^{\lambda=\lambda_{max}} I_{in}(\lambda) LEE(\lambda) d\lambda}{\int_{\lambda=\lambda_{min}}^{\lambda=\lambda_{max}} I_{in}(\lambda) d\lambda}.\end{aligned}\tag{II-30}$$

For some cavity work, the spectral distribution of the emission patterns can offer good insight into the behavior of the Fabry-Pérot modes. In that regard, one could exploit the spectrally resolved farfield (SRF) patterns evaluated as follows:

$$SRF(\lambda, \theta_{1(2)}) = \frac{I_{in}(\lambda) \Pi_{out}(\lambda, \theta_{1(2)})}{\int_{\lambda_i=\lambda_{min}}^{\lambda_i=\lambda_{max}} I_{in}(\lambda_i) d\lambda_i},\tag{II-31}$$

<sup>5</sup> The uniformity of the carrier distribution depends on multiple factors such as the epitaxial design, the current density, carrier diffusion lengths, etc. For non-uniform carrier distribution, those averages need to be weighted by the carrier concentration along  $z$  as in [9].

<sup>6</sup> SpE process is incoherent, thus there are no interference effects between light waves generated by different dipoles.

Using the previous formula, one can easily obtain the expression of the output spectrum:

$$I_{out}(\lambda) = \int_{\theta_{1(2)}=0}^{\theta_{1(2)}=\frac{\pi}{2}} \int_{\varphi=0}^{\varphi=2\pi} SRF(\lambda, \theta_{1(2)}) \sin(\theta_{1(2)}) d\theta_{1(2)} d\varphi. \quad (\text{II-32})$$

This formula can be useful in structures with strong cavity effects, where SpE redistribution can induce a spectral redistribution, which can change the output spectrum of the device (compared to the intrinsic spectrum).

#### II.2.4.c Completely isotropic emitter's distribution

Depending on the dipole moments, emitter's orientations in semiconductor devices can be neither only horizontal nor only vertical, but rather a complex combination of those two depending on the confinement conditions. For the simple case of bulk semiconductors, the emitters are arbitrarily oriented leading to an isotropic distribution, where one third of the dipoles are vertical. In that regard, we can write for the internal emission and farfields that:

$$\begin{aligned} \Pi_{int(out)}^{combined} &= \frac{1}{3} \Pi_{int(out)}^v + \frac{2}{3} \Pi_{int(out)}^h, \\ \Pi_{int(out)}^v &= \Pi_{int(out)}^{v,p}, \\ \Pi_{int(out)}^h &= \Pi_{int(out)}^{h,s} + \Pi_{int(out)}^{h,p}. \end{aligned} \quad (\text{II-33})$$

On the other hand, for LEE, one needs to account for the different radiation dynamics between *s*- and *p*-polarized light through their Purcell factor and write **Eq. (II-34)**.

$$\begin{aligned} LEE^{combined} &= \frac{1}{3} LEE^v + \frac{2}{3} LEE^h, \\ LEE^v &= LEE^{v,p}, \\ LEE^h &= \frac{LEE^{h,s} \times F_p^{h,s} + LEE^{h,p} \times F_p^{h,p}}{F_p^{h,s} + F_p^{h,p}}. \end{aligned} \quad (\text{II-34})$$

For quantum-well-based devices such as MQW CCL, most of the emitters are generally in-plane polarized [10]; consequently the contribution of vertical dipoles could be dropped. For more complex confinements conditions such as in Q-dots, the factors 1/3 and 2/3 need to be replaced by the proper dipole concentrations.

#### II.2.5 Flow chart summary of the implementation procedure

All the equations required for the implementation of the herein-developed model have now been provided. To help make its numerical implementation less tricky, we provide in **Figure II-4** a detailed flow chart pointing out at the equation needed at each step of the process. The full-matrix formalism helps make it very convenient. The equivalent matrix *M* is to be calculated for both polarizations. Hence, when the dipole orientation is switched from vertical to horizontal, only the source matrix *S* needs to be changed.

This model can give good insight into LEE, farfield emission patterns (and therefore directionality), Purcell factors, photonic weights (fraction of the guided energy carried by each guided mode), etc, which qualifies it as a key tool for designing incoherent light-emitting devices.

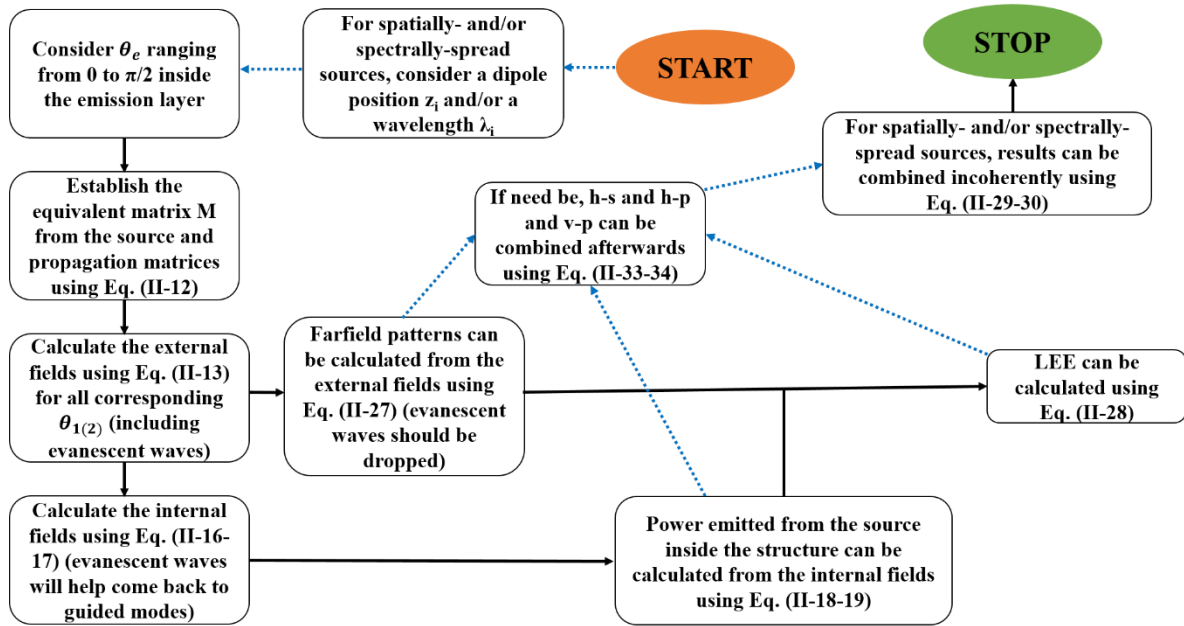


Figure II-4: Detailed flow chart of the implement procedure of the generalized transfer-matrix model.

In the following section, we first perform a convergence study and verify the accuracy of the model compared to rigorous electromagnetic simulations. Subsequently, we demonstrate its applicability through various configurations of MQW CCL mimicked by high-index slabs. This way, we will better understand light emission processes in incoherent light-emitting structures and highlight key design rules that are going to be crucial to the design choices that we make in this PhD thesis.

## II.2.6 Application examples: high-index slabs to mimic MQW color-converters

To mimic MQW CCL, we consider a high-index slab ( $n_e=3$ ) enclosed within semi-infinite ambient media. Guided modes are accounted for by introducing two identical damping layers (ultrathin absorbing layers) on each side of the source plane, which need to be thin enough (e.g.  $\lambda/10^3$ ) not to modify direct light emission<sup>7</sup> and close enough to the source (e.g.  $\lambda/10^6$ ) to have the same coupling to guided modes [2]. All the opto-geometrical parameters are described in **Figure II-5**. Let us recall that in the planar case, a single dipole in a source plane can account for all the dipoles in it due to the system symmetry, whereas in the case of patterned devices many dipoles need to be distributed in the source plane along one period of the pattern (see **Subsection II.3.7**).

<sup>7</sup> Direct light emission is the part of the emitted light that is directly extracted in air or towards the substrate.

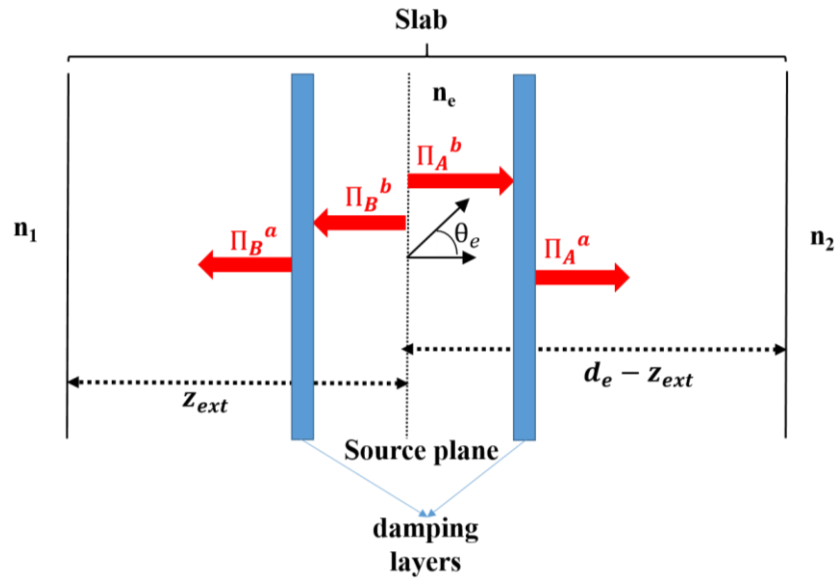


**Figure II-5:** High-index slab enclosed with semi-infinite ambient media (not at scale).

### II.2.6.a MQW color-converters in vacuum

In this first case, we study the behavior of the bare slab placed in vacuum ( $n_1=n_2=1$ ).

#### 1) Convergence study and accuracy

Let us consider the simplest case of a single monochromatic horizontal<sup>8</sup> ( $h$ ) dipole (or equivalently source plane) centered in the slab ( $z_{ext}=d_e/2$ ).

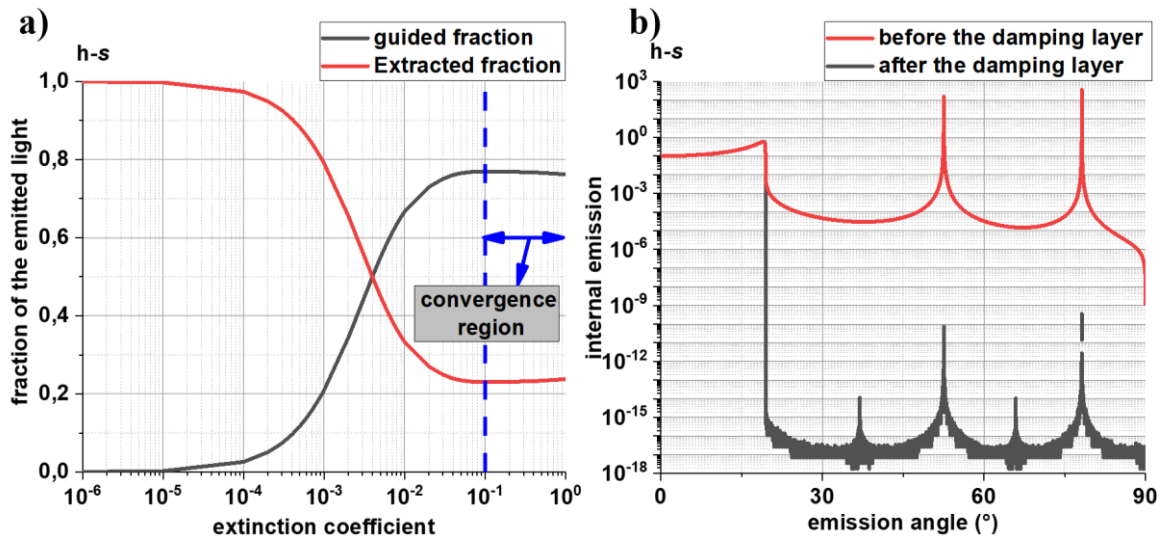


**Figure II-6:**  $s$ -polarized light from a single monochromatic horizontal dipole centered in a high-index slab. a) Extracted and guided fractions of the total emitted light as a function of the extinction coefficient of the damping layers. b) Angular internal emission before and after the damping layers damping layers with an extinction coefficient fixed at  $10^{-1}$ .

We start by a convergence study to determine the extinction coefficient of the damping layers required to properly account for guided modes. The results are reported in **Figure II-6-a** where guided and extracted fractions of the total (top and bottom) emitted power in  $s$ -polarization are plotted as a function

<sup>8</sup> Since our MQW are quantum-well-based, light emission is mostly in plane polarized.

of the extinction coefficient of the damping layers. When the extinction coefficient is less than  $\sim 10^{-4}$ , the damping layers are not sufficiently absorbing. Therefore, LEE artificially equals unity (no guided power) which leads to incorrect results. Then, the guided power progressively increases until it reaches saturation for values over  $10^{-1}$ . LEE saturates as well around 21%, which corresponds to values found by Benisty et al. in [2] for the same structure. This highlights the importance of the damping layers.

We confirm these considerations by plotting the angular distribution of the internal emission before and after the damping layers in order to analyze their impact for an extinction coefficient fixed at  $10^{-1}$ . The shape of the internal emission will be thoroughly explained in the next subsection, but we can already see that, as expected, dipole emission couples to two guided modes displayed as the two sharp peaks outside the air light cone ( $\theta_e > 20^\circ$ ) located at  $\sim 52.6^\circ$  and  $78.2^\circ$ . After passing through the damping layers, all the power in those modes is absorbed (peaks' intensities decrease from  $\sim 10^2$  to  $10^{-10}$  before and after the damping layers, respectively), while the internal emission inside the air cone ( $\theta_e < 20^\circ$ ) remains unchanged, which confirms our previous considerations. The guided power is thence calculated by evaluating the power imbalance before and after the damping layers.

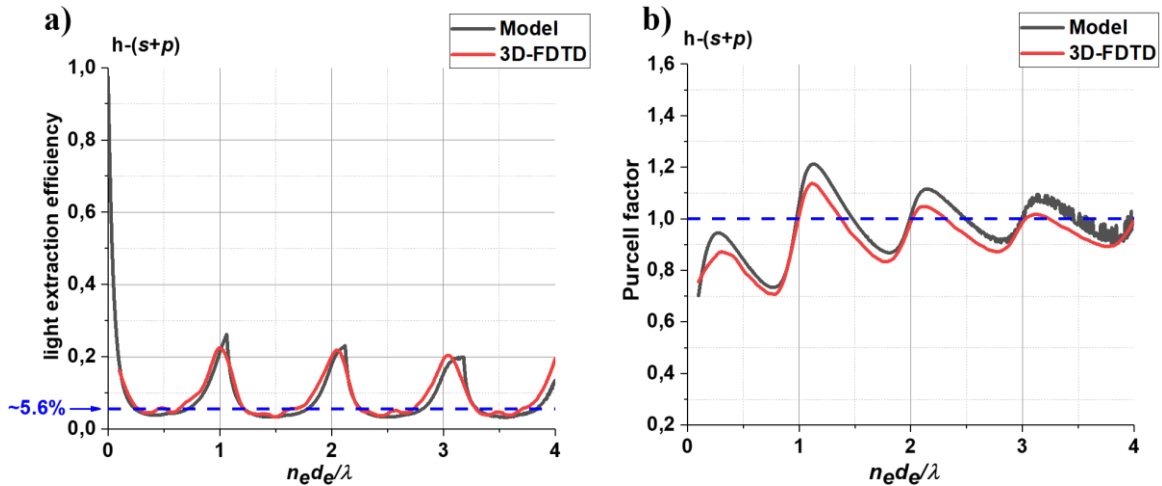


**Figure II-7:** Single horizontal dipole centered in a high-index slab.  $s$ - and  $p$ -polarizations are combined. a) LEE and b) Purcell factor as a function of the reduced thickness. The blue dashed line indicates the asymptotic values of LEE and Purcell factor.

We now verify the accuracy of our model by comparing its results to rigorous electromagnetic simulations with 3D Finite-Difference Time-Domain (FDTD) from commercially available software (FullWAVE and LED Utility from the Rsoft Design Suite). More details about the FDTD simulation method can be found in **Appendix A.1**. The simulation domain for FDTD was surrounded by perfectly matched layers (PML) and was  $4\mu\text{m}$ -sized. Additionally, the mesh sizes along all spatial directions were chosen to be 10nm. The results are displayed in **Figure II-7**, which reports both total LEE and Purcell factor as a function of the reduced optical slab thickness. Both  $s$ - and  $p$ -polarizations have been combined<sup>9</sup>. The results are quite in accordance with each other, which confirms the accuracy of our modeling framework. Spontaneous emission dynamics strongly depends on the slab thickness as it was

<sup>9</sup> Both  $s$ - and  $p$ -polarizations need to be combined for our model to be comparable to 3D-FDTD, because Maxwell's equations are coupled and cannot be separated for 3D-FDTD simulations.

already well established in various reports [2,11], which translates into the oscillations we can see. For very high values of slab thickness (e.g.  $n_e d_e / \lambda > 20$ ), the modes would become so numerous that these oscillations would smear out and reach the asymptotic values of LEE. LEE can be approximated only in those cases to the fraction of solid angles below the critical angle [1]. Besides, it is worth noticing that the maximum LEE is reached for ultrathin slabs ( $n_e d_e / \lambda \sim 1$ ).

This highlights the key importance of damping layers in order to reach convergence in this modeling framework. In addition, the generalized transfer-matrix model can provide quite accurate results in accordance with those of rigorous electromagnetic simulations. In the following, we use this model to examine light emission processes in planar MQW color converters.

## 2) Physical origins of spontaneous emission distribution: antinode factor, Airy function

In this section, we wish to explain the origin of the SpE angular distribution and its role in the performances of real-life devices. We still consider a single monochromatic horizontal dipole centered inside the high-index slab.

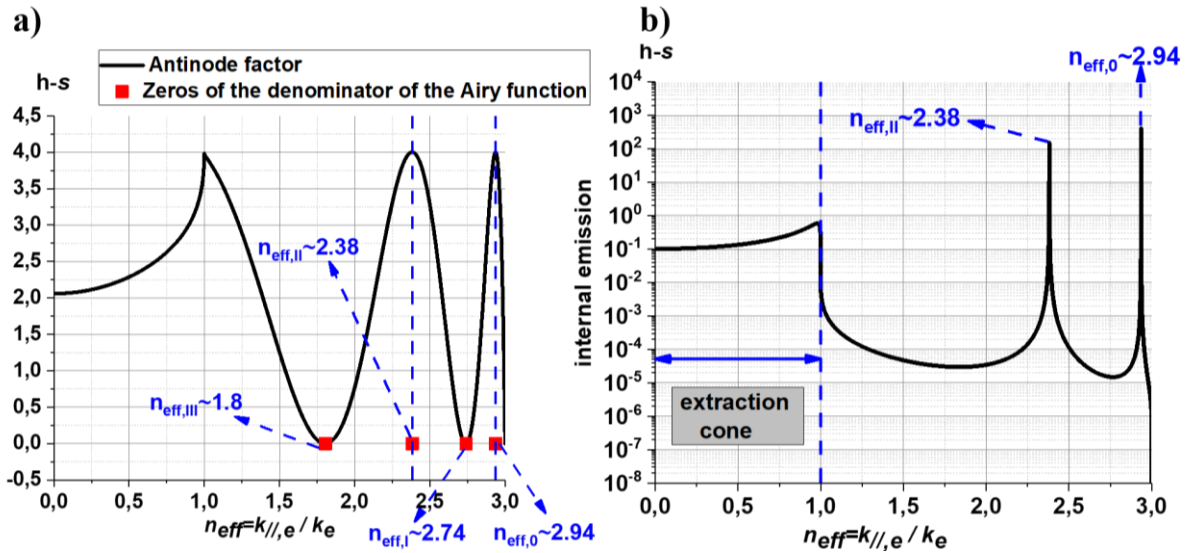


**Figure II-8:**  $s$ -polarized light from a single horizontal dipole centered in a slab. a) Antinode factor and zeros of the denominator of the Airy function as well as the b) internal emission as a function of the emission angle.

As we have shown in Eq. (II-20), SpE is set by the antinode factor, the Airy function and the internal emission in an unbounded medium. In Figure II-8, we plot the zeros of the denominator of the Airy function and the antinode factor as well as the corresponding angular distribution of the internal emission for  $s$ -polarized light. As already mentioned, those zeros correspond to modes, which satisfy the unity round-trip conditions. These self-sustained modes called guided modes propagate along the  $xy$  plane and do not contribute to light extraction in planar MQW CCL. In the results, we see that the slab supports four guided modes with effective indices<sup>10</sup> of 2.94 (fundamental mode labelled 0), 2.74, 2.38 and 1.8.

<sup>10</sup> We have introduced a useful variable called the effective index, which gives information on the refractive index experienced by the guided mode. It is the ratio between the in-plane wavevector and the wavevector in vacuum. In this particular case, it reads as  $n_{eff} = n_e \sin(\theta_e)$ .

However, the odd ones fall at the minima of the antinode factor, thus they do not appear in the SpE distribution outside the air cone ( $n_{\text{eff}} > 1$ ). Indeed, since the dipole is centered, only the even modes couple to the dipole emission. Thus, the Airy function governs the behavior of the bare cavity while the antinode factor sets the coupling between the emitters and the available cavity modes. Looking at the internal emission, we see that dipole emission excites different types of modes. Part of the emitted light is directly extracted into air ( $n_{\text{eff}} < 1$ ). This is called the direct light emission and accounts for the shape of the farfield emission and thus the values of directionality in planar cases. A very large part of the emitted light (over 70%) will excite the available guided modes inside the membrane and eventually set the LEE. These are the modes we aim at extracting.

It thus appears that SpE is the key element for controlling LEE along with directionality. Its origin has also been elucidated with the Airy function that sets the discrete angular positions of the guided modes and the antinode factor, which controls the coupling of each mode to dipole emission. In the following, we will see how SpE distribution is modified when implementing parameters of real-life devices (emission spectrum and emitter's distribution) and how it affects LEE and directionality.

### 3) Monochromatic distributed dipole source planes

In this part, we implement a source plane distribution and study its impact. We consider five monochromatic horizontal regularly spaced (along  $z$ ) dipole source planes (10nm between one another). In **Figure II-9**, we report on the internal emission as a function of the effective index for the two cases of five emitters or dipole source planes and a single dipole as a comparison.

For the single dipole, only even modes are coupled to light emission as seen before. However, when the five emitters are implemented, additional peaks corresponding to the odd modes start to appear. Indeed, the antinode factor depends on the dipole emission, thus any position-shift will change the coupling conditions between light emission and guided modes.

To quantify this phenomenon, we plot their photonic weight<sup>11</sup>, which is the fraction of the guided energy carried by each mode, in **Figure II-9-b**. If we note  $P_i$  the peak intensity of the guided mode labelled  $i$  and  $\theta_i$  its angular position, then by taking into account the solid angle, the photonic weight of the mode can simply be expressed<sup>12</sup> as  $P_i \sin(\theta_i) / \sum_j P_j \sin(\theta_j)$ . We can note that as we go from a single dipole to five emitters, the photonic weights of even modes remain quasi intact, whereas the additional odd modes only carry a negligible fraction of the guided energy (~1%). This can be understood by differentiating the phase shift  $\varphi_c$  of the antinode factor over the source position (see **Eq. (II-21)**). We can find that  $d\varphi_c = -\pi \cos(\theta_e) \frac{dz_{\text{ext}}}{\lambda/4n_e}$ . Consequently, as a rule of thumb, we can see that as long as the emitters are embedded into a region small enough compared to  $\lambda/4n_e$ , the whole emitter's region is equivalent to a single centered dipole, which is the case in our simulation.

<sup>11</sup> We will see in the next chapter that the photonic weight is of crucial interest for directional emission in multimode corrugated structures.

<sup>12</sup> In the case of broader modal distributions, the integral form of this expression needs to be used instead.

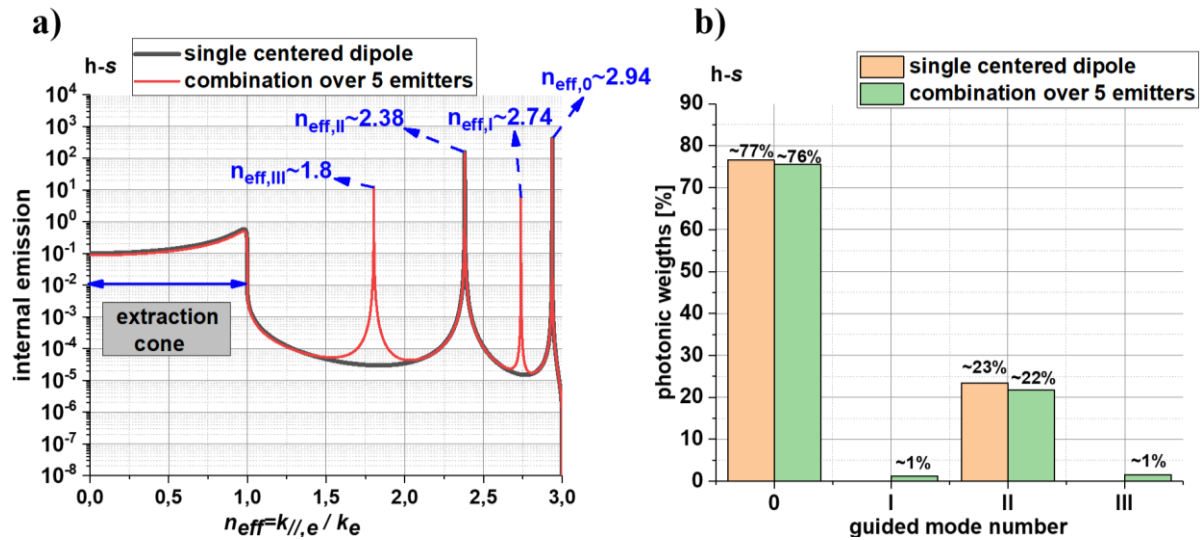


**Figure II-9:** *s*-polarized light from horizontal dipoles. a) Internal emission as a function of the effective index and b) the corresponding photonic weights for a single centered dipole and combined results over five emitters.

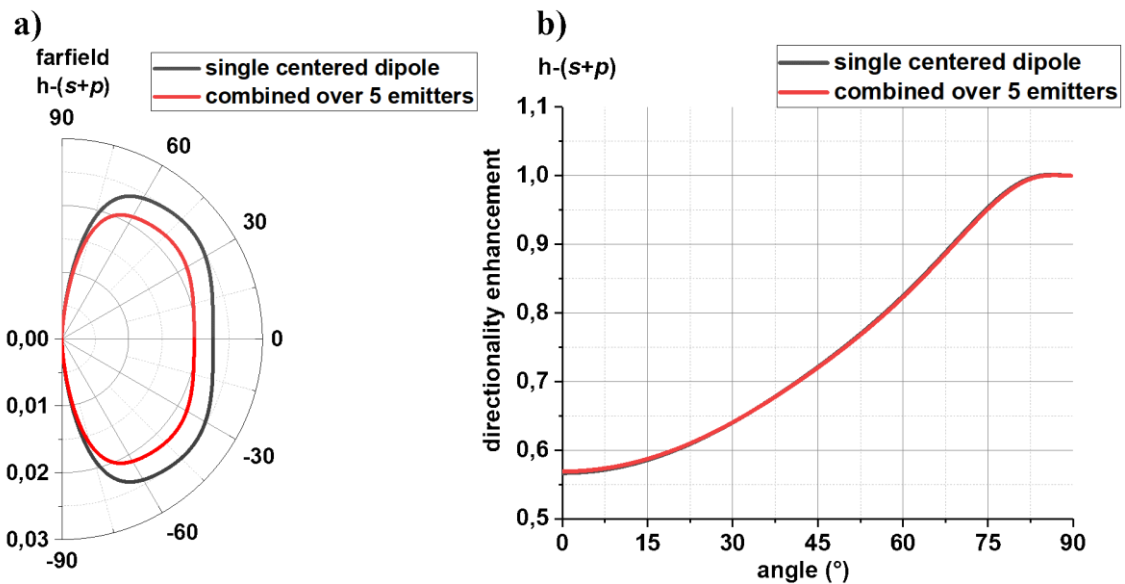


**Figure II-10:** Horizontal dipole (*s*- and *p*-polarizations combined). a) Farfield emission patterns and b) directionality enhancement over Lambertian emission for a single centered dipole and combined results over five emitters.

Furthermore, we can notice that the dipole position only slightly influences the internal emission inside the air cone. In terms of directionality<sup>13</sup> on the other hand, we can see in **Figure II-10** that despite the farfield intensity is changed when we consider all the five emitters, its shape does not change compared to a Lambertian emission.

We finally plot the resulting LEE and Purcell factors as a function of the dipole position in **Figure II-11**. Notwithstanding their dependency on the emitter's position, their combined values for the five emitters can be approximated by the value for the single centered dipole.

<sup>13</sup> Directionality will be mathematically defined in **Chapter III**. For now, one must keep in mind that a directional emission is an emission where most of emitted light is close to normal incidence (vertical emission). The Lambertian emission pattern is broad and unsuitable for AR applications, which is why we take it as a reference.

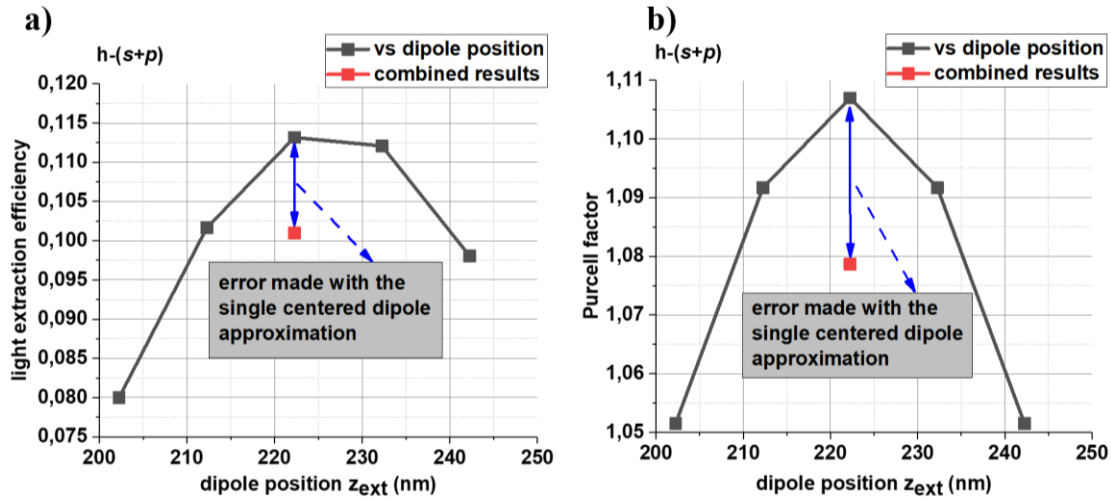


**Figure II-11:** Horizontal dipole ( $s$ - and  $p$ -polarizations combined). a) LEE and b) Purcell factor as a function of the dipole position. On each figure, the red dot represents the incoherently combined results.

It thus appears that for structures whose emission regions are thinner than a quarter-wavelength, increasing the number of dipoles does not help much in improving LEE or directionality of the emission. The single-centered-dipole approximation holds. Moreover, for devices with larger emission regions, all dipoles need to be accounted for. Either way, our modeling framework enables the implementation of any type of emitter's spatial distribution. These considerations will help in the choice of the number of quantum wells inside our MQW CCL.

#### 4) Spectrally-broadened single-plane emitters

In this section, we seek to grasp the impact of the emission spectrum on LEE and directionality. To do so, we consider a single polychromatic horizontal red emitter with an input spectrum centered at 640nm and a full width at half-maximum (FWHM) of 20nm as shown in **Figure II-12-a**.

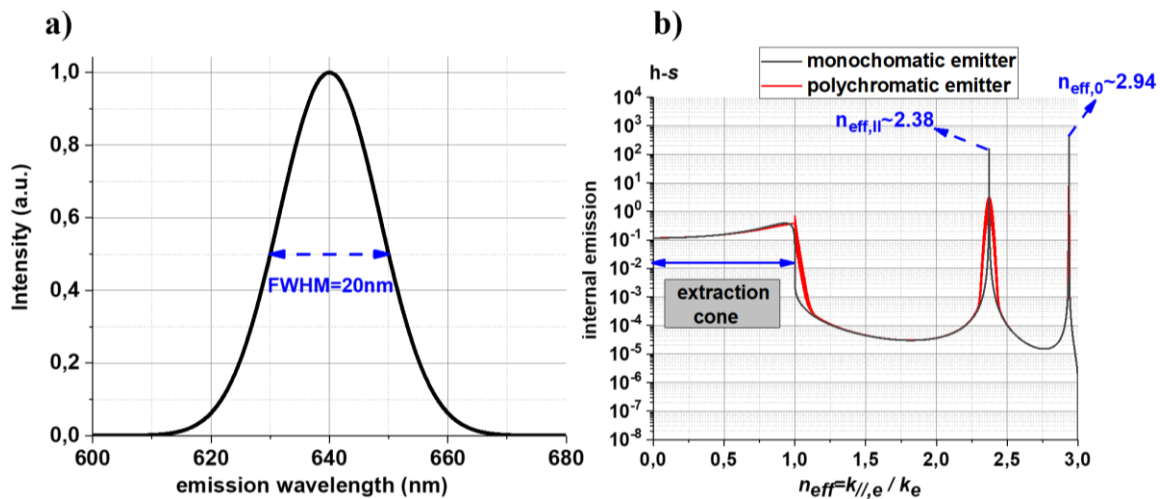


**Figure II-12:**  $s$ -polarized light from horizontal dipoles. a) Input emission spectrum. b) Internal emission per unit solid angle as a function of the effective index for the peak emission wavelength and for combined results over the input spectrum.

As we will see in the next chapter, these parameters are close to the ones of our red MQW CCL.

The internal emission is displayed on the right for both the monochromatic (peak emission wavelength) and polychromatic cases. We observe that the sharp peaks representing the guided modes are now

broadened into Lorentzian-shape functions, with a broadening that seems to decrease as the order of the guided modes decreases. This is because both antinode factor and Airy function are wavelength-dependent.

Similarly to the previous case of distributed emitters, by differentiating the phase shift of the antinode factor over wavelength, one can easily find that:  $d\varphi_c \propto -\frac{\cos(\theta_e)}{\lambda^2} d\lambda$ . This broadening is clearly cosinus-dependent on the emission angle, which explains why low-order modes<sup>14</sup> are less affected than high-order ones. Besides, since the internal emission shape inside the air cone is also altered, the radiation pattern and thus directionality are impacted, albeit very slightly as displayed in **Figure II-13**.

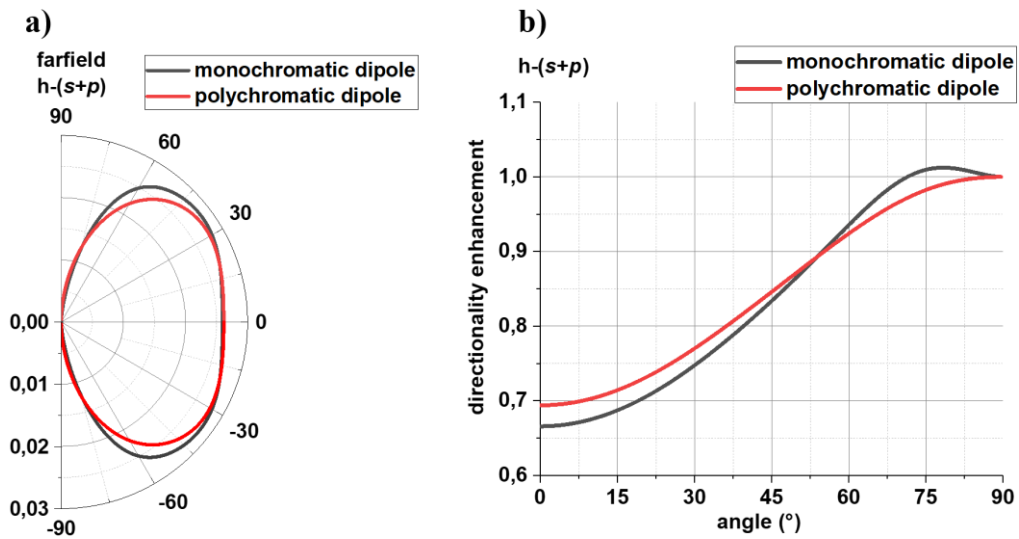


**Figure II-13:** Horizontal dipole ( $s$ - and  $p$ -polarizations combined). a) Farfield emission patterns and b) directionality enhancement over Lambertian emission for a monochromatic and polychromatic light source.

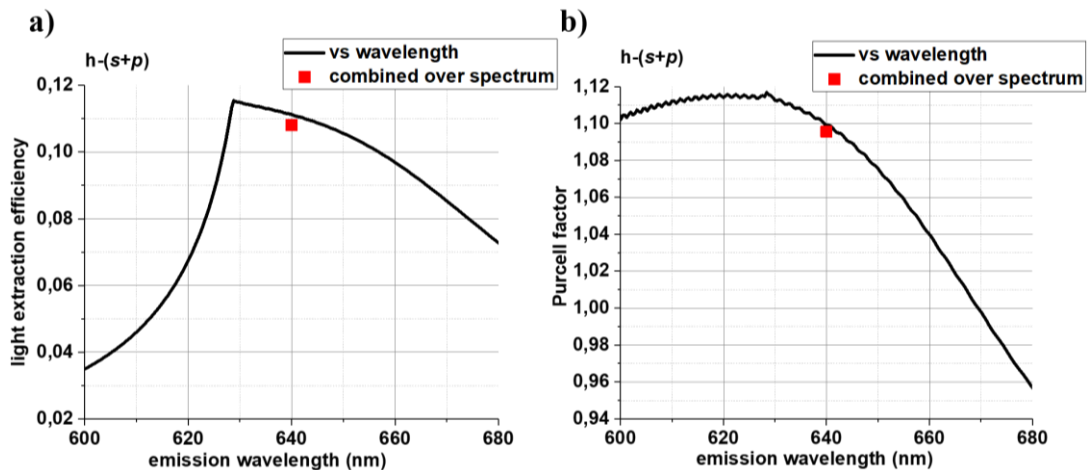


**Figure II-14:** Horizontal dipole ( $s$ - and  $p$ -polarizations combined). a) LEE and b) Purcell factor as a function of the emission wavelength. On each figure, the red dot represents the incoherently combined results.

Similarly, the combined values of LEE and Purcell factor over the whole emission spectrum are also quite close to the one at the peak emission wavelength as displayed in **Figure II-14**.

<sup>14</sup> Low-order guided modes (starting from the fundamental mode) correspond to the high emission angles and therefore low cosinus values.

More generally, as we have seen in the differential before, as long as the FWHM of the source is negligible, the single monochromatic dipole approximation holds. For structures with much broader sources, it is worth considering in the modal analysis that low-order modes are less modified than high-order ones.

This concludes our discussion on the opto-geometrical parameters of the bare MQW color-converters and their quantum wells along with their impact on LEE and directionality. In the following, we investigate the impact of the optical environment around the color-converters on spontaneous emission.

### II.2.6.b On a substrate

The MQW color converters will lie in asymmetric optical environments all along this PhD work. In the first set of devices that we are going to investigate (Lot I), they are bonded on transparent substrates to study the behavior of the bare photonic crystals. In this section, we wish to evaluate the impact of the substrate on spontaneous emission (SpE). A single monochromatic horizontal dipole source plane is centered inside the slab which is now surrounded by a transparent substrate ( $n_2=1.45$ ) and an air superstrate ( $n_1=1$ ). The total internal emission distribution for both  $s$ - and  $p$ -polarized light is displayed in **Figure II-15**.

The asymmetric environment imposed by the transparent substrate completely redistributes SpE. Part of the emitted light (directly emitted light), which now totals up to  $\sim 17\%$ , is still directly extracted into air ( $n_{\text{eff}} < 1$ ). Another fraction (substrate light), which amounts to  $\sim 12\%$ , is propagative in the substrate but not in air ( $1 < n_{\text{eff}} < 1.45$ ). Finally, a very large portion of the emitted light ( $\sim 71\%$ ) excites the four available guided modes inside the so-formed membrane ( $n_{\text{eff}} > 1.45$ ). This guided light is still a major efficiency bottleneck and innovative strategies need to be devised to reduce its amount (increase LEE) while keeping a very directional emission. What strikes most is that compared to what we have seen in the previous subsections, the asymmetric optical environment created by the substrate has redistributed SpE changing the balance between the guided and extracted powers.

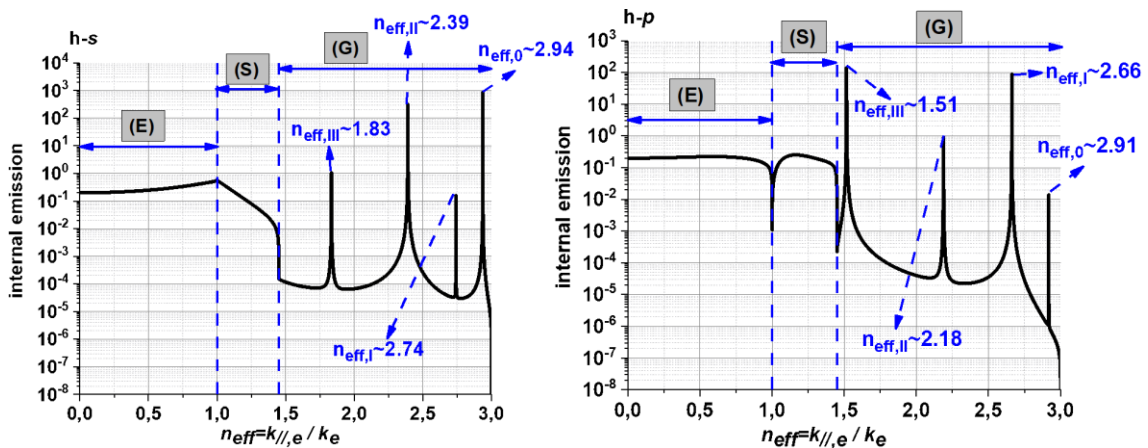


**Figure II-15:**  $s$ - and  $p$ - polarized light from horizontal dipoles. Internal emission per unit solid angle as a function of the effective index. E=directly emitted light, S=substrate light, G= guided light.

In the following and last example section, we are going to investigate the possibility of alleviating both LEE and directionality issues at the same time by a controlled SpE redistribution.

### II.2.6.c With a distributed Bragg reflector: LEE vs directionality

We wish to investigate the extent to which it is possible to improve both LEE and directionality by benefiting from controlled cavity effects that can happen inside the color converters. In that regard, the high-index slab is placed on top of a distributed Bragg reflector (DBR) whose parameters are indicated in **Figure II-16**. In-between those two, we interleave a tuning layer whose thickness will be varied to control the cavity effects. Let us recall that a cavity is tuned when its opto-geometrical parameters are so that the main Fabry-Pérot (FP) mode occurs at normal incidence.

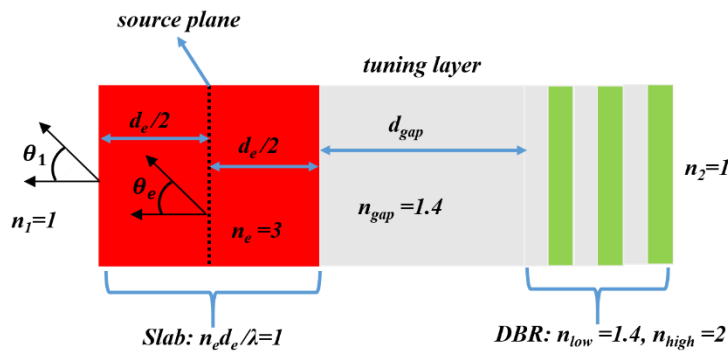


**Figure II-16:** Schematics of the high-index slab with a bottom Distributed Bragg reflector consisting of 3 pairs of alternate indices 1.45 and 2. The emitter is a horizontal dipole centered inside the cavity.

A single monochromatic horizontal dipole source plane is placed at the center of the slab.

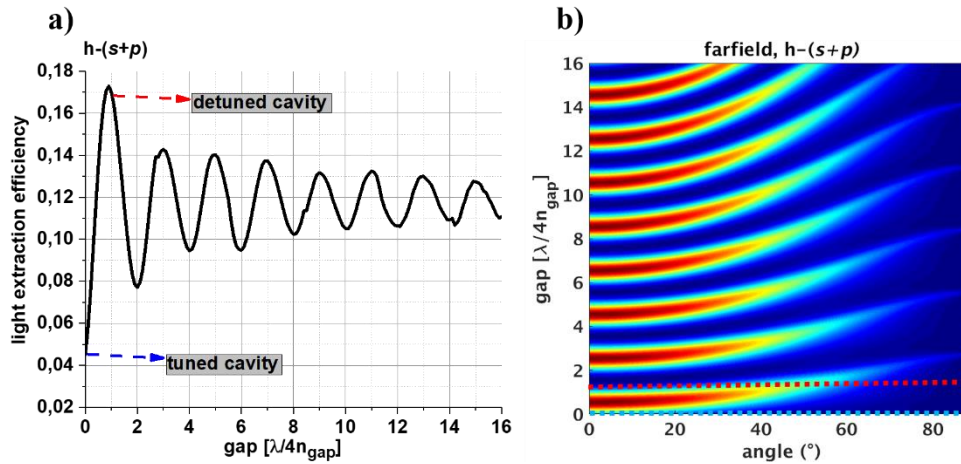


**Figure II-17:** Horizontal dipole ( $s$ - and  $p$ -polarizations combined). a) LEE and b) farfield patterns as a function of the thickness of the tuning layer. Blue and red dashed lines indicate gaps corresponding to a tuned and detuned cavity, respectively.

In **Figure II-17**, both LEE and the radiation patterns are plotted as a function of the thickness of the tuning layer. When there is no tuning layer, LEE is at its lowest ( $\sim 4\%$ ) while the farfield pattern is very directional with a peak emission angle at normal incidence. As the gap is set to reach the maximum LEE of  $\sim 16\%$  at  $\lambda/4n_e$ , the peak emission angle is shifted to  $\sim 42^\circ$  leading to a non-directional emission pattern. Afterwards, both LEE and farfield patterns oscillate with a periodicity of  $\lambda/2n_e$ , with the emission patterns exhibiting the standard “boomerang”-shaped lines typical of Fabry-Pérot interferences. Let us

note that more generally we see that the maxima of the LEE (at  $(2p+1) \lambda/4n_{gap}$ ) correspond to the non-directional farfields while the minima of LEE (at  $(2p) \lambda/4n_{gap}$ ) occur with directional patterns,  $p$  being an integer.

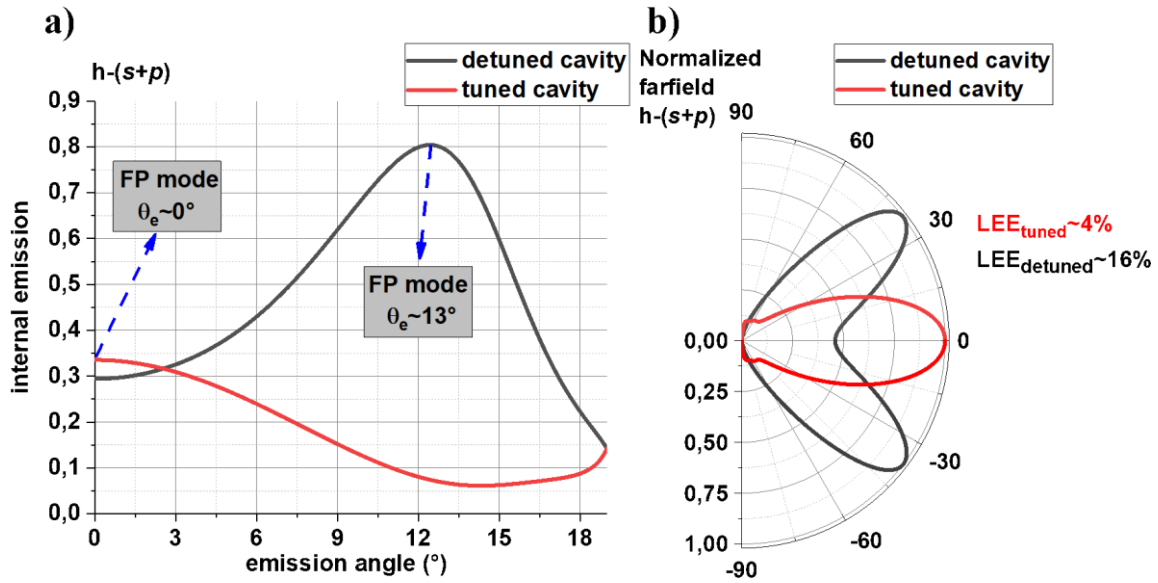


**Figure II-18:** Horizontal dipole ( $s$ - and  $p$ -polarizations combined). a) Angular internal emission distribution within the extraction cone and b) normalized farfield patterns for tuned and detuned cavity.

We now focus on two values of gaps (0 and 1) to better our understanding of the previous considerations. In **Figure II-18**, we show the corresponding internal emission inside the air cone for these two gap values as well as the corresponding normalized emission patterns. As we can see, without tuning layer ( $gap=0$ ), the cavity is already tuned so that the main FP lobe occurs at normal incidence, which leads to a directional farfield shape, albeit the lowest LEE ( $\sim 4\%$ ). As the gap is optimized to increase LEE ( $\sim 16\%$  at  $gap=1$ ), SpE is redistributed so that the main FP lobe is shifted from normal incidence to  $\sim 13^\circ$ <sup>15</sup>. The emission patterns, often referred to as “rabbit’s ears”, loses its directionality as we see in **Figure II-18-b**. This maximum LEE is still far below the required values described in the previous chapter.

It therefore seems that with this planar strategy of SpE redistribution, LEE and directionality cannot be optimized simultaneously. This strategy is then not viable for the AR microdisplays targeted in this PhD thesis, since both high efficiency and directional emission are required.

## II.2.7 Conclusion on the SpE modeling framework and planar strategies

Spontaneous emission (SpE) is the key physical phenomenon underlying light emission in MQW CCL. In the previous sections, we have developed a novel SpE modeling framework based on generalized 3x3 transfer-matrices, whose accuracy compared to rigorous electromagnetic simulations with 3D-FDTD and applicability have been demonstrated. This model has thus been pointed out to be a key tool for designing incoherent light-emitting structures. In particular, it has enabled us to highlight that in MQW CCL, light extraction is drastically hindered by the coupling between dipole emission and the available

<sup>15</sup> Using the Snell-Descartes’ law, we can find that  $13^\circ$  as an internal angle corresponds to an external angle of  $\sim 42^\circ$  as we have seen in the farfield patterns.

guided modes (more than 70% of the emitted light), which is one of the main efficiency bottlenecks of those devices. The importance of SpE in that matter has also been emphasized as well its origin through the antinode factor and the Airy function, since it eventually sets LEE and the directionality of the emission. To alleviate the light extraction issues, we have evaluated different routes ranging from epitaxial design (controlling the thickness of the color-converters, the number of quantum wells, their positions, the emission spectrum) to SpE redistribution (through tuning and detuning the total optical thickness of the CCL), but none of them allows the simultaneous optimization of both LEE and directionality.

There is thereby a need for photonic-crystals (PhCs) which so far have been demonstrated to possess the unique ability to provide a superior control of the guided-mode diffraction out of high-index materials, thus increasing LEE and directionality at the same time [12]. They have yet to be properly designed and implemented in MQW CCL! That is the reason why it is the strategy we adopt in this PhD thesis. In the following, we present the basic physics required to understand light diffraction by PhCs.

## II.3 Principle of operation of photonic-crystals for light diffraction

### II.3.1 Starting point: extraction issue in a single-mode waveguide

In order to understand the basic physics of the diffraction process of PhCs, we consider a single-mode waveguide operating in transverse-electric (TE) polarization at 640nm. The refractive index of the layer is close to the one of red MQW CCL ( $n=3.49$ ). In a photonic-crystal membrane, each guided mode experiences its own diffraction conditions. Therefore, despite our fabricated MQW CCL are multimode structures (see the next chapter); we restrict the demo to a single-mode case for the sake of simplicity, which can later be applied to other modes as well.

To determine the height of the waveguide for single-mode operation, we use the FemSIM tool from the Rsoft Design Suite, which is a mode solver based on the finite element method (FEM).

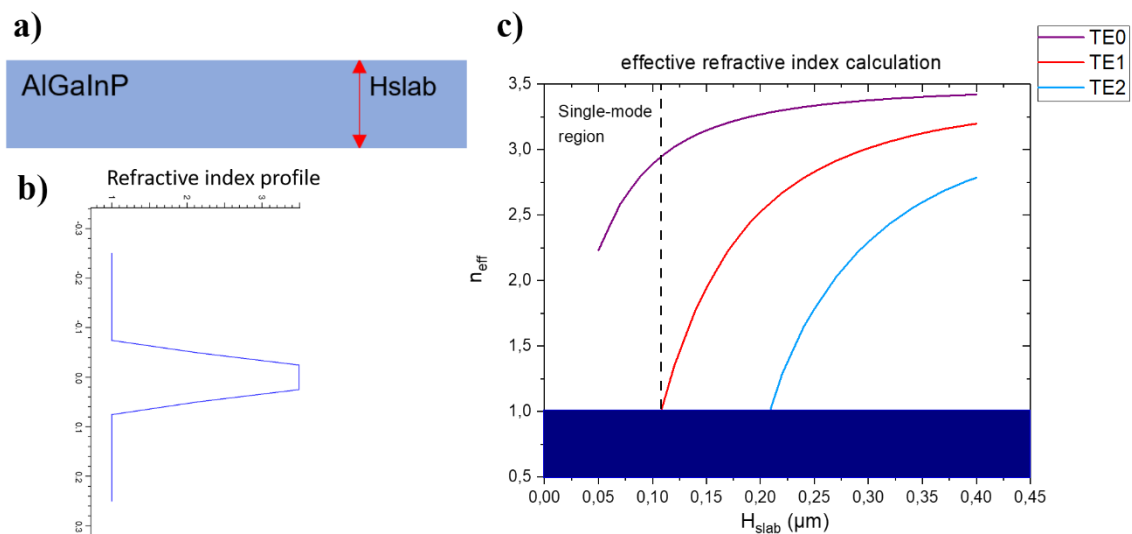


**Figure II-19:** a) Schematics of the AlGaInP thin-film surrounded by air and b) the associated refractive index profile. c) Effective index calculation of the existing wave-guided modes as a function of the height of the AlGaInP-slab ( $H_{\text{slab}}$ ).

As displayed in **Figure II-19-c**, the number of guided modes supported by the slab decreases with its height, until single-mode operation is reached for heights under  $\sim 110\text{nm}$ . In this preliminary study, we then choose  $H_{\text{slab}}=100\text{nm}$ .

For starters, we perform FDTD simulations (see **Appendix A.1** for details about the FDTD method) to determine the electric field maps of the transitory and stationary regimes as well as quantify the evolution of the flow of light. The results are reported in **Figure II-20** for a single  $y$ -oriented dipole centered inside the slab.

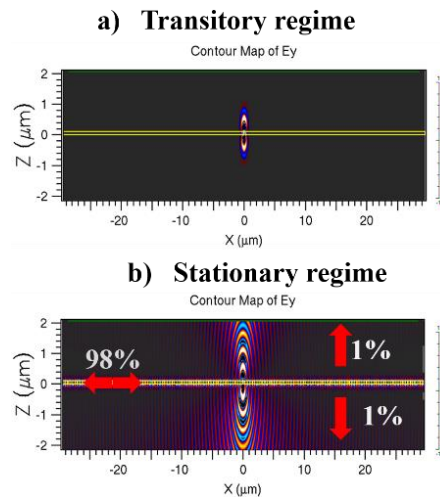


**Figure II-20:** FDTD simulation of a dipole centered in a 100nm-thick AlGaInP slab. Contour map of the electric field ( $E_y$ ) in: a) the transitory regime and b) the stationary regime.

We can see that only 1% of the emitted light is directly and symmetrically extracted upwards and downwards, while 98% is coupled to the only available  $TE_0$  guided mode. As we have seen in the previous section, this is worst-case scenario in terms of light extraction ( $H_{\text{slab}}$  near  $\lambda/2n$ ). In addition, the farfield pattern (not shown here) is almost as directional as a Lambertian emission.

In the following, we investigate how light diffraction by PhCs works for one mode and how it could improve the performance of MQW CCL.

### II.3.2 General overview of photonic-crystals

#### II.3.2.a Foreword

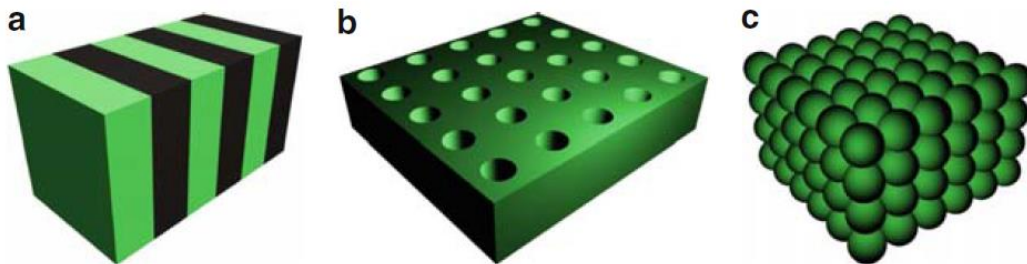


**Figure II-21:** Examples of a) 1D, b) 2D and c) 3D photonic-crystals [13].

Photonic crystals (PhCs) are a class of optical media represented by natural or artificial structures with periodic modulations of the dielectric constant. Depending on the number of spatial directions in which

the modulations occur, they can be divided into three broad categories, namely one-dimensional (1D), two-dimensional (2D) and three-dimensional (3D) structures as displayed in **Figure II-21**.

Understanding the physics of PhCs is clearly a matter of analogy. Similarly to an electron propagating within crystals such as semiconductors, when a photon propagates within a PhC lattice, its “interaction” with the periodicity of the dielectric constant can introduce photonic band gaps (PBG), frequency gaps in which no mode, regardless of  $k$ , can propagate. In **Figure II-22**, we can see the plot of dispersion relations of an unpattern medium (simple band folding of the uniform free-photon dispersion relation of light:  $\omega = k_{//}c$ ) and the one of a PhC where we can observe the PBG. In the latter (right plot), we can see that the dispersion curve just below and above the band gap is flatter than the free-photon dispersion (left plot). The higher density of photonic states at these frequencies can be utilized to enhance the radiative recombination rate (Purcell effect). The reduced group velocity of the light  $v_g = \partial\omega/\partial k$  near those band-edges enables “slow light propagation” – a regime where non-linear effects are enhanced [14].

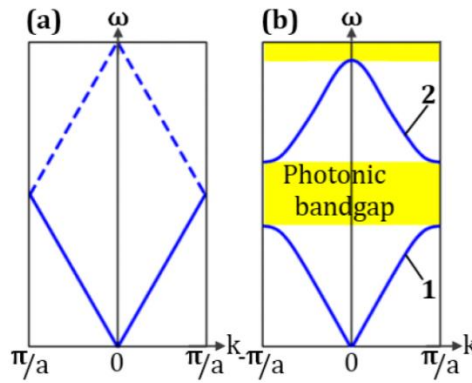


**Figure II-22:** Photonic band structure for on-axis propagation in the case of a) bulk and b) layered media [15].

The reader is referred to [16] for a more detailed description of photonic crystals and its applications. In this PhD thesis, photonic-crystals are etched inside a slab (MQW CCL) as we will see later.

### II.3.2.b Photonic crystal parameters

A photonic crystal is described by its lattice symmetry, pattern type, lattice period ( $a$ ), surfacic air-filling factor ( $FF$ ), lateral extent ( $L$ ) and etch depth. In this PhD thesis, we focus on 1D and 2D lattices (square and hexagonal ones<sup>16</sup>) with two types of patterns (holes and pillars). Those lattices are displayed in **Figure II-23** and their behavior and interest will be thoroughly studied in the next chapter.

All the other parameters of the PhCs are shown in **Figure II-24** for a color converter on a substrate.

The air-filling ( $FF$ ) factor is defined as the ratio of air to total volume of a unit cell. It thus depends on the symmetry of the lattice. For 1D, square and hexagonal lattices, it is defined as follows<sup>17</sup>:

$$FF_{1D} = \frac{D}{a}, \quad FF_{square} = \frac{\pi R^2}{a^2}, \quad FF_{hexa} = \frac{2\pi}{\sqrt{3}} \left(\frac{R}{a}\right)^2 \quad (\text{II-35})$$

<sup>16</sup> A detailed study of the lattice symmetry and its impact will be performed in **Chapter III**.

<sup>17</sup> For pillars, this corresponds to the “material” filling factor.

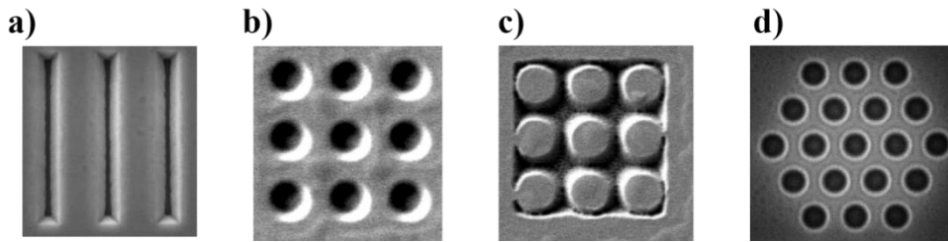


**Figure II-23:** SEM images of the different lattice symmetries and pattern types. a) 1D lattice, b) square lattice of air holes, c) square lattice of pillars and d) triangular lattice of pillars.

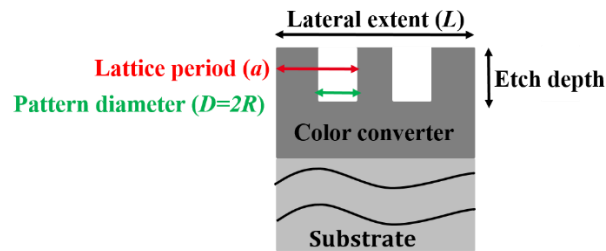


**Figure II-24:** Description of the parameters of the photonic crystals etched in a color converter on a substrate.

### II.3.2.c Different photonic-crystal integration for increasing light extraction

There could be different design strategies for increasing light extraction in a MQW color converters using photonic crystals [17]. Let us consider a slab within the different cases described in **Figure II-25** with its emission region in red.

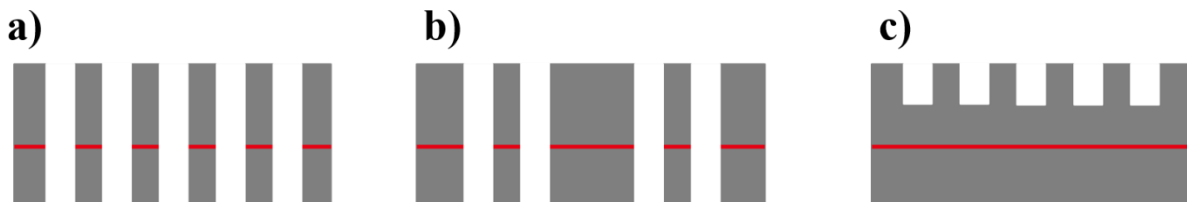


**Figure II-25:** Possible PhC designs. a) Strongly coupled PhC with the active region within the PhC. b) Strongly coupled PhC with the emission region separated from the extraction region. c) Weakly corrugated PhC with PhC above the active layer.

The first case (see **Figure II-25-a**) is the initial implementation of photonic crystals with complete etching of the slab all the way through the active region for SpE control [18]. By operating within frequencies inside the PBG or near the band-edges, emission into guided modes could be totally inhibited forcing light emission into radiating modes that can escape the color converter. Although this strategy seems appealing, we are going to see in the next chapter that etching though the active region is very detrimental since it creates non-radiative recombination centers.

The second approach consists in separating the emission and extraction regions. Due to the reduction of the effective emission region and the size of the pixel targeted in AR microdisplays, this strategy would not be viable.

That is the reason why in this PhD thesis, we will adopt the strategy where the photonic crystals are etched above the active regions. For those relatively weakly corrugated PhCs (low filling factors and/or etch depths), we end up in the “free-photon approximation regime” where band bending or splitting is hardly observed [19–21]. In this case, PhCs are merely used for light diffraction with a dispersion related

to the band folding of the free-photon dispersion shown in **Figure II-22-a**. In the following, we demonstrate how light diffraction by PhCs works.

### II.3.3 Bragg's law in a basic 2D problem: case of a single-mode waveguide

In a PhC, light diffraction is ruled by the vectorial Bragg's law, which reads as [19]:

$$\vec{k}_d = \vec{k}_i + \vec{G} = \vec{k}_i + m\vec{G}_0 \quad (\text{II-36})$$

In the presence of a PhC whose reciprocal lattice vector is  $\vec{G}$ , an incident guided mode with an in plane wavevector  $\vec{k}_i$  becomes Bloch-modes by coupling to other harmonics ( $\vec{k}_i + m\vec{G}_0$ ). When the parameters of the PhCs satisfy the diffraction condition in **Eq. (II-37)**, the guided light is diffracted into air [12].

$$|\vec{k}_i + m\vec{G}_0| < \frac{2\pi}{\lambda} \quad (\text{II-37})$$

The Bloch-modes are then referred to as leaky modes, since their power leaks to air as they propagate.

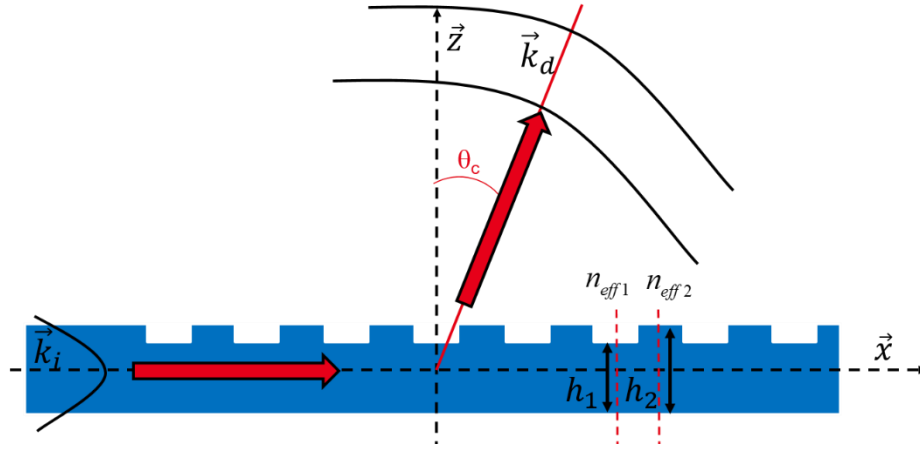


**Figure II-26:** Principle of operation of a corrugated waveguide. The incident mode (with a wavevector  $k_i$ ) interacts with the grating that out-coupled it toward free space with an angle  $\theta_c$ . The Bragg law determines the out-coupling angle.

In the simple 2D case described in **Figure II-26**, this vectorial Bragg's law that determines the out-coupling angle to free space becomes:

$$\vec{k}_d \cdot \vec{x} = \vec{k}_i \cdot \vec{x} + \vec{G} \cdot \vec{x} \quad \text{leading to} \quad k_d \sin(\theta_c) = k_i + \frac{2\pi m}{a} \quad (\text{II-38})$$

Here  $m$  is the diffraction order and  $G_0 = 2\pi/a$ . The in-plane wavevector  $k_i$  of the guided mode interacting with the grating is defined as a function of the average refractive index<sup>18</sup> of the grating  $\bar{n}_{eff}$ :

$$k_i = \frac{2\pi}{\lambda} \bar{n}_{eff} \quad \text{where} \quad \bar{n}_{eff} = \frac{n_{eff1} + n_{eff2}}{2} \quad (\text{II-39})$$

Here  $n_{eff1}$  and  $n_{eff2}$  depend on the local height of the etched slab as depicted in **Figure II-26** and their values are determined with the modal calculations in **Figure II-19-c**. We will investigate next the necessary conditions to obtain efficient out-coupling of a guided mode to free space with a high directionality.

<sup>18</sup> This formula for the average effective index holds in the simple effective medium approximation [22] with a filling factor of 50%.

### II.3.4 First-order Bragg lattice: reflection of the guided mode

A schematic overview of the reflectivity process in a first-order Bragg grating as well as the photonic band structure in the first Brillouin zone calculated using the Plane Wave Expansion (PWE) algorithm are depicted in **Figure II-27**.

The latter shows that the optical mode operates within the first photonic band gap where light propagation is strictly forbidden. The interaction with free-space is not allowed. The first propagation constant  $k_i$  corresponding to the incident mode is connected to the propagation constant  $k_d$  of the reflected mode via the grating constant  $G$ .

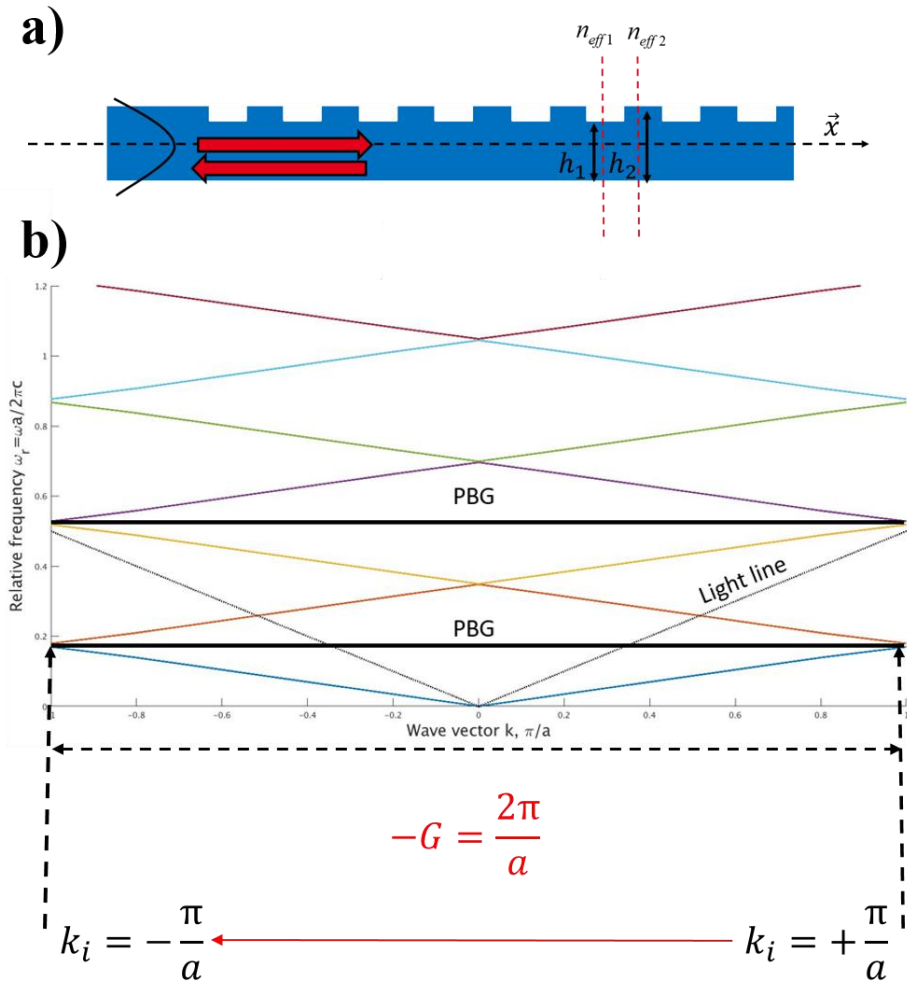


**Figure II-27:** a) Schematic overview of the reflectivity process in a first-order Bragg grating and b) the associated photonic band structure shows that the optical mode operates within the first photonic band gap where the propagation is strictly forbidden.

Following the Bragg relation in **Eq. (II-38)**, we end up with the following relation for the lattice period:

$$\begin{cases} |\vec{k}_i| = |\vec{k}_d| \\ |\sin(\theta_c)| = 1 \end{cases} \text{ which leads to } a = \frac{\lambda}{2\bar{n}_{eff}} \quad (\text{II-40})$$

This mode of operation is widely used in lasers where photonic-crystals are implemented as DBRs [23], but will not be our focus in this PhD thesis.

### II.3.5 Second-order grating: total extraction and vertical beaming to free space

The second order gratings, and more generally the higher even-order grating-periods, are structures that will be implemented in practical devices since they operate at the  $\Gamma$ -point, i.e. vertically or at normal incidence. In **Figure II-28**, we present the principle of operation of the vertical extraction process in a second-order Bragg grating as well as the photonic band structure showing that the optical mode operates in the middle of first Brillouin zone.

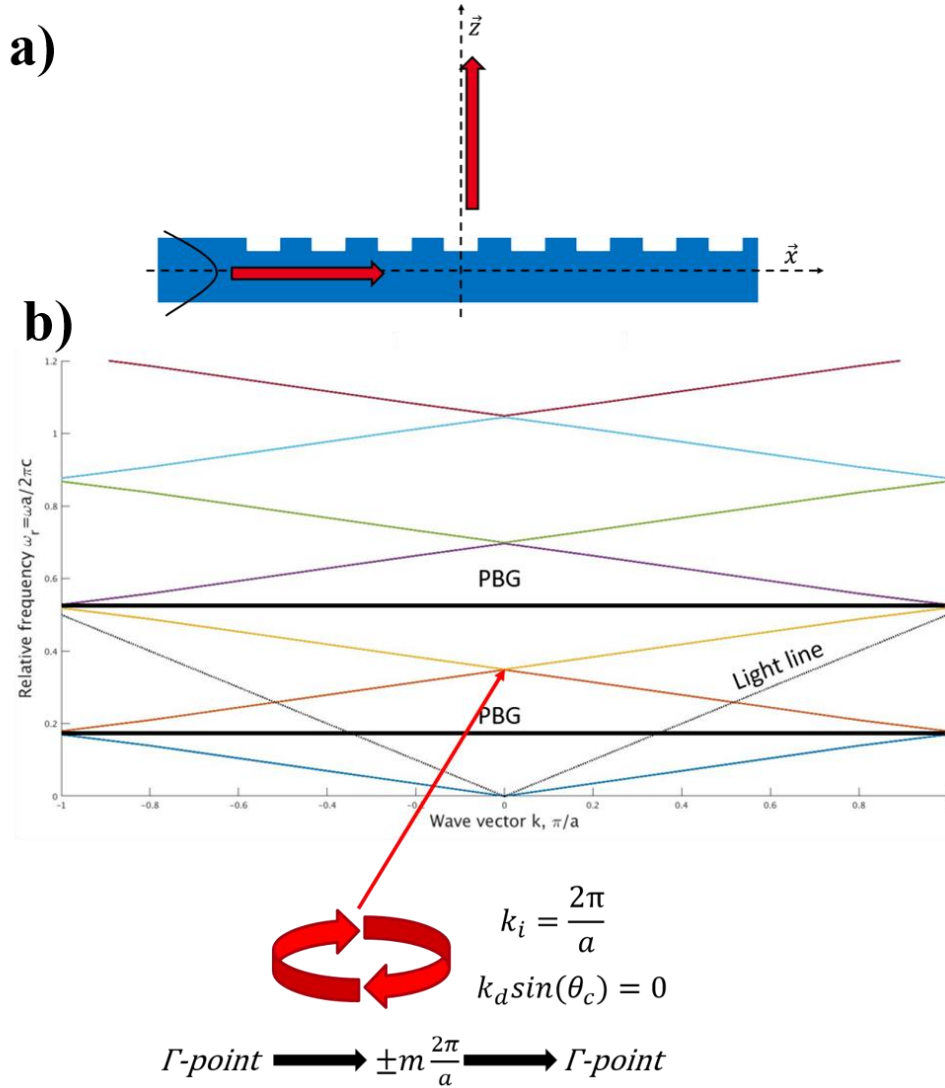


**Figure II-28:** a) Principle of operation of the vertical extraction process in a second-order Bragg grating and b) the associated photonic band structure showing that the optical mode operates in the middle of the first Brillouin zone, at the  $\Gamma$ -point.

In this configuration, the first propagation constant  $k_i$  corresponding to the guided mode interacts with the propagation constant  $k_d$  ( $\theta_c=0$ ,  $\Gamma$ ) of the extracted mode via the grating constant  $G=2\pi/a$ . Since the relative energy frequency falls above the light line, then only for the  $\Gamma$ -point, and not for other  $\Gamma \pm m2\pi/a$ , vertical-emission is the only way to communicate with free-space. According to the Bragg's law, we can write:

$$\sin(\theta_c) = 0 \text{ which leads to } a = \frac{\lambda}{\bar{n}_{eff}} \quad (\text{II-41})$$

We use additional FDTD simulations to validate the previous semi-analytical approach. In **Figure II-29**, we report on the layout of the corrugated structure as well as the initial conditions. The height of the slab and the etch depth are 110nm and  $H_{slab}/3$ . In order to prevent from diffractive-effects occurring at the edges of the structure, we choose a device length  $L_{device}$  higher than the free-space coupling length<sup>19</sup>  $L_{coupling}$  so that the structure can be considered quasi-infinite. The fundamental TE0 mode, the only available mode in this single-mode waveguide, is launched from the left side of the waveguide.

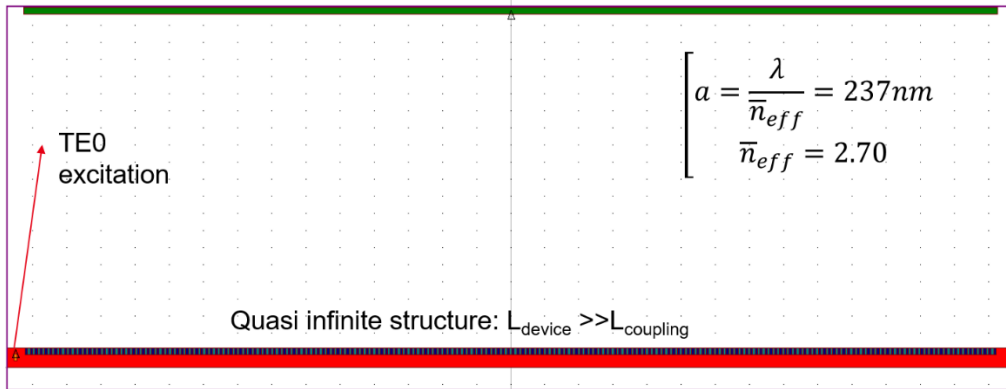


**Figure II-29:** Layout of the device and initial conditions used for FDTD simulations.

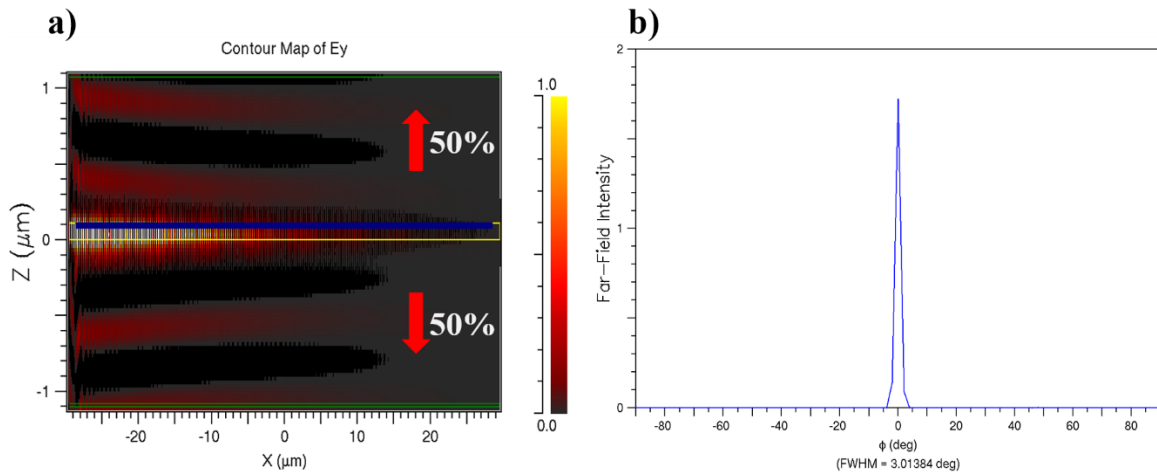


**Figure II-30:** FDTD simulation results. a) Contour map of the electric field ( $E_y$ ) in the stationary regime and b) farfield.

In **Figure II-30**, we show the FDTD simulation results. We can see in the left plot that all the power carried by the waveguided-mode is equally extracted upwards and downwards (50%). As shown in the right figure, the emission is highly directive and its FWHM is  $\sim 3^\circ$ <sup>20</sup>. It is worth noticing that for the same lattice period, one cannot diffract at the  $\Gamma$ -point two different effective indices. In the next chapter, we will propose a novel methodology for shaping the radiation patterns into directional ones even in multimode waveguides (sustaining more than one effective index).

<sup>19</sup> The coupling or saturation length is the device length necessary for all the guided light to be extracted in air. It is different from the extraction length, which is the 1/e decay length.

<sup>20</sup> In the next chapter, we will see that this value strongly depends on the grating strength, which fixes the “natural” penetration depth in the grating before being out-coupled.

### II.3.6 Higher order Bragg gratings

For higher even-order ( $m > 2$ ), other free-space Bloch modes are available above the light line, thus the guided mode can be diffracted within different angles. Using FDTD simulations with a grating period of 474nm ( $2\lambda/\bar{n}_{eff}$ ) corresponding to the 4<sup>th</sup> Bragg order, we obtain (see **Figure II-31-a**) that all the power carried by the waveguided-mode is equally extracted upwards and downwards (50%) as for the second-order grating. However, we can observe in the electric field map distribution that the penetration depth is significantly lower. This can be understood as follows: for vertical extraction, the penetration depth is higher because the associated grating strength is lower and for other diffraction angles, especially large ones, the extraction process occurs faster since the grating strength is higher. This particular point will be further investigated in the next chapter.

In **Figure II-31-b**, we see the resulting farfield emission pattern, which, as predicted, present additional peaks at  $\pm 69^\circ$ . This thus results into a less directional farfield than the one of the second Bragg order.

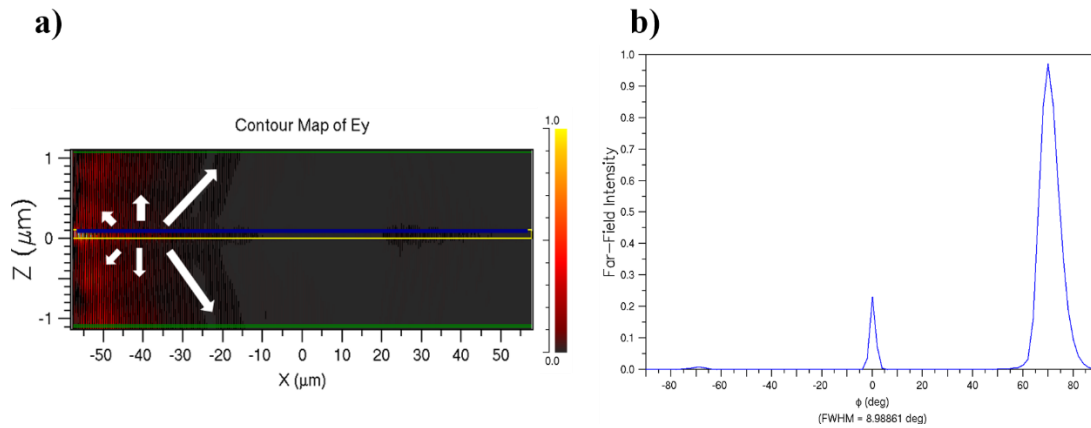


**Figure II-31:** FDTD simulation results. a) Contour map of the electric field ( $E_y$ ) in the stationary regime and b) farfield pattern showing with three peaks at  $0^\circ$  and at  $\pm 69^\circ$ .

### II.3.7 Incoherent multiple-dipoles emission in a second-order grating

We have explained the principle of operation of the interaction in-between a guided mode and a free-space mode through a grating. In particular, we saw that interaction with radiation modes occurs for even orders. In the case of a quasi-infinite structure, the directionality of the emission is ensured with a grating operating at the second-Bragg order. In this subsection, we will investigate the emission of an incoherent source distributed along the device similar to conditions of our MQW CCL. To simulate the incoherence, FDTD simulations of dipoles were combined (see **Appendix A.1**) and the convergence was obtained with a single source plane comprising 50 dipoles (or equivalently 50 simulations) homogeneously distributed along one period of the PhC patterns.

In **Figure II-32** and **Figure II-33**, we show the electric field plot ( $E_y$  component) and the extraction ratio (light extraction efficiency) as a function of the number of periods, respectively. From these simulations, we can extract the coupling length defined by the asymptote highlighted in red. More than 130 periods are needed to extract all the light. We can also notice that light extraction is equally distributed, upwards and downwards.

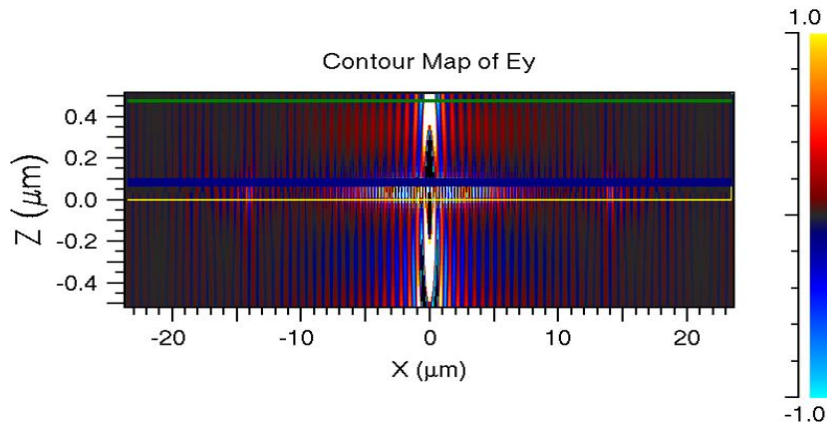


**Figure II-32:** FDTD simulation of one dipole located in the middle of the slab: contour map of the electric field ( $E_y$ ) in the stationary regime.

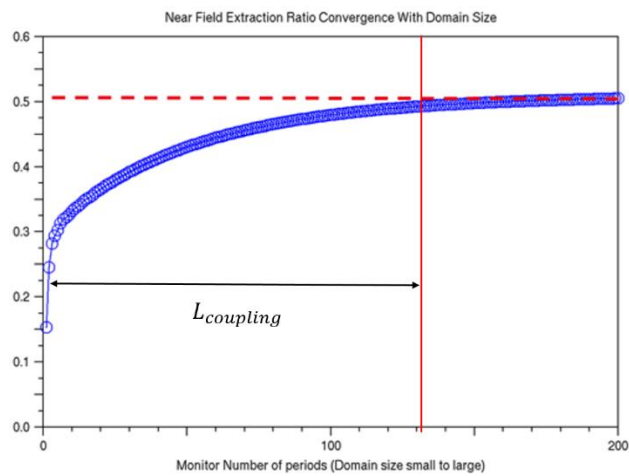


**Figure II-33:** 50 dipoles FDTD simulation: Extraction ratio convergence as a function of the domain size (number of periods).

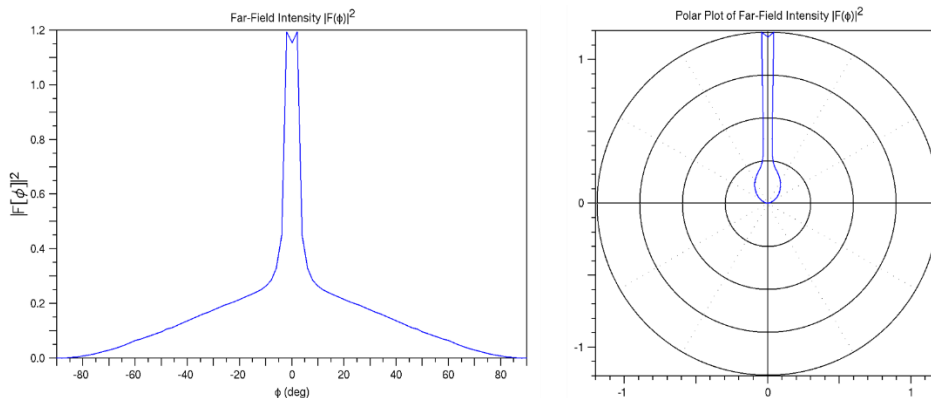


**Figure II-34:** 50 dipoles FDTD simulation: farfield emission diagram (Cartesian and polar plot).

The farfield emission diagram is presented in **Figure II-34**. The pattern is different from the previous study (see **Figure II-30-b**) since its shape is now the result of a combination of direct emission to free-space and the extraction of the guided-mode. However, the emission remains highly directive compared to unpatterned structures.

This concludes our discussion on how diffraction by PhCs works.

### II.3.8 Conclusion on the analytical and numerical analysis

We have seen in the previous 2D analysis that a photonic-crystal light extractor has a coupling length, which is set by its coupling strength and partly depends on the grating depth. Theoretically, all the light can be extracted if the lateral extent of the device is higher than its coupling length. The second important feature of the gratings concerns their ability to shape at the same time the Lambertian-like radiation patterns into directional ones depending on their lattice period: a second-order grating ensures a vertical beaming at the wavelength-scale. The link between the grating strength and the FWHM has also been pointed out.

## II.4 Conclusion

Spontaneous emission (SpE) is the key physical phenomenon underlying light emission processes in MQW color-converters. We have developed a novel SpE-modification modeling framework based on generalized 3x3 transfer-matrices. Its accuracy and validity have been demonstrated. Using this model, light extraction issues have been thoroughly analyzed, emphasizing the fact that standard planar strategies ranging from epitaxial design to SpE redistribution fail to optimize simultaneously both LEE and directionality. On the other hand, we have seen that when properly designed, photonic-crystals have the unique ability to alleviate the light extraction issues while shaping the radiation patterns into directional ones.

In the next chapter, we deal with the investigation of the roles of opto-geometrical properties of bare PhCs (lattice symmetry, lattice period, filling factor, lateral extent, etch depth) in real-life MQW color converters bonded on transparent substrates in order to devise innovative routes to circumvent the issues related to light extraction and extraction lengths as well as radiation-pattern control.

## II.5 References

1. E. F. Schubert, *Light-Emitting Diodes*, 2nd ed. (Cambridge University Press, 2006).
2. H. Benisty, R. Stanley, and M. Mayer, "Method of source terms for dipole emission modification in modes of arbitrary planar structures," *J. Opt. Soc. Am. A* **15**, 1192 (1998).
3. K. Kang, Y. Lee, J. Kim, H. Lee, and B. Yang, "A Generalized Fabry–Pérot Formulation for Optical Modeling of Organic Light-Emitting Diodes Considering the Dipole Orientation and Light Polarization," *IEEE Photonics J.* **8**, 1–19 (2016).
4. W. Lukosz, "Theory of optical-environment-dependent spontaneous-emission rates for emitters in thin layers," *Phys. Rev. B* **22**, 3030–3038 (1980).
5. W. Lukosz and R. E. Kunz, "Light emission by magnetic and electric dipoles close to a plane dielectric interface. II. Radiation patterns of perpendicular oriented dipoles," *JOSA* **67**, 1615–1619 (1977).
6. W. Lukosz, "Light emission by magnetic and electric dipoles close to a plane dielectric interface. III. Radiation patterns of dipoles with arbitrary orientation," *JOSA* **69**, 1495–1503 (1979).
7. P. Royo, R. P. Stanley, and A. Ilegems, "Analytical calculation of the extraction efficiency of microcavity light-emitting diodes for display and fiber coupling applications," *IEEE J. Sel. Top. Quantum Electron.* **8**, 207–218 (2002).
8. Anonymous, "Proceedings of the American Physical Society," *Phys. Rev.* **69**, 674–674 (1946).

9. M. Chakaroun, A. T. Diallo, S. Hamdad, S. Khadir, A. P. A. Fischer, and A. Boudrioua, "Experimental and Theoretical Study of the Optical Properties Optimization of an OLED in a Microcavity," *IEEE Trans. Electron Devices* **65**, 4897–4904 (2018).
10. C.-F. Lai, J.-Y. Chi, H.-C. Kuo, H.-H. Yen, C.-E. Lee, C.-H. Chao, H.-T. Hsueh, and W.-Y. Yeh, "Far-field of GaN film-transferred green light-emitting diodes with two-dimensional photonic crystals," *Opt. Express* **17**, 8795–8804 (2009).
11. H. Benisty, H. De Neve, and C. Weisbuch, "Impact of planar microcavity effects on light extraction-Part II: selected exact simulations and role of photon recycling," *IEEE J. Quantum Electron.* **34**, 1632–1643 (1998).
12. J. J. Wierer, A. David, and M. M. Megens, "III-nitride photonic-crystal light-emitting diodes with high extraction efficiency," *Nat. Photonics* **3**, 163–169 (2009).
13. I. A. Sukhoivanov and I. V. Guryev, *Photonic Crystals: Physics and Practical Modeling* (Springer, 2009).
14. T. F. Krauss, "Slow light in photonic crystal waveguides," *J. Phys. Appl. Phys.* **40**, 2666 (2007).
15. B. E. A. Saleh and M. C. Teich, *Fundamentals of Photonics* (John Wiley & Sons, 2019).
16. J.-M. Lourtioz, H. Benisty, J.-M. Gerard, V. Berger, D. Maystre, and A. Tchelnokov, *Photonic Crystals: Towards Nanoscale Photonic Devices* (Springer Science & Business Media, 2005).
17. A. David, H. Benisty, and C. Weisbuch, "Photonic crystal light-emitting sources," *Rep. Prog. Phys.* **75**, 126501 (2012).
18. E. Yablonovitch, "Inhibited Spontaneous Emission in Solid-State Physics and Electronics," *Phys. Rev. Lett.* **58**, 2059–2062 (1987).
19. C. Wiesmann, K. Bergenek, N. Linder, and U. T. Schwarz, "Analysis of the emission characteristics of photonic crystal LEDs," in *Photonic Crystal Materials and Devices VIII* (SPIE, 2008), Vol. 6989, pp. 118–126.
20. E. Rangel, E. Matioli, Y.-S. Choi, C. Weisbuch, J. S. Speck, and E. L. Hu, "Directionality control through selective excitation of low-order guided modes in thin-film InGaN photonic crystal light-emitting diodes," *Appl. Phys. Lett.* **98**, 081104 (2011).
21. C. Wiesmann, K. Bergenek, N. Linder, and U. t. Schwarz, "Photonic crystal LEDs – designing light extraction," *Laser Photonics Rev.* **3**, 262–286 (2009).
22. V. Torres-Costa and R. J. Martín-Palma, "Application of nanostructured porous silicon in the field of optics. A review," *J. Mater. Sci.* **45**, 2823–2838 (2010).
23. H. Duprez, A. Descos, T. Ferrotti, C. Sciancalepore, C. Jany, K. Hassan, C. Seassal, S. Menezo, and B. B. Bakir, "1310 nm hybrid InP/InGaAsP on silicon distributed feedback laser with high side-mode suppression ratio," *Opt. Express* **23**, 8489–8497 (2015).

## **Chapter III**

*Photonic crystals for light extraction from  
MQW III-V membrane on transparent  
substrate: modeling and experimental study.*

## Table of contents

III.1	Introduction .....	61
III.2	Device fabrication .....	61
III.3	Characterization procedures .....	65
III.3.1	Micro-photoluminescence .....	65
III.3.2	Back focal plane imaging for radiation-pattern measurements .....	66
III.4	Extraction lengths .....	67
III.5	Light extraction efficiency enhancement .....	70
III.6	Directionality .....	71
III.6.1	Azimuthal radiation patterns and directionality .....	71
III.6.2	Spectrally-resolved farfield emission profiles .....	74
III.6.3	Novel design approach for highly directional emission from MQW CCL .....	78
III.6.3.a	Tailoring spontaneous emission distribution .....	78
III.6.3.b	Fine tuning the lattice period .....	80
III.6.3.c	Analysis of a measured photonic band-structure .....	82
III.6.4	Additional levers to control the directionality of the farfield patterns .....	84
III.6.4.a	Air-filling factor .....	85
III.6.4.b	Lattice symmetry .....	86
III.6.5	Conclusion .....	87
III.7	Identification of the different contributions in the experimental LEE enhancement .....	88
III.8	Coupling to an optical system with limited numerical aperture ( $NA < 1$ ) .....	90
III.8.1	Extraction length vs acceptance angle .....	91
III.8.2	Directional light extraction efficiency enhancement .....	93
III.9	Preliminary design guidelines .....	94
III.10	Conclusion .....	94
III.11	References .....	95

### III.1 Introduction

The overall integration strategy presented in the first chapter is very intricate, which is why we have devised strategies aiming at decorrelating all the physical phenomena at play through three fabrication lots. In this chapter, we deal with the LOT I, where AlGaInP/InGaP MQW color-converting layers (CCL) are bonded on transparent substrates and then etched for photonic-crystal (PhC) fabrication. We will start with the device fabrication from the bonding of the CCL on substrates to the PhC fabrication. Next, we use photoluminescence (PL) measurements for proof-of-principle demonstration of blue-to-red color conversion. We ultimately tackle the challenges related to MQW CCL before highlighting design guidelines to pave the way for their implementation on RGB microdisplays [1,2].

### III.2 Device fabrication

Red MQW CCL are grown lattice matched on 3-inch diameter GaAs substrates. One of the critical technological steps of their integration on blue  $\mu$ -LED arrays is their transfer on receiving substrates. This transfer is done on the same technological basis as used for bonding hybrid III-V lasers onto SOI<sup>1</sup> substrates in integrated photonics and will be demonstrated on transparent substrates.

The MQW CCL are epilayers from Landmark<sup>2</sup> and the technique used for their development will not be detailed here. Its structure is provided in **Table III-1**, with its peak emission wavelength at  $\sim 640$ nm and a full width at half-maximum (FWHM) of  $\sim 20$ nm. Layers from 0 to 3 will be removed during the integration process. The device fabrication was achieved in CEA-LETI's 200mm cleanroom facilities. Process development was performed on most of the steps of the flow before obtaining a functional process flow for these devices, but we only highlight here the main ones.

**Table III-1:** III-V epitaxial growth layer structure and characteristics.

Layer	Material	Thickness	Refractive indices at $\lambda=640$ nm
0: Substrate	GaAs	625 $\mu$ m	
1: Buffer layer	U-GaAs	200 nm	
2: Etch-stop layer	U-InGaP	300 nm	
3: Sacrificial layer	U-GaAs	50 nm	
4: Cladding	U-(Al <sub>x2</sub> Ga <sub>1-x2</sub> ) <sub>0.52</sub> In <sub>0.48</sub> P	200 nm	n=3.4
5: MQW barrier	U-(Al <sub>x1</sub> Ga <sub>1-x1</sub> ) <sub>0.52</sub> In <sub>0.48</sub> P	70 nm	n=3.44
6: MQW region	4 $\times$ U-In <sub>y</sub> Ga <sub>1-y</sub> P/	4.4 nm/	n <sub>average</sub> =3.49
	5 $\times$ U-(Al <sub>x1</sub> Ga <sub>1-x1</sub> ) <sub>0.52</sub> In <sub>0.48</sub> P	8.7 nm	
7: MQW barrier	U-(Al <sub>x1</sub> Ga <sub>1-x1</sub> ) <sub>0.52</sub> In <sub>0.48</sub> P	70 nm	n=3.44
8: Cladding	U-(Al <sub>x2</sub> Ga <sub>1-x2</sub> ) <sub>0.52</sub> In <sub>0.48</sub> P	200 nm	n=3.4
9: Bonding interface	U-GaAs	20 nm	

The first step is to transfer this epilayer onto a transparent substrate. The receiving substrate is a 200mm transparent borosilicate wafer encapsulated with a 1.2 $\mu$ m-thick SiO<sub>2</sub> layer deposited by PECVD,

<sup>1</sup> Silicon On Insulator

<sup>2</sup> Landmark Optoelectronics Corporation is a major supplier in GaAs and InP epitaxial wafers using MOCVD reactors.

followed by chemical-mechanical polishing (CMP) to enable planarization of the wafer and limit the interface roughness<sup>3</sup>. Since SiO<sub>2</sub> does not adhere well on GaAs, we use a 10nm-thick alumina intermediate bonding layer deposited by atomic layer deposition (ALD) on layer 9. The two surfaces are then cleaned and oxygen plasma ensues to activate them by creating a high density of hydroxyl groups (-OH) [4], which will allow the formation of covalent Al<sub>2</sub>O<sub>3</sub>-SiO<sub>2</sub> bonds. We then achieve the bonding by putting the wafers in contact at room temperature. Subsequently, to reinforce it they are then annealed at 200°C for 2 hours, which enables to release the gasses produced and trapped during the bonding reaction [4]. This post-bonding annealing will thus limit the formation of bonding interface voids [5], which could be detrimental to the remaining process steps<sup>4</sup>. A scanning acoustic microscopy<sup>5</sup> (SAM) image of the bonded red MQW CCL is shown in **Figure III-1-a**, where we can observe that we achieved a successful transfer of the epilayer with a high bonding yield (>90%).

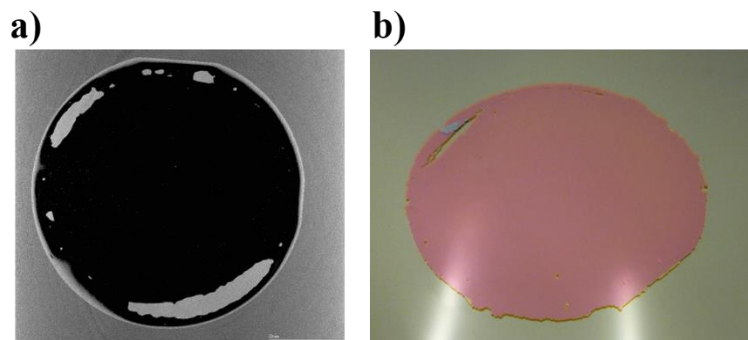


**Figure III-1:** a) Scanning acoustic microscopy (SAM) image of the bonded epi-layer before substrate removal. b) Picture of the bonded epi-layer (in red) after substrate and sacrificial layer removal.

Thereupon, the GaAs substrate and the sacrificial layers (layers 0 to 3) are removed by highly selective wet etching processes. The GaAs substrate and GaAs buffer layer (layers 0 and 1) are both removed using NH<sub>4</sub>OH (1) / H<sub>2</sub>O<sub>2</sub> (1) / H<sub>2</sub>O (5) heated solution. Afterwards the InGaP etch-stop layer (layer 2) is removed using HCl (1) / H<sub>3</sub>PO<sub>4</sub> (1) solution at ambient temperature, and then the last GaAs sacrificial layer (layer 3) is removed using the same NH<sub>4</sub>OH-based chemical solution. All those wet etching processes are followed by a water rinse. In **Figure III-1-b**, we show a picture of the bonded epi-layer after substrate and sacrificial layer removal on the 200mm transparent substrate<sup>6</sup>. The remaining epi-layer thickness is ~600nm, which is enough for complete blue-light absorption as mentioned before.

We then define the PhCs using a top-down pattern transfer method. First, a hard mask comprising a 150nm-thick PECVD SiN and a 10nm-thick PVD TiN has been deposited. The SiN hard mask is used because of selectivity issues between the photoresist and the III-V material while the additional TiN

<sup>3</sup> To make the bonding possible, interfaces' roughness for both the epilayer and the transparent substrate needs to be less than 0.5nm root-mean-square (RMS) [3].

<sup>4</sup> During the PECVD-SiN hard-mask deposition at high temperatures, the voids in the unbonded regions can cause delamination of the III-V red epilayer.

<sup>5</sup> In an acoustic analysis, the parts in white correspond to places where the bonding energy is not strong enough.

<sup>6</sup> The transparent substrates were made opaque with a SiN-TiN bilayer to be able to adapt to 200mm cleanroom facilities.

layer is for charge evacuation during e-beam lithography. After a 400nm-thick photoresist<sup>7</sup> was spun on the hard mask, PhC patterns were defined using e-beam lithography, preceded by an exposure dose sweep across the wafer to determine the optimal dose for the fabrication of patterns with the most critical dimensions. The said patterns are then transferred into the hard mask by chlorine-based and by fluorocarbon-based RIE for TiN and SiN layers, respectively. After hard mask etching, the photoresist residues were stripped by O<sub>2</sub> plasma in nitrogen atmosphere. The PhC patterns were subsequently transferred into the epi-layer. This transfer was performed using chlorine-based ICP-RIE (Cl<sub>2</sub> /Ar), where the etch rate was controlled in-situ using laser end-point detection. The hard mask was then removed by SF<sub>6</sub>-based RIE to preserve the surface of the epilayer.

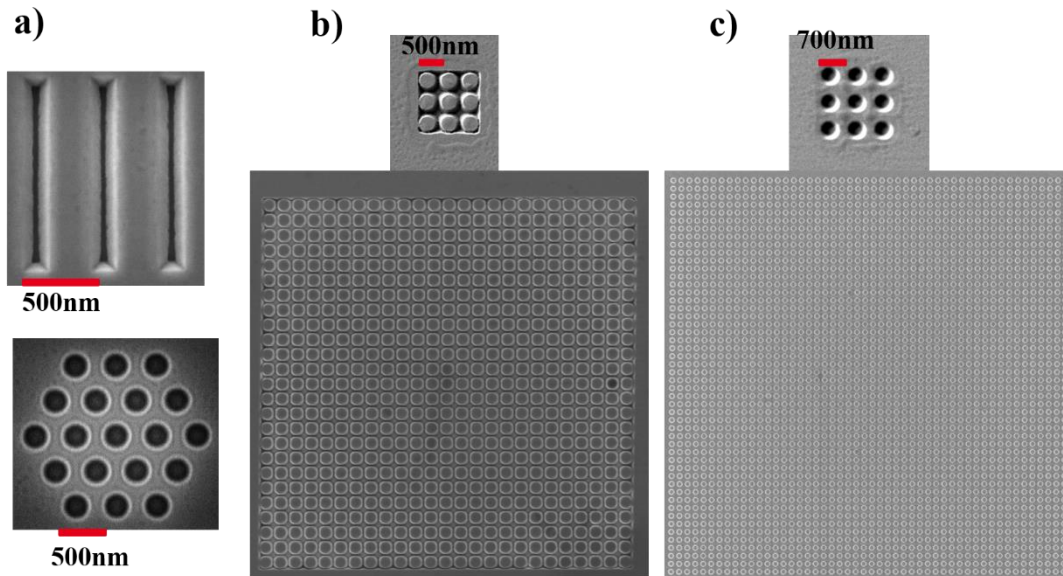


**Figure III-2:** Scanning electron microscopy (SEM) images of the fabricated photonic-crystal structures. a) 1D lattice (top) and hexagonal lattice of air holes (bottom) with a lattice period of  $a=500\text{nm}$  and lateral extents  $L_{\text{extent}}$  of 3 and 5 periods, respectively. b) Square lattice of nanopillars with  $a=500\text{nm}$  and  $L_{\text{extent}}$  of 3 (top) and 25 periods (bottom). c) Square lattice of air holes with  $a=700\text{nm}$  and  $L_{\text{extent}}$  of 3 (top) and 50 periods (bottom).

We have fabricated PhCs with different opto-geometrical parameters. The lattice symmetry order has been increased from two- to six-fold (1D, square and hexagonal), with two pattern-types for the square lattice (air holes and nanopillars) and only air holes for others. Square lattice of air holes, square lattice of nanopillars and hexagonal lattice of air holes will be referred as SLAH, SLNP and TLAH, respectively. For each lattice and pattern-type, different structures with different lattice periods have been fabricated: lattice periods from 400nm to 700nm with a step of 50nm. The lower and upper limits are to ensure that each of the guided modes supported by our CCL can be prone to diffraction into air<sup>8</sup> and there can be enough diffractive elements in pixel sizes compatible with microdisplay applications, respectively. For a given lattice period, PhC structures with different lateral extents (lateral sizes in number of periods of the photonic crystals) have been fabricated: 3, 5, 10, 25, 50 and 100 periods. For

<sup>7</sup> During e-beam lithography, the thickness of the photoresist needs to be low enough to be able to write the patterns with the most critical dimensions (CDs) on the layout and high enough for the hard-mask etching. The value of 400nm has been chosen according to that.

<sup>8</sup> With very low lattice periods, guided modes with high effective indices might not be diffracted outside.

all those fabricated structures, variants with two different etch depths have been fabricated: etch depths of  $\sim 188\text{nm}$  ( $\sim 82\text{nm}$  above the emission region) and  $\sim 288\text{nm}$  (when PhC patterns are etched in the active region). The air-filling factor (FF) defined in the previous chapter was kept around 20% for 1D lattice, SLAH and TLAH, whereas it was around 60% for the SLNP, due to technological constraints. We additionally fabricate SLAH with  $\text{FF} \sim 50\%$  to better our understanding of the effect of this parameter. SEM images of some of the fabricated structures are displayed in **Figure III-2** along with the detailed process flow of the devices in **Figure III-3**. Moreover, in order to be able to perform statistical analyses and rule out fabrication errors, we fabricated arrays of structures ( $>5 \times 5$ ) for each set of opto-geometrical parameters as shown in **Figure III-4**.

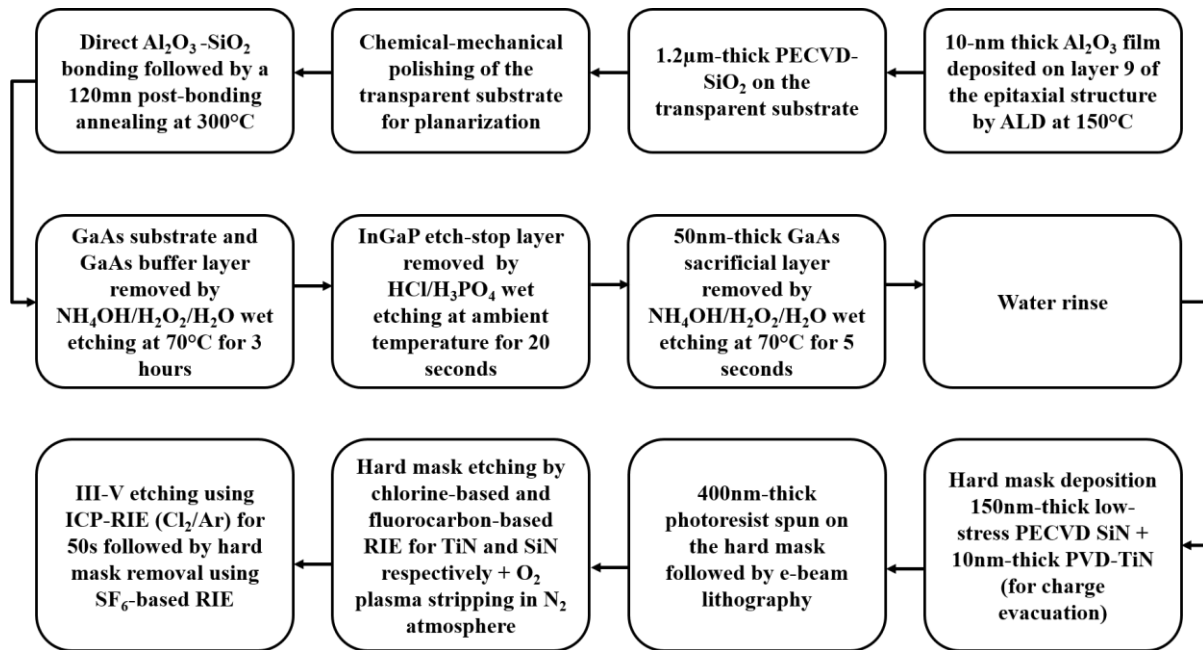


**Figure III-3:** Detailed flow chart of the device fabrication process.

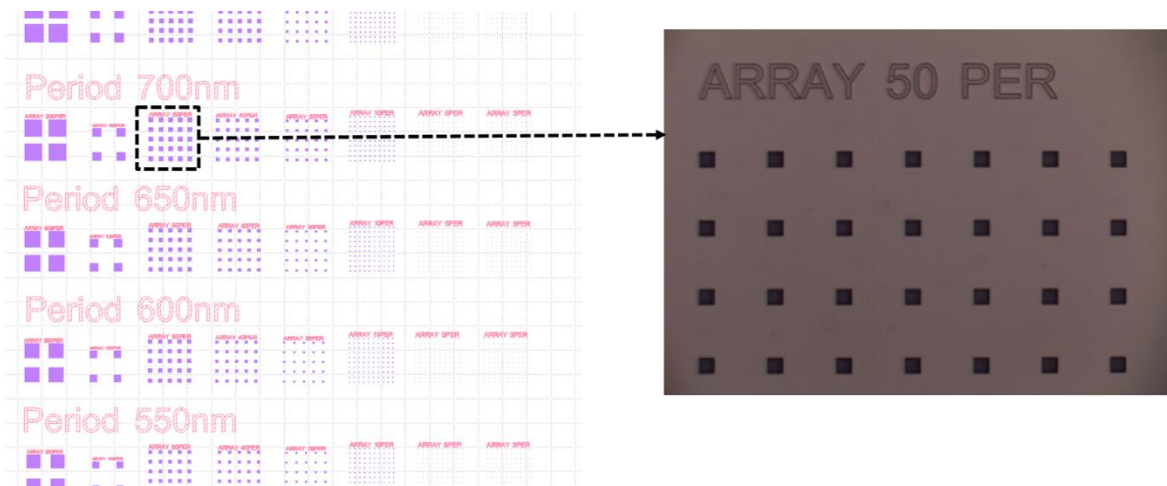


**Figure III-4:** GDS design (left) and optical microscope image of the fabricated devices at the end of the process (right).

We have thus demonstrated a robust process flow based on an oxide-mediated molecular bonding with high bonding yield ( $>90\%$ ), which is promising for the transfer of those MQW CCL on blue  $\mu$ -LED

arrays. The PhC patterns have also been successfully fabricated with quite controlled opto-geometrical parameters (variations of  $\pm 10\text{nm}$  depending on the pattern type) over the whole wafer.

### III.3 Characterization procedures

In this section, we present the two characterization setups used in this PhD work.

#### III.3.1 Micro-photoluminescence

To evaluate the photoluminescence enhancement factors by the PhCs, we performed micro-photoluminescence ( $\mu\text{-PL}$ ) measurements with a LabRAM PL setup from Horiba described in **Figure III-5**. An incoming laser line (405nm or 514nm for blue or green excitations, respectively) is focused at normal incidence by an excitation microscope objective. The same objective was also used to collect the emitted PL signals, which are then dispersed by a spectrometer. The resulting spectra are then collected with a CCD camera.

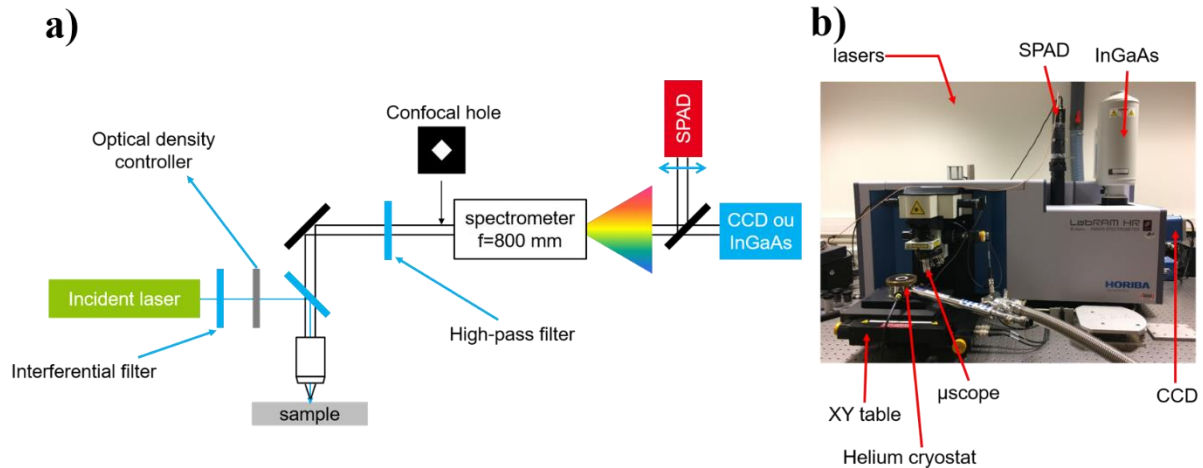


**Figure III-5:** a) Schematics and b) annotated picture of the micro-photoluminescence setup at CEA-LETI.

For LEE enhancement factors, we use an excitation objective whose numerical aperture (NA) is 0.9, which is enough<sup>9</sup> to collect all the emitted light. Simultaneously, both reference spectra (for unpatterned MQW) and spectra of the patterned structures were measured to evaluate PL enhancement factors by the PhCs and thus LEE enhancement.

We also conducted time-resolved PL measurements (TRPL) to analyze the variations of the internal quantum efficiency (IQE) induced by the PhCs. This was performed using the aforementioned setup, albeit slightly modified. For the excitation, we used instead a picosecond laser-diode head with an excitation wavelength of  $376\text{nm}$ <sup>10</sup>, a FWHM of 50ps with a repetition rate of 5MHz for pulsed operation.

<sup>9</sup> Additional 3D-FDTD simulations of the farfield patterns shown in the **Appendix B.2** help us determine that more than 85% of the emitted light is collected with a NA of 0.9.

<sup>10</sup> This was the only pulsed laser available in our lab. Carrier dynamics and thermalisation processes are not the same for UV and visible (blue or green) light, however these TRPL measurements provide us with a good insight of IQE variations.

TRPL signals were collected using the single photon avalanche diode (SPAD) displayed in **Figure III-5-a**, that counts photons emitted at the peak emission wavelength  $\sim 640\text{nm}$ .

### III.3.2 Back focal plane imaging for radiation-pattern measurements

To analyze the directionality of the fabricated MQW CCL, we also performed azimuthal and spectrally resolved (SR) farfield measurements using back focal plane (BFP) imaging. An overview of the core principle of BFP imaging from a geometric optics point of view is sketched in **Figure III-6** along with an annotated picture of the setup.

A 405nm laser line was focused at normal incidence by a microscope objective (MO) with  $\text{NA}=0.75$  that also collected the emitted PL signals. Light emitted in a certain direction  $\theta$  is focused into a point in the BFP of the MO. We re-image the back focal plane by using a Fourier lens and a focus lens. The Fourier lens is placed so that its object-side focal plane corresponds to the BFP of the MO. Thus, light rays coming out of the Fourier lens are parallel. Subsequently, light is focused into a point at the BFP of the focus lens.

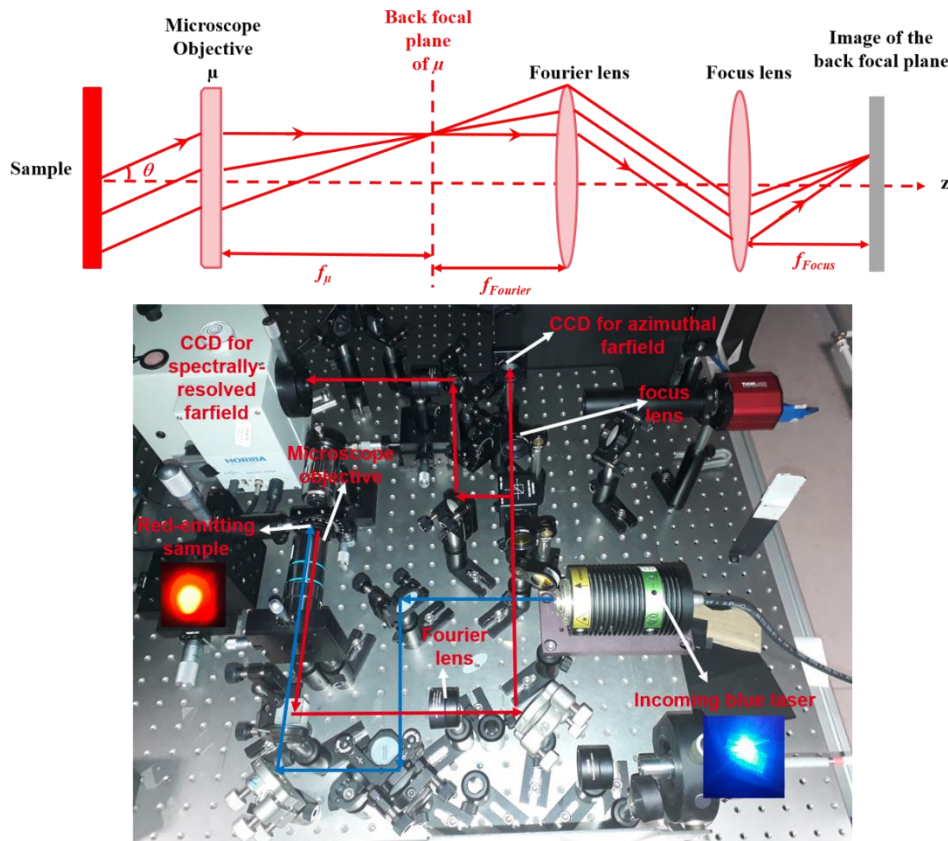


**Figure III-6:** Sketch of the back focal plane imaging setup at INL (top) and annotated picture of it (bottom).

Concerning azimuthal radiation measurements, the image of the BFP is directly collected with a 1024 x 256 CCD camera Sincerity, Horiba. We thus obtain the 2D momentum space ( $k_x, k_y$ ) distribution of the PL signal emitted from the CCL, integrated over the whole emission spectrum. For better visualization, the obtained patterns will be plotted in polar coordinates where the polar radius and angle

correspond to the acceptance angle ( $\theta$ ) and the azimuthal angle ( $\varphi$ ), respectively, as displayed in **Figure III-7-a**.

For the SR farfield measurements, the image of the BFP is projected onto the entrance slit of a spectrometer microHR, Horiba. The sample needs to be positioned so that the high symmetry direction along which we wish to perform the measurements is aligned with the entrance slit. In this scheme, the grating inside the spectrograph disperses the incoming signal along the energy axis. The spectrometer output signal is then captured in the CCD camera. This setup eventually provides the energy-momentum dispersion diagram along a selected direction as shown in **Figure III-7-b**.

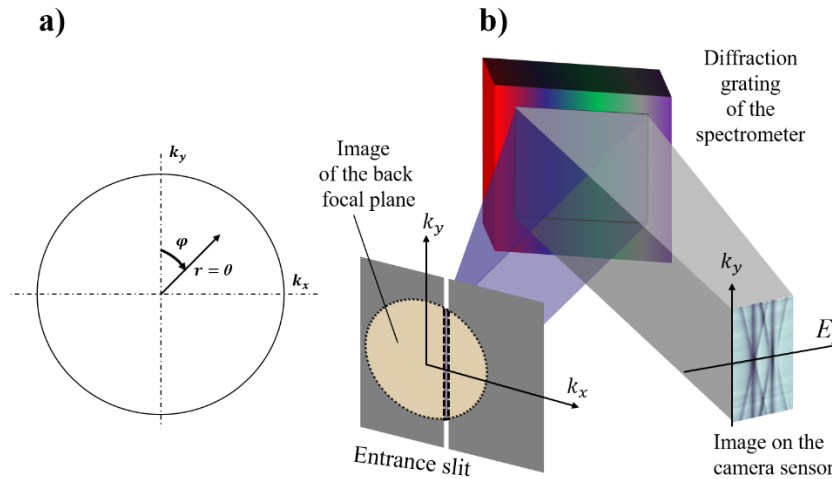


**Figure III-7:** a) Image of the BFP (azimuthal patterns). b) Setup for acquisition of spectrally resolved farfield measurements.

### III.4 Extraction lengths

In this section, we establish some key design guidelines regarding the optimization of the extraction lengths.

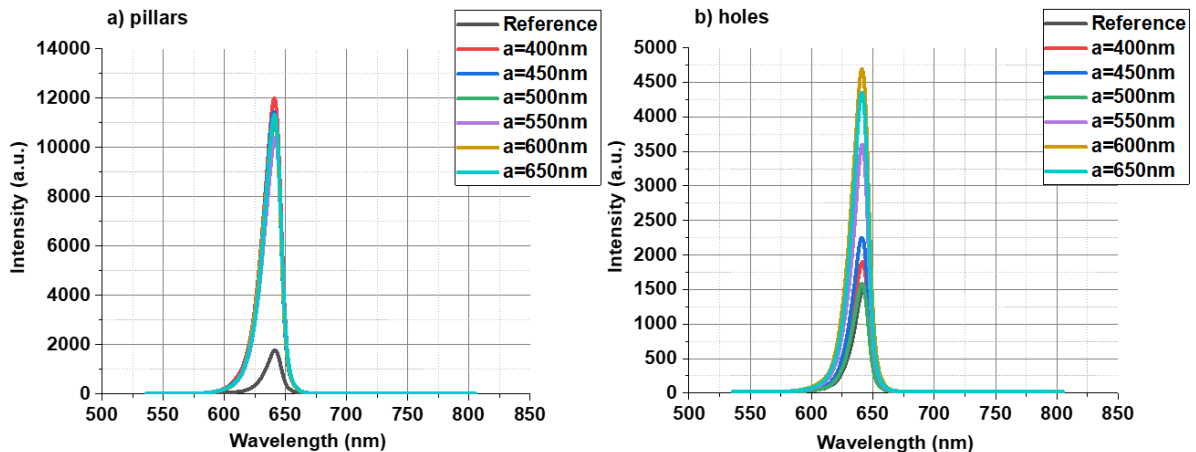


**Figure III-8:** Emitted PL spectra from a laser excitation at 514nm, for the microscope objective with NA=0.9, for 10-period structures. a) SLNP and b) SLAH (FF~20%). PL spectra of the unpatterned structures are also added.

In **Figure III-8**, some of the measured PL spectra for the MO with NA=0.9 are reported. These measurements were performed using the micro-PL setup presented in the previous section. Since we obtain similar results for both excitation lasers at 405nm and 514nm, only results with the 514nm laser

line are shown here for the sake of clarity. Moreover, for **sections III.4, III.5, III.6 and III.8**, we only investigate devices with an etch depth of  $\sim 188\text{nm}$ . Both PhC and reference structures have spectra with the same Lorentzian shapes (emission peak at  $\sim 640\text{nm}$ , FWHM of  $\sim 20\text{nm}$ ) with much higher peak intensities for patterned structures depending on the opto-geometrical parameters of the PhC structures. To better quantify those PL gains, we rely on LEE enhancement factors, which are the ratios between spectrally integrated PL signals for the patterned and unpatterned structures. It thus reads as:

$$\eta_{LEE} = \frac{\int_{550\text{nm}}^{750\text{nm}} I_{PhC}(\lambda) d\lambda}{\int_{550\text{nm}}^{750\text{nm}} I_{unpatterned}(\lambda) d\lambda}. \quad (\text{III-1})$$

Here  $I_{PhC}$  and  $I_{unpatterned}$  are PL intensities collected by the microscope objective with  $\text{NA}=0.9$  for patterned and unpatterned structures, respectively.

In **Figure III-9-a**, we present the experimental LEE enhancement factors as a function of the lateral extent for SLNP with a lattice period of  $400\text{nm}$ .

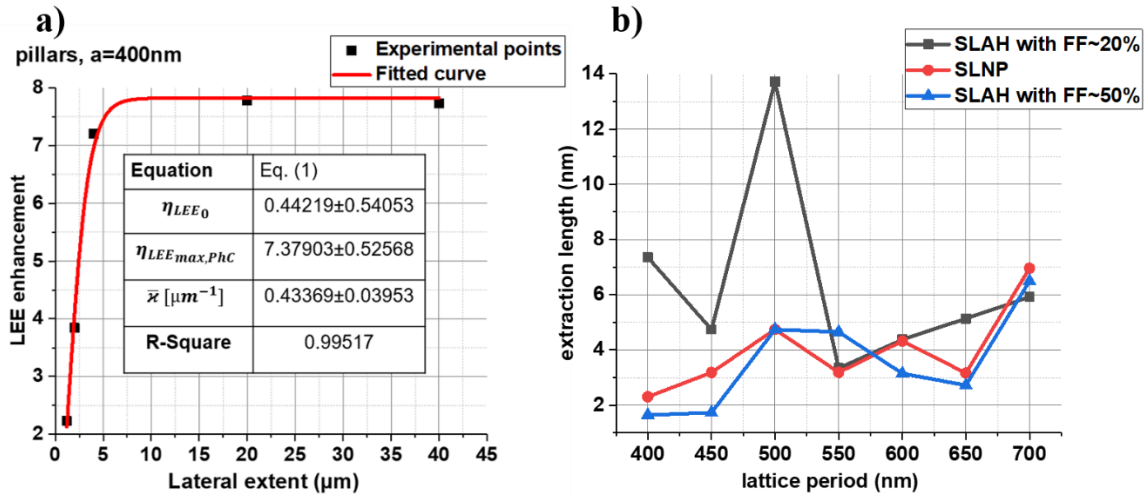


**Figure III-9:** a) LEE enhancement as a function of the lateral extent for SLNP with  $a=400\text{nm}$ . b) Experimental extraction lengths as a function of the lattice period for SLAH with FF of  $\sim 20\%$  and  $\sim 50\%$  and for SLNP.

As the lateral extent increases, the amount of extracted light increases as well which increases LEE enhancement until it saturates at  $\sim 7.75$  for SLNP with  $a=400\text{nm}$ . To extract the corresponding extraction lengths for each of our devices, we propose a phenomenological model derived from the standard coupled-mode theory<sup>11</sup>, which expresses LEE enhancement as a function of the PhC lateral extent  $L$ . In the framework of our model, LEE enhancement reads as:

$$\eta_{LEE}(L) = \eta_{LEE_0} + \eta_{LEE_{max,PhC}} \times \tanh^2(\bar{\kappa} \times L). \quad (\text{III-2})$$

Here  $\eta_{LEE_0}$  accounts for direct light emission without guided Bloch-mode extraction (see the previous chapter), while  $\eta_{LEE_{max,PhC}}$  accounts for the maximum light extraction of guided Bloch-modes. The  $\tanh$  function takes into account both propagating and counterpropagating guided Bloch modes,  $\bar{\kappa}$  is the

<sup>11</sup> This phenomenological model is derived from the standard formula that links the reflectivity of a distributed Bragg reflector (1<sup>st</sup> order Bragg grating) to the associated coupling strength and grating length.

mean coupling strength (strength of the coupling between the guided Bloch-modes inside the CCL and the radiated modes in the air) over all the diffracted modes and  $L$  is the PhC lateral extent [6].

We implemented this model to fit the measured LEE enhancement factors as a function of the lateral extent of the PhC structures. The fitted curve is displayed in **Figure III-9-a** along with fit details in the inset, which allows us to determine the mean coupling strength as a function of the lattice period. We subsequently repeated this procedure for each lattice type, pattern and period to obtain the coupling strengths of all the fabricated devices<sup>12</sup>. Thereupon, from those mean coupling strengths, we calculate the mean extraction lengths using the equation below [7]:

$$L_{\text{extraction}} = \frac{1}{\bar{\kappa}} \quad (\text{III-3})$$

The results are displayed in **Figure III-9-b** for SLNP (FF~60%) as well as SLAH (FF~20% and FF~50%). The nature of the diffracted mode (effective index and order) depends on the lattice period through the Bragg's law. Since each of the guided Bloch-modes possesses its own coupling strength depending on its interaction with the phC patterns [8], then the extraction lengths strongly depend on the lattice period as we can observe.

For SLAH with FF~20%, the extraction lengths are the highest (between ~3 and up to ~13 $\mu\text{m}$ ). This suggests that the coupling strength between the guided Bloch-modes and radiated modes is not optimized at this low FF. SLNP on the other hand (FF~60%) exhibits a far better interaction with the guided Bloch-modes and therefore displays shorter extraction lengths between ~2 $\mu\text{m}$  and ~7 $\mu\text{m}$ . Moreover, by increasing the FF of SLAH from ~20% to ~50% near the ones of SLNP, we end up shortening the extraction lengths down to values between ~1.6 and 6.5 $\mu\text{m}$ . A further increase of FF would have a detrimental impact on the coupling strength as explained in [8,9]. Indeed, higher FF values over ~50% decrease the squared Fourier transform of the PhC dielectric map, which is proportional to grating strength [9]. Therefore, FF values of ~50% are enough to provide quite efficient coupling between guided Bloch-modes and PhC patterns.

On a device point of view, there are thus two main conclusions from this brief analysis. On the one hand, it appears that the extraction lengths can be optimized (made shorter than the lengths of our devices) with a proper choice of the lattice period and etch depth. In this study, we have maintained the etch depth at around the third of the epilayer thickness, which ensures an efficient coupling between the guided modes and the PhC patterns<sup>13</sup>. In addition, we have seen that the air-filling factor is another key lever to optimize the coupling strength and shorten down the extraction length. It appears that keeping it around 50% could help reach extraction lengths as short as 1.6 $\mu\text{m}$ , which is clearly suitable for our targeted AR applications.

---

<sup>12</sup> Since for each set of opto-geometrical parameters, arrays of structures have been fabricated, statistical analyses were also performed by randomly choosing four PhC structures for each measurement. The resulting standard deviations between measurements are very small (<0.05), which shows very good repeatability of the fabrication process in the 200mm clean room facilities and consistency of the measurements.

<sup>13</sup> A thorough discussion on the role of the etch depth will be conducted in **Section III.7**.

### III.5 Light extraction efficiency enhancement

It appeared from the previous observations that the extraction lengths for all the fabricated devices are between  $\sim 1.6$  and  $\sim 13\mu\text{m}$ . Hence, the structures with a lateral extent of 100 periods can be considered “infinite” since their lateral extents are far longer than the extraction lengths in the range of our lattice periods. The LEE enhancement factors are displayed in **Figure III-10** as a function of the lattice period for the structures with a lateral extent of 100 periods. For SLAH, due to similar values for the two different air-filling factors, only devices with  $\text{FF}\sim 20\%$  are displayed for the sake of clarity.

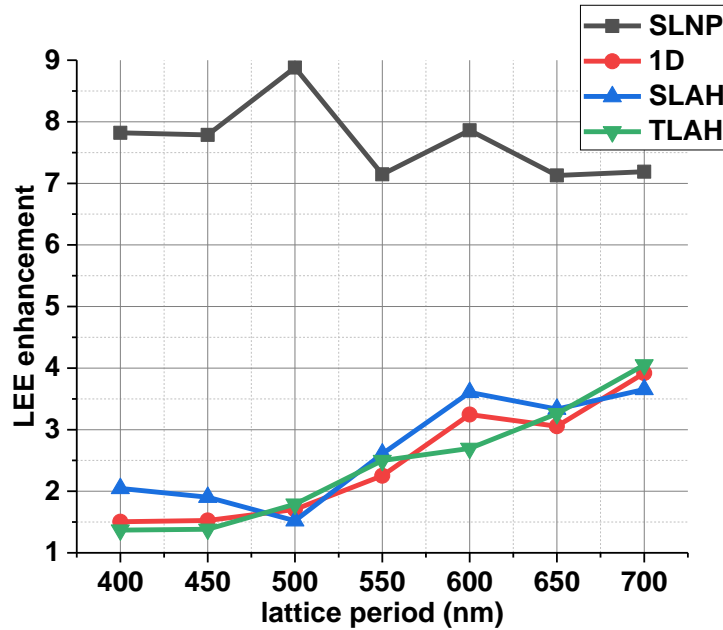


**Figure III-10:** Light extraction efficiency enhancement as a function of the lattice periods for 1D lattice, SLAH, SLNP and TLAH with a lateral extent of 100 periods.

For SLNP, LEE enhancement only weakly depends on the lattice periods with high enhancement factors between  $\sim 7$  and  $\sim 9$ . For the other lattices on the other hand, there is a slight increase of LEE enhancement with increasing lattice period from  $\sim 1.5$  for  $a=400\text{nm}$  to  $\sim 3$  for  $a=700\text{nm}$ . Thus, the highest values of LEE enhancement are obtained for SLNP.

Light extraction is generally in competition with absorption processes such as metal absorption or QW re-absorption. However, typical QW re-absorption lengths in our structures are  $\sim 100\mu\text{m}$  [10], which is much larger than our found extraction lengths and there is no metallic layer in our structures. We can therefore safely say that light extraction plays the preponderant role in our structures. Excitation-power dependent PL measurements have also been performed (see **Appendix B.1**) to verify that the experimental enhancement factors do not vary with the excitation power, which confirms the previous considerations. The remaining part of the light is then diffracted toward the substrate, since PhC structures with large lattice periods (larger than second Bragg order, which is around  $200\text{nm}$  in our case) can open many diffraction channels toward the transparent substrate [8]. Therefore, the highest LEE enhancement obtained for pillars means there is more diffraction toward the substrate for holes than for pillars [1]. In the next chapter, we will investigate the possibility of benefiting from the electrical contact

at the bottom of the blue  $\mu$ -LED as a back reflector, to harness this light diffracted toward the substrate and thus favor top emission. We will then see that, in terms of LEE enhancement, pillars and holes, no matter the lattice symmetry, can reach similar values.

Therefore, it appears that we can obtain high LEE enhancement factors up to  $\times 9$  paired with very short extractions down to  $\sim 2\mu\text{m}$ , which is compatible with our targeted AR applications. It was also found that LEE enhancement could be quasi-independent on the lattice period. Moreover, we have highlighted the importance of harnessing light diffracted toward the substrate to grasp the ultimate performances of our devices. We can finally note that increasing the lattice symmetry order over four-fold (more than a square symmetry) does not seem to help much in the optimization of light extraction. Even 1D lattices only lead to a slight decrease in LEE enhancement compared to square lattices. These considerations will be further examined in the next chapter for on-silicon devices with a back-reflector.

In the next section, we tackle the directionality issues.

## **III.6 Directionality**

In this section, we provide novel design guidelines for directional emission from our MQW CCL through an in-depth analysis of the measured azimuthal and spectrally resolved farfield radiation patterns as well as a modal analysis based on coupled-mode theory and the herein-developed spontaneous emission (SpE) model. The first three subsections will only concern square lattices (SLAH with FF $\sim$ 20% and SLNP with FF $\sim$ 60%). The impact of the lattice symmetry and FF on the farfield shape will then be further examined in **Subsection III.6.4**. Besides, we only consider structures with lateral extent of 100 periods so that the MQW CCL can be considered laterally “infinite”.<sup>14</sup>

### **III.6.1 Azimuthal radiation patterns and directionality**

The measurements were performed using the BFP imaging setup described in **Section III.3.2** and the resulting azimuthal radiation patterns (each of them normalized with its maximum value) are displayed in **Figure III-11**.

For the unpatterned CCL, we unsurprisingly obtain shapes with concentric rings and the highest intensities emitted at  $\theta\sim 45^\circ$ , since only directly emitted light inside the air cone, which exhibits a circular symmetry in the planar case, appears in the farfield pattern. However, for the patterned CCL, the farfield shapes are more intricate. Indeed, both pattern types exhibit emission shapes where bands corresponding to the diffraction of guided Bloch-modes by the PhC are superimposed on a homogeneous background corresponding to the directly emitted light [11]. The previous circular symmetry is now broken into a four-fold symmetry, which is inherent to the square symmetry of the PhC lattice.

---

<sup>14</sup> It is a bit a tricky to measure farfield patterns of devices with a short lateral extent. Indeed, since our measurements are based on BFP imaging, the Heisenberg uncertainty principle applies. It implies that structures with a short lateral extent (in the real space) will result into farfield shapes with high  $\Delta k$  in the Fourier space. As a result, with short-sized pixels, we often end up with farfield patterns without any diffracted bands making the band-structure analysis impossible.

Regarding SLAH, the radiation patterns are strongly lattice-period dependent. For example, while the structures with lattice periods of 400 and 450 nm reveal highly directional emission patterns with most of the diffracted light inside a cone with an apex angle of  $\sim 9^\circ$  for  $a=450$  nm, the radiation pattern for  $a=500$  nm exhibits almost no diffraction close to normal incidence. For  $a=550$  nm, the radiation pattern is more intricate with emission close to normal incidence and at the periphery of the farfield shape<sup>15</sup>.

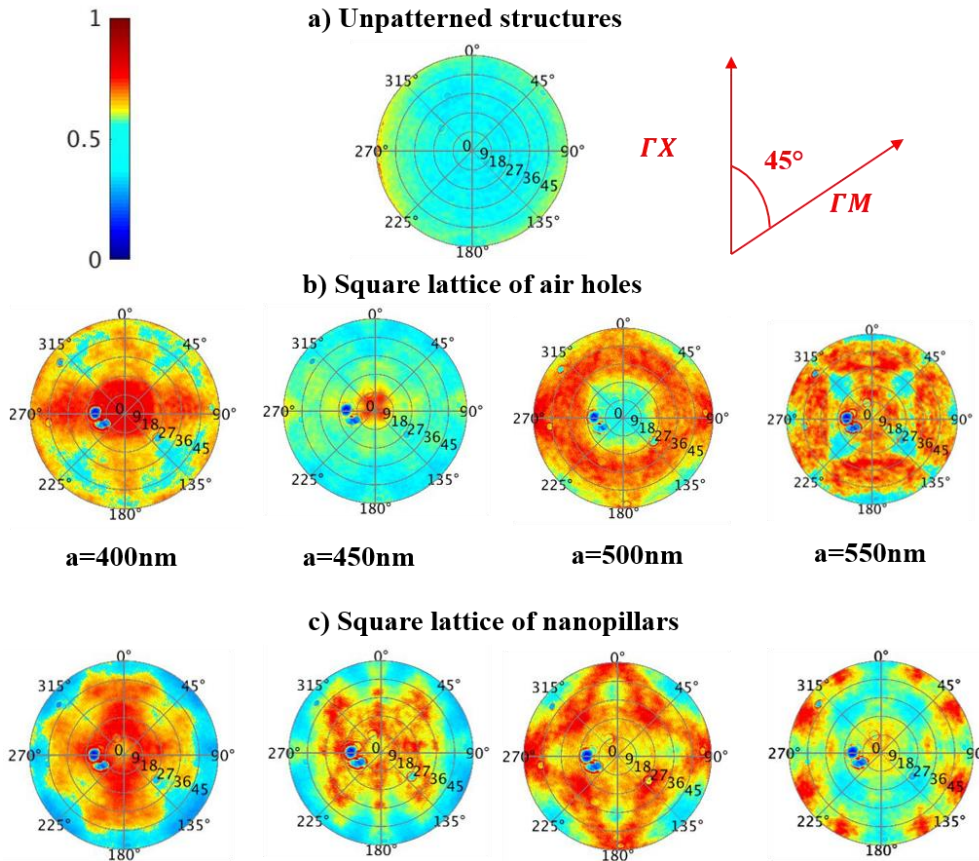


**Figure III-11:** Normalized azimuthal farfield emission shapes for the a) unpatterned CCL, CCL with b) SLAH and c) SLNP.

For SLNP on the other hand, there is light diffraction close to normal incidence for all lattice periods with farfield shapes different from those of SLAH. Particularly, for  $a = 500$  nm, the radiation pattern exhibits two sets of four diffraction bands rotated by an angle of  $45^\circ$ , yielding a four-branch-star-shaped farfield pattern. This corresponds to the azimuthal angle difference between the  $\Gamma X$ - and  $\Gamma M$ -directions of the square lattice and, therefore, suggests that both first and second order diffraction (first and second nearest sets of four neighbors in the reciprocal lattice)<sup>16</sup> contribute to the light extraction processes at this lattice period [11,12]. The same behavior can also be observed for SLNP with lattice periods of 450 and 550 nm and for SLAH with a lattice period of 550 nm. Additional 3D-FDTD simulations of these

<sup>15</sup> As we have seen in the numerical analysis of the second chapter, increasing the lattice period allows additional diffraction orders to occur.

<sup>16</sup> In the reciprocal lattice, the first nearest set of neighbors are responsible for the first diffraction order, the second nearest neighbors for the second diffraction order, etc. Thus, in the case of a square lattice, the first diffraction order corresponds to  $\Gamma X$ , the second to  $\Gamma M$ , the third to  $2 \cdot \Gamma X$ , etc.

farfield patterns have been performed for the sake of comparison. The corresponding results can be found in **Appendix B.2**, with shapes that are in close agreement with the measured ones.

As we have already mentioned in the introductory chapter, directionality is a key figure of merit (FoM) for our targeted AR applications. It then needs to be quantified from the above-displayed farfield patterns. The total integrated intensity within the acceptance angle  $\theta$  can be calculated as follows:

$$P(\theta) = \int_{\theta'=0}^{\theta'= \theta} \int_{\varphi=0}^{\varphi=2\pi} I(\theta', \varphi) \sin(\theta') d\theta' d\varphi, \quad (\text{III-4})$$

Here  $I$  is the emitted intensity (integrated over the whole emission spectrum),  $\theta$  is the acceptance angle [apex angle of the acceptance cone related to the numerical aperture (NA) by  $\text{NA} = \sin(\theta)$ ], and  $\varphi$  is the azimuthal angle. In this framework, directionality reads as:

$$D(\theta) = \frac{P(\theta)}{P(90^\circ)}, \quad (\text{III-5})$$

For a Lambertian emitter [2], the directionality is  $D_{\text{Lambertian}}(\theta) = (\sin(\theta))^2$ . In particular, it means that only 25% of the emitted light is concentrated into a cone with an apex angle of  $30^\circ$ , which would imply light losses in the whole AR devices. In the following, we use the measured azimuthal farfield radiation patterns to evaluate directionality enhancement as the ratio between directionality of the PhC structures and directionality of a Lambertian emitter used as a reference. It reads as:

$$\eta_D(\theta) = \frac{D_{\text{PhC}}(\theta)}{D_{\text{Lambertian}}(\theta)}. \quad (\text{III-6})$$

This quantity needs to be optimized for our targeted AR applications, particularly close to normal incidence ( $\theta \rightarrow 0^\circ$ ).

The results are given in **Figure III-12** on a semi-log scale. For the sake of comparison, the directionality enhancement of the unpatterned CCL is also displayed. As expected from the azimuthal farfields, directionality enhancement depends on both the pattern type and the lattice period.

For SLAH, while directionality enhancement depends only weakly on the lattice period at high acceptance angles, it becomes lattice-period dependent for decreasing acceptance angles as a result of the strong variations of the azimuthal farfield patterns observed previously. Although almost all lattice periods exhibit a substantial increase in directionality enhancement for decreasing acceptance angles, the optima for SLAH are  $a = 400$  nm and  $a = 450$  nm, offering the highest directionality enhancement factors close to normal incidence ( $\sim 4.25$  and  $\sim 4.75$ , respectively), as expected from their highly directional emission patterns in **Figure III-11**. The lattice period  $a = 500$  nm, on the other hand, exhibits the lowest directionality enhancement close to normal incidence, even lower than that of the unpatterned CC, with a decrease from  $\sim 2$  at  $49^\circ$  to less than  $\sim 1.5$  at  $\sim 5^\circ$  before reaching  $\sim 2.7$  close to normal incidence. This stems from the quasi-absence of light diffraction close to normal incidence in the corresponding farfield pattern (see **Figure III-11**). The lattice period 550 nm, on the other hand, exhibits an intermediate value of  $\sim 3.25$  close to normal incidence (still higher than the unpatterned CC), as a result of the light diffraction close to normal incidence and at the periphery of its farfield shape.

For SLNP, directionality enhancement depends similarly on the acceptance angles with lower values for some lattice periods. Nonetheless, contrary to SLAH, it only weakly depends on the lattice period: e.g., close to normal incidence, it is between  $\sim 3.4$  for  $a = 500$  nm and  $\sim 3.6$  for  $a = 450$  nm. Besides, we can note that all lattice periods exhibit higher directionality enhancement than the unpatterned reference CCL.

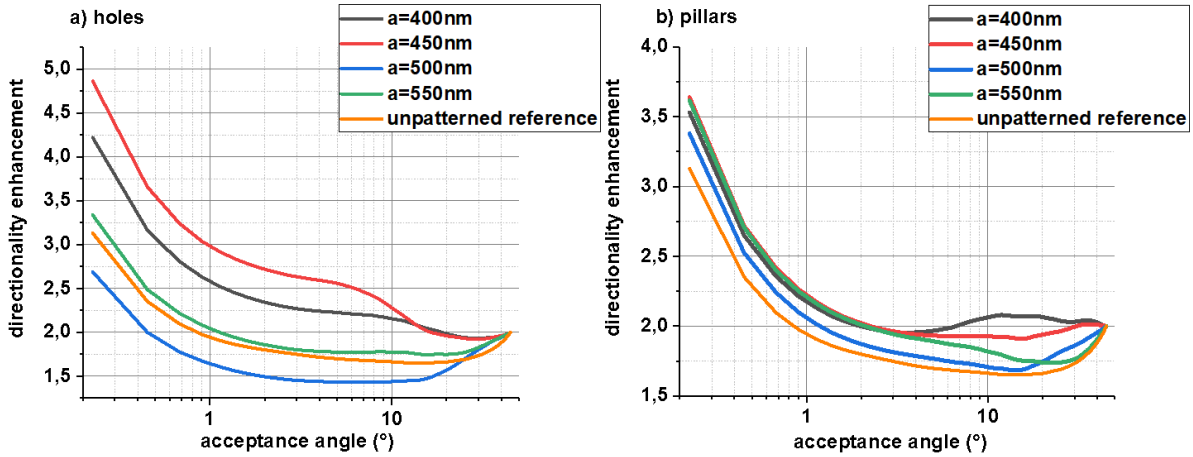


**Figure III-12:** Directionality enhancement for patterned CCL with a) SLAH and b) SLNP along with unpatterned CCL.

From this analysis, it appears that by correctly choosing the pattern type and the lattice period, directionality can be significantly enhanced over Lambertian emission. For our fabricated structures, SLAH with lattice periods of 400 and 450 nm are the optima, exhibiting sizable gains in directionality in the range of the measured acceptance angles (up to  $\times 4.75$  close to normal incidence). Besides, we have seen that increasing the lattice period to higher order diffraction leads to a directionality decrease in our structures due to additional diffraction angles occurring away from normal incidence. We can also note a peculiar behavior of SLAH with a lattice period of 500 nm whose directionality enhancement is even lower than that of the unpatterned reference for low acceptance angles because of the quasi-absence of light diffraction close to normal incidence. For the same lattice type and the same lattice period, SLNP did not exhibit this type of behavior.

All these points will be analyzed in next subsection.

### III.6.2 Spectrally-resolved farfield emission profiles

In this section, we further investigate the diffractive properties of the PhC structures and their impact on the directionality of our CCL by using spectrally resolved farfields. The experimental setup is the one described in **Section III.3.2**. A polarizer was used to detect selectively *s*- and *p*-polarized light [13]. For the sake of comparison, we also performed similar measurements for the unpatterned CCL.

The results are displayed in **Figure III-13** for the unpatterned CCL in a  $\lambda$ - $\theta$  representation,  $\theta$  being the acceptance angle, each of them being normalized with its maximum value. As expected, the farfield shapes are polarization-dependent due to the polarization dependency of the directly emitted light inside the air cone. From the *p*-polarized light, a quite homogeneous farfield shape arises except for high

intensity broad lobes around  $\theta = \pm 45^\circ$ . These lobes become more visible for *s*-polarized light and correspond to angular modulations of the internal emission inside the air cone due to Fabry-Pérot interferences inside the CCL membrane (see **Chapter II**).

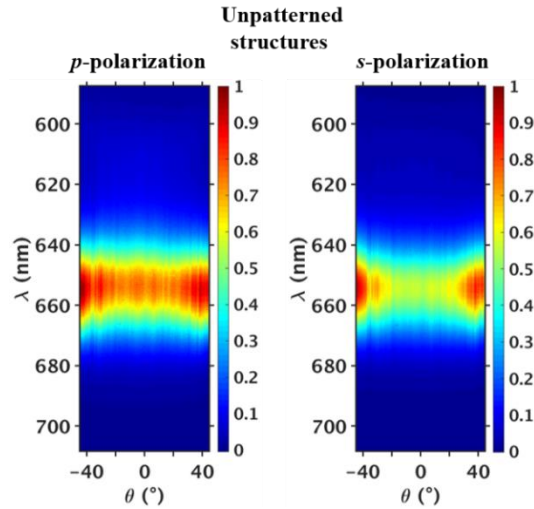


**Figure III-13:** Normalized spectrally resolved farfields from the unpatterned CCL for *s*- and *p*-polarized light.

The spectrally resolved farfield shapes for SLAH and SLNP along the  $\Gamma X$ -direction are displayed in **Figure III-14** and **Figure III-15**, respectively. Contrary to the unpatterned CCL, oblique bands are now superimposed on top of the directly emitted light. Each of them corresponds to the diffraction of a guided Bloch-mode into air by the PhC patterns according to Bragg's law, which explains why their angular position shifts with the wavelength [11]. As explained in the second chapter, the CCL acts as a multimode waveguide ( $\sim 600$  nm-thick). Due to its rather low thickness, all those guided modes are prone to an efficient interaction with the PhC patterns and thus diffraction into air, leading to intricate spectrally resolved farfield patterns.

For SLAH, the emission patterns are strongly lattice-period dependent. The lattice period  $a = 400$  nm, for instance, can exhibit farfield shapes with a strong light diffraction close to normal incidence, particularly for the *p*-polarization. It can be observed that this arises when the most intense diffraction band crosses the  $\Gamma$ -point close to the peak emission wavelength. Similar conclusions hold for  $a = 450$  nm, which resulted in the large directionality enhancement factors obtained previously for those two lattice periods. For  $a = 500$  nm, on the other hand, there is a quasi-absence of guided light diffraction close to normal incidence for both polarizations. With a closer look at the most intense band of the farfield patterns at this lattice period, we can note that this low light diffraction close to normal incidence arises from its slight detuning with the emission spectrum near the  $\Gamma$ -point. It actually crosses the  $\Gamma$ -point at the short-wavelength edge of the emission spectrum (near  $\lambda = 634$  nm, with low PL intensity) as indicated by the white dashed line, resulting in the lowest directionality enhancement factors. For the lattice period 550 nm, additional diffraction bands tend to appear, with the most intense ones overlapping the emission spectrum away from the  $\Gamma$ -point, near  $\theta = \pm 20^\circ$ . This is consistent with the azimuthal

farfield shapes in **Figure III-11**. Still, it results in intermediate values of directionality enhancement factors since some of the less intense bands cross the  $\Gamma$ -point close to the peak emission wavelength.

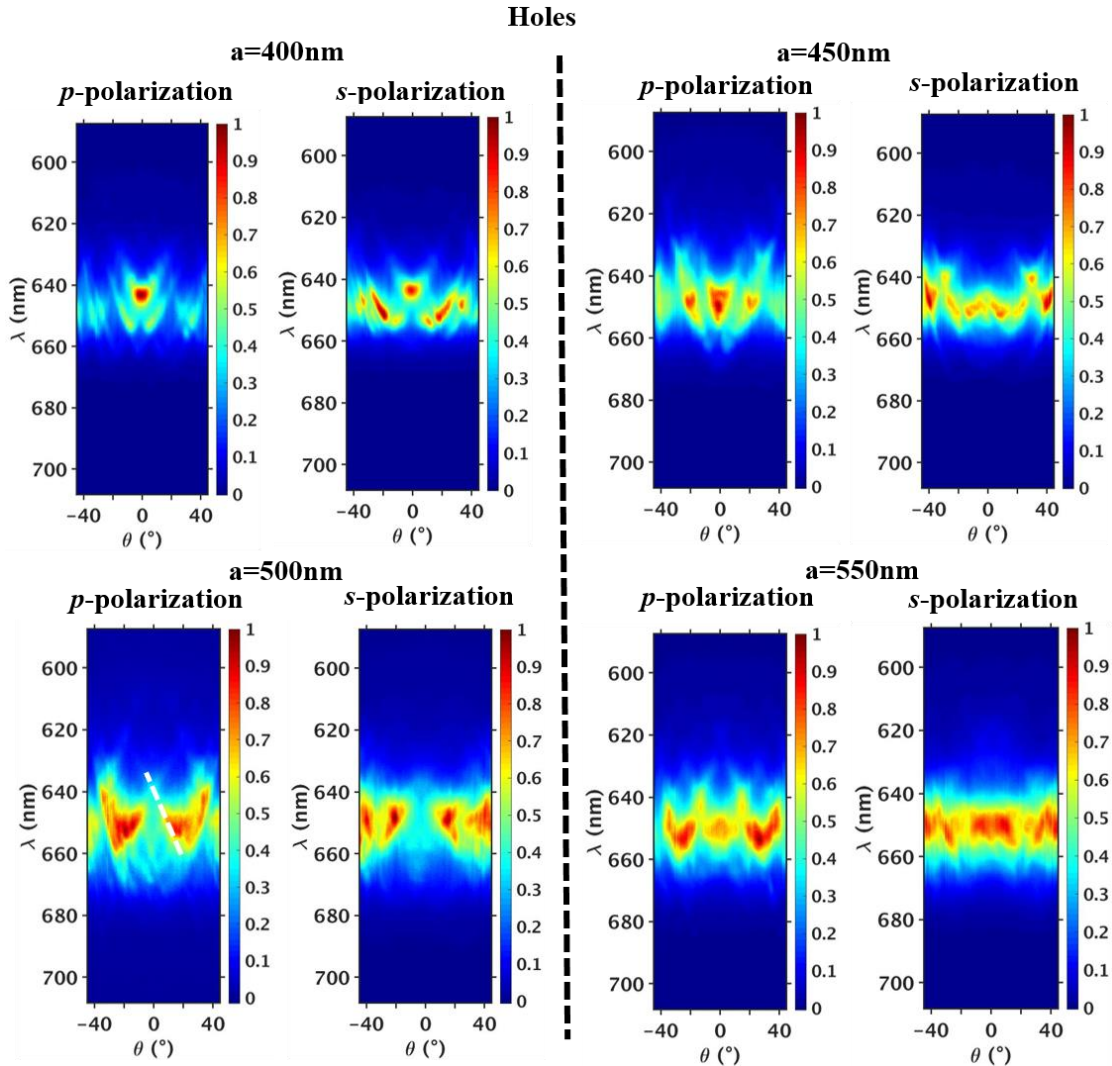


**Figure III-14:** Normalized spectrally resolved farfields for the SLAH with lattice periods from  $a=400\text{nm}$  to  $a=550\text{nm}$  and in the GX-direction. Both  $s$ - and  $p$ -polarized light are measured. The white dashed line for  $a=500\text{nm}$  indicated the most intense band crossing the  $\Gamma$ -point at the short-wavelength edge of the emission spectrum near  $\lambda = 634\text{ nm}$ . The said white dashed line is not an actual calculated band.

On the other hand, SLNP exhibits light diffraction close to normal incidence for all lattice periods and light polarizations with farfield shapes different from those of holes. Particularly, for  $a = 500\text{ nm}$ , there can be a strong light diffraction close to normal incidence as opposed to SLAH with a lattice period of  $500\text{ nm}$ , which exhibited an absence of light diffraction near the  $\Gamma$ -point close to the peak emission wavelength. The fact that at the same lattice period some of the diffracted bands of pillars can cross the  $\Gamma$ -point close to the peak emission wavelength suggests that pillar- and hole-based CCL have different effective index distributions inside their membrane, as we will see in next section. Moreover, we can observe that the diffraction bands for SLNP are broader in the  $k_{\parallel}$ -space (corresponding to the  $\theta$ -axis in **Figure III-14** and **Figure III-15**) than those of holes, which makes them trickier to distinguish. Indeed, the stronger coupling between the guided Bloch-modes and the air radiated modes for pillars results in shorter extraction lengths. Since for a given guided Bloch mode the broadening in the  $k_{\parallel}$ -space is

inversely proportional to its extraction length [7] [ $\Delta k_{\parallel} \sim (L_{\text{extraction}})^{-1}$ ], then the latter yields broader diffraction bands for SLNP. Due to those broader bands, the farfield shapes of pillars can exhibit strong light diffraction within a broader angular range, resulting in lower directionality than for holes close to normal incidence as previously observed. Thus, a compromise needs to be made between the extraction length and directionality through the broadness of the diffracted bands.

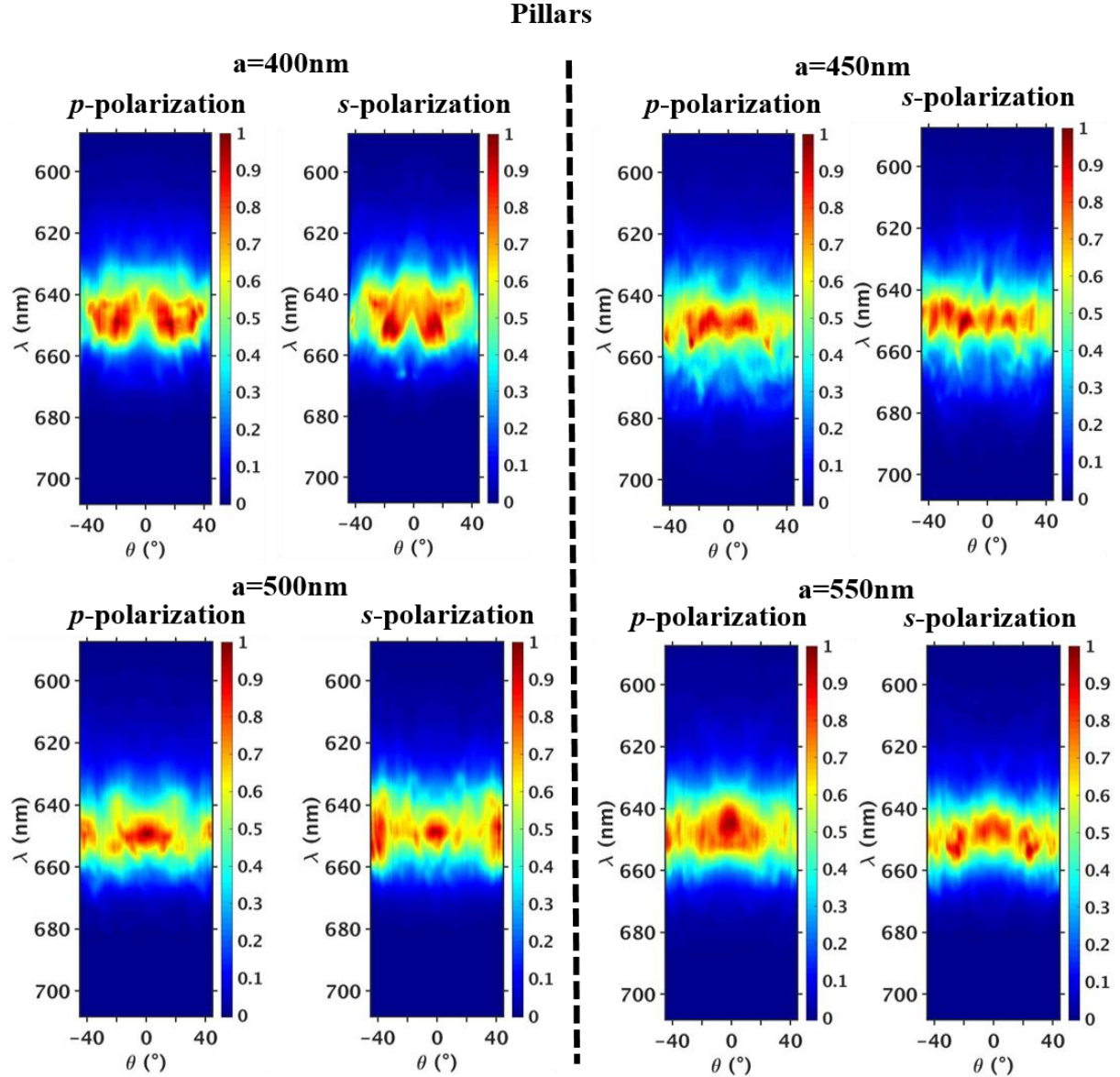


**Figure III-15:** Normalized spectrally resolved farfields for the SLNP with lattice periods from  $a=400\text{nm}$  to  $a=550\text{nm}$  and in the GX-direction. Both  $s$ - and  $p$ -polarized light are measured.

We can hitherto conclude from the analysis that emission directionality is ultimately not only determined by light diffraction according to Bragg's law, but also depends on the relative intensities of the diffracted bands arising from each mode. The highest directionality is achieved when the lattice period is fine-tuned so that the most intense diffraction bands cross the  $\Gamma$ -point close the peak emission wavelength. In the next subsection, we devise a novel design strategy for achieving directional emission from this latter point.

### III.6.3 Novel design approach for highly directional emission from MQW CCL

We have previously seen that the highest directionality is achieved when the lattice period is tuned so that the most intense diffraction bands cross the  $\Gamma$ -point close to the peak emission wavelength. In the following, we devise a design approach to reach this fundamental condition combining spontaneous emission (SpE) control and band-folding mechanism in a 2D (1D) configuration for 2D (1D) PhCs. The so-devised approach will then be used to analyze the experimental photonic band-structure of one of the fabricated devices.

#### III.6.3.a Tailoring spontaneous emission distribution

As previously mentioned, directionality depends on the relative intensities of the diffraction bands arising from each mode, which will ultimately depend on the fraction of the guided energy carried by the mode as compared to the other modes [14]. To investigate how light emitted by the MQW is shared among the guided modes in our CCL, we performed numerical simulations using the SpE model developed in the second chapter of this manuscript for planar cases. The schematics of the architecture used in this simulation for our MQW CCL is depicted in **Figure III-16**. The corresponding optical and structural parameters for each layer are taken from the literature [15–17]. The PhC patterns are treated as a homogeneous layer with a filling-factor-weighted average refractive index<sup>17</sup>.

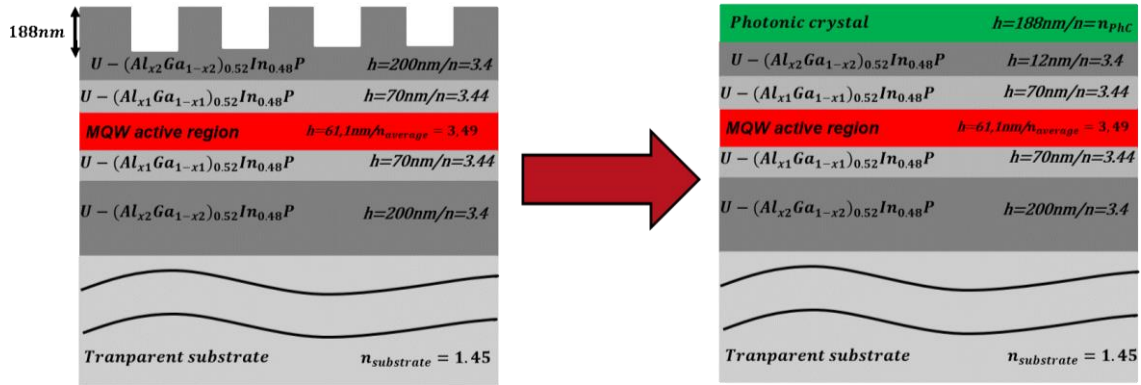


**Figure III-16:** Schematics of the architecture used for the numerical simulations.

The internal emission distribution is displayed in **Figure III-17** as a function of the effective index for a CCL based on SLAH with FF~20%. As we can see, the radiation dynamics depends on the light polarization, which explains the polarization-dependency of the farfield shapes in **Figure III-13**, **Figure III-14** and **Figure III-15**. As already detailed in the second chapter of this manuscript, light emitted inside the CCL can couple to different types of modes. A fraction of the emitted light which is in the air cone ( $n_{\text{eff}} < 1$ ) directly radiates in the air or towards the substrate. This is the so-called directly emitted light and features the background farfield observed in **Figure III-14** and **Figure III-15**. Another fraction of the emitted light is propagative in the transparent substrate but not in air ( $1 < n_{\text{eff}} < 1.45$ ). Most of the

<sup>17</sup> This approximation stems from the effective medium theory [18] and holds for weakly corrugated gratings [19,20] as we have seen in the second chapter of this manuscript.

emitted light excites the available guided modes supported by the CCL, which are represented by sharp peaks outside the air and substrate cones ( $n_{\text{eff}} \geq 1.45$ ) [2].

The intensity of those peaks sets the fraction of the guided energy carried by each mode, which we will refer to as the photonic weight of the mode. If we note  $P_i$  the peak intensity of the guided mode labelled  $i$  and  $\theta_i$  its angular position, then by taking into account the solid angle, the fraction of the guided energy carried by the mode (its photonic weight) can be simply evaluated<sup>18</sup> by  $P_i \sin(\theta_i) / \sum_j P_j \sin(\theta_j)$ . In **Figure III-17**, the corresponding photonic weights of each of the guided modes are given in the bar plot on the bottom.

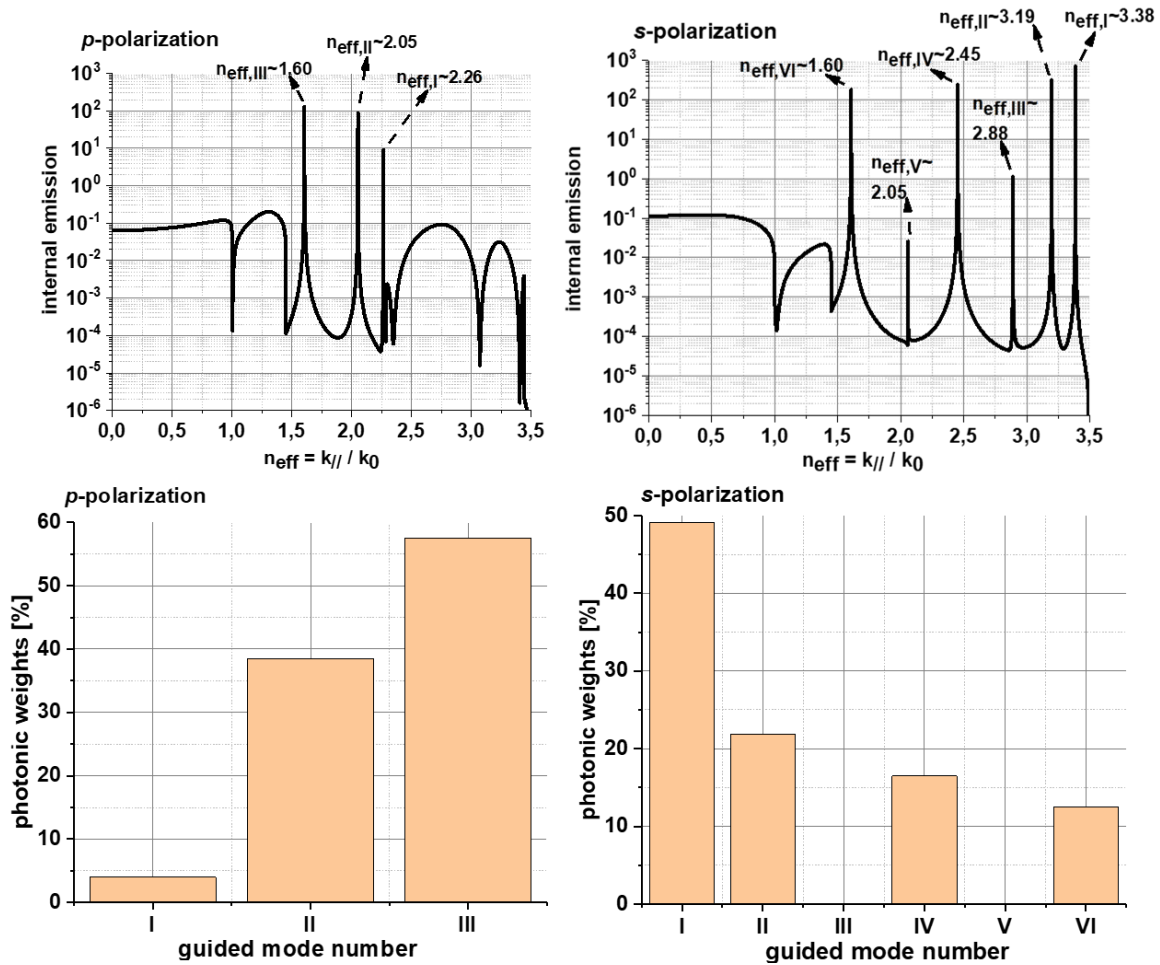


**Figure III-17:** Internal emission per unit solid angle as a function of the effective index for PhC-based CCL with SLAH with FF~20% and the corresponding photonic weights of each mode for both  $s$ - and  $p$ -polarization.

For instance, for  $p$ -polarization the guided mode with  $n_{\text{eff}} = 1.6$  (mode III) carries more than half of the guided energy. Therefore, if the lattice period is tuned so that the band arising from this mode crosses the  $\Gamma$ -point close to the peak emission wavelength, then the resulting spectrally resolved farfield patterns should have high directionality close to normal incidence. We can note that, since SLNP have different air filling factors than SLAH, their guided-mode distribution is different from that of holes, which

<sup>18</sup> For SpE distribution where guided-modes' angular widths are broader, the integral form of this formula needs to be used.

explains the different farfield shapes previously observed for the same lattice period when we change the lattice pattern from holes to pillars. The air-filling factor is thus another lever to control properly SpE distribution.

It thus appears that the relative intensity of the diffracted bands depends on the spontaneous emission distribution between the guided modes supported by the CCL. Each guided mode has a photonic weight, which corresponds to the fraction of the guided energy that it carries. This photonic weight can be quantified using our herein-developed SpE model. As we have seen in the second chapter of this manuscript, it depends on all the opto-geometrical parameters of the MQW CCL. We can thus identify two main levers that can help tailor the guided mode distribution to have suitable photonic weights: epitaxial design (controlling the thickness of the CCL, the number of quantum wells, their positions, the emission spectrum, etc.) and controlling certain parameters of the PhCs (air-filling factor and etch depth).

In the following, we will discuss the second step of our design approach: fine-tuning the lattice period so that those modes with high photonic weights give rise to diffraction bands that cross the  $\Gamma$ -point close to the peak emission wavelength.

### III.6.3.b Fine tuning the lattice period

Now that we have devised a way to determine the effective indices of the guided modes with the highest photonic weights, we go on with the second step of the design approach: fine-tuning the lattice period to target the corresponding modes at the  $\Gamma$ -point. This step will only be investigated for square lattices, but similar methodology could be adopted for 1D and hexagonal lattices. Light diffraction is ruled by the vectorial Bragg's law from which we can derive the 2D grating equation that reads in the case of a square lattice as [21]:

$$\begin{aligned} \sin(\theta_{mn}) \cos(\varphi_{mn}) &= n_{effi} \cos(\varphi_i) + m \frac{\lambda}{a}, \\ \sin(\theta_{mn}) \sin(\varphi_{mn}) &= n_{effi} \sin(\varphi_i) + n \frac{\lambda}{a}, \end{aligned} \quad (\text{III-7})$$

Here  $n_{effi}$  is the effective index of the incident guided mode (the one with the high photonic weight in our case),  $\theta_{mn}$  and  $\varphi_{mn}$  are the polar and azimuthal angles of the diffracted wave with  $m$  and  $n$  corresponding to the diffracted orders along the  $x$  and  $y$  directions (see **Figure III-18**) and  $a$  is the lattice period. In this framework, the effective indices that couple to the  $\Gamma$ -point ( $\theta_{mn}=0^\circ$ ) satisfy the following equations:

$$\begin{aligned} 0 &= n_{effi} \cos(\varphi_i) + m \frac{\lambda}{a}, \\ 0 &= n_{effi} \sin(\varphi_i) + n \frac{\lambda}{a}, \end{aligned} \quad (\text{III-8})$$

For measurements along the  $\Gamma X$ -direction ( $x$  or  $y$  in **Figure III-18**), an effective index propagating in a 2D PhC structure gives rise to two types of Bloch modes [13]: A- and B-type Bloch-modes stemming

from guided modes propagating along the  $\Gamma X$ -direction ( $\varphi_i=0$  or  $\pi$ ) and off the  $\Gamma X$ -direction ( $\varphi_i \neq 0$  and  $\varphi_i \neq \pi$ ). Those modes can be coupled either to  $G_{\Gamma X}$  or to  $G_{\Gamma M}$  vectors described in **Figure III-18**. For a given incident effective index, the normalized frequencies at which A-type Bloch-modes couple to the  $\Gamma$ -point can be expressed as:

$$a = m \frac{\lambda}{n_{effi}}, \quad (III-9)$$

$$n = 0.$$

Thus, A-type Bloch-modes have properties close to a “plane wave” (nearly free photon dispersion folded by periodicity) and behave as if they experience the 2D PhC as a superposition of independent 1D PhCs. For our measurements along the  $\Gamma X$  direction, they are then coupled to the  $G_{\Gamma X}$ -type reciprocal lattice vectors  $(m, 0)$ .

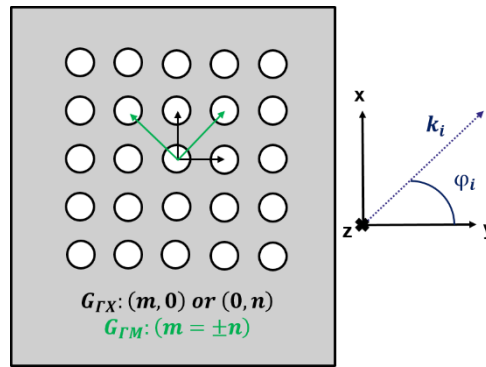


**Figure III-18:** Reciprocal lattice vectors along the high-symmetry directions of a square lattice.

For B-type Bloch-modes on the other hand ( $\varphi_i \neq 0$  and  $\varphi_i \neq \pi$ ), coupling to both vectors  $(0, n)$  and  $(m = \pm n)$  is possible. B-type Bloch-modes that are coupled to vectors  $(0, n)$  cross the  $\Gamma$ -point at the same normalized frequencies as A-type Bloch-modes. However, for B-type Bloch-modes coupled to vectors  $(m = \pm n)$ , the normalized frequencies at the  $\Gamma$ -point can be expressed as:

$$a = m \frac{\lambda}{n_{effi}} \sqrt{2}, \quad (III-10)$$

$$m = \pm n.$$

B-type Bloch-modes are therefore specific to 2D PhC structures. The two previous equations describe the 2D band-folding mechanism at the  $\Gamma$ -point for a square lattice and the basis for the fine-tuning of the lattice period. Similar formula could be found for hexagonal lattices by considering their high-symmetry directions  $\Gamma M$  and  $\Gamma K$ . For 1D lattices, only A-type Bloch-modes exist and thus only **Eq. (III-9)** is needed.

Thereupon in our spectrally resolved farfield patterns along the  $\Gamma X$ -direction, the strong coupling to the  $\Gamma$ -point observed for some lattice periods can arise from two sets of  $\Gamma$ -points (corresponding to different normalized frequencies) for a given effective index. The first set (odd diffraction orders) will be referred to as  $\Gamma_{A+B,m}$ . It stems from A- and B-type Bloch-modes coupled to  $G_{\Gamma X}$ -type reciprocal lattice vectors and its normalized frequencies are given by **Eq. (III-9)**. The second set (even diffraction orders) on the

other hand will be referred to as  $\Gamma_{B,m}$  and arises from B-type Bloch-modes coupled to  $G_{\Gamma M}$ -type reciprocal lattice vectors. The corresponding normalized frequencies are given by **Eq. (III-10)**.

We confirm these analytical considerations by calculating the band structure of a square lattice of air holes for a TE mode with an effective index of 1.6 using the Plane Wave Expansion (PWE) algorithm of the Rsoft Design Suite in the free-photon approximation regime [22].

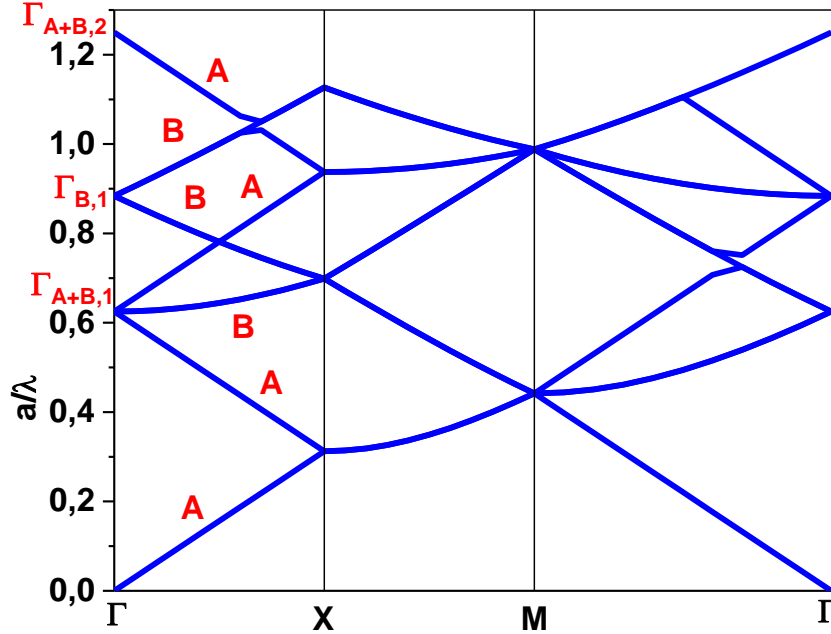


**Figure III-19:** Band structure of a SLAH for a TE mode with  $n_{\text{eff}}=1.6$  in the free-photon approximation regime.

As we can see in **Figure III-19**,  $\Gamma_{A+B,1}$  and  $\Gamma_{A+B,2}$  have been identified as well as  $\Gamma_{B,1}$  and the corresponding normalized frequencies match those given in **Eq. (III-9)** and **Eq. (III-10)**, which confirms our previous analysis.

It thus appears that for a given effective index corresponding to a mode with high photonic weight and at a given peak emission wavelength, the lattice period has to be properly tuned so that it matches **Eq. (III-9)** and **Eq. (III-10)** based on the simple band folding mechanisms in the case of square lattices. A slight detuning between the most intense bands at the  $\Gamma$ -point and the emission spectrum can lead to a large decrease of the directionality (see SLAH with  $a=500\text{nm}$ ). The lattice period therefore needs to be properly controlled during fabrication.

This concludes the development of our design approach for directional emission. In the next subsection, we confirm this design strategy by analyzing the experimental photonic band-structures of one the fabricated devices.

### III.6.3.c Analysis of a measured photonic band-structure

In this section, we confirm the previously devised design-approach for directional emission by analyzing the results for SLAH with  $a=400\text{nm}$  (high directional enhancement close to normal incidence). The corresponding experimental photonic band structure is directly obtained from the spectrally resolved

farfield patterns in **Figure III-14** by converting the wavelength and angle into the normalized frequency and in-plane wave vectors, respectively [23].

The resulting photonic band structures for  $p$ - and  $s$ -polarized light are reported in **Figure III-20**.

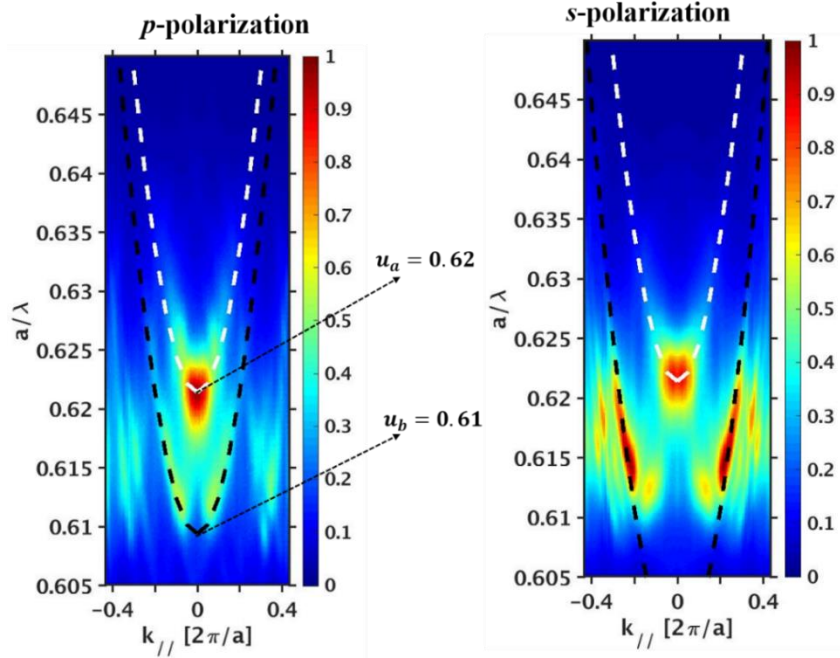


**Figure III-20:** Measured photonic band structures for SLAH with  $a=400\text{nm}$  for  $p$ - and  $s$ -polarized light. Calculated band structures for modes with  $n_{\text{eff}a}=1.6$  (white dashed lines) as well as with  $n_{\text{eff}b}=1.64$  (black dashed lines for  $p$ -polarization) and  $n_{\text{eff}b}=1.67$  for  $s$ -polarization.

We have identified the intense band crossing the  $\Gamma$ -point at  $a/\lambda \approx 0.62$  to stem from the guided mode with  $n_{\text{eff}}=1.6$  arising from the first diffraction order<sup>19</sup>. The corresponding calculated band using the plane-wave expansion (PWE) algorithm in the free-photon approximation regime (white dashed line in **Figure III-20**) is superimposed on the measured band structures. The calculated bands are in good agreement with the measured ones, which confirms our identification procedure. We can also note the presence of a second closely spaced parallel band arising for both  $s$ - and  $p$ -polarized light. Indeed, albeit the weakly corrugated regime, the PhC pattern will induce for each guided mode a slight modal index-contrast [23,24] giving rise to two different modes with very close effective indices. This slight index-contrast will result into a mini-band-splitting that can be modelled using the standard coupled-mode theory. In this framework, the spectral width between the two resulting bands reads as [6,25]:

$$\Delta u_{ab} = \frac{a}{2\pi} \times \frac{4\kappa_{\text{ext}}}{n_{\text{eff}a} + n_{\text{eff}b}} \quad (\text{III-11})$$

Here,  $u$  is the normalized frequency,  $\Delta u_{ab}$  accounts for the spectral width between the two bands,  $\kappa_{\text{ext}}$  is the modal coupling constant between the Bloch-mode and the air radiated modes,  $n_{\text{eff}a}$  and  $n_{\text{eff}b}$  are the effective indices of the two modes. The previous free-photon approximation needs then to be “corrected” using coupled-mode theory. For  $p$ -polarization, we found that the second diffracted bands (labelled “ $b$ ”)

<sup>19</sup> For the identification, we take the corresponding normalized frequency, calculate the possible effective indices (in the range of those in **Figure III-17**) using **Eq. (III-9)** and **Eq. (III-10)** and then we compare the obtained values with those that couple to spontaneous emission in **Figure III-17**.

crosses the  $\Gamma$ -point at  $u_b=0.61$ , which gives  $n_{\text{eff}}=1.64$  using **Eq. (III-9)** and  $\Delta u_{\text{ab}}=0.01$ . The corresponding calculated bands using PWE (black dashed line in **Figure III-20**) are superimposed on the measured ones showing very good agreement, which supports our analysis. Similar treatments are performed for  $s$ -polarization as displayed. Let us note that using the values extracted from the measured band structure, we obtain a modal coupling constant of  $\kappa_{\text{ext}}\approx 0.1\mu\text{m}^{-1}$  (corresponding to an extraction length of about  $10\mu\text{m}$ ), which is consistent with the values found in **Section III.4**.

From this analysis of the photonic band-structure, it has appeared that the spectrally resolved farfield patterns in **Figure III-14** for SLAH with  $a=400\text{nm}$  are dominated at the  $\Gamma$ -point by the guided mode with  $n_{\text{eff}}\approx 1.6$  arising from the first diffraction order ( $\Gamma X$ ). For  $p$ -polarization, we have evaluated that this mode (mode III) can carry more than half of the guided energy (see **Figure III-17**). Since the lattice period is properly tuned so that the corresponding band crosses the  $\Gamma$ -point close to the peak emission wavelength, we obtain an enhanced directionality close to normal incidence, which is characterized by a strong light diffraction at the  $\Gamma$ -point for  $p$ -polarization. We have seen that the guided energy for  $s$ -polarized light on the other hand is shared among more modes, which tends to mitigate the previously mentioned effect. This results into a less directional emission close to normal incidence than for  $p$ -polarization, as evidenced by some very intense bands away from the  $\Gamma$ -point, near  $\theta=\pm 30^\circ$  (see **Figure III-14**). This confirms our above-devised design methodology for achieving directional emission in our PhC-based MQW CCL.

Overall, throughout **Subsections III.6.1, III.6.2 and III.6.3** we have highlighted a fundamental condition necessary to achieve directional emission in our MQW: the lattice period needs to be properly tuned so that the most intense diffraction bands cross the  $\Gamma$ -point close to the peak emission wavelength. From this condition, we have devised a design approach for such structures resting on a simultaneous control of SpE distribution between the guided modes to identify the ones with the highest photonic weights and an optimized choice of the lattice period based on the 2D band-folding mechanism. This approach has been experimentally confirmed helping us reach directionality enhancement over  $\times 4$  close to normal incidence as compared to standard Lambertian emission, which is promising for our targeted AR applications.

Furthermore, we have emphasized that epitaxial design (thickness of the CCL, the number of quantum wells, their positions, the emission spectrum) as well as controlling some PhC parameters such as the air filling factor and etch depth could be levers to tailor suitable SpE distributions and photonic weights. In the following subsection, we further investigate the impact of some of the PhC parameters such as lattice symmetry and air-filling factor (FF) on the farfield shapes before concluding **Section III.6**.

#### **III.6.4 Additional levers to control the directionality of the farfield patterns**

In this section, we briefly describe the impact of the air-filling factor and the lattice symmetry on the directionality of the farfield patterns.

### III.6.4.a Air-filling factor

As we have seen in the previous sections, in addition to its impact on the coupling strength, the air-filling factor (FF) also changes the effective refractive index of the PhC. It thus changes the farfield shape for a fixed lattice symmetry and lattice period. To illustrate this particular point, we measure the azimuthal radiation patterns of the SLAH with FF~50% and compare them to the ones with FF~20%. The corresponding farfield shapes are displayed in **Figure III-21** along with the associated values of directionality in **Figure III-22**.

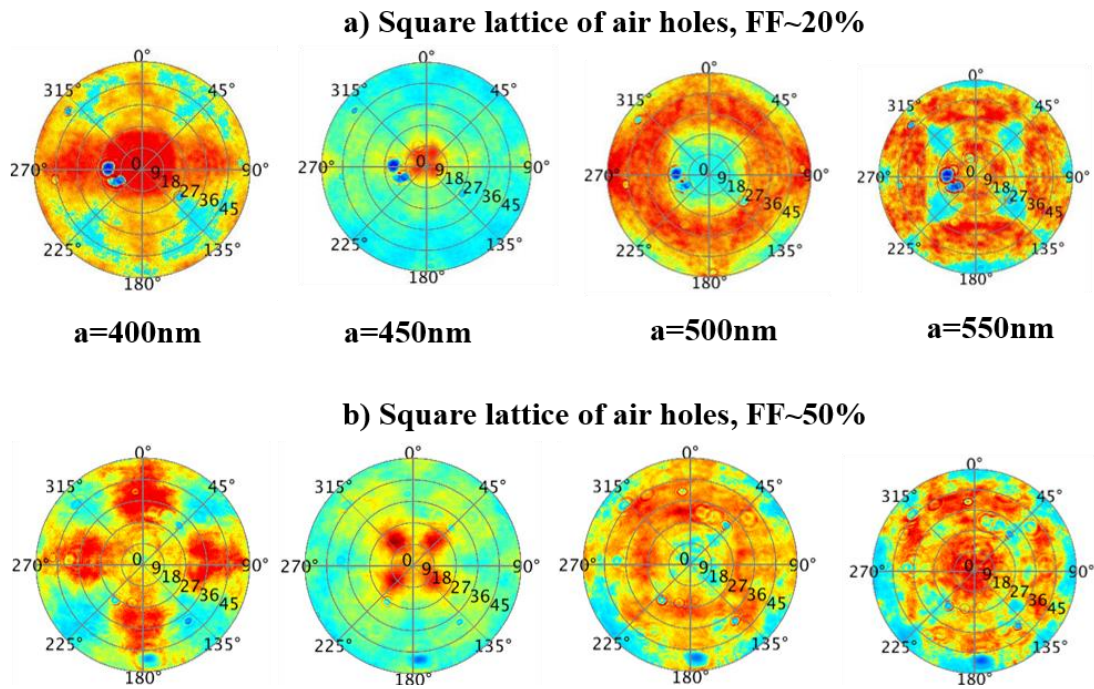


**Figure III-21:** Azimuthal farfield radiation patterns for square lattice of air holes with a) FF~20% and b) FF~50%.

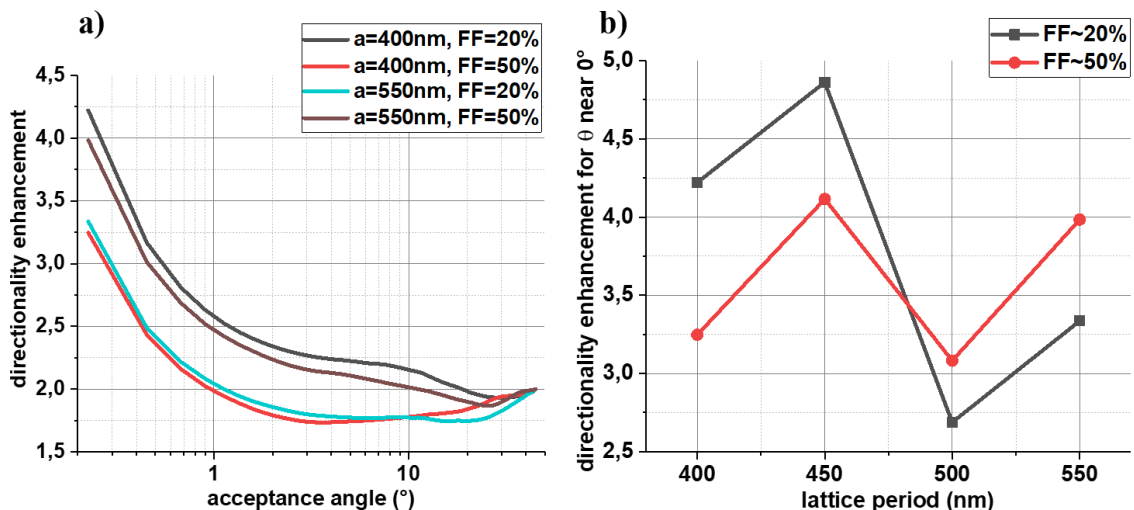


**Figure III-22:** a) Directionality enhancement as a function of the acceptance angle for SLAH and b) directionality enhancement near normal incidence as a function of the lattice period for FF~20% and FF~50%.

Since the FF changes the effective refractive index of the PhC, then it also influences the SpE distribution inside the MQW CCL. These changes of effective indices will afterwards lead to different

diffraction angles and to a change in the shapes of radiation patterns as evidenced by the patterns above. The four-fold symmetry is still preserved. However, for low diffraction orders (low lattice periods below 500nm), increasing the FF leads to a directionality decrease. Particularly, for  $a=400\text{nm}$ , this directionality decrease can amount to 20% as shown in **Figure III-22-b**. For higher diffraction orders, increasing the FF actually improves the directionality to more than 20% for  $a=550\text{nm}$ . Either way, it appears that if the PhC-based MQW CCL are designed at fixed values of FF to achieve directional emission, one should make sure that these values are preserved during the fabrication process. For instance, the tapered profiles at the sidewalls of the PhC patterns can lead to local changes of the air-filling factors, which can affect the shape of the farfield patterns (see the 3D-FDTD simulations in **Appendix B.3**). All these considerations need then to be accounted for during the design process.

### III.6.4.b Lattice symmetry

Spontaneous emission is by nature an azimuthally omnidirectional process, thus an efficient PhC light-extractor needs to be able to diffract guided Bloch-modes within most of the in-plane directions. The ability to diffract different in-plane directions is set by the lattice symmetry, since the symmetry order tells how many nearest-neighbor reciprocal-lattice points the crystal has [12]. 1D, square and hexagonal lattices<sup>20</sup> have a symmetry order of 2, 4 and 6, respectively. As we have seen in **Section III.5**, we have experimentally demonstrated that for our fabricated devices, increasing the symmetry order over 4 does not seem to help in the optimization of light extraction. We now turn to the impact of lattice symmetry on the directionality. In **Figure III-23**, we display the azimuthal farfield patterns of some of the fabricated PhC-based MQW CCL with 1D and hexagonal lattices.

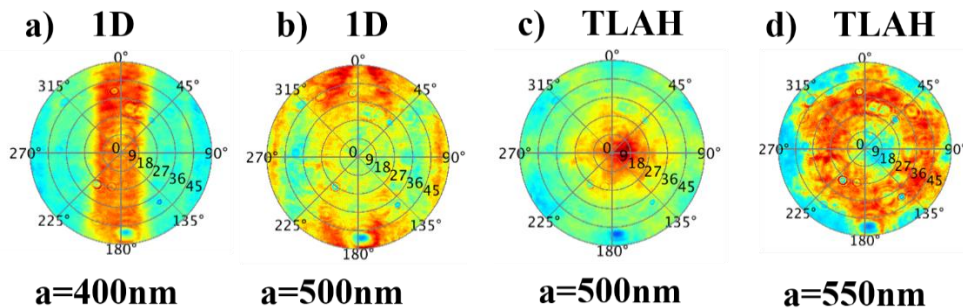


**Figure III-23:** Normalized azimuthal farfield patterns for some of the fabricated 1D lattices and triangular lattices of air holes.

As expected, the azimuthal farfield patterns of 1D lattices exhibit sets of 2 diffraction bands typical to the two-fold symmetry of the lattice, while the ones of the hexagonal lattices exhibit sets of six diffraction bands. Increasing the lattice symmetry definitely improves much the azimuthal uniformity of the radiation patterns as already explained in [8,12].

<sup>20</sup> Lattice symmetries with higher symmetry orders do exist. For instance, there are Archimedean tilings, which are quasi- or non-strictly periodic crystals and have twelve nearest reciprocal lattice points. However, it has been experimentally demonstrated that using those kinds of quasi-crystals does not bring any advantage in terms of light extraction compared to hexagonal lattices [12]. That is why our investigations have been limited to hexagonal lattices.

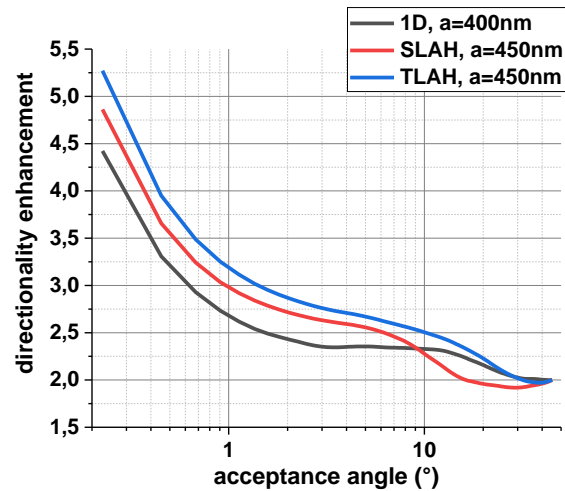


**Figure III-24:** directionality enhancement as a function of the acceptance angle. For each lattice symmetry (FF~20%), only the structure with the highest values has been displayed.

**Figure III-24** reports on the corresponding directionality enhancement factors for the structures with the highest directionality per lattice symmetry. On the contrary to light extraction where increasing the lattice symmetry order over four did not seem to help, directionality, particular close to normal incidence, is improving for higher symmetry order. The directionality increases by ~10% from 1D to square lattices and by ~8% from square to hexagonal ones.

Thereupon, increasing the lattice symmetry order enables a better azimuthal uniformity as well as a moderate directionality increase in the case of color-converters on transparent substrates.

Additional investigations of the impact of lattice symmetry on the coupling strength will be performed in the next chapter.

### III.6.5 Conclusion

Throughout **Section III.6**, we have highlighted a fundamental condition necessary to achieve directional emission in our MQW: the lattice period needs to be properly tuned so that the most intense diffraction bands cross the  $\Gamma$ -point close to the peak emission wavelength. From this condition, we have devised a design approach for such structures resting on a simultaneous control of SpE distribution between the guided modes to identify the guided modes with the highest photonic weights and an optimized choice of the lattice period based on the 2D band-folding mechanism. This approach has then been experimentally confirmed helping us reach directionality enhancement over  $\times 4$  close to normal incidence as compared to standard Lambertian emission, which is promising for our targeted AR applications. Furthermore, we emphasized that epitaxial design (thickness of the CCL, the number of quantum wells, their positions, the emission spectrum) as well as controlling some of the PhC parameters such as the air filling factor and etch depth could be levers to tailor suitable SpE distributions and photonic weights. It has eventually been pointed out that increasing the symmetry order of the lattice brings a certain advantage in terms of directionality (~10% increase from 2 to 4 and from 4 to 6 close to normal incidence), which could be of use for color converters on transparent substrates.

All along our analyses on the extraction length, LEE and directionality, we have pointed out that the etch depth could play a significant role on the optimization of the three former FoM. In that regard, we further investigate its impact in the next section before opening some perspectives on a system point of view.

### III.7 Identification of the different contributions in the experimental LEE enhancement

The experimental enhancement factors embed light absorption efficiency, internal quantum efficiency (IQE) and light extraction efficiency (LEE) as described in the first chapter of this manuscript. This section aims at investigating separately those three figure of merits (FoM) to have a better insight of their actual contributions.

We start by performing additional incoherent 3D-FDTD simulations (see **Appendix A.1** for details on the FDTD method) in a pulsed regime to evaluate LEE for some of the fabricated structures. The lateral dimensions of the computational domain were fixed at 10 lattice periods for computing time issues and surrounded by perfectly matched layers (PML). The PhC etch depth is  $\sim 188\text{nm}$ . The input spectrum is Gaussian-shaped with a center wavelength at  $640\text{nm}$  and a FWHM of  $20\text{nm}$  as in our PL measurements. The MQW region was represented by a source plane of 50 transverse electric (TE)-polarized dipoles in the middle of the CCL. As a reference, we also performed calculations for flat structures to evaluate LEE enhancement factors. **Figure III-25** displays the measured and simulated LEE enhancement factors for 10-period structures with varying lattice periods. Only SLAH with  $\text{FF} \sim 20\%$  and SLNP are considered.

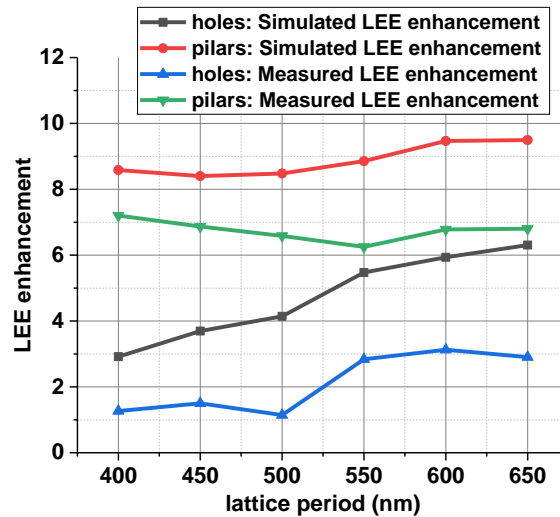


**Figure III-25:** Measured and simulated LEE enhancement for PhC structures with a lateral extent of 10 periods.

For SLNP, both measured and simulated LEE enhancement only weakly depend on the lattice periods whereas for SLAH both measured and simulated LEE enhancement increase for increasing lattice periods. 3D-FDTD is therefore in agreement with our measurements in terms of variations, which supports our previous analysis. However measured LEE enhancement factors are lower than the

simulated ones, which means there are other contributions (either absorption efficiency or IQE) that tend to decrease the measured enhancement factors.

Regarding light absorption efficiency, we performed numerical simulations based on the rigorous coupled-wave analysis (RCWA) method from the Rsoft Design Suite [1] (see **Appendix B.4** for the simulations results) showing that the PhCs enhance light absorption by factors between  $\sim 1.4$  and  $\sim 1$ , which is clearly not responsible of the discrepancies in **Figure III-25**.

Moreover, quantitative determination of the IQE would require further extensive studies and experiments that are out of the scope of the present discussion [26]. Instead, we conducted time-resolved PL measurements (TRPL) to estimate the decay lifetime of the PhC compared to the reference structures using the  $\mu$ -PL setup described in **Subsection III.3.1**. The IQE is given by the ratio of probabilities of radiative ( $1/\tau_R$ ) and total recombination ( $1/\tau=1/\tau_R+1/\tau_{NR}$ ), where  $\tau_R$  and  $\tau_{NR}$  are the radiative and non-radiative recombination lifetimes [27]. Since the radiative lifetimes do not vary between the PhC structures and the reference structures in this case<sup>21</sup>, the ratios of the total lifetimes for PhC and unpatterned structures directly give the IQE ratios between those two.

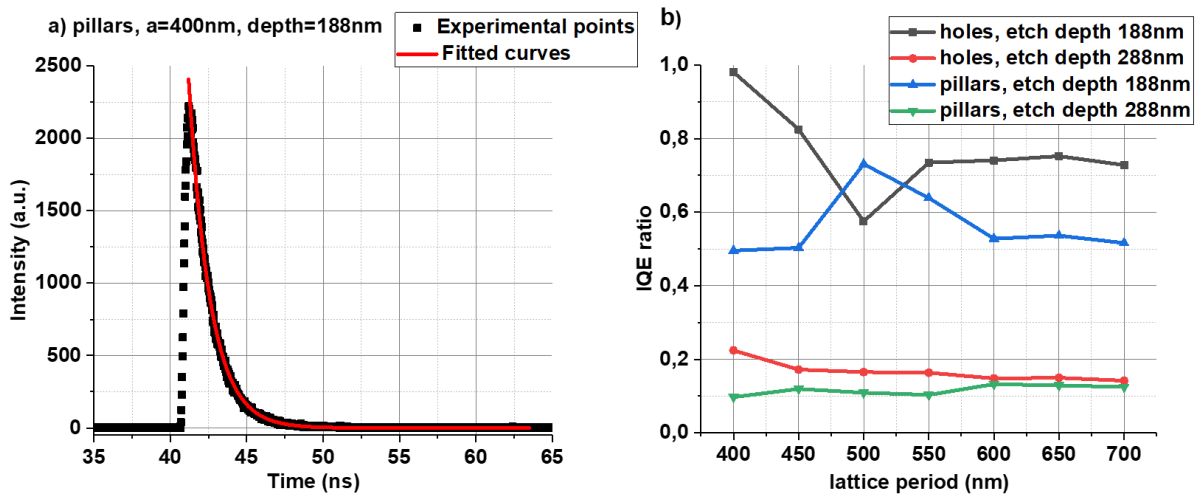


**Figure III-26:** TRPL results for two etch depths as a function of the lattice period. a) Transient curve for SLNP with  $a=400$  nm. b) IQE ratios between PhC and unpatterned structures.

The TRPL results are shown in **Figure III-26**. The left plot shows one of the TRPL transient curves with the fitting function. All the transient curves were best fit with a single exponential decay function, given by  $I_{TRPL}=A \times \exp(-t/\tau)$ , where  $A$  is the amplitude and  $\tau$  the total recombination lifetime as in [28]. The right plot displays the IQE ratios for holes and pillars as a function of the lattice period. We also added the IQE ratios for devices with an etch depth of  $\sim 288$  nm to have a better insight on the role of the PhC depth on the overall conversion efficiency.

Depending on the lattice periods and the etch depth, we can observe an IQE decrease of the PhC structures compared to the reference structures. For instance, the IQE of the PhC structures decreases down to half of the one of the unpatterned regions for SLNP with  $a=400$  nm and an etch depth of 188 nm. We also notice that when PhC patterns are etched in the active region (etch depth  $\sim 288$  nm in **Figure**

<sup>21</sup> 3D-FDTD simulations show that the Purcell factors are around 1 for both patterned and unpatterned cases.

**III-26-b**), the IQE of the PhC structures strongly decreases (almost five times lower compared to etch depth ~188nm). For the samples with etch depth ~288nm, the experimental LEE enhancement factors (not shown here) are in fact less than 1, meaning that the IQE decrease is so high that PL gains cannot be observed and PhC patterns actually decrease the PL intensity. This is a result of the large number of surface defect states created at the sidewall of the PhC patterns combined with high surface recombination velocities and high carrier diffusion lengths in AlGaInP [28]. It thus appears that to fabricate highly efficient color converters with the InGaP/AlGaInP material system, the active region should not be etched at all unless efficient passivation techniques are developed.

It should however be noted that in our experiments, the incoming excitation light is focused on the top side of the PhC structures and so carrier generation mostly occurs in the etched regions. For example in the sample with etch depth ~188nm we could expect that carrier generation would preferentially happen in the unetched zones, with a pump on the bottom side of the CCL, which would then mitigate the IQE ratios in **Figure III-26-b**. Thereupon, a more robust design rules would be twofold. On the one hand, the etch depth should be high enough to ensure efficient coupling between the guided Bloch-modes and the PhC patterns as explained in [8]. On the other hand, it should not be so high that the carrier generation happens in the etched zones. Additional 3D-FDTD simulations (see **Appendix B.5**) combined with our experimental results help us determine that in our MQW CCL an etch depth around one third of the epilayer thickness is enough, as evidenced by our short extraction lengths paired with high LEE enhancement factors.

We have thus devised ways to alleviate issues related to the extraction length ( $L_{\text{extraction}}$ ) and LEE as well as directionality. However, as of now for  $L_{\text{extraction}}$  and LEE, all our experiments have been performed with a numerical aperture (NA) high enough so that all the emitted light is collected by the microscope objective. As mentioned in the introductory chapters, our targeted AR applications often include optical systems with limited numerical apertures (NA). In the next section, we examine in that regard how LEE and  $L_{\text{extraction}}$  evolve when coupled to those kinds of optical systems.

### **III.8 Coupling to an optical system with limited numerical aperture (NA<1)**

Our targeted AR applications may involve optical systems with limited numerical apertures (NA), thus common LEE is not enough anymore to assess the performances of the PhC-based MQW CCL [1]. Indeed only part of the emitted light couples to the optical system and this quantity depends on both LEE and farfield emission pattern. Therefore a new figure of merit (FoM) needs to be defined taking into account both LEE and radiation pattern shape. We call it directional light extraction efficiency (DLEE). Using the integrated intensity within the acceptance angle  $\theta$  provided in **Eq.(III-4)**, DLEE reads:

$$DLEE(\theta) = \frac{P(\theta)}{P_{\text{int}}} = \frac{P(\theta)}{P(90^\circ)} \times \frac{P(90^\circ)}{P_{\text{int}}} = D(\theta) \times LEE. \quad (\text{III-12})$$

Here  $P_{int}$  is the emitted intensity inside the structure (in our case the CCL) and  $D(\theta)$  is the directionality of the radiation patterns of the CCL (see **Eq.(III-5)**). For  $\theta=90^\circ$ , this definition corresponds to the common LEE expressed in **Eq. (III-1)**. More generally, it accounts for light extraction inside a cone whose apex angle is  $\theta$ . The directional light extraction efficiency enhancement is then given by the ratio between DLEE of PhC structures and DLEE of the unpatterned reference structures and expresses as:

$$\eta_{DLEE}(\theta) = \frac{DLEE_{PhC}(\theta)}{DLEE_{unpatterned}(\theta)} = \frac{P_{PhC}(\theta)}{P_{unpatterned}(\theta)} = \frac{\int_{550nm}^{750nm} I_{PhC}(\lambda) d\lambda}{\int_{550nm}^{750nm} I_{unpatterned}(\lambda) d\lambda} \quad (\text{III-13})$$

Here  $I_{unpatterned}$  and  $I_{PhC}$  refer to the emitted intensities for the reference and PhC structures respectively integrated within the acceptance cone with an apex angle of  $\theta$ .

Subsequently, we follow the same experimental procedure as in **Section III.4**, albeit using different excitation objectives with different NA: NA=0.9 ( $\sim 64^\circ$ ), NA=0.75 ( $\sim 49^\circ$ ), NA=0.6 ( $\sim 37^\circ$ ), NA=0.5 ( $\sim 30^\circ$ ) and NA=0.25 ( $\sim 14^\circ$ ). Those numerical apertures allow us to scan acceptance angles between  $64^\circ$  (high acceptance angles where most of the emitted light is collected) and  $14^\circ$  (very low acceptance angle). Only SLAH with FF $\sim 20\%$  and SLNP are considered in this analysis.

### III.8.1 Extraction length vs acceptance angle

**Figure III-27** displays the experimental DLEE enhancement factors as a function of the lateral extent for the PhC structures with a lattice period of 600nm and for the excitation objective with NA=0.6.

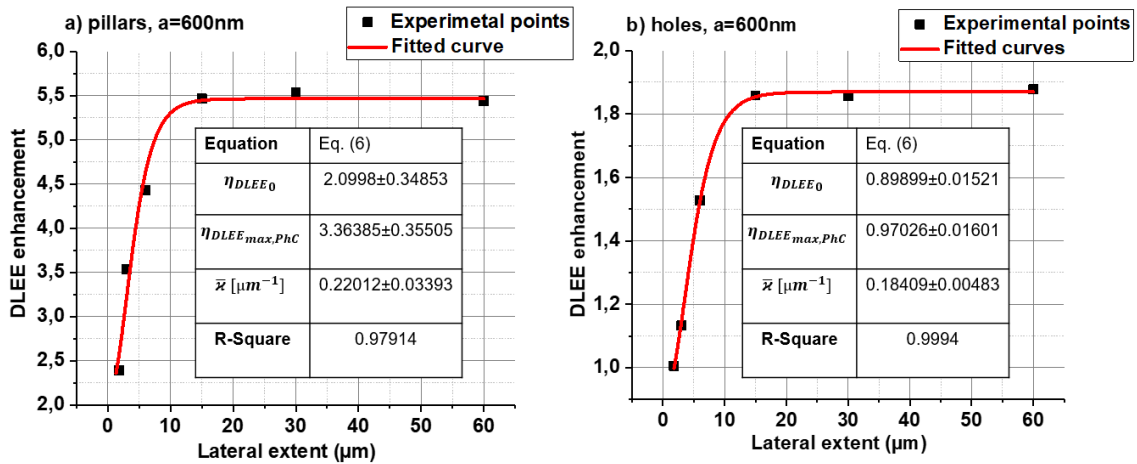


**Figure III-27:** Experimental DLEE enhancement as a function of the PhC lateral extent for a) SLNP and b) SLAH (FF $\sim 20\%$ ) with a lattice period  $a=600nm$ . NA=0.6. Experimental points are fitted with the proposed phenomenological model derived from the standard coupled-mode theory. Fit details are given in the inset.

We can observe that similarly to LEE enhancement, DLEE enhancement also increases with the lateral extent of the PhC until it saturates at  $\sim 5.5$  and  $\sim 1.9$  for SLNP and SLAH, respectively. Using the same phenomenological model derived from the standard coupled-mode theory as in **Eq. (III-2)**, we fit our experimental points and then derive the mean coupling strength (over all the guided Bloch-modes diffracted within the cone with an apex angle  $\theta$ ). The corresponding extraction lengths as a function of the acceptance angle are provided in **Figure III-28**.

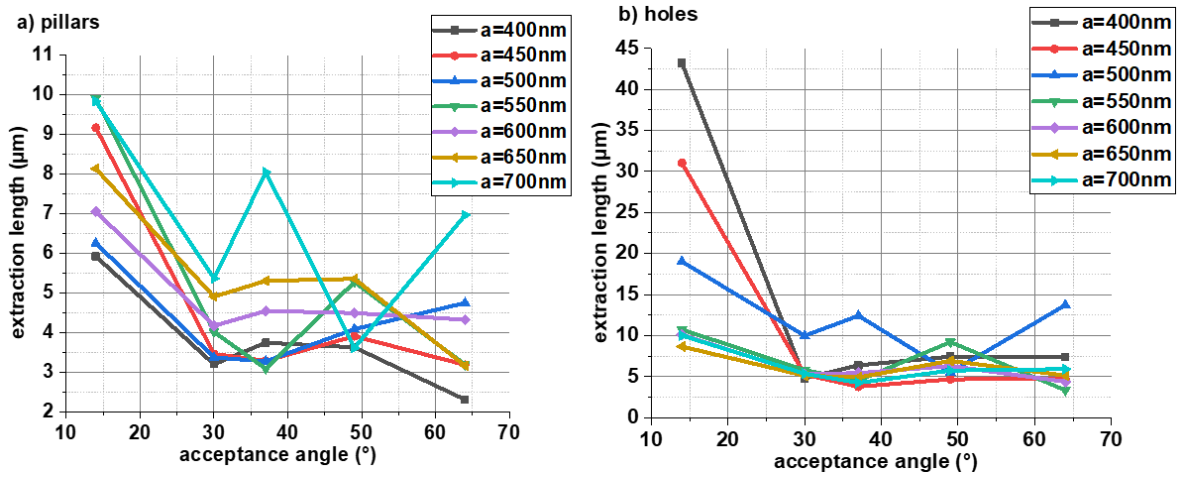


**Figure III-28:** Mean extraction lengths as a function of the acceptance angle for a) SLNP and b) SLAH (FF~20%).

We notice that for both lattices the extraction lengths strongly depend on the acceptance-angle, which results from the variations of the mean coupling strengths as a function of the acceptance angle. This dependency can be understood by conventional diffraction theory. Each of the guided Bloch-modes supported by the multimode CCL has its own coupling strength depending on its interaction with the PhC patterns. Since all those modes are diffracted to air within different angles according to Bragg's law, the modes collected by the microscope objective are not the same when the acceptance angle changes. This induces strong variations of mean coupling strengths as a function of the acceptance angle and therefore leading to strong variations of mean extraction lengths [1].

For SLNP, the optimal lattice period is  $a=400\text{nm}$  offering the shortest extraction lengths (between 2 and 6 μm). In addition, we notice that for almost all lattice periods, there is an increase of the mean extraction lengths with decreasing acceptance angles: for  $a=400\text{nm}$ , there is almost a three-time increase from  $64^\circ$  to  $14^\circ$ .

For SLAH however, the optimal lattice period shifts to a higher lattice period ( $a=700\text{nm}$ ) with extraction lengths between  $\sim 5\mu\text{m}$  at  $64^\circ$  and  $\sim 10\mu\text{m}$  at  $14^\circ$ . The dependency of extraction lengths on the acceptance angles are similar to those observed for pillars with longer extraction lengths obtained for SLAH as explained before. As SLNP, there is large increase of the extraction length for decreasing acceptance angles (e.g. for  $a=450\text{nm}$ ,  $L_{\text{extraction}}$  goes from  $\sim 5\mu\text{m}$  at high  $\theta$  to up to  $30\mu\text{m}$  for low  $\theta$ ).

On a device point of view, there are two main conclusions that can be drawn from this analysis. On the one hand, it appears that the extraction lengths can be optimized (made shorter than the lengths of our devices) with a proper choice of the lattice period and pattern as already emphasized in **Section III.4**. On the other hand, for applications including optical systems with very low numerical apertures, CCL with longer lateral extents are needed. That last remark is of crucial interest since it sets the final pixel size in our RGB microdisplay, which is dependent on the acceptance angle of the external optical system within the AR headset. We can also note that it matches the preliminary numerical analyses we made in the second chapter.

### III.8.2 Directional light extraction efficiency enhancement

As aforementioned, LEE is not enough anymore to assess performances when dealing with systems with limited numerical apertures. **Figure III-29** displays DLEE enhancement for structures with a lateral extent of 100 periods (when all the guided light is extracted) as a function of the acceptance angles.

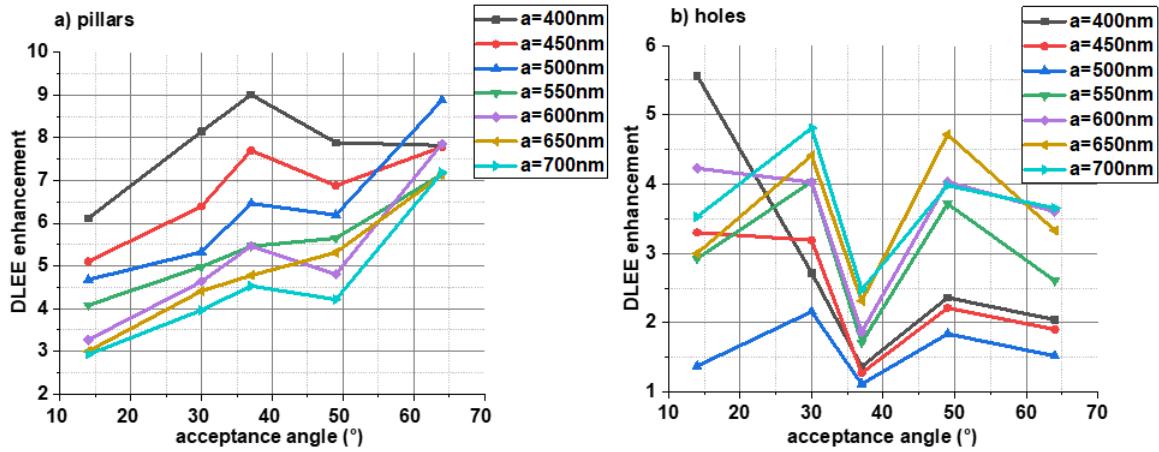


**Figure III-29:** DLEE enhancement measured for different lattice periods as a function of the acceptance angle. a) For SLNP and b) SLAH with a lateral extent of 100 periods.

DLEE enhancement takes into account both LEE as well as directionality of the emission patterns as described before and accounts for light that effectively couples into the external optical system. Since the shape of the emitted patterns from our CCL can exhibit strongly intricate shapes due to the multimode nature of the CCL, then DLEE enhancement depends on the acceptance angle.

At high acceptance angles, DLEE enhancement corresponds to LEE enhancement. Therefore, for SLNP, DLEE enhancement only weakly depends on lattice periods at high acceptance angles as seen previously. However, DLEE enhancement becomes lattice-period dependent for decreasing acceptance angles, because of strong variations of the emission pattern. The optimal lattice period for pillars is  $a=400\text{nm}$  offering at the same time high DLEE enhancement factors at all the measured acceptance angles (from  $\sim 8$  at  $64^\circ$  to  $\sim 6$  at  $14^\circ$ ).

For holes on the other hand, the optimal lattice period clearly depends on the acceptance angle with a shift to lower lattice periods for decreasing acceptance angle because of stronger variations of the emission pattern than for pillars. Particularly, for  $a=400\text{nm}$  and  $a=450\text{nm}$  the DLEE enhancement factors go from  $\sim 2$  at  $64^\circ$  to  $\sim 5.5$  and  $\sim 3$  respectively. The highest DLEE enhancement factors for the measured angles are obtained for  $a=400\text{nm}$  at low acceptance angle ( $\sim 5.5$  at  $14^\circ$ ) and for  $a=700\text{nm}$  at high acceptance angles ( $\sim 4$  at  $64^\circ$ ). We can note that despite the fact that at high acceptance angles SLNP exhibit better DLEE enhancement (LEE enhancement), at low acceptance SLAH catch up due to their better directionality close to normal incidence.

It thus appears that the choice of the optimal lattices is then not an easy task, since it also depends on the acceptance angle of the external systems. For a given acceptance angle, both the extraction length and coupling efficiency to external optical systems with limited numerical apertures can be optimized by correctly choosing the lattice type and the lattice periods.

### III.9 Preliminary design guidelines

**Table III-2** provides an in-depth compilation of the design guidelines drawn from all our previous analyses.

**Table III-2:** Summary of the preliminary design guidelines of photonic-crystals for directional light emission, enhanced LEE and short extraction length from AlGaInP/InGaP MQW color-converters.

Photonic-crystal parameter	Preliminary design rules
Lattice symmetry	<ul style="list-style-type: none"> <li>*Square lattice can provide good extraction efficiency, short extraction length and directional emission</li> <li>*Increasing the symmetry order over 4 does not help much in terms of light extraction but enables moderate directionality increase (~10% from 4 to 6).</li> </ul>
Air filling factor (FF)	<ul style="list-style-type: none"> <li>*Should be kept around 50% to reach high coupling strengths</li> <li>*Is also a lever to control spontaneous emission distribution through the effective refractive index of the photonic-crystal</li> </ul>
Pattern type	<ul style="list-style-type: none"> <li>*Holes or pillars</li> <li>*Pillars could induce directionality decrease by ~20%.</li> </ul>
Lattice period (a)	<ul style="list-style-type: none"> <li>*Should be fine-tuned to target guided Bloch-modes with high photonic weights near the <math>\Gamma</math>-point with low diffraction orders</li> <li>*400-450nm are the optima in the range of the fabricated devices in terms of directionality</li> </ul>
Lateral extent	<ul style="list-style-type: none"> <li>*Depends on the acceptance angle <math>\theta</math> of the external optical system</li> <li>*Needs to be longer than the extraction length, which depends on <math>\theta</math>: directional emission implies longer extraction lengths.</li> </ul>
Etch depth	<ul style="list-style-type: none"> <li>*Should allow efficient interaction between photonic-crystal patterns and guided Bloch-modes</li> <li>*Should not affect the IQE: carrier generation must happen in unetched regions</li> <li>*Depends on the epitaxial structure: ~1/3 of the epilayer thickness</li> </ul>

A further investigation of the impact of the lattice symmetry on the coupling strengths will be performed in the next chapter with on-silicon devices.

### III.10 Conclusion

Optimizing a photonic-crystal (PhC) for efficient MQW CCL appears to be a tricky endeavor, due to the large parameter-space of PhCs and the incoherent nature of spontaneous emission. To do so we started by developing a robust process flow based on an oxide-mediated molecular bonding with high bonding yield (>90%), which is promising for the transfer of those MQW CCL on blue  $\mu$ -LED arrays. The PhC patterns have also been successfully fabricated with quite controlled opto-geometrical parameters over the whole wafer. Afterwards, using micro-photoluminescence measurements we have emphasized the main roles played by the opto-geometrical parameters of the PhCs on the performances of our devices and modelled them when necessary. For each of those parameters, we have proposed precise preliminary design guidelines (see **Table III-2**) that helped us realize PhC-based MQW color-converters on transparent substrates exhibiting unique characteristics: enhanced light extraction efficiency and directional emission, both within ultra-short extraction lengths. All these considerations

could help pave the way for the use of inorganic MQW epi-layer color-converters to achieve a monolithic integration of full-color microdisplays on a single wafer.

To go further, we have studied how the aforementioned figure of merits (FoM) vary as a function of the acceptance angle. We particularly highlighted that the extraction lengths can be strongly increased when coupling to an external optical system with a very limited numerical aperture. Thus, the levers that we have studied for optimizing the coupling strength (etch depth, FF, etc.) might not be enough for pixels with very short lateral sizes and thus additional strategies need to be devised. Moreover, once the color-converters are transferred on blue  $\mu$ -LED arrays, they will be pixelated. Their optical environment will then drastically change. First, they will interact with the electrical contact at the backside of the blue  $\mu$ -LEDs, which will act as a back reflector for the red light. Next, they will also be surrounded by lateral mirrors on their sidewalls, which could affect their performances.

In that regard, the next chapter of this manuscript is dedicated to the “fully integrated” pixels, where we investigate ways to benefit from the electromagnetic environment of the CCL as a pixel in order to improve its performances. It starts with an investigation of the possibility of harnessing the light that is diffracted towards the transparent substrate by studying the interplay between light diffraction and a metallic back-reflector (Lot II), mimicking the electrical contact at the bottom of the blue  $\mu$ -LEDs. Secondly, we go on with the process to singularize the CCL into pixels, where we examine the possibility of virtually extending the lateral size of pixels (particularly the very short ones) using a principle we refer to as Bloch-mode replication. Finally yet importantly, the whole process flow of these pixelated MQW CCL will be given, while highlighting all the challenges we have encountered during the integration of those PhC-based MQW CCL in 200mm cleanroom facilities on Silicon, which could help during the fabrication of the final RGB microdisplay.

### **III.11 References**

1. A. Ndiaye, A. Ghazouani, C. Seassal, E. Drouard, N. Olivier, and B. B. Bakir, "Enhanced light-extraction efficiency and emission directivity in compact photonic-crystal based AlGaInP thin-films for color conversion applications," *Opt. Express* **29**, 35965–35979 (2021).
2. A. Ndiaye, H. S. Nguyen, C. Seassal, E. Drouard, and B. Ben Bakir, "Farfield pattern and guided-mode extraction analysis for highly directional emission from photonic-crystal based AlGaInP/InGaP MQW color-converters in thin-film geometry," *AIP Adv.* **12**, 045122 (2022).
3. C. Gui, M. Elwenspoek, N. Tas, and J. G. E. Gardeniers, "The effect of surface roughness on direct wafer bonding," *J. Appl. Phys.* **85**, 7448–7454 (1999).
4. D. Pasquariello and K. Hjort, "Plasma-assisted InP-to-Si low temperature wafer bonding," *IEEE J. Sel. Top. Quantum Electron.* **8**, 118–131 (2002).
5. D. Bordel, M. Argoud, E. Augendre, J. Harduin, P. Philippe, N. Olivier, S. Messaoudène, K. Gilbert, P. Grosse, B. B. Bakir, and J.-M. Fedeli, "Direct and Polymer Bonding of III-V to Processed Silicon-On-Insulator for Hybrid Silicon Evanescent Lasers Fabrication," *ECS Trans.* **33**, 403 (2010).
6. L. A. Coldren, S. W. Corzine, and M. L. Mashanovitch, *Diode Lasers and Photonic Integrated Circuits* (John Wiley & Sons, 2012).

7. E. Matioli, B. Fleury, E. Rangel, E. Hu, J. Speck, and C. Weisbuch, "Measurement of extraction and absorption parameters in GaN-based photonic-crystal light-emitting diodes," *J. Appl. Phys.* **107**, 053114 (2010).
8. A. David, H. Benisty, and C. Weisbuch, "Optimization of Light-Diffracting Photonic-Crystals for High Extraction Efficiency LEDs," *J. Disp. Technol.* **3**, 133–148 (2007).
9. K. Bergenek, C. Wiesmann, H. Zull, C. Rumbolz, R. Wirth, N. Linder, K. Streubel, and T. F. Krauss, "Strong High Order Diffraction of Guided Modes in Micro-Cavity Light-Emitting Diodes With Hexagonal Photonic Crystals," *IEEE J. Quantum Electron.* **45**, 1517–1523 (2009).
10. R. G. Baets, D. G. Delbeke, R. Bockstaele, and P. Bienstman, "Resonant-cavity light-emitting diodes: a review," in *Light-Emitting Diodes: Research, Manufacturing, and Applications VII* (SPIE, 2003), Vol. 4996, pp. 74–86.
11. J. J. Wierer, A. David, and M. M. Megens, "III-nitride photonic-crystal light-emitting diodes with high extraction efficiency," *Nat. Photonics* **3**, 163–169 (2009).
12. K. Bergenek, C. Wiesmann, H. Zull, C. Rumbolz, R. Wirth, N. Linder, K. Streubel, and T. F. Krauss, "Beam-shaping properties of InGaN thin-film micro-cavity light-emitting diodes with photonic crystals," in *Light-Emitting Diodes: Materials, Devices, and Applications for Solid State Lighting XIII* (SPIE, 2009), Vol. 7231, pp. 21–31.
13. C.-F. Lai, J.-Y. Chi, H.-C. Kuo, H.-H. Yen, C.-E. Lee, C.-H. Chao, H.-T. Hsueh, and W.-Y. Yeh, "Far-field of GaN film-transferred green light-emitting diodes with two-dimensional photonic crystals," *Opt. Express* **17**, 8795–8804 (2009).
14. C. Wiesmann, K. Bergenek, R. Houdre, R. P. Stanley, N. Linder, and U. T. Schwarz, "Theoretical Investigation of the Radiation Pattern From LEDs Incorporating Shallow Photonic Crystals," *IEEE J. Quantum Electron.* **45**, 1273–1283 (2009).
15. S. Turcotte and M. Daraselia, "Generalized model of the dielectric function of AlInGaP alloys," *J. Appl. Phys.* **113**, 093103 (2013).
16. M. F. Schubert, S. Chhajed, J. K. Kim, E. Fred Schubert, and J. Cho, "Polarization of light emission by 460nm GaInN/GaN light-emitting diodes grown on (0001) oriented sapphire substrates," *Appl. Phys. Lett.* **91**, 051117 (2007).
17. M. Boucenna and N. Bouarissa, "Refractive index and dielectric constants of  $GaxIn_{1-x}P$ : Disorder effect," *Optik* **125**, 6611–6615 (2014).
18. J. H. Schmid, P. Cheben, P. J. Bock, R. Halir, J. Lapointe, S. Janz, A. Delage, A. Densmore, J.-M. Fedeli, T. J. Hall, B. Lamontagne, R. Ma, I. Molina-Fernandez, and D.-X. Xu, "Refractive Index Engineering With Subwavelength Gratings in Silicon Microphotonic Waveguides," *IEEE Photonics J.* **3**, 597–607 (2011).
19. E. Rangel, E. Matioli, Y.-S. Choi, C. Weisbuch, J. S. Speck, and E. L. Hu, "Directionality control through selective excitation of low-order guided modes in thin-film InGaN photonic crystal light-emitting diodes," *Appl. Phys. Lett.* **98**, 081104 (2011).
20. C. Wiesmann, K. Bergenek, N. Linder, and U. T. Schwarz, "Analysis of the emission characteristics of photonic crystal LEDs," in *Photonic Crystal Materials and Devices VIII* (SPIE, 2008), Vol. 6989, pp. 118–126.
21. G. J. Lee and Y. M. Song, "Theoretical analysis and experiment of subwavelength structure-integrated red AlGaInP light-emitting diodes for uniform field distribution and enhanced light extraction efficiency," *AIP Adv.* **6**, 035104 (2016).
22. C. Wiesmann, K. Bergenek, N. Linder, and U. t. Schwarz, "Photonic crystal LEDs – designing light extraction," *Laser Photonics Rev.* **3**, 262–286 (2009).
23. A. David, C. Meier, R. Sharma, F. S. Diana, S. P. DenBaars, E. Hu, S. Nakamura, C. Weisbuch, and H. Benisty, "Photonic bands in two-dimensionally patterned multimode GaN waveguides for light extraction," *Appl. Phys. Lett.* **87**, 101107 (2005).
24. C.-F. Lai, C.-H. Chao, H.-C. Kuo, H.-H. Yen, C.-E. Lee, and W.-Y. Yeh, "Directional light extraction enhancement from GaN-based film-transferred photonic crystal light-emitting diodes," *Appl. Phys. Lett.* **94**, 123106 (2009).
25. S. Olivier, H. Benisty, C. Weisbuch, C. J. M. Smith, T. F. Krauss, and R. Houdré, "Coupled-mode theory and propagation losses in photonic crystal waveguides," *Opt. Express* **11**, 1490–1496 (2003).

26. P. Altieri, A. Jaeger, R. Windisch, N. Linder, P. Stauss, R. Oberschmid, and K. Streubel, "Internal quantum efficiency of high-brightness AlGaInP light-emitting devices," *J. Appl. Phys.* **98**, 086101 (2005).
27. E. F. Schubert, *Light-Emitting Diodes* (Cambridge University Press, 2003).
28. Y. Boussadi, N. Rochat, J.-P. Barnes, B. B. Bakir, P. Ferrandis, B. Masenelli, and C. Licitra, "Investigation of sidewall damage induced by reactive ion etching on AlGaInP MESA for micro-LED application," *J. Lumin.* **234**, 117937 (2021).

## **Chapter IV**

*Pixelated photonic-crystal MQW III-V  
membrane with back- and lateral reflectors:  
design and experimental demonstration.*

## Table of contents

IV.1	Introduction .....	100
IV.2	Design principles .....	100
IV.2.1	Preliminary investigations with 2D-FDTD .....	101
IV.2.1.a	Influence of a back-reflector (LOT II) .....	101
IV.2.1.b	Red color converters with vertical and lateral mirrors: Bloch-mode replication. ....	104
IV.2.2	Full 3D-FDTD simulations.....	106
IV.2.2.a	Phase-matching layer.....	107
IV.2.2.b	Gap between the MQW CCL and the bottom reflector .....	109
IV.2.3	Conclusion.....	109
IV.3	Device fabrication .....	110
IV.4	Harnessing the bottom emitted light using back reflectors: LOT II.....	115
IV.4.1	Extraction lengths, LEE enhancement and directionality.....	116
IV.4.2	Towards polarized light emission with 1D lattices .....	119
IV.4.3	Experimental evaluation of light extraction efficiency .....	120
IV.4.4	Conclusion.....	121
IV.5	Enhancing light extraction efficiency using Bloch-mode replication: LOT III.....	122
IV.5.1	Proof-of-principle experimental demonstration of Bloch-mode replication .....	122
IV.5.2	Modeling the impact of lateral-mirror losses .....	124
IV.5.3	Conclusion on the Bloch-mode replication principle .....	127
IV.6	Conclusion.....	127
IV.7	References .....	128

## IV.1 Introduction

In the previous chapter of this manuscript, we have proposed preliminary design guidelines that helped us realize unpixelated PhC-based MQW color-converting layers (CCL) on transparent substrates exhibiting promising characteristics: enhanced light extraction efficiency (LEE) and directional emission, both within ultra-short extraction lengths. In real-life RGB microdisplays, the CCL are pixelated and often surrounded by an environment comprising back- and lateral reflectors (see **Figure I-10**). The aim of this chapter is thus to devise strategies for benefiting from that electromagnetic environment in order to improve the performances of the MQW CCL. It starts with preliminary design principles using FDTD simulations before coming back to the whole process flow of the MQW CCL from the metal-metal bonding to their pixelization. Next, we examine the possibility of harnessing the light diffracted towards the transparent substrate by studying the interplay between light diffraction and a metallic back-reflector (Lot II), mimicking the electrical contact at the bottom of the blue  $\mu$ -LEDs. In addition, we have highlighted in the previous section that photons are not completely extracted by the grating during their first pass in pixels with short lateral sizes (shorter than the saturation lengths), due to their low number of diffractive elements. Therefore, in the last section of this chapter (LOT III), we investigate the possibility of virtually extending the pixel lateral sizes using the lateral mirrors, allowing the non-extracted photons to be reflected back and given other chances to escape. This latter principle will be referred to as Bloch-mode replication (BMR).

## IV.2 Design principles

In this section, we use FDTD simulations to examine the impact of the optical environment of the CCL on its performances and devise strategies to benefit from it. In the typical final integration strategy (see **Figure I-10**), this electromagnetic environment often comprises back- and lateral mirrors as depicted in **Figure IV-1**.

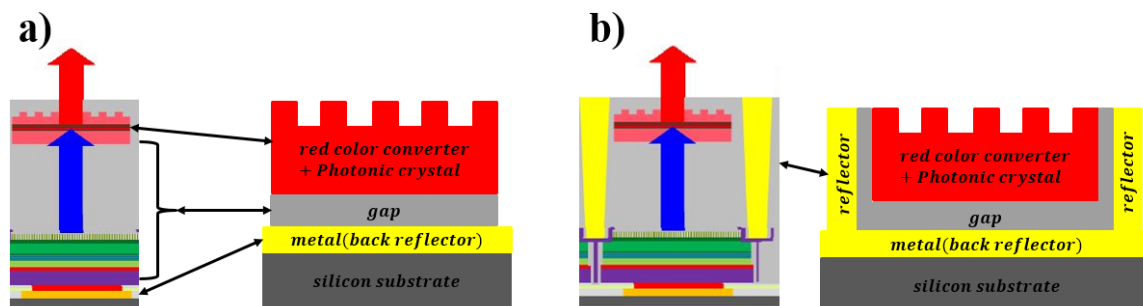


**Figure IV-1:** From the full integration strategy to our fabrication lots. a) Interplay between light diffraction and a metallic back-reflector (LOT II). b) Demonstration of Bloch-mode replication (LOT III). The gap mimics all the layers embedded between the CCL and the electrical contact, while the back-reflector represents the contact. Lateral mirrors on the other hand enables the optical isolation of the pixels between on another.

LOT II investigates the possibility of harnessing the bottom emitted light in MQW CCL with a back-reflector (see **Figure IV-1-a**). The gap mimics all the layers embedded between the CCL and the electrical contact at the bottom of the blue  $\mu$ -LEDs (bonding layers, blue epilayer, etc.), while the back-

reflector represents said contact. On the other hand, lateral mirrors first enable the optical isolation of the red pixels between one another to avoid optical crosstalk<sup>1</sup>. In LOT III, they are used to take advantage of the Bloch-mode replication principle, as we will see later on.

#### IV.2.1 Preliminary investigations with 2D-FDTD

To define preliminary design guidelines regarding the back- and lateral-reflectors, we start by performing 2D-FDTD simulations in the basic case of a single-mode waveguide<sup>2</sup> operating transverse-electric (TE) polarization at 640nm. The other parameters are the ones used in the **Section II.3** of the second chapter of this manuscript (lattice period corresponding to the second Bragg order and etch depth at the third of the membrane thickness).

##### IV.2.1.a Influence of a back-reflector (LOT II)

In this section, we analyze the impact of the bottom reflector and the gap on LEE, directionality and extraction length of a single-mode PhC-membrane. Let us recall that if a second-order Bragg grating structure is implemented in a lossless single-mode thin-film layer, we can theoretically extract almost all the guided light in each vertical direction (50% upwards / 50% downwards) as seen in the second chapter of this manuscript. **Figure IV-2** displays the layout of said membrane including the bottom reflector.

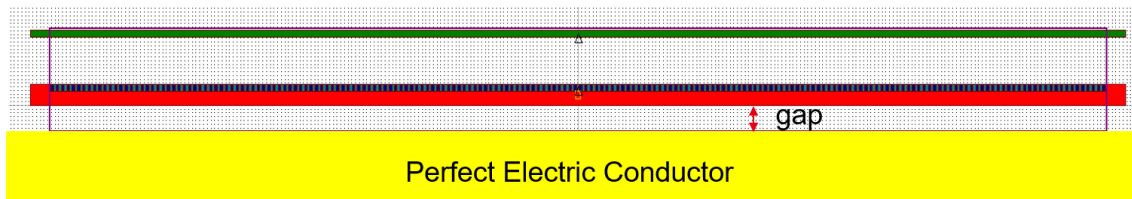


**Figure IV-2:** Layout of the device and initial conditions used for 2D-FDTD simulations. Excitation mode: multiple dipole emission. The bottom reflector is a Perfect Electric Conductor (no losses). A varying air gap separates the MQW CCL and the back reflector.

For the sake of simplicity, the back reflector is a perfect electric conductor (PEC)<sup>3</sup> which is separated from the CCL by an air-gap. This gap thickness is variable in order to evaluate its impact on both farfield and LEE, as well as the extraction length. For each FDTD simulation run, a single source-plane enclosing 50 dipoles is used to reach the convergence (see **Appendix A.1** for more details on the FDTD method).

<sup>1</sup> Due to short pixel lateral sizes in microdisplays, optical crosstalk has become an issue of paramount importance. Indeed, it can disrupt the image fidelity, deteriorate the color gamut and affect the final resolution of the display [1].

<sup>2</sup> Although our MQW CCL are multimode, for the sake of a better understanding of the physics inside those devices, we start by the simplest case of a monomode waveguide with 2D-FDTD. Multimode operation will be implemented in the 3D-FDTD simulations to define the “real” set of parameters that we choose for our fabricated devices.

<sup>3</sup> In a perfect electric conductor (PEC), the skin depth becomes so small that the electromagnetic wave hardly penetrates. It is thus a lossless reflector.

**Figure IV-3** shows a parametric study of the farfield emission diagram (Phi is the acceptance angle in the 2D framework) as a function of the gap size. 60 runs of 50 FDTD simulations were done to cover a range from 0 to 0.6 $\mu\text{m}$ . Two phenomena can be observed:

- For low gap size (from 0 to 50nm typically), the farfield diagram is strongly altered and it exhibits two peaks around  $\pm 35^\circ$ . This can be attributed to near-field effects where a strong interaction occurs between the evanescent tail of the guided mode and the bottom reflector, which also affects the light extraction process.
- For higher gap sizes, where the strong near-field coupling effect does not occur anymore, we observe that the emission diagram oscillates with a periodicity of  $\lambda/2$  (unity round-trip condition). The farfield is highly directive for gap values around  $\sim (2p+1) \lambda/4$  and less directive for gap values of  $\sim (2p) \lambda/4$ , which can be attributed to destructive/constructive interference processes.

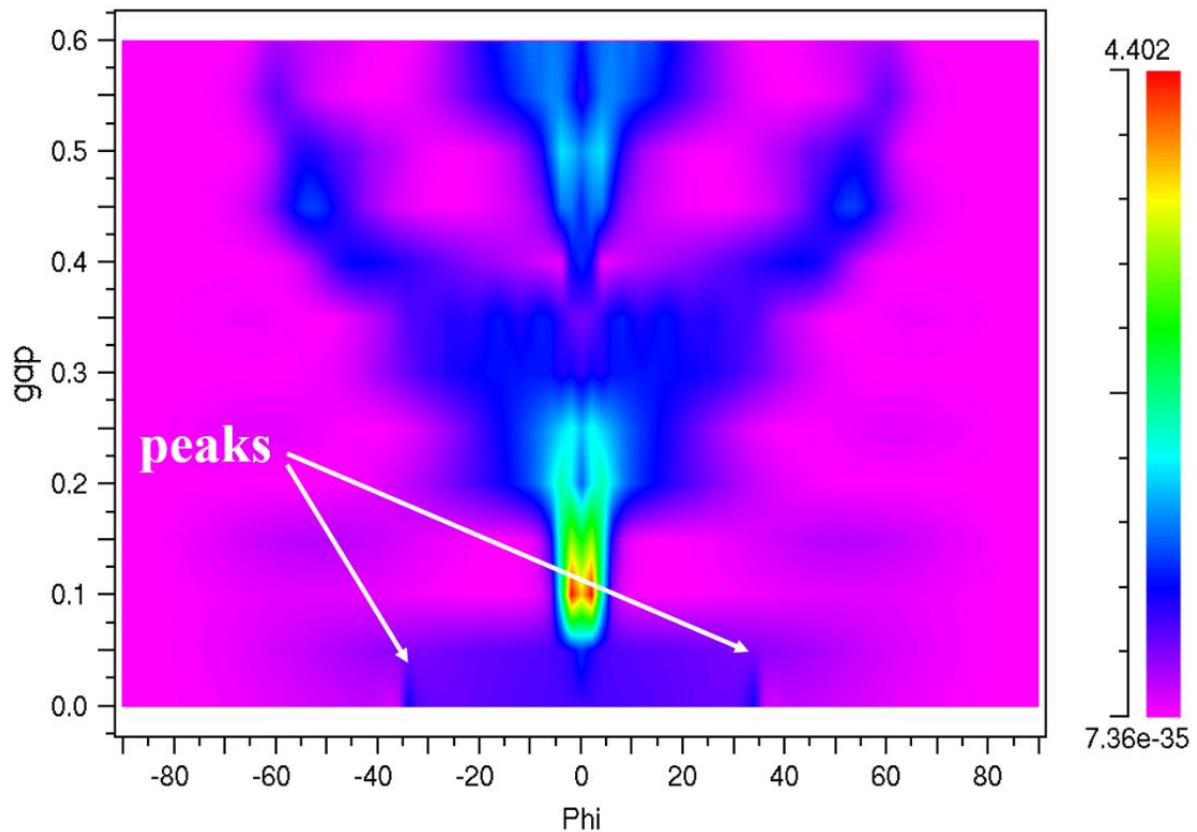


**Figure IV-3:** Farfield patterns obtained for different gap sizes ranging from 0 to 0.6 $\mu\text{m}$ . Phi is the acceptance angle in the 2D framework.

**Figure IV-4** presents the light extraction efficiency (LEE) convergence as a function of the domain size (in number of periods) for different gap sizes ranging from 0 to 0.6 $\mu\text{m}$ .

We can clearly observe that the gap influences the coupling length ( $L_{\text{coupling}}$ ) and LEE. As for the farfield-pattern study, we can spot two different regimes:

- Near-field coupling regime: for lower gap sizes (in the range of 0 to 50nm), LEE is close to 100% and the coupling length is around 40 periods. The simultaneous interaction of the guided mode with both the grating and the reflector enhances light extraction. We can however note that we considered a lossless back reflector. In the case of a real-life mirror, guided-modes' evanescent tails could slightly penetrate the metal and absorption could become so strong that only a small amount of the guided light is extracted, which could be very detrimental for the overall performances of the devices [2].
- For higher gap sizes, we have the same periodicity of  $\lambda/2$  as before. LEE varies between 75% and 100%, which can also be attributed to destructive/constructive interference processes.

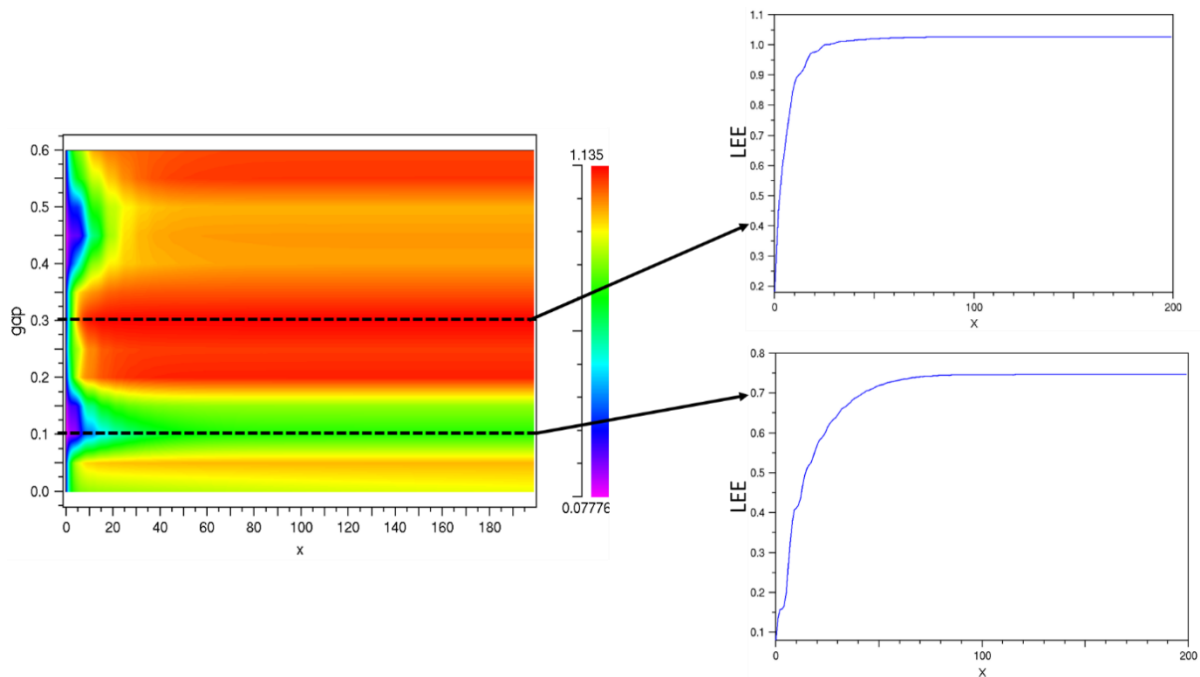


**Figure IV-4:** LEE convergence as a function of the domain size (in number of periods) for different gap sizes ranging from 0 to  $0.6\mu\text{m}$ .

It thus appears that two interaction regimes have been identified. On the one hand, there is the near-field regime (low gap sizes), where a strong interaction between the evanescent tail of the guided mode and the bottom reflector occurs. This regime can be very detrimental for the LEE of the CCL in the case of real back-reflectors, which includes absorption losses. On the other hand, for higher gap values, this strong interaction does not occur anymore and light extraction is mainly ruled by interference processes. In our case of interest (MQW CCL transferred on blue  $\mu$ -LED arrays), the gap embeds bonding layers and thick blue  $\mu$ -LEDs<sup>4</sup> (see **Figure IV-1**), so that the bottom reflector is sufficiently away from the MQW CCL for the near-field regime not to occur. This can consequently enable us to enhance simultaneously both LEE and the directivity of the emission with a judicious design of the gap, mainly

<sup>4</sup> The typical thickness of blue  $\mu$ -LEDs is within the order of magnitude of the micron [3].

ruled by interference processes. We can note that the coupling length is also modified by the bottom reflector.

#### IV.2.1.b Red color converters with vertical and lateral mirrors: Bloch-mode replication

We have previously evaluated the impact of the implementation of a back mirror in the device and we saw that LEE, extraction length and directionality could be significantly altered. These strong emission modifications depend on the position of the mirror with respect to the dipole source planes (optical distance between the dipoles and the reflector). In this section, we study the possibility of benefiting from the lateral mirrors to virtually extend the lateral size of pixels for enhancing LEE.

To do so, we first consider the same single-mode membrane as before; albeit with a lateral extent of only four periods and with a back-reflector well positioned to reach maximum LEE, as explained in the previous subsection. Without lateral mirrors, the numerically evaluated LEE of such devices is  $\sim 45\%$  (see **Figure IV-4**), limited by the short lateral extent of the PhCs. Next, we wish to obtain the same LEE as a quasi-infinite structure by properly positioning lateral mirrors in order to recycle photons that are not extracted by the grating during a roundtrip (see **Figure IV-5-a**). Those photons will then have a “chance” to escape out of the 3D structure by interacting with the grating during the next round-trip. Considering the case of perfectly phase-matched lateral mirrors (without losses and whose induced phase-shift is compensated), this would mean that the coupling length equals the pixel lateral extent ( $L_{\text{coupling}} = L_{\text{extent}}$ ) and that the LEE can theoretically reach 100%. This quasi-3D confinement strategy is achieved through a 2D+1D optical engineering.

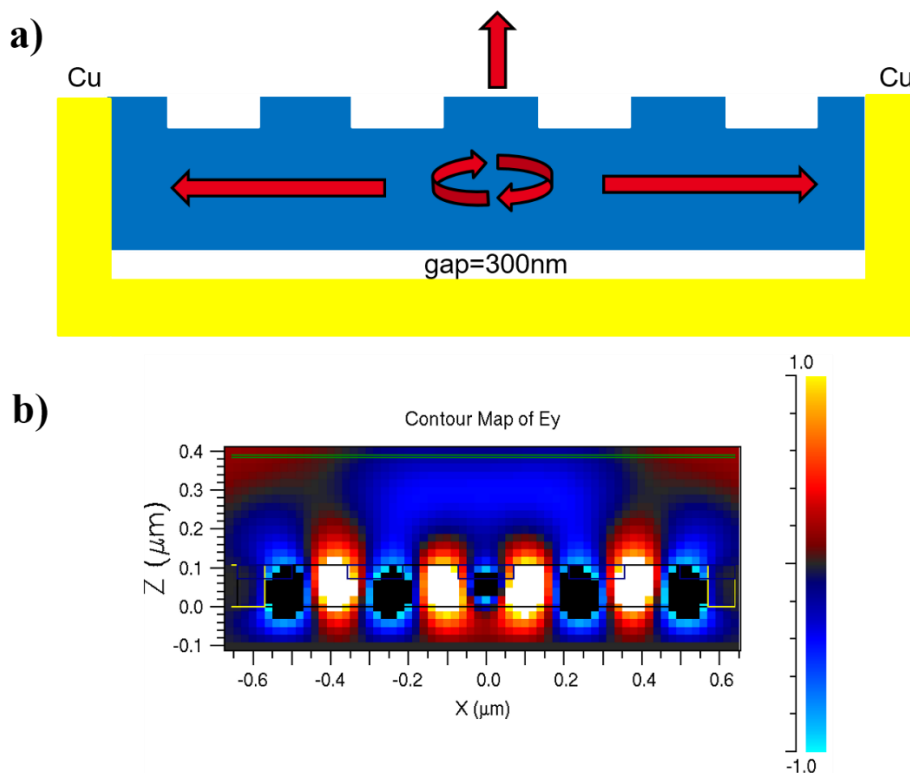


**Figure IV-5:** Schematic of the laterally and vertically confined MQW microstructure. The lateral extent of the device is four periods. The lateral Cu-mirrors are exactly located at two periods away from the center of the structure. FDTD simulation,  $E_y$  electric field profile, showing the vertical beaming process at the wavelength scale in a quasi-3D structure.

From a photonic band-structure standpoint, the aforementioned process can be seen as a “perfect” Bloch-mode replication thanks to the mirror effect. Phase and amplitude distribution should be conserved by placing the mirrors in an appropriated way, as shown in **Figure IV-5-b**.

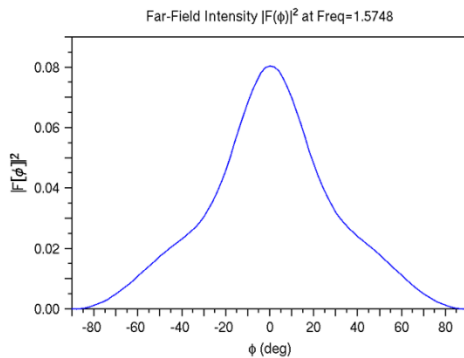
Micro-devices with and without gratings are studied in order to evaluate LEE enhancement as well as the impact of the patterning on the directivity. For the sake of completeness, we also include Cu-mirror losses so that the efficiency will be limited by the effective reflectivity of the lateral mirrors ( $<1$ ). 2D-FDTD simulation results for both configurations are presented in **Figure IV-6**:

- **Configuration without grating:** The LEE is limited 8.6% with a good directivity.
- **Configuration with a grating:** The LEE is now 63% and is enhanced more than six times compared to case without grating. The farfield analysis shows that the patterning brings a vertical beaming at the wavelength scale and almost all the light is now contained in a solid angle of  $\pm 30^\circ$ .

#### WITHOUT GRATING

- LEE~8.6%
- Directivity:+

```
Completed Combining FarField Results Incoherently
Starting PostProcessing of FarField
Applying LED spectrum ...Done
Results:
At Frequency=1.5748:
Extraction Ratio = 0.0861108
Purcell Factor = 44.909
```



#### WITH GRATING

- LEE~63%
- Directivity:++

```
Completed Combining FarField Results Incoherently
Starting PostProcessing of FarField
Applying LED spectrum ...Done
Results:
At Frequency=1.5748:
Extraction Ratio = 0.628334
Purcell Factor = 11.2103
```

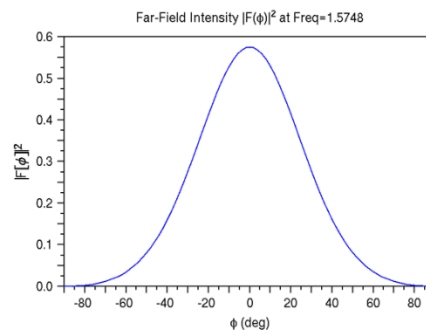


**Figure IV-6:** FDTD simulation results with and without gratings. NB: frequency is expressed in unit of  $1/\lambda$  [ $\mu\text{m}^{-1}$ ].

The LEE enhancement factors can be further improved if we take into account the phase-shift induced by the penetration depth inside the lateral Cu mirrors by shifting them  $\sim 45\text{nm}$  ( $\sim \lambda/4n_{\text{membrane}}$ ) away from their initial position. In that case, as depicted in **Figure IV-7**, LEE increases up to 80% and the farfield emission become more directive. Overall, Bloch-mode replication has thus helped increase LEE by a factor up to 2 compared to the same structure without lateral mirrors. LEE is however still limited due to the Cu-mirrors losses.

It is thus possible to benefit from lateral mirrors to virtually extend the lateral sizes of the MQW CCL using Bloch-mode replication. Within this framework, LEE could be significantly enhanced compared to structures without lateral mirrors while keeping a directional emission. We have also highlighted that

for this principle to properly work, the lateral mirrors need to have high reflectivity values and their reflection phase-shift needs to be matched.

Even if the aforementioned preliminary design rules with 2D-FDTD in the single-mode case are helpful to understand the underlying principles of this quasi-3D light-harnessing strategy, one needs to resort to full 3D-FDTD simulations to have a good insight into the behavior of “real” 3D devices. This will be conducted in the next subsection.

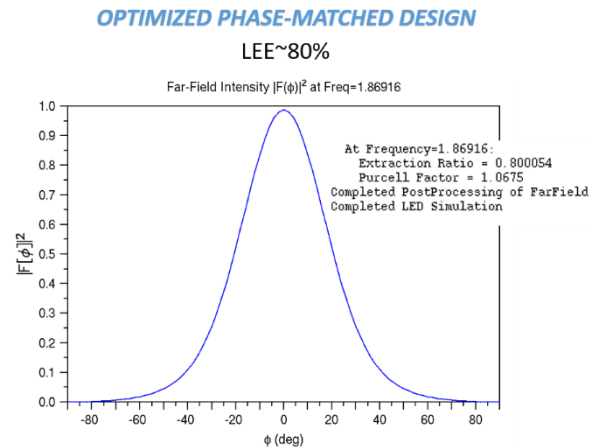


**Figure IV-7:** FDTD simulation results of the optimized configuration. Lateral mirrors are shifted  $\sim 45\text{nm}$  away from their initial position to take into account the phase-shift induced by the penetration depth inside the copper material. NB: frequency is expressed in unit of  $1/\lambda$  [ $\mu\text{m}^{-1}$ ].

#### IV.2.2 Full 3D-FDTD simulations

Now that we have better understood the roles of the back- and lateral mirrors, we wish to determine the set of opto-geometrical parameters of the “real” devices that we will fabricate as a proof-of-principle demonstration of the aforementioned quasi-3D harnessing of light. To do so, we perform additional incoherent 3D-FDTD simulations in a pulsed regime to calculate LEE and farfield patterns (see **Appendix A.1** for details on the FDTD method). The simulations are performed on the real-life MQW CCL fabricated in this PhD thesis (see previous chapter). The photonic crystals (PhCs) are square lattice of nanopillars with a lattice period of  $a=400\text{nm}$ , a lateral extent of 5 periods (for computing time issue), an etch depth of  $188\text{nm}$  and an air-filling factor of 50% (for better coupling strengths as explained in the previous chapter). The input spectrum is Gaussian-shaped with a center wavelength at  $640\text{nm}$  and a FWHM of  $20\text{nm}$ . The MQW region is represented by a single source plane of 50 transverse electric (TE)-polarized dipoles in the middle of the CCL.

We use Al as a bottom reflector to mimic the electrical contact at the bottom of the blue  $\mu$ -LEDs in the final integration strategy<sup>5</sup>. As explained above, one needs lateral mirrors with high reflectivity values for the Bloch-mode replication (BMR) to be optimal. Therefore, we opted for Cu lateral mirrors instead due to their higher reflectivity values in the red spectral range. In addition, we also interleaved a SiN layer on the sidewall surface, between the MQW CCL and the Cu mirrors in order to limit internal

<sup>5</sup> Ti/Al based metallization schemes have been widely employed to form Ohmic contacts for GaN  $\mu$ -LEDs [4].

quantum efficiency (IQE) decrease for pixels with short lateral sizes [5], but also, as we will discuss the next subsection, to control the reflection phase shift.

#### IV.2.2.a Phase-matching layer

As explained before, it is of paramount importance to ensure that the reflection phase-shift induced by the penetration inside the Cu lateral mirrors is compensated. In that regard, we use the SiN passivation layer as a phase matcher (PM) to overcome this issue. For this simulation, the MQW CCL lie on a transparent substrate (to decorrelate the effect of back- and lateral-mirrors) and are surrounded by Cu lateral mirrors. To determine the optimal values of the PM thickness, we performed 3D-FDTD simulations on the devices described in **Figure IV-8** and with the above-mentioned conditions.

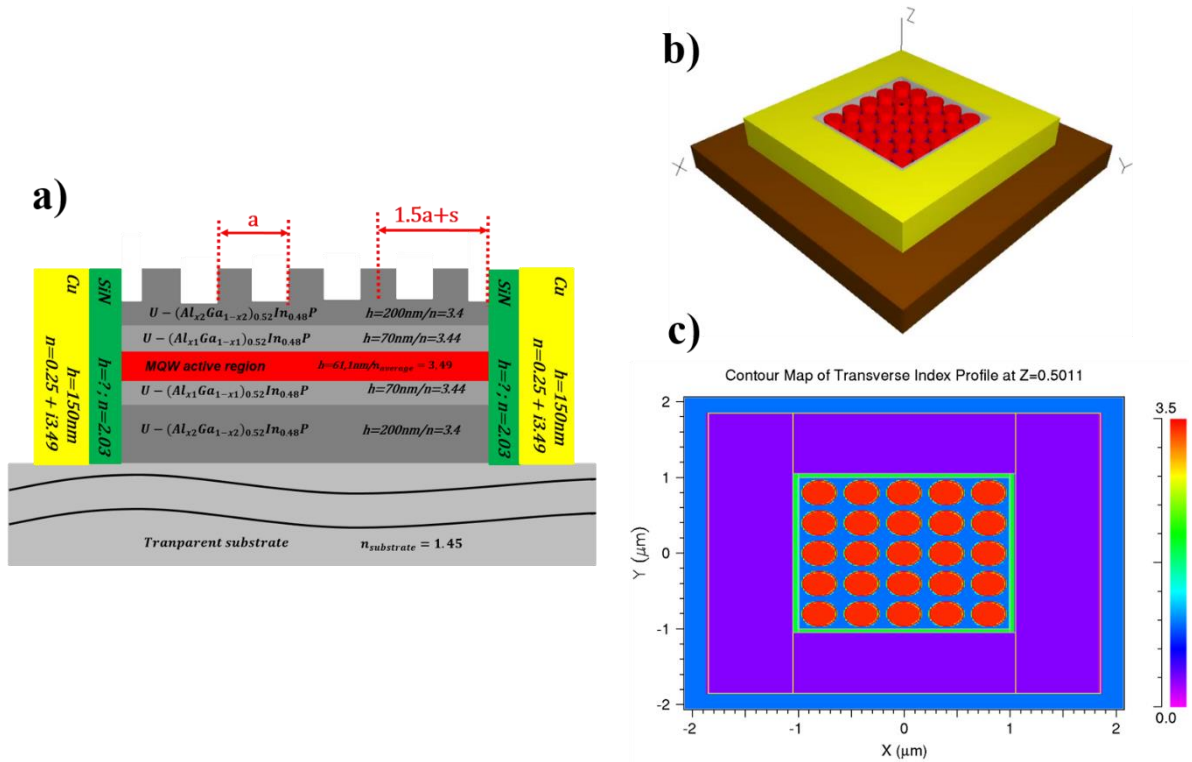


**Figure IV-8:** Full 3D-FDTD simulations to determine the phase-matching layer thickness. a) Description of the MQW color-converter on a transparent substrate surrounded by lateral Cu mirrors and SiN phase-matching layer to compensate the reflection phase-shift. b) 3D view and c) top view of the refractive index profile used in the simulation software. The parameter  $s$  represents a technological oversizing ( $s > 0$ ) or an under-sizing ( $s < 0$ ) of the mesa and  $a$  is the lattice period.

**Figure IV-9** reports on LEE on the top side of the device as a function of the optical thickness of the SiN PM. We see that in the near-field regime (low optical thicknesses) LEE has intricate variations but overall increases as the PM optical thickness increases. It then reaches a first maximum of  $\sim 24\%$  for  $n_{\text{PM}}d_{\text{PM}}/\lambda = 0.75$  where near-field effects do not seem to occur anymore and reflection phase-shift appears to be matched. It subsequently continues to oscillate due to interference processes with a  $\lambda/2$  periodicity and decreasing amplitudes.

These variations can be easily understood by considering the case of an ideal reflector. If we note  $\varphi_{\text{metal}}$  the phase-shift induced by the lateral mirror and  $\varphi_{\text{PM}}$  the additional phase stemming from the propagation in the PM, we can write that for a perfect BMR the following condition needs to be satisfied:

$$\varphi_{\text{metal}} + 2\varphi_{\text{PM}} = 2p\pi, \text{ with } p \text{ an integer and } \varphi_{\text{PM}} = 2\pi \frac{\tilde{n}_{\text{PM}} d_{\text{PM}}}{\lambda} \quad (\text{IV-1})$$

Here  $d_{\text{PM}}$  is the thickness of the PM and  $\tilde{n}_{\text{PM}}$  is a mean effective index, taking into account the multimode nature of the structure. For an ideal mirror ( $\varphi_{\text{metal}}=\pi$ ), the previous condition implies that the maxima of LEE are reached for:

$$\frac{\tilde{n}_{\text{PM}} d_{\text{PM}}}{\lambda} = 0.25 \times (2p - 1) \text{ with } p \text{ a non-zero integer} \quad (\text{IV-2})$$

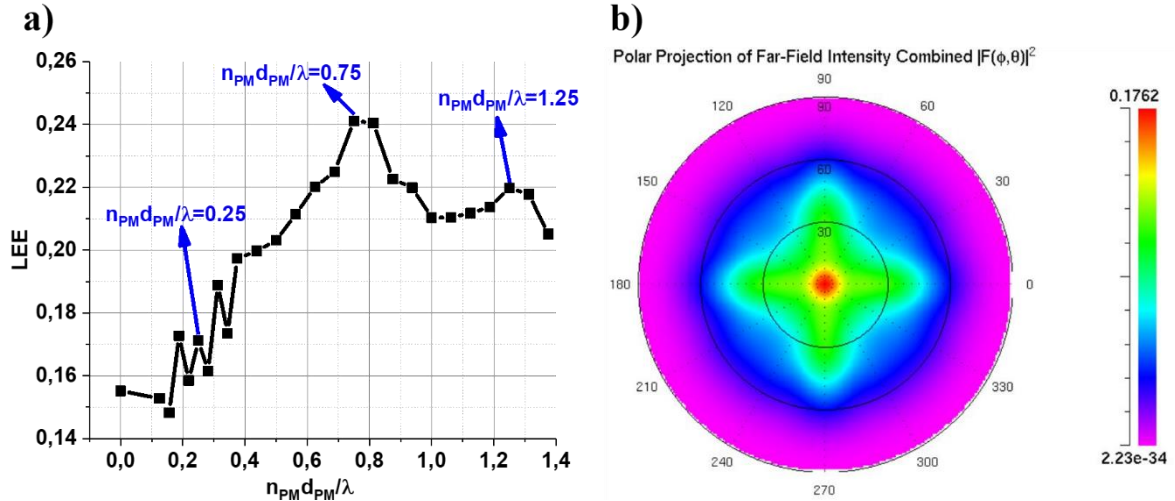


**Figure IV-9:** 3D-FDTD simulation results for determining the phase-matcher (PM) thickness. a) Light extraction efficiency as a function of the PM optical thickness. b) Azimuthal farfield radiation patterns for a PM optical thickness of 0.75.

In **Figure IV-9-a**, the first maximum at  $\sim 0.25$  is not reached due to near-field effects, however the second (0.75,  $p=2$ ) and third (1.25,  $p=3$ ) ones appear located closely to the positions predicted in the former equation. As the lateral thickness increases to very high values, the amplitudes of the maximum values decrease suggesting a reduced interaction between the guided light and the lateral mirrors. It is worth noting that due to the multimode nature of the MQW CCL (many different effective indices) the phase-condition in **Eq. (IV-1)** is not ideal, which is why the oscillations after the near-field regime are not clear-cut.

Either way, the optimal value for the optical thickness of the PM (in the case of Cu lateral mirrors) is  $\sim 0.75\lambda$ , which would correspond to a SiN thickness of 240nm. This very thick layer can be technologically tricky<sup>6</sup> to deposit on the sidewall surface of the MQW CCL. Consequently, as we will see in the fabrication chapter, we only deposit a  $\sim 70\text{nm}$ -thick SiN layer ( $\sim 0.2\lambda$ ) on the sidewalls and the remaining optical thickness ( $\sim 0.55\lambda$ ) will be compensated by slightly increasing the mesa size. At this optimal condition, directional emission can also be reached as shown in the calculated azimuthal radiation patterns in **Figure IV-9-b**, where most of the emitted light is concentrated into a  $\pm 15^\circ$  cone. The maximum LEE on the top side of the structure is  $\sim 24\%$  because part of the emitted light ( $\sim 50\%$ <sup>7</sup>) is

<sup>6</sup> To obtain 240nm-thick SiN layer on the sidewall of the MQW CCL, one needs to deposit more than  $\sim 350\text{nm}$  on the top side. Because of selectivity issues between the photoresist and SiN, this could be detrimental later in the etching process for the SiN-layer removal.

<sup>7</sup> We evaluated the bottom emitted light by placing a monitor inside the transparent substrate during the FDTD simulations (see **Appendix A.1** for more details)

extracted inside the transparent substrate and another one is lost due to absorption in the lateral mirrors. An additional study of the robustness of the design (not shown here) has also been performed using 3D-FDTD simulations to evaluate the impact of a technological oversizing or under-sizing of the mesa ( $s>0$  or  $s<0$ , see **Figure IV-8**) due to a misalignment between the mesa and grating levels. It has been found that as long as  $s$  is kept under 30nm both LEE and directionality are only slightly impacted.

#### IV.2.2.b Gap between the MQW CCL and the bottom reflector

In real-life RGB microdisplays (see **Figure I-10**), the MQW CCL are bonded on blue  $\mu$ -LED arrays with intermediate oxide bonding layers in-between. For the sake of demonstration, a  $\text{SiO}_2$  gap layer is interleaved between the MQW CCL and the Al back reflector in the fabricated devices to mimic the blue  $\mu$ -LEDs and said bonding layers. The SiN thickness is set to the optimal value found in the previous subsection. We conduct 3D-FDTD simulations to determine the optical thickness of the gap to be added. The simulated structure (see **Figure IV-10-a**) is the same as the one before, albeit on an Al back reflector and with a  $\text{SiO}_2$  gap in-between. **Figure IV-10-b** displays LEE on the top side of the device as a function of the  $\text{SiO}_2$  gap optical thickness. Similarly to before, LEE increases in the near-field regime until it reaches its first maximum of  $\sim 45\%$  at  $n_{\text{gap}}d_{\text{gap}}/\lambda=0.63$ . It then continues to oscillate due to interference processes with also a  $\lambda/2$  periodicity (unity round-trip condition) and decreasing amplitudes. Since dipolar emission is omnidirectional, the oscillations after the near-field regime are not as clear-cut as they would be for a plane-wave impinging on the back reflector at normal incidence.

During the fabrication, we will thus choose a 350nm-thick  $\text{SiO}_2$  gap, which is close to the aforementioned first maximum.

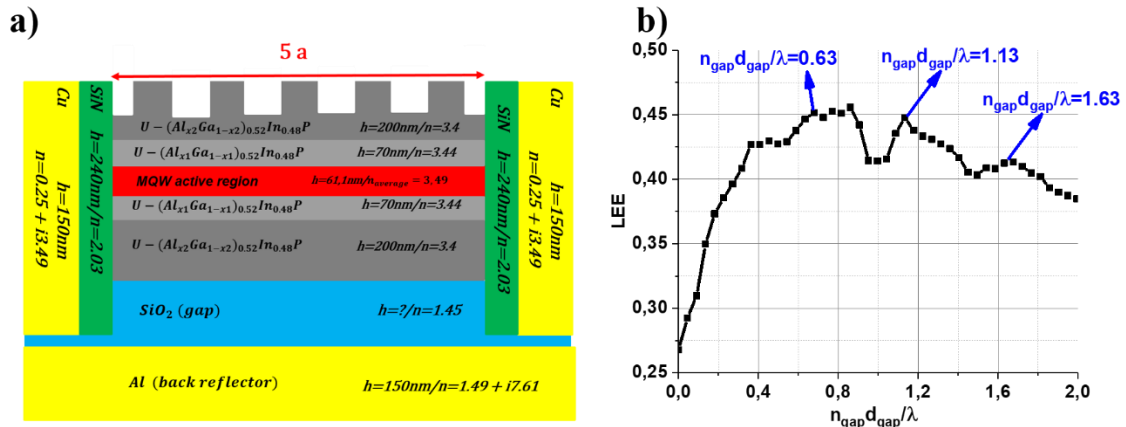


**Figure IV-10:** 3D-FDTD simulation results to determine the optimal gap ( $\text{SiO}_2$ ) thickness. a) Cross section of the final devices comprising MQW CCL surrounded by Cu lateral mirrors with a SiN phase matcher as well as Al back reflector with a  $\text{SiO}_2$  gap. b) Light extraction efficiency as a function of the gap optical thickness.

### IV.2.3 Conclusion

It appears that one could efficiently benefit from the electromagnetic environment of the MQW CCL to increase its LEE in two ways, while keeping a directional emission. FDTD simulations have first helped us show that using a 350nm-thick  $\text{SiO}_2$  gap between an Al back reflector and the MQW CCL, one could harness some of the bottom emitted light to favor top emission. Moreover, when the reflection phase-

shift induced by the penetration inside the lateral mirrors is matched, Bloch-mode replication could be a promising way to increase the LEE further. This latter requires an additional phase matching medium with an optical thickness of  $\sim 0.75\lambda$  in the case of Cu lateral mirrors, which can be performed with a simultaneous adaptation of the SiN passivation layer thickness and the lateral size of the mesa structure. In the following section, two sets of devices (LOT II and LOT III) will be fabricated on metallized silicon substrates with a 350nm-thick SiO<sub>2</sub> gap between the CCL and the bottom reflector as proof-of-concept demonstration of the two above-mentioned principles.

### **IV.3 Device fabrication**

All the devices are fabricated on metallized silicon substrates with a 350nm-thick SiO<sub>2</sub> gap between the CCL and the bottom reflector. LOT II, where MQW CCL are not pixelated, aims at demonstrating the possibility of harnessing the bottom emitted light using back reflectors. On the other hand, in LOT III MQW CCL are pixelated and their trenches are successively filled with SiN passivation layers and Cu lateral mirrors to investigate Bloch-mode replication (BMR).

The red epitaxial layers are the same as the ones from the previous chapter (see **Table III-1**) and the fabrication was achieved in CEA-LETI's 200mm cleanroom facilities. The complete and functional integration flow described in **Figure IV-11** is a result of extensive process development on most of the technological steps, but we only highlight here the main ones.

The first step is to transfer the red epilayer onto the receiving substrates, which are 200mm Si substrates metallized with Ti bonding layers deposited by PVD and followed by CMP to enable planarization. The 350nm-thick SiO<sub>2</sub> is deposited on the layer 9 of the epitaxial structure, preceded by a 10nm-thick ALD alumina intermediate layer to favor optimal adherence. Next, a PVD-deposited 150nm-thick Al on top of the SiO<sub>2</sub> gap acts as a back reflector. A 5nm-thick PVD-Ti layer was interleaved between the SiO<sub>2</sub> and the back reflector for adherence purposes and then followed by an additional Ti bonding layer. The two surfaces are cleaned and oxygen plasma ensued to activate them. We then achieve the bonding by putting the wafers in contact at room temperature, followed by a 300°C annealing for 90 minutes to reinforce the bonding interfaces.

Scanning acoustic microscope (SAM) images of the bonded red MQW CCL before and after annealing are displayed in **Figure IV-12-a** and **Figure IV-12-b** showing that it helps reach high bonding yield (>95%).

Thereupon, the GaAs substrate and the sacrificial layers (layers 0 to 3) are removed by highly selective wet etching techniques as in the previous chapter. **Figure IV-12-c** reports on the bonded epilayer after substrate and sacrificial layer removal on 200mm metallized silicon substrate. The remaining thickness of the red MQW CCL is around 600nm.

After the bonding and substrate removal, the next steps of the process are achieved throughout a 3-etching-level lithography (see **Figure IV-11**): texturing level for photonic-crystal (PhC) fabrication, trench level for mesa definition and open level after metallization to uncover light-emitting areas.

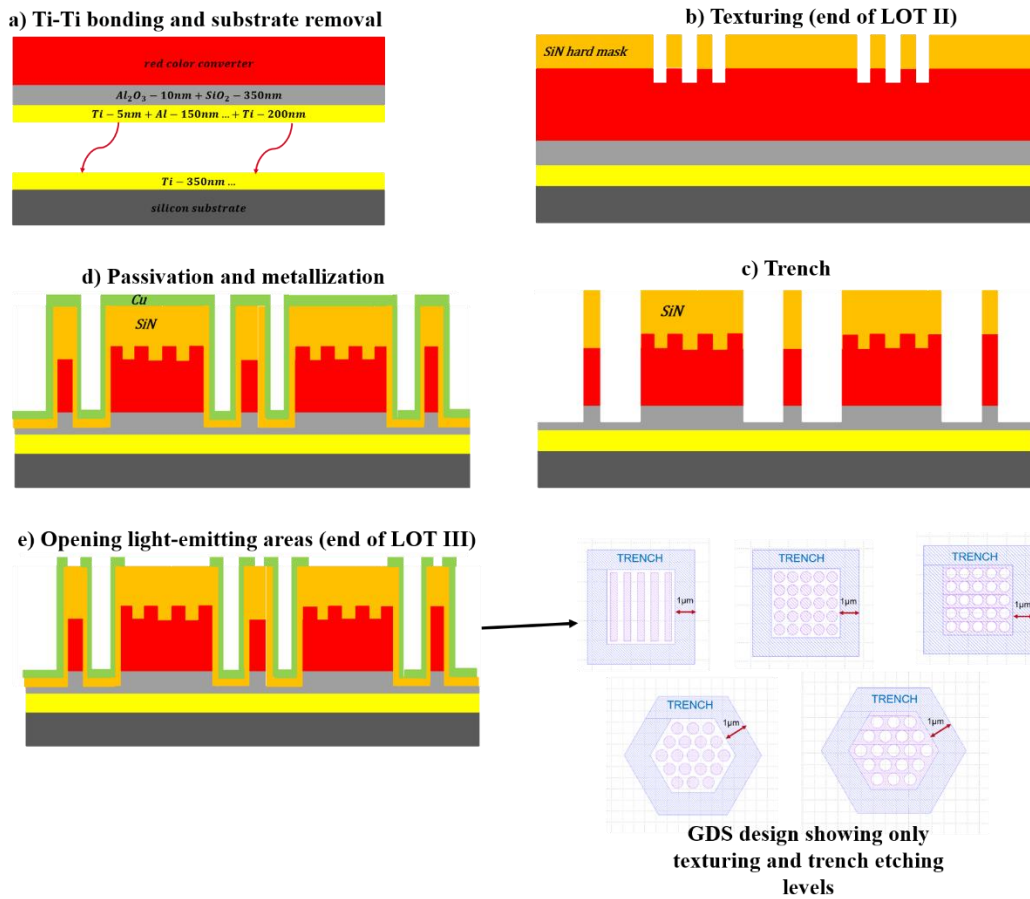


**Figure IV-11:** Complete fabrication process flow of MQW CCL on metallized silicon substrates in 3 etching levels to demonstrate the harnessing of the bottom emitted light (LOT II) and Bloch-mode replication (LOT III). LOT II ends after the texturing level and LOT III goes on to the pixelization, metallization and opening. A screenshot of the GDS design with the texturing and trench etching levels is shown in the inset.

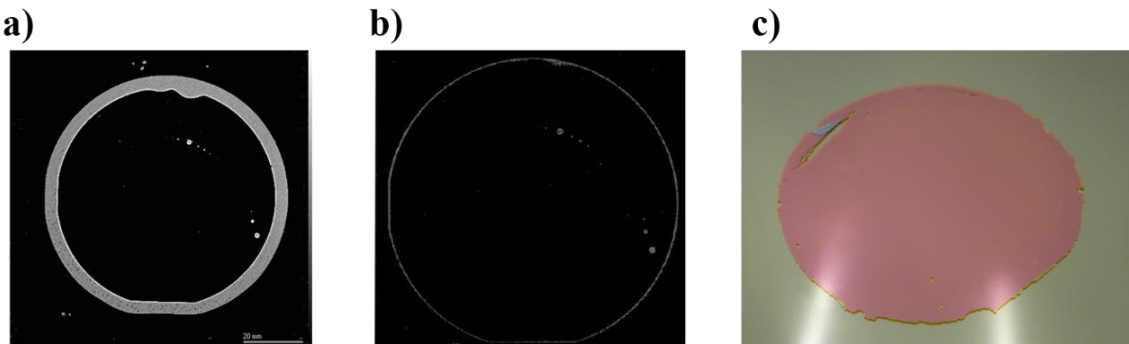


**Figure IV-12:** Scanning acoustic microscopy (SAM) image of the bonded epilayer a) after it is put in contact with the silicon substrate and b) after a 300°C annealing during 90 minutes to reinforce the bonding interface. c) Picture of the bonded epilayer (in red) after substrate removal.

The texturing level was achieved similarly to the previous chapter using e-beam lithography and a top-down pattern-transfer approach through a SiN hard mask, which is however not removed after epilayer etching. 1D lattices as well as square and hexagonal lattices of air holes and pillars (later referred to as SLAH, SLNP, TLAH and TLNP) have been fabricated with varied opto-geometrical parameters. For each one, lattice periods have been varied from 400nm to 700nm with a step of 50nm. In addition, for each lattice period, PhC structures with different lateral extents have been fabricated: 3, 5, 10, 25 and 40 periods. The etch depth and air-filling factor have been set to the optimal values found in the previous

chapter ( $\sim 180\text{nm}$  and  $\sim 50\%$ , respectively). SEM images of some of the fabricated structures are displayed in **Figure IV-13**. We can note the presence of SiN blisters<sup>8</sup>, which are some defaults resulting from the non-conformity of the low-stress PECVD-SiN on GaAs. The process flow of the devices of the LOT II, which only aim at demonstrating the possibility of harnessing the bottom emitted light, ends here. For the devices of LOT III on the other hand, which are to be used for the experimental demonstration of Bloch-mode replication (BMR), we need to go on with the process to the trench and open etching levels.

For the trench level, we opted for UV lithography followed by RIE etching, since the critical dimension (CD) of the trenches is  $1\mu\text{m}$ . The etching process is similar to the one used during PhC-pattern definition, albeit with a thicker SiN hard mask<sup>9</sup> ( $250\text{nm}$ ). In **Figure IV-14**, we display a focused ion beam (FIB) image of the 1D lattice during the etching process for the trench level right after the hard-mask opening.

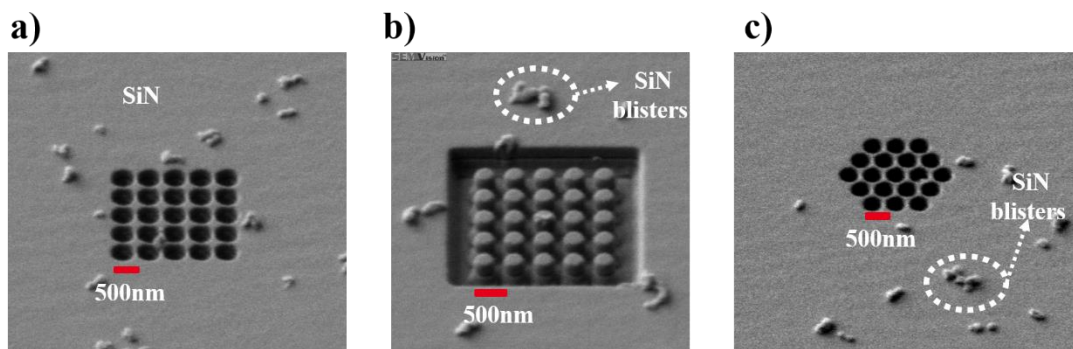


**Figure IV-13:** Scanning electron microscopy (SEM) images of some of the fabricated devices after texturing (end of LOT II). a) Square lattice of air holes and b) nanopillars. c) Triangular lattice of air holes with a lattice period of  $a=500\text{nm}$  and a lateral extent of 5 periods. Due to a non-conformity of the PECVD-SiN on GaAs, we notice the presence of SiN blisters mostly outside the emitting regions.

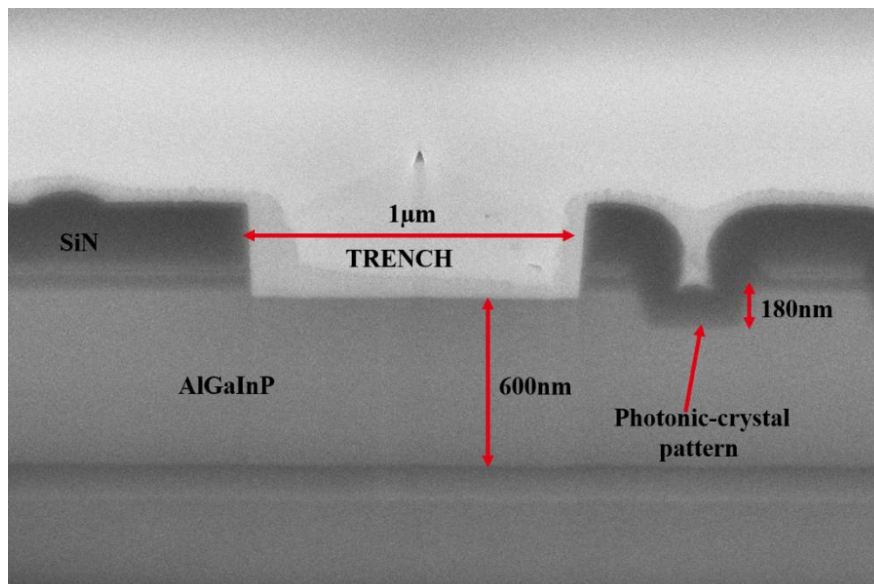


**Figure IV-14:** Focused ion beam (FIB) image of the 1D lattice after hard-mask etching for the trench level. The trench sidewalls are almost vertical while the ones of the photonic-crystal patterns are a bit tapered.

<sup>8</sup> In the previous chapter, these blisters were not visible because the SiN hard mask was removed after III-V etching.

<sup>9</sup> The AlGaInP:SiN etching selectivity is around 3:1 within our technological conditions.

As we can see the trench's sidewalls (at least in the hard mask) appear almost vertical, whereas the ones of the PhCs are slightly tapered. Subsequently, the structure is etched all the way through the remaining 600nm-thick red epilayer with a stop inside the  $\text{SiO}_2$ , which has been confirmed by additional energy dispersive X-ray (EDX) analyses (not shown here). SEM images of some of the devices of LOT III after the trench etching levels are shown in **Figure IV-15**. It is worth pointing out that during the UV lithography, the overlay measurements showed that the misalignment between the texturing and trench levels was kept under 10nm, which is of paramount interest for phase matching during BMR as pointed out in the previous section. In addition, the trench symmetry follows the ones of the PhC lattice to ensure efficient Bloch-mode replication (hexagonal trenches for hexagonal lattices and square ones for square lattices).

Afterwards, the trenches were filled<sup>10</sup> by a 100nm-thick PECVD-SiN passivation and phase-matching layer as well as 150nm-thick PVD Cu lateral mirrors, preceded by 5nm-thick PVD-Ti for adherence purposes. Following this metallization, we opened light-emitting areas using UV lithography followed by ion-beam etching (IBE) for removing the Cu layer on top of the device<sup>11</sup>.

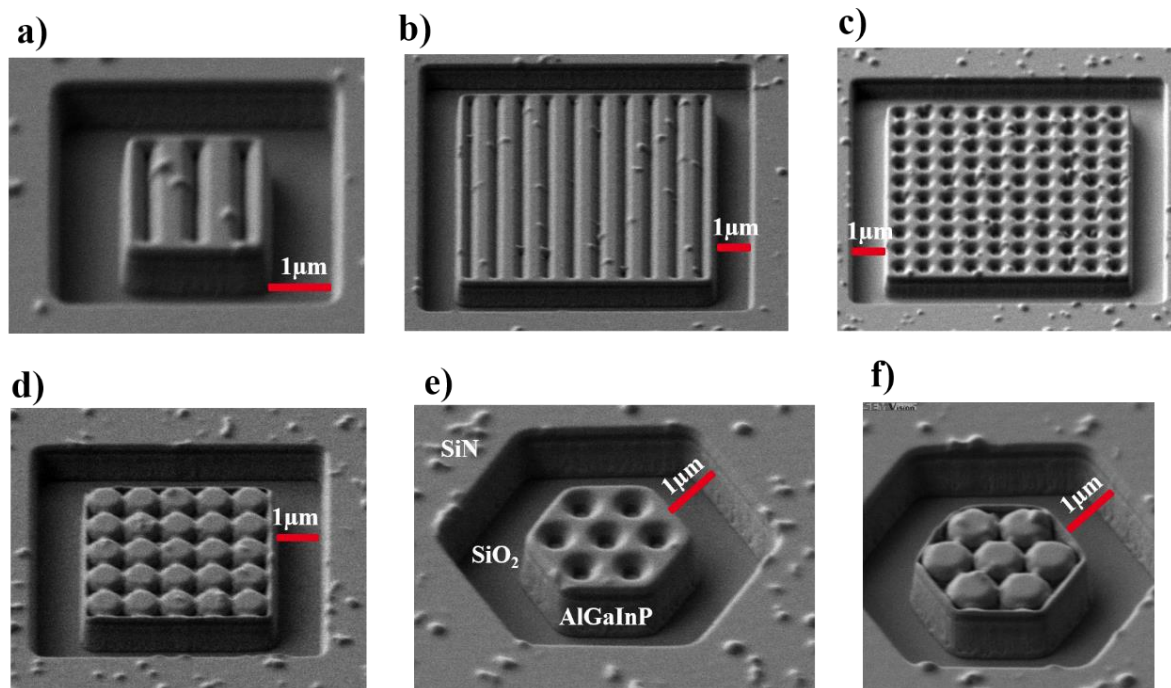


**Figure IV-15:** Scanning electron microscopy (SEM) images of some of the fabricated devices after the trench etching level. a-b) 1D lattices with lateral extents of 3 and 10 periods, respectively. Square lattices of c) air holes and d) nanopillars. Hexagonal lattices of e) air holes and f) nanopillars.

**Figure IV-16** shows SEM-EDX analyses performed on 1D lattices before and after metal etching, confirming that Cu has been completely etched on top of the light-emitting areas. The photoresist was then stripped, which concludes the process flow for the devices of LOT III.

<sup>10</sup> Following the trials made in our lab, around 70% of the thickness deposited on top of the device will be found on the sidewalls.

<sup>11</sup> Another possible integration could have been to use CMP at this stage, but we did not pursue this route due to issues related to the availability of the equipment in CEA-LETI cleanroom facilities.

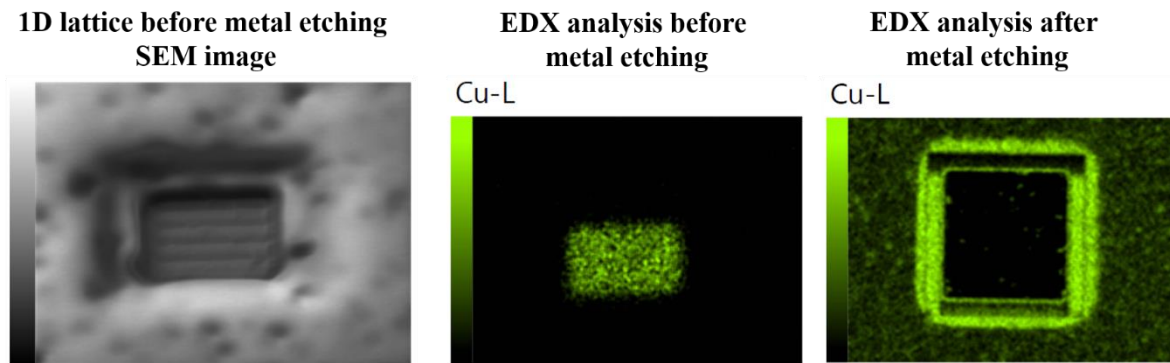


**Figure IV-16:** SEM-EDX analysis of 1D lattices before and after metal etching focusing on the presence of copper.

We eventually performed additional scanning transmission electron microscopy (STEM) analysis on some of the final devices of LOT III to better visualize all the layers deposited during fabrication, particularly the SiN phase-matching layer and the lateral mirrors. **Figure IV-17** reports on high-resolution high-angle annular dark-field (HAADF) STEM images of a square lattice of air holes with  $a=700\text{nm}$  and a lateral extent of 3 periods, along with images with a zoom on the trenches. In addition, we conducted STEM-EDX analysis (see **Figure IV-18**) to have a better insight on all the atoms and layers present in our final devices. The SiN phase-matching layer and Ti-Cu lateral mirrors, as well as the atoms composing the epitaxial structure (Al, Ga, As, In, P) have been well identified with thicknesses matching those we expected during fabrication.

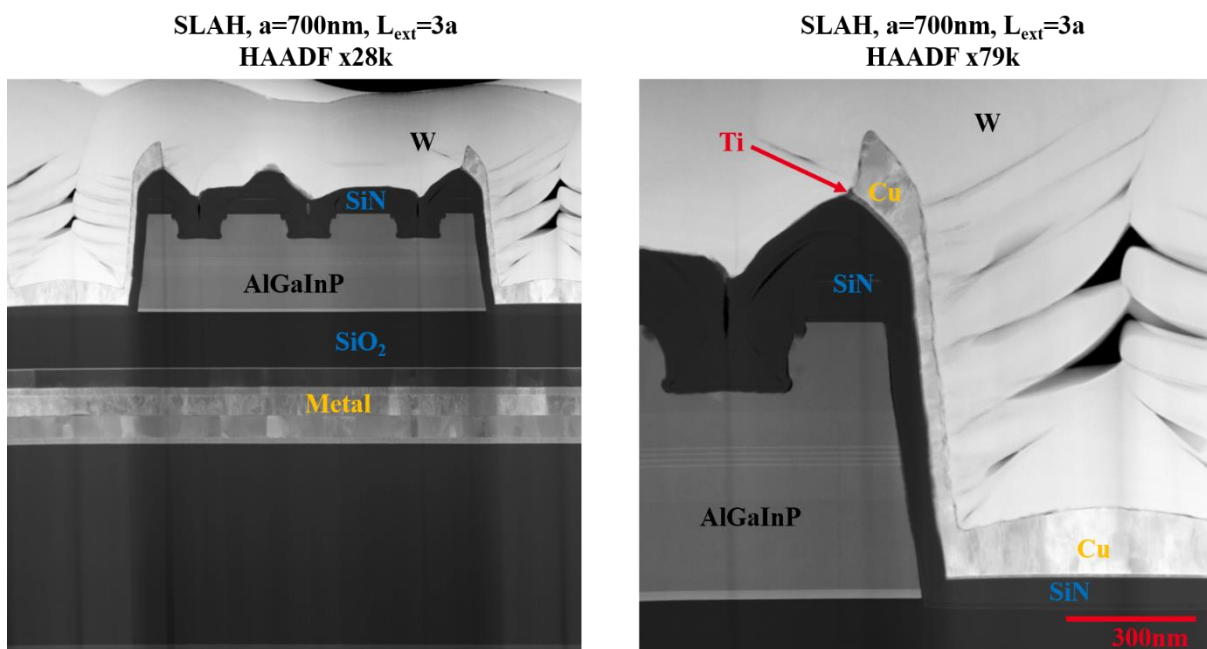


**Figure IV-17:** HAADF-STEM images of the square lattice of air holes with  $a=700\text{nm}$  and  $L_{\text{ext}}=3a$ .

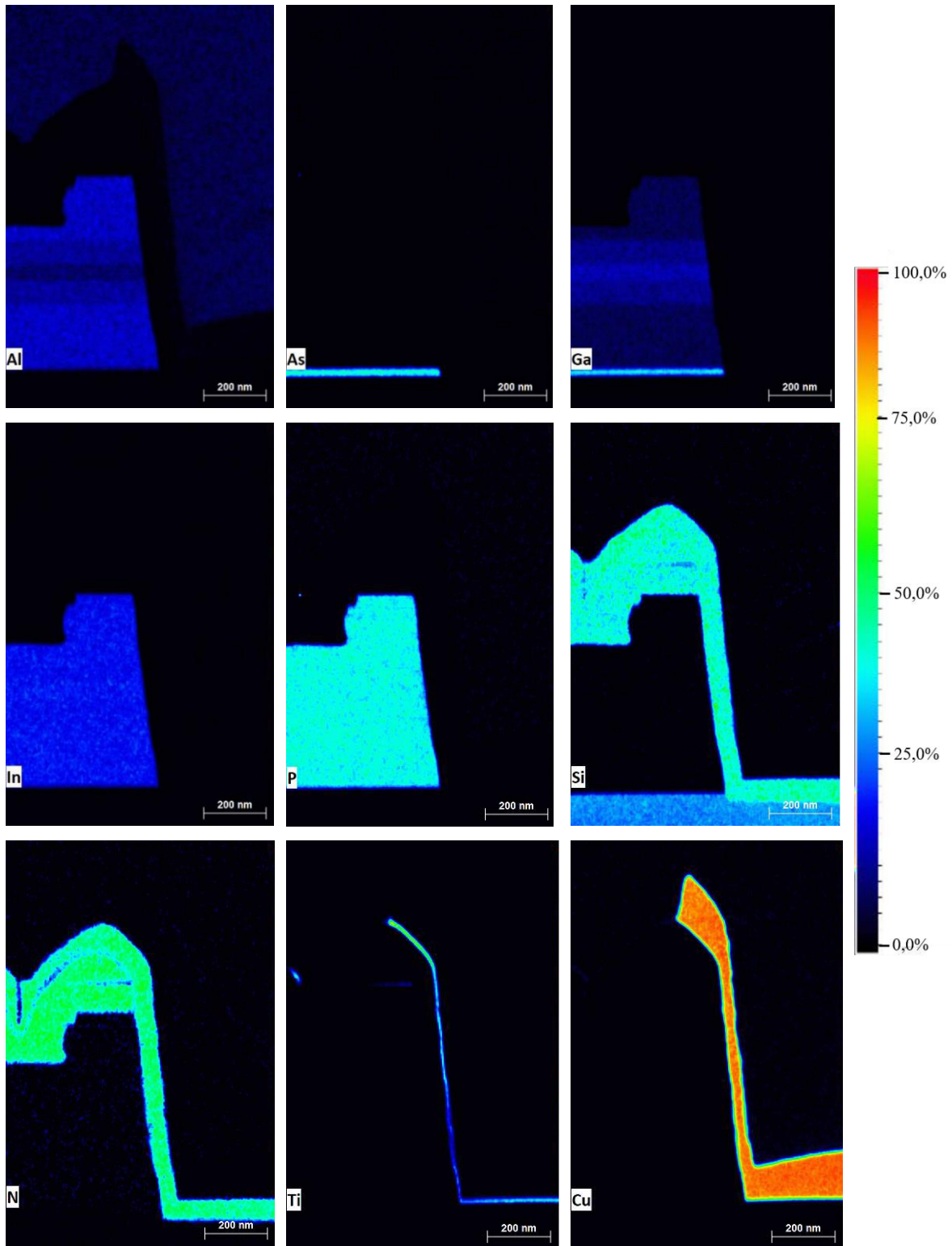


Figure IV-18: STEM-EDX analyses of the trenches along with a quantification in terms of atomic percentage.

#### IV.4 Harnessing the bottom emitted light using back reflectors: LOT II

In this section, we wish to perform an experimental investigation of the possibility to harness the bottom emitted light using Al back reflectors. The devices are those of LOT II (unpixelated but patterned MQW CCL on metallized silicon substrates, see **Figure IV-11**). We first analyze LEE enhancement, extraction

lengths and directionality, before having a closer look into 1D lattices. Next, we conduct an evaluation of the experimental LEE and compare it to the targeted values provided in the first chapter of the manuscript.

#### IV.4.1 Extraction lengths, LEE enhancement and directionality

For the extraction lengths, we follow the same procedure as in the previous chapter. Micro-PL measurements are performed using a MO with NA=0.9. For each lattice symmetry, pattern and period, we evaluate PL gains with respect to the unpatterned surfaces as a function of the PhC lateral extent. In **Figure IV-19-a**, we display LEE enhancement factors as a function of the lateral extent for SLNP with a lattice period of 400nm. As expected, the amount of extracted light increases with increasing lateral extents until it saturates at  $\sim 4$ . Similar measurements were also achieved for other devices and the extraction lengths are obtained using the same model derived from coupled-mode theory as in the previous chapter.

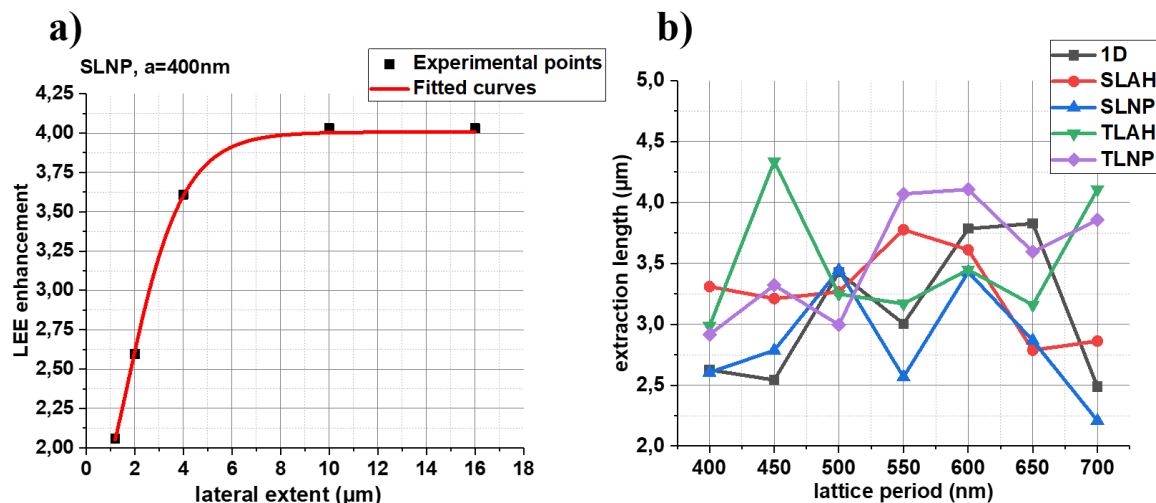


**Figure IV-19:** a) LEE enhancement as a function of the lateral extent for SLNP with  $a=400\text{nm}$ . b) Experimental extraction lengths as a function of the lattice period for 1D lattice, SLAH, SLNP, TLAH and TLNP with FF $\sim 50\%$  and an etch depth of about 180nm.

**Figure IV-19-b** shows the extraction lengths for all the fabricated structures as a function of the lattice period. As explained in the previous chapter, we observe a strong lattice-period-dependency. However, since all the air filling factors (FFs) are kept around 50%, the obtained extraction lengths are very short and range between  $\sim 2\mu\text{m}$  and  $\sim 4\mu\text{m}$ . Thus, increasing the lattice symmetry does not seem to bring any significant advantage in terms of coupling strengths, nor does changing the pattern type as long as the FFs are maintained around 50%. This confirmed the conclusions drawn in the previous chapter, highlighting the fact that the FFs and etch depths are the main optimizing levers for the grating strength at a fixed lattice period.

Since the extraction lengths are between  $\sim 2\mu\text{m}$  and  $\sim 4\mu\text{m}$ , the devices with a lateral extent of 40 periods, whose LEE enhancement factors are provided in **Figure IV-20** as a function of the lattice period, can be considered quasi-infinite.

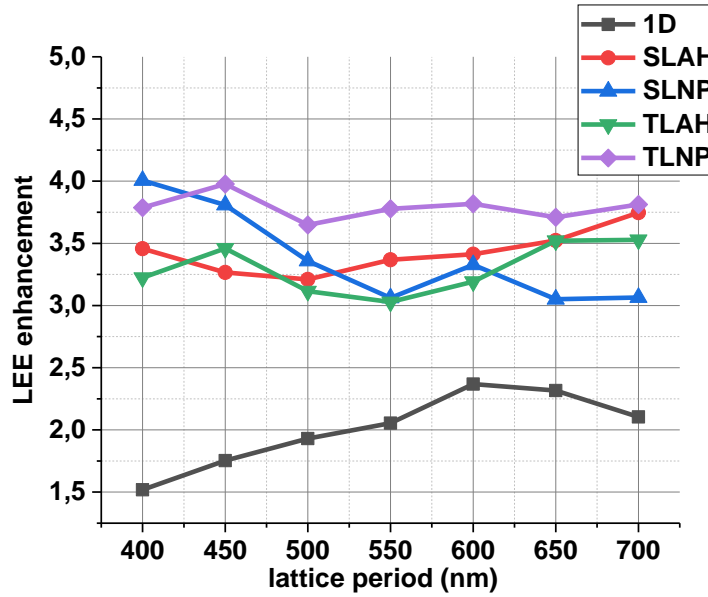


**Figure IV-20:** Light extraction efficiency enhancement as a function of the lattice periods for 1D lattice, SLAH, SLNP, TLAH and TLNP with a lateral extent of 40 periods.

LEE enhancement is found to depend only weakly on the lattice period. For 1D lattices, there is a slight increase of LEE enhancement factors from  $\sim 1.5$  for  $a=400\text{nm}$  to  $\sim 2.25$  at  $a=600\text{nm}$  and  $\sim 2$  at  $a=700\text{nm}$ . For other lattices, we observe similar variations but LEE enhancement is kept between  $\sim 3$  and  $\sim 4$ . The highest value of  $\sim 4$  is obtained for SLNP with  $a=400\text{nm}$ , which confirms that increasing the lattice symmetry order over four-fold (square lattice) does not seem to bring any advantage in terms of light extraction. In addition, the lowest values for 1D lattices could be attributed to their intrinsic inability to extract guided modes incident from all in-plane directions as already discussed in [6]. It is worthy noticing that contrary to the devices on transparent substrates, where there were high discrepancies between LEE enhancement for holes and pillars due the higher diffraction towards the substrates for holes, the obtained values with a back reflector are quite close. This validates an efficient harnessing of the bottom emitted light by the Al back reflector and the interleaved  $\text{SiO}_2$  gap.

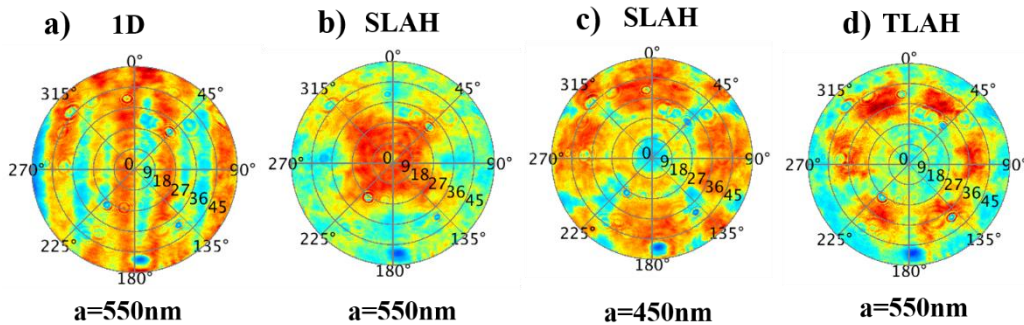


**Figure IV-21:** Measured normalized azimuthal farfield patterns for some of the fabricated devices of LOT II with a lateral extent of 40 periods a) 1D, b) SLAH and d) TLAH with a lattice period of 550nm and a lateral extent of 40 periods. c) SLAH with a lattice period of 550nm.

We now wish to examine whether this harnessing of the bottom emitted light is achieved while keeping a directional emission. To do so, we use the BFP imaging setup described in **Section III.3.2** of the previous chapter to measure the azimuthal farfield patterns of all the fabricated devices with a lateral

extent of 40 periods and lattice periods between 400nm and 550nm. Some of them are shown in **Figure IV-21** and normalized with their maximum values. We can observe two-, four- and six-fold symmetries, which are inherent to the symmetry orders of 1D, square and hexagonal lattices.

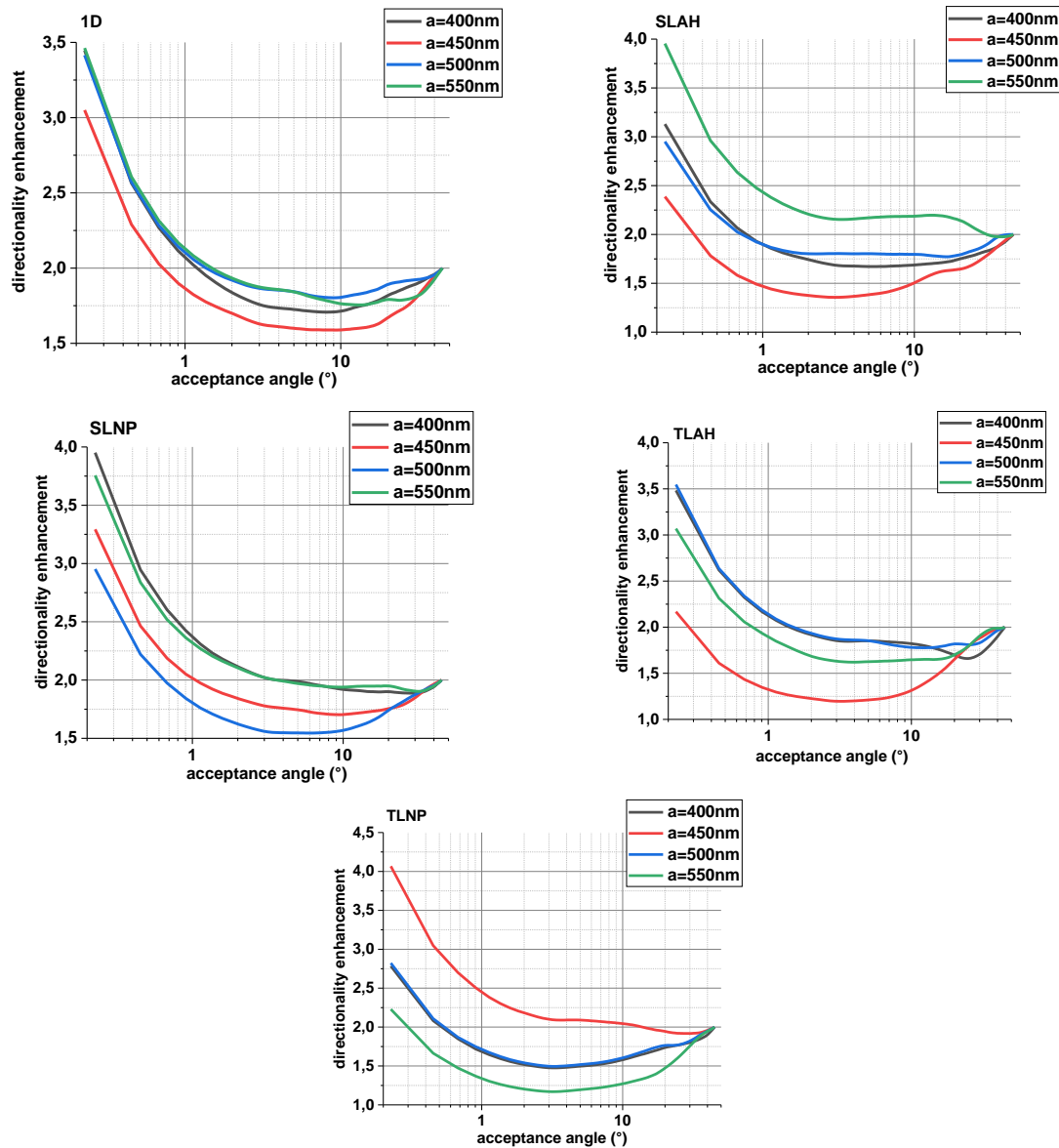


**Figure IV-22:** Directionality enhancement for 1D lattices, SLAH, SLNP, TLAH and TLNP as a function of the acceptance angle and the lattice period.

From those farfield patterns, we evaluated directionality enhancement factors with respect to Lambertian emission (see previous chapter) to quantify the emission directionality and compared it to what we obtained on transparent substrates. The results are provided in **Figure IV-22** on a semi-log scale. As expected from the azimuthal farfield patterns, directionality enhancement depends on both the pattern type and the lattice period. The highest values are obtained for SLAH with a=550nm, SLNP with a=400nm and TLNP with a=450nm. With those structures, directionality enhancement reaches values of  $\sim 4$  close to normal incidence and  $\sim 1.8$  at  $30^\circ$ . 1D gratings on the other hand exhibit lower directionality enhancement values than higher-order lattices. Let us note that on transparent substrate and for the same opto-geometrical parameters, SLAH with a=450nm had the highest directionality

values which is now the other way round. Indeed, due to the presence of the back reflector, light diffracted downwards is now reflected back upwards and redistributed, which induces a change in the emission shape. Besides, now that all the FFs are kept around 50%, the coupling strengths do not differ much between holes and pillars as seen in **Figure IV-19-b**. Since the directionality losses observed for pillars compared to holes stemmed from the broadening of the diffracted bands in the  $k_{//}$ -space of the associated guided Bloch-modes, those discrepancies are now mitigated. This explains why highest values of directionality enhancement are also achieved with pillars. Thus, similarly to light extraction, increasing the lattice symmetry order over four or even changing the patterns does not seem to bring any improvement in terms of directionality.

Therefore, it appears that by harnessing the bottom emitted light using Al back-reflector coupled with a  $\text{SiO}_2$  gap, one could achieve high LEE enhancement factors, paired with ultra-short extraction lengths and directional emission. The best performing devices are SLNP with  $a=400\text{nm}$  exhibiting LEE  $\sim 4$  times higher than those of unpatterned references, along with an ultra-short extraction length of  $\sim 2.5\mu\text{m}$  and a directionality  $\sim 4$  and  $\sim 1.8$  times better than lambertian emission, close to normal incidence and at  $\sim 30^\circ$ , respectively. Due to their lack of in-plane omnidirectionality, 1D lattices were found to have the lowest LEE and directionality enhancement factors. However, they could be of key interest for certain applications, as we will briefly investigated in the next subsection.

#### IV.4.2 Towards polarized light emission with 1D lattices

In display applications such as LCD, which operate through spatial modulation of polarized light,  $\mu$ -LEDs emitting polarized light are of paramount interest [7]. However, conventional incoherent light sources are usually unpolarized because the electric fields do not have a preferred orientation. Using PhC light extractors help enhance LEE as demonstrated above, but 1D lattices have the particularity of better extracting electric fields aligned with their grating patterns [8], which could increase the polarization ratios of the emitted light from our MQW CCL. The polarization ratio is defined as the ratio between the difference and sum of the intensities emitted perpendicular ( $\perp$ ) and parallel ( $//$ ) to the grating lines and expresses as (**Figure IV-23**):

$$\rho = \frac{I_{//} - I_{\perp}}{I_{//} + I_{\perp}} \quad (\text{IV.3})$$

To evaluate the polarization-ratio difference between 1D and other lattices, we use the micro-PL setup described in the previous chapter and inserted a rotating polarizer before the CCD camera to acquire the parallel and perpendicular intensities for each devices. We did the measurements for all lattices with  $a=400\text{nm}$  and a lateral extent of 40 periods and then evaluated the polarization ratios. Similar

measurements were also performed for unpatterned surfaces for the sake of comparison. A bar plot of the obtained polarization ratios is displayed in **Figure IV-23**.

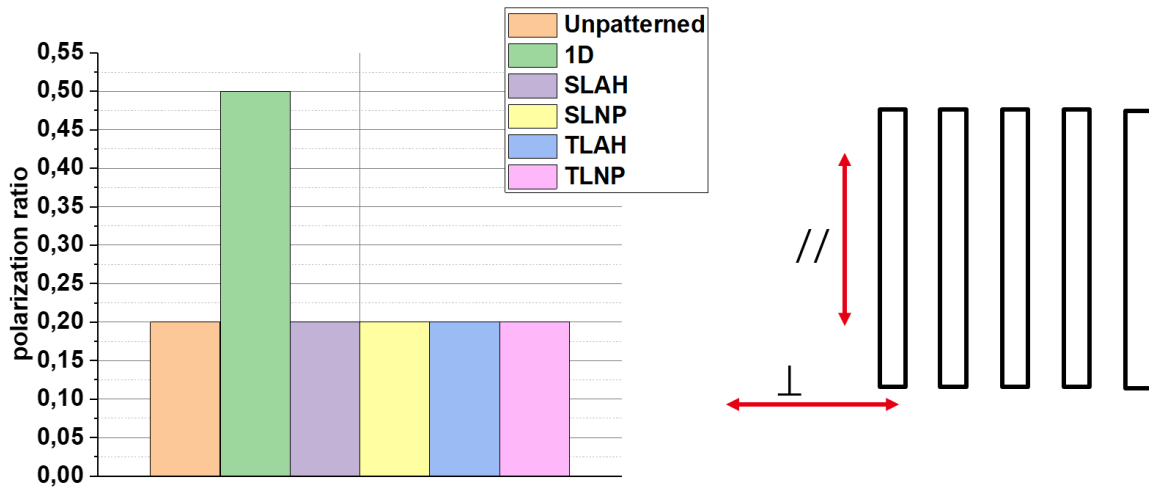


**Figure IV-23:** Measured polarization ratios of the fabricated devices with all the different lattices, lattice periods of  $a=400\text{nm}$  and lateral extent of 40 periods. The conventions for the orientation for the electric field are described in the inset.

Unpatterned structures have a certain degree of polarization, which is here found to be  $\sim 20\%$ , as evidenced by the spectrally resolved farfield patterns measured in the previous chapter. We observe that this 20% polarization ratio value is unchanged for structures with 2D lattices (square or hexagonal lattice, no matter which pattern type). For 1D lattices on the other hand, the polarization ratio increases from 20% to 50%, which corresponds to a 2.5 gain, due to their preferential light extraction along the direction parallel to their grating lines. This highlights the promising interest of 1D lattices for polarized light emission from MQW CCL.

#### IV.4.3 Experimental evaluation of light extraction efficiency

Before concluding **Section IV.4**, we wish to evaluate experimental values of LEE for the best performing devices so far (SLNP with  $a=400\text{nm}$ ) and see where we are at as compared to the initially targeted values for AR microdisplays. To do so, we use the LEE of the unpatterned structures and the LEE enhancement factors in **Figure IV-19-a**. Let us recall that LEE of MQW CCL on transparent substrates without PhCs was evaluated to  $\sim 3\%$  in the previous chapters. Comparing the PL spectra of unpatterned MQW CCL on transparent and metallized-silicon substrates (see **Figure IV-24-a**), we find that the use of back-reflector with a  $\text{SiO}_2$  gap helps enhance LEE  $\sim 4$  times without PhC. This means that LEE of the reference unpatterned MQW CCL on metallized-Si substrates is around 12%. By multiplying this reference value with the LEE enhancement factors obtained in **Figure IV-19-a**, we evaluated experimental values of the LEE of SLNP with  $a=400\text{nm}$  as a function of the lateral extent. It is worth reminding that these values are naturally underestimation of the real values of LEE, since IQE decrease due to PhC is embedded within, as explained in the previous chapter, but they still could give us a good insight into the performances reached.

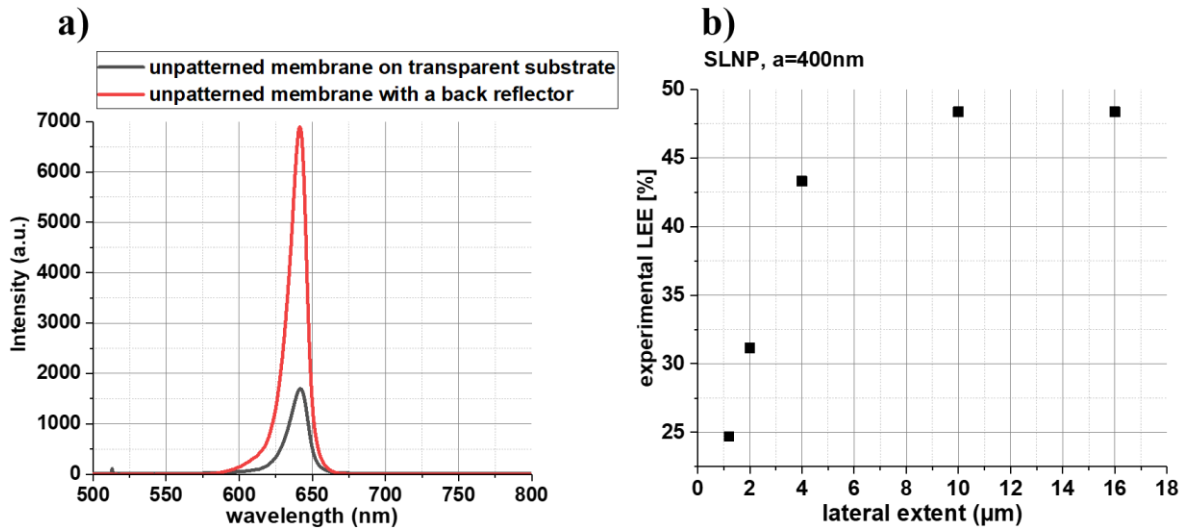


**Figure IV-24:** a) PL spectra of unpatterned CCL on transparent and metallized-silicon substrates with  $NA=0.9$ . b) Experimental LEE evaluated from the LEE enhancement factors above for SLNP with  $a=400\text{nm}$ .

We can observe that the initially targeted LEE values to reach the high luminances required for AR microdisplays (between 40 and 50%) are achieved as long as the pixel lateral sizes are kept over  $4\mu\text{m}$  (for the sake of simplicity, we do not consider IQE decrease in this evaluation). In the devices with very short lateral sizes, there can be two light loss factors. The first ones are the absorption losses due to the Al back reflector, whose reflectance values have been measured to be around 65% (see **Appendix C.1**) and could potentially be further improved with more suitable deposition conditions. Besides, the short lateral extents of those devices are not enough to extract the remaining part of the guided light, which is the second source of light loss. This latter one could be alleviated by virtually extending the lateral size of those pixels and allowing the photons multiple round-trips inside the cavity using Bloch-mode replication (BMR), as explained in **Section IV.2**.

This latter concept will be investigated experimentally in **Section IV.5** using the devices of LOT III.

#### IV.4.4 Conclusion

The potential of harnessing the bottom emitted light using back reflectors has been experimentally demonstrated with the devices of LOT II. In this framework, LEE has become only weakly dependent on the lattice period and pattern type. As long as the lattice symmetry order is kept over four, LEE close to 50% can be reached for pixel sizes over  $4\mu\text{m}$ , which fulfilled the requirements of AR microdisplay applications. Although the low in-plane omnidirectionality of their light extraction processes resulted into low LEE and directionality, 1D lattices could be promising candidates in applications where  $\mu$ -LEDs with polarized light emission are required.

We have also emphasized that the targeted LEE values are not reached anymore when pixel sizes become very short ( $<4\mu\text{m}$ ), which could be alleviated by implementing the BMR principle and will be investigated in the next section.

## IV.5 Enhancing light extraction efficiency using Bloch-mode replication: LOT III

In this section, we deal with an experimental demonstration of the potential interest of Bloch-mode replication (BMR) to overcome the light extraction limit of pixels with very short lateral sizes. We start by a proof-of-concept demonstration of this principle using micro-PL experiments on the devices of LOT III, before taking a closer look into the lateral-mirror losses. We then conclude on this strategy.

### IV.5.1 Proof-of-principle experimental demonstration of Bloch-mode replication

Using the micro-PL setup described in the previous chapter, we evaluate LEE enhancement for the devices of LOT III. For the sake of comparison, the reference structures to evaluate LEE enhancement factors are the unpatterned and unpixelated devices. The results are shown in **Figure IV-25** for some of the most performing devices in terms of LEE (SLNP with  $a=400\text{nm}$  and  $a=700\text{nm}$ ). LEE enhancement values for the unpixelated devices of LOT II are also added to observe the LEE improvement due to BMR.

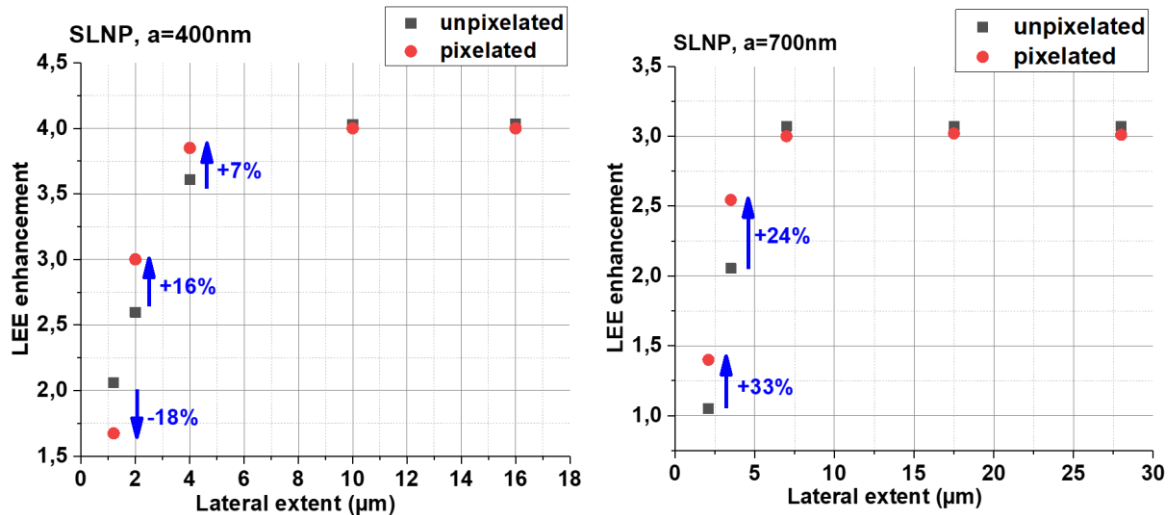


**Figure IV-25:** LEE enhancement as a function of the lateral extent for SLNP with  $a=400\text{nm}$  and  $a=700\text{nm}$ . The results for unpixelated and pixelated devices are provided for the sake of comparison.

For SLNP with  $a=700\text{nm}$ , we can see that LEE enhancement follows the same variations for pixelated devices as those of unpixelated devices, albeit with different values. For pixelated devices, LEE enhancement increases from  $\sim 1.4$  to  $\sim 2.55$  when the lateral extents go from  $2.1\mu\text{m}$  to  $3.5\mu\text{m}$ , respectively, before reaching saturation values close to those of unpixelated devices. As shown in **Figure IV-25**, those two former values are  $\sim 33\%$  and  $\sim 24\%$  better than those of unpixelated structures, respectively, which confirms the key interest of BMR in increasing LEE for pixels with short lateral sizes. These variations can be understood as follows. For pixels with short sizes (shorter than the saturation lengths), photons are not completely extracted by the grating during their first pass. Thus, they continue to propagate within the cavity and are eventually lost for unpixelated devices, whereas for pixelated ones they are reflected off by the lateral mirrors and given other chances to escape, which improves the LEE enhancement, as explained before. Subsequently, as the pixel sizes increase over the

saturation lengths, the PhC lateral extent becomes sufficient to extract photons, which is why both pixelated as well as unpixelated devices reach the same saturation values.

SLNP with  $a=400\text{nm}$  exhibit similar variations, albeit with lower values. For instance, we can notice that with BMR LEE enhancement of pixelated devices can be  $\sim 16\%$  and  $\sim 7\%$  better than those of unpixelated ones for lateral extents of  $2\mu\text{m}$  and  $4\mu\text{m}$ , respectively. Thus, the target LEE values for AR microdisplays can now be reached even for pixels with lateral sizes of  $2\mu\text{m}$ , which also confirms the key interest of the BMR principle. Nonetheless, we notice a peculiar behavior of pixels with a lateral size of  $\sim 1.2\mu\text{m}$  ( $<2\mu\text{m}$ ) where pixelization actually decreases LEE enhancement by factors up to  $\sim 18\%$ .

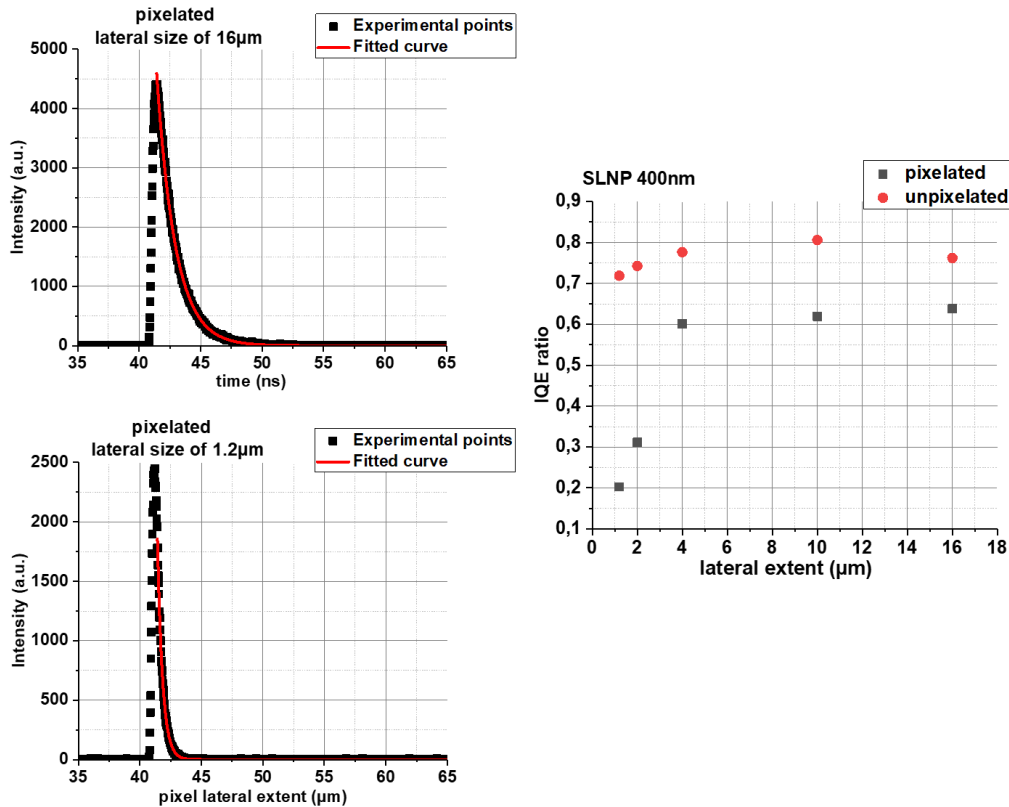


**Figure IV-26:** IQE ratio estimated by TRPL for pixelated and unpixelated patterned CCL with respect to unpatterned and unpixelated references. (Left) transient curves for pixelated structures with lateral extents of  $1.2\mu\text{m}$  and  $16\mu\text{m}$ . (Right) IQE ratio as a function of the lateral extent.

Let us recall that the experimental LEE enhancement embeds both absorption efficiency and IQE. As explained in the previous chapter, absorption efficiency does not change much in this case. Therefore, the size-dependency of the IQE needs to be further investigated. We do so by conducting TRPL measurements on the micro-PL setup presented in the previous chapter. We evaluate the total recombination lifetimes as a function of the lateral extent for unpixelated (and patterned with PhC) as well as pixelated (and patterned) devices. The total recombination lifetime of the unpatterned and unpixelated devices is used as a reference to evaluate the size-dependency of the IQE in our structure. The results are displayed in **Figure IV-26** (right plot) along with transient curves (left plot), which were best fit with a single exponential decay function. For the unpixelated devices, IQE ratios are only slightly size-dependent, with an overall decrease (for all sizes) of  $\sim 20\%$  stemming from the photonic-crystal

patterns as explained in the previous chapter. For pixelated devices on the other hand, IQE ratios rapidly decrease when pixel lateral sizes reach values under  $4\mu\text{m}$  because of non-radiative recombinations at the pixel's sidewalls. This limit of  $4\mu\text{m}$  in terms of pixel lateral sizes matches the standard values of carrier diffusion lengths reported for AlGaInP-based devices [9]. We can recall that these phenomena are more detrimental in AlGaInP-based devices than for example in GaN-based devices, because the former have a larger number of surface defect states at their sidewall combined with higher carrier diffusion lengths as well as higher recombination velocities [10]. This is thus the reason why the potential of BMR is hindered for pixel lateral sizes under  $2\mu\text{m}$  as seen for SLNP with  $a=400\text{nm}$  and a lateral size of  $\sim 1\mu\text{m}$ . Further extensive experiments that are out of the scope of this PhD thesis would be required to tackle this issue. In that regard, we can conclude that for now, unless efficient passivation techniques are developed, pixel sizes need to be kept at least over  $2\mu\text{m}$ . In that framework, BMR could help improve LEE by factors up to  $\sim 33\%$ , for instance for pixel lateral sizes of  $\sim 2.1\mu\text{m}$  (SLNP with  $a=700\text{nm}$ ). It is also worth noting that the difference between the saturation values of unpixelated and pixelated devices can be attributed to differences of etch depths wafer-to-wafer due to the technological variations during fabrication.

It thus appears that BMR could help us benefit from the lateral mirrors isolating the pixels between one another. Its potential has been experimentally demonstrated, helping us improve LEE by  $\sim 33\%$  for pixels with very short lateral sizes ( $\sim 2\mu\text{m}$ ), which is promising for the final integration of the MQW CCL on blue  $\mu\text{-LED}$  arrays. It has also been emphasized that, unless efficient passivation techniques are developed, pixel lateral sizes need to be kept at least over  $2\mu\text{m}$ , otherwise IQE decrease would hinder said efficiency improvements.

In addition to the importance of matching the reflection phase-shift due to the lateral mirrors, we have pointed out that the core principle of BMR relies on an interplay between the light-extraction processes by the grating (characterized by the coupling strength) and the reflection by the lateral mirrors (characterized by the lateral-mirror reflectance values). In the next section, we model this interaction to have a better understanding of our results.

#### **IV.5.2 Modeling the impact of lateral-mirror losses**

We wish to model the dependency of LEE on the coupling strength and the lateral-mirror reflectance to have a good insight into the interplay between light extraction and reflection and understand its role on BMR. To do so, we herein propose a four-wave intensity model whose operating principle is depicted in **Figure IV-27**. We start by assuming that the reflection phase-shift induced by the penetration depth inside the lateral mirrors is matched. In that framework, light emitted inside the CCL is either extracted outside by the grating, characterized by its coupling strength  $\kappa$  (mean coupling strength over all the guided Bloch-modes), or lost via lateral-mirror losses due to their reflectance values denoted  $R (<1)$ . We note  $L$  the lateral extent of the grating,  $I_{\text{int}}^z$  the intensity of the emitted light remaining inside the CCL after  $z$  half round-trips,  $I_{\text{out}}^z$  the intensity of the portion of the emitted light extracted outside after  $z$  half

round-trips and  $I_0$  the initial emitted light inside the cavity ( $I_{int}^0 = I_0$ ). The final light extraction efficiency at the end of this process is denoted LEE (on the top and bottom sides).

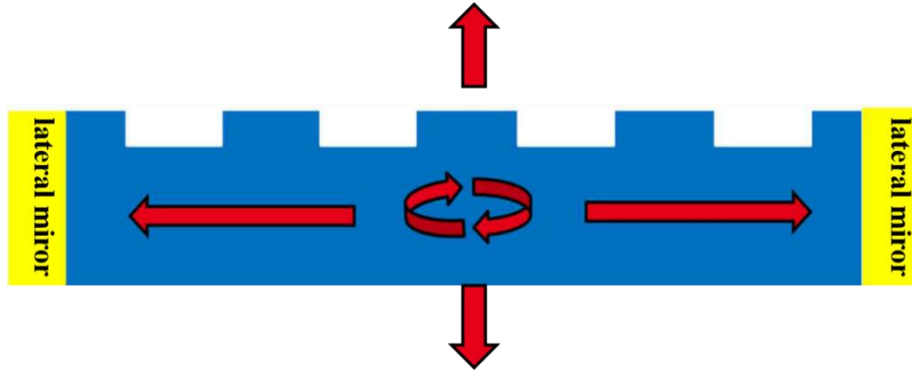


**Figure IV-27:** Overview of the principle of the four-wave intensity model.

Within that framework, the light intensity extracted outside after the first half roundtrip can be expressed using the same couple-mode-theory-derived model as in the previous chapter:

$$I_{out}^1 = I_0 \tanh^2(\kappa L) \quad (IV.4)$$

From that, we derive the remaining intensity inside the cavity, which writes as<sup>12</sup>:

$$I_{int}^1 = R(I_0 - I_{out}^1) = R(I_0 - I_0 \tanh^2(\kappa L)) = R^1 I_0 (1 - \tanh^2(\kappa L))^1 \quad (IV.5)$$

We can thus more generally write that the remaining light intensity inside the cavity after  $z$  half roundtrips reads as:

$$I_{int}^z = R(I_0 - I_0 \tanh^2(\kappa L)) = R^z I_0 (1 - \tanh^2(\kappa L))^z \quad (IV.6)$$

To determine LEE, we need to evaluate  $I_{out}^\infty$  which is the total light intensity extracted outside at the end of the process. Using the previous equations, we can write:

$$I_{out}^{z+1} = I_{out}^z + I_{int}^z \times \tanh^2(\kappa L) = I_{out}^z + R^z I_0 (1 - \tanh^2(\kappa L))^z \times \tanh^2(\kappa L) \quad (IV.7)$$

By summing this previous equation over all the roundtrips, we obtain:

$$\sum_{z=0}^{\infty} (I_{out}^{z+1} - I_{out}^z) = \sum_{z=0}^{\infty} (R(1 - \tanh^2(\kappa L)))^z \times I_0 \times \tanh^2(\kappa L) \quad (IV.8)$$

This expression can be simplified using a geometric-progression sum on the right side of the previous equation within which we end up with the following relationship:

$$I_{out}^\infty = I_0 \frac{\tanh^2(\kappa L)}{1 - R(1 - \tanh^2(\kappa L))} \quad (IV.9)$$

The final light extraction efficiency can then be expressed as a function of the lateral extent of the PhC, the grating strength and the reflectance of the lateral mirrors:

$$LEE = \frac{I_{out}^\infty}{I_0} = \frac{\tanh^2(\kappa L)}{1 - R(1 - \tanh^2(\kappa L))} \quad (IV.10)$$

<sup>12</sup> A half roundtrip also includes reflection by one lateral mirror.

As we can notice, for devices with high lateral extent ( $L \gg L_{\text{ext}}$  and then  $\kappa L \rightarrow +\infty$ ),  $\tanh^2(\kappa L)$  reaches values close to unity and the denominator becomes quasi-independent on  $R$ . Therefore, the light extraction values for pixelated ( $R > 0$ ) and unpixelated ( $R = 0$ ) devices become the same. This matches with the measurement results plotted in **Figure IV-25**, where LEE enhancement for both pixelated and unpixelated devices have the same saturation values for high pixel lateral sizes. For pixels with short lateral sizes ( $L < L_{\text{ext}}$ ), the denominator is reflectance-dependent and less than unity. Thus, for given coupling strength  $\kappa$  and lateral extent  $L$ , LEE is higher when the devices are pixelated ( $R > 0$ ), which supports the validity of this four-wave model to have a better understanding of our experimental results. We now wish to understand how LEE is impacted by the reflectance values for a given device. The coupling strengths of our devices can be deduced from the extraction lengths provided in **Figure IV-19** (e.g., for  $L_{\text{ext}}$  of  $\sim 3\mu\text{m}$ , we obtain  $\kappa \sim 1/[3\mu\text{m}]$ ). Using **Eq. (IV.10)**, we evaluate LEE as a function of the lateral extent for different reflectance values ( $R$ ).

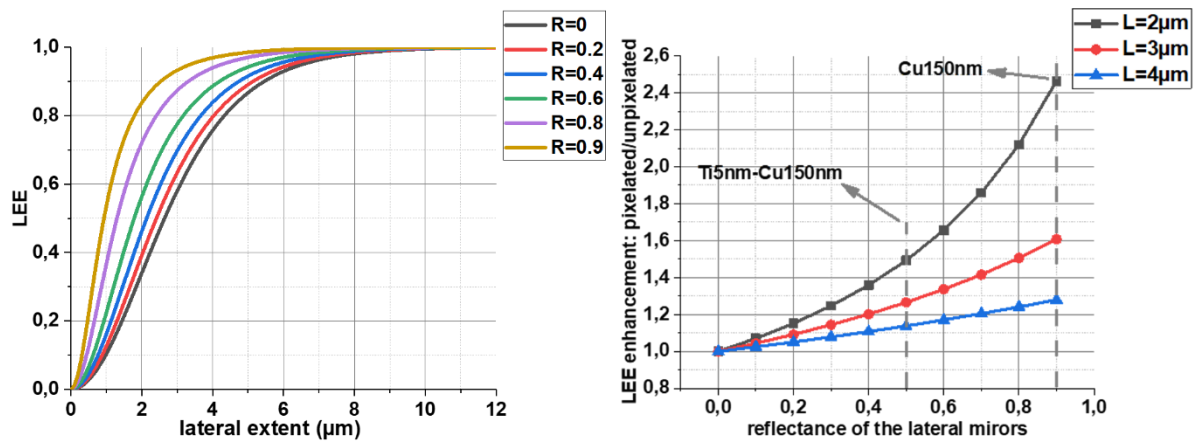


**Figure IV-28:** Simulation results using the herein-developed four-wave model. (Left): LEE as a function of the PhC lateral extent for different values of the lateral-mirror reflectance. (Right): ratios between LEE enhancement factors of pixelated ( $R > 0$ ) and unpixelated ( $R = 0$ ) devices to evaluate the improvement factors due to BMR.

As we can observe in the left plot of **Figure IV-28**, when saturation is not reached yet (pixel with short lateral sizes), increasing the reflectance of the lateral mirrors directly improves LEE at a given lateral extent, which tends to be more significant for reflectance values over  $\sim 50\%$ . On the right plot of the same figure, we focus on three particular lateral extents close to those of the short-lateral-size pixels we measured in **Figure IV-25** ( $2\mu\text{m}$ ,  $3\mu\text{m}$  and  $4\mu\text{m}$ ). We then plotted LEE enhancement factors of pixelated devices over unpixelated (but patterned with PhC) ones as a function of the reflectance values. As we can see, the reflectance values have a significant impact on the efficiency of the BMR principle. For instance for pixels with a lateral extent of  $2\mu\text{m}$ , LEE enhancement over unpixelated devices is close to 1 for low reflectance values (meaning that BMR doesn't have any impact on LEE), reaches  $\sim 1.5$  for reflectance around  $50\%$ , before going over  $\sim 2.5$  for high-reflecting mirrors. We measured the reflectance values of our lateral mirrors (Ti5nm-Cu150nm) and obtained  $\sim 50\%$  (see **Appendix C.1**), which shows that the potential of BMR within our fabricated devices is drastically hindered by losses in the lateral mirrors. Those low reflectance values were found to be the result of absorption losses within the thin Ti layer, used for optimal adhesion of Cu on the SiN layer. Additional reflectance measurements (see

**Appendix C.1)** performed on bare Ti and Cu layers showed us that reflectance values of Ti mirrors are around 50%, while Cu itself reaches reflectance values over 90%. By eliminating this thin Ti layer one could hence expect the improvement factors in **Figure IV-25** for pixelated devices to be even higher, as evidenced by the herein-developed model.

### IV.5.3 Conclusion on the Bloch-mode replication principle

To sum up, Bloch-mode replication (BMR) could be a viable strategy to increase the LEE further by benefiting from the lateral mirrors initially employed to isolate the pixels.

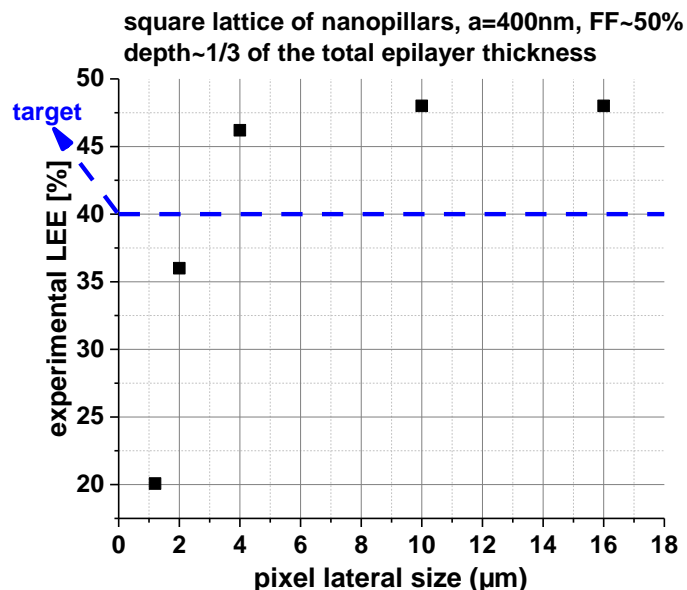


**Figure IV-29:** Experimental LEE evaluated from the LEE enhancement factors above for SLNP with  $a=400\text{nm}$  as well as back- and lateral mirrors (final devices of LOT III).

**Figure IV-29** displays the experimental LEE evaluated from the LEE enhancement factors above for SLNP with  $a=400\text{nm}$  as well as back- and lateral mirrors. As we can see, within the BMR principle, we were able to design and fabricate devices exhibiting LEE values over ~40%, which is compatible with the initial requirements to reach high luminances for AR microdisplays. Next, it has been emphasized that those high LEE values are maintained provided the lateral extents of the pixels are kept over  $2\mu\text{m}$ , due to large IQE decrease that hinders the overall efficiencies of the devices and which occurs unless efficient passivation techniques are developed (see **Figure IV-29**). Eventually, using a herein-developed four-wave intensity model, we have pointed out that there is further room for improvement within the BMR principle by increasing the reflectance values of the lateral mirrors. The 3D-FDTD simulations performed in the design section indicates that BMR is compatible with directional emitters, but it should be further investigated experimentally using back-focal plane measurements.

## IV.6 Conclusion

A quasi-3D harnessing of the emitted light can be performed by benefiting from the electromagnetic environment of the MQW CCL. In the typical final integration strategy (see **Figure I-10**), the said

environment comprises the electrical contact at the bottom of the blue  $\mu$ -LEDs and all the layers embedded in-between the CCL and said contact (blue epilayer, bonding layers, etc.) as well as lateral mirrors. We mimicked the former with an Al bottom reflector following a SiO<sub>2</sub> gap (for harnessing of the bottom emitted light), while the latter was represented by Cu lateral mirrors combined with a SiN phase-matching layer (for Bloch-mode replication), all suitably designed using FDTD simulations. Next, by implementing all these design principles, we fabricated MQW CCL on metallized silicon substrates exhibiting promising characteristics, which meet the initial targeted requirements for AR microdisplays: light extraction efficiencies over 40% (as long as the pixel lateral sizes are kept over  $\sim 2\mu\text{m}$ ), short extraction lengths and emission patterns with high directionality. The whole process flow has also been detailed, which could pave the way for the integration of those devices on blue  $\mu$ -LED arrays. Eventually using TRPL measurements and a herein-developed four-wave intensity model, we emphasized that there is still further room for improvement in terms of light extraction efficiencies within an increase of the reflectance values of both back- and lateral-mirrors, as well as a development of efficient passivation techniques particularly for pixel lateral sizes under  $2\mu\text{m}$ .

#### IV.7 References

1. P.-X. Zeng, W.-J. Guo, C.-D. Tong, R.-Z. Zhang, L.-L. Zheng, G.-L. Chen, Y.-Y. Chen, W.-P. Zhu, Y.-L. Gao, Y.-J. Lu, and Z. Chen, "Optical Crosstalk Among Mini-LEDs Packaged in a Four-in-One Integrated Matrix Device," *IEEE Trans. Electron Devices* **69**, 4366–4370 (2022).
2. A. David, T. Fujii, B. Moran, S. Nakamura, S. P. DenBaars, C. Weisbuch, and H. Benisty, "Photonic crystal laser lift-off GaN light-emitting diodes," *Appl. Phys. Lett.* **88**, 133514 (2006).
3. M.-C. Wu, M.-C. Chung, and C.-Y. Wu, "3200 ppi Matrix-Addressable Blue MicroLED Display," *Micromachines* **13**, 1350 (2022).
4. W. Y. Fu and H. W. Choi, "Development of chipscale InGaN RGB displays using strain-relaxed nanosphere-defined nanopillars," *Nanotechnology* **33**, 285202 (2022).
5. B. O. Jung, W. Lee, J. Kim, M. Choi, H.-Y. Shin, M. Joo, S. Jung, Y.-H. Choi, and M. J. Kim, "Enhancement in external quantum efficiency of AlGaInP red  $\mu$ -LED using chemical solution treatment process," *Sci. Rep.* **11**, 4535 (2021).
6. A. David, H. Benisty, and C. Weisbuch, "Optimization of Light-Diffracting Photonic-Crystals for High Extraction Efficiency LEDs," *J. Disp. Technol.* **3**, 133–148 (2007).
7. H. J. Cornelissen, H. J. B. Jagt, D. J. Broer, and C. W. M. Bastiaansen, "Efficient and cost-effective polarized-light backlights for LCDs," in *Eighth International Conference on Solid State Lighting* (SPIE, 2008), Vol. 7058, pp. 187–196.
8. E. Matioli, S. Brinkley, K. M. Kelchner, Y.-L. Hu, S. Nakamura, S. DenBaars, J. Speck, and C. Weisbuch, "High-brightness polarized light-emitting diodes," *Light Sci. Appl.* **1**, e22–e22 (2012).
9. J.-T. Oh, S.-Y. Lee, Y.-T. Moon, J. H. Moon, S. Park, K. Y. Hong, K. Y. Song, C. Oh, J.-I. Shim, H.-H. Jeong, J.-O. Song, H. Amano, and T.-Y. Seong, "Light output performance of red AlGaInP-based light emitting diodes with different chip geometries and structures," *Opt. Express* **26**, 11194–11200 (2018).
10. Y. Boussadi, N. Rochat, J.-P. Barnes, B. B. Bakir, P. Ferrandis, B. Masenelli, and C. Licitra, "Investigation of sidewall damage induced by reactive ion etching on AlGaInP MESA for micro-LED application," *J. Lumin.* **234**, 117937 (2021).

# **Chapter V**

## *Conclusions and outlook*

## Table of contents

V.1	Work overview .....	131
V.2	Perspectives towards the integration of MQW CCL on blue $\mu$ -LED arrays .....	134
V.2.1	Near-field coupling between the color converters and the blue pump for mode-to-mode absorption: proof of concept.....	134
V.2.2	Does further thinning the MQW epilayer help? .....	136
V.3	References .....	137

## V.1 Work overview

MQW color conversion layers (CCL) could be the next “big thing” in AR microdisplays, since they could substitute state-of-the-art Q-dot color converters when the required luminances are too high (photostability issues) and/or high resolutions are at stake (need for compact integration schemes). However, in the beginning of this PhD thesis, their implementation was still hindered by some challenges, particularly for blue-to-red color conversion.

The first one was related to their low light extraction efficiency (LEE) inherent to their high refractive indices. Indeed AlGaInP has refractive indices over three in the red spectral range, so that most of the emitted red light couple to the available guided modes inside the so-formed cavity and drastically limit their maximum reachable overall conversion efficiency to ~3%. It has recently been evaluated that for a CCL to be able to reach the targeted luminances (between  $10^6$  and  $10^7$  cd/m<sup>2</sup>) in AR microdisplays, its LEE must reach values between 40 and 50% [1]. These light-extraction issues needed then to be dealt with and there was still a large gap to bridge. In addition, the extraction length  $L_{ext}$  (the lateral extent needed to extract most of the guided light) needs to be shorter than the pixel lateral size  $L_{pixel}$  in order to reach the required resolutions in AR microdisplays. Moreover, the final light emitter needs to be as directional as possible in an AR headset to avoid the use of additional optics such as collimating refractive lenses, which is not met yet due to the Lambertian-like farfield emission patterns of unstructured AlGaInP MQW CCL. Finally yet importantly, some technological steps needed to be further developed to efficiently transfer the said MQW CCL on blue  $\mu$ -LED arrays and then pixelate them.

Thus, the main goal of this PhD work was to devise strategies to alleviate of the aforementioned issues in order to pave the way for monolithic RGB AR microdisplays based on MQW CCL.

We started by investigating spontaneous emission (SpE) in layered medium, which is the key physical phenomenon underlying light emission in MQW CCL. For that matter, we have developed a novel SpE modeling framework based on generalized 3x3 transfer-matrices, where dipole emission is directly treated in the matrix formulation as a source matrix, on the contrary to standard 2x2 transfer-matrix method with dipole source terms [2]. The accuracy of the said model has been validated using rigorous electromagnetic simulations with 3D-FDTD and its applicability has been demonstrated through various examples, which pointed it out to be a key tool for designing incoherent light-emitting structures. In particular, it has enabled us to highlight that in MQW CCL, light extraction is drastically hindered by the coupling between dipole emission and the available guided modes inside the medium (more than 70% of the emitted light), which is one the main efficiency bottlenecks of those devices. The importance of SpE distribution among guided modes in that matter has also been emphasized as well its origin through the antinode factor and the Airy function, since it eventually sets LEE and the directionality of the emission. To alleviate the light extraction issues, we have subsequently evaluated different routes ranging from epitaxial design (controlling the thickness of the color-converters, the number or positions

of quantum wells, the emission spectrum) to SpE redistribution (through tuning and detuning the total optical thickness of the membrane), but none of them allows the simultaneous optimization of both LEE and directionality.

Therefore, we used photonic-crystals (PhCs) as light extractors, which then had been demonstrated to have the unique ability to provide a superior control of the guided-mode diffraction out of high-index materials, thus increasing LEE and directionality at the same time.

Optimizing PhC patterns for efficient MQW CCL is a tricky endeavor, due to the large parameter-space of PhCs and the incoherent nature of spontaneous emission. To do so, we then designed, fabricated and tested blue-to-red InGaP/AlGaInP MQW CCL bonded on transparent substrates and unpixelated (LOT I) to have a good insight on the behavior of the bare PhCs. A robust process flow starting from an oxide-mediated molecular bonding with high bonding yield (>90%) has been developed in 200mm cleanroom facilities, followed by a top-down pattern-transfer to fabricate PhC patterns with controlled opto-geometrical parameters over the whole wafer. Afterwards, using micro-photoluminescence, measurements we have emphasized the main roles played by the opto-geometrical parameters of the PhCs on the performances of our devices and modelled them when necessary. For each of those parameters, we have proposed precise design guidelines (see **Table III-2**) that helped us realize PhC-based MQW color-converters on transparent substrates exhibiting enhanced light extraction efficiency within ultra-short extraction lengths.

Regarding directionality, we have highlighted a fundamental condition necessary to achieve directional emission in our MQW: the lattice period of the PhC needs to be properly tuned so that the most intense diffraction bands cross the  $\Gamma$ -point close to the peak emission wavelength. From this condition, we have devised a novel design approach for such structures resting on a simultaneous control of SpE distribution between the guided modes to identify the guided modes with the highest photonic weights (that carry a larger fraction of the guided energy) and an optimized choice of the lattice period based on the 2D band-folding mechanism. This approach has then been experimentally confirmed helping us reach directionality enhancement over x4 close to normal incidence as compared to standard Lambertian emission, which is promising for our targeted AR applications. Furthermore, we emphasized that epitaxial design (thickness of the CCL, the number of quantum wells, their positions, the emission spectrum) as well as controlling some of the PhC parameters such as the air filling factor and etch depth could be levers to tailor suitable SpE distributions and photonic weights.

Finally yet importantly, we implemented a quasi-3D light harnessing strategy to benefit from the electromagnetic environment of the MQW CCL to improve LEE, while keeping a directional emission. In the typical final integration strategy (see **Figure I-10**), the said environment comprises the electrical contact at the bottom of the blue  $\mu$ -LEDs and all the layers embedded in-between the CCL and said contact (blue epilayer, bonding layers, etc.) as well as lateral mirrors. We mimicked the former with an Al bottom reflector following a SiO<sub>2</sub> gap (LOT II) for harnessing of the bottom emitted light, while the

latter was represented by Cu lateral mirrors combined with a SiN phase-matching layer (LOT III) for Bloch-mode replication, all suitably designed using 3D-FDTD simulations.

Devices of LOT II are unpixelated MQW CCL with a back-reflector and aimed at experimentally investigating the possibility of harnessing of the bottom emitted light. Those of LOT III on the other hand are pixelated and seek to demonstrate Bloch-mode replication for a virtual extension of the lateral sizes of the pixels. By implementing all these design principles, we fabricated MQW CCL on metallized silicon-substrates exhibiting promising characteristics, which meet the initial targeted requirements for AR microdisplays: light extraction efficiencies over 40%, short extraction lengths and emission patterns with high directionality. In addition, we have pointed out that the targeted LEE values are reached as long as the pixel lateral sizes are kept over  $\sim 2\mu\text{m}$  due to IQE large IQE decrease for short sizes (increase of non-radiative recombination on the pixel's sidewalls).

Furthermore, using TRPL measurements and a herein-developed four-wave intensity model, we emphasized that there is still further room for improvement in terms of light extraction efficiencies within an increase of the reflectance values of both back- and lateral-mirrors, as well as a development of efficient passivation techniques particularly for pixel sizes under  $2\mu\text{m}$  as in [3]. The whole process flow has also eventually been detailed, while highlighting the key technological challenges for the integration of those devices on blue  $\mu\text{-LED}$  arrays as well as the compatibility between the design requirements and the fabrication capabilities.

**Figure V-** depicts a summary of the main light extraction efficiency improvements made during this PhD work, while keeping a directional emission along with short extraction lengths. Let us recall that these experimental LEE are underestimation of real LEE values, evaluated from the measured enhancement factors taking also into IQE decrease.

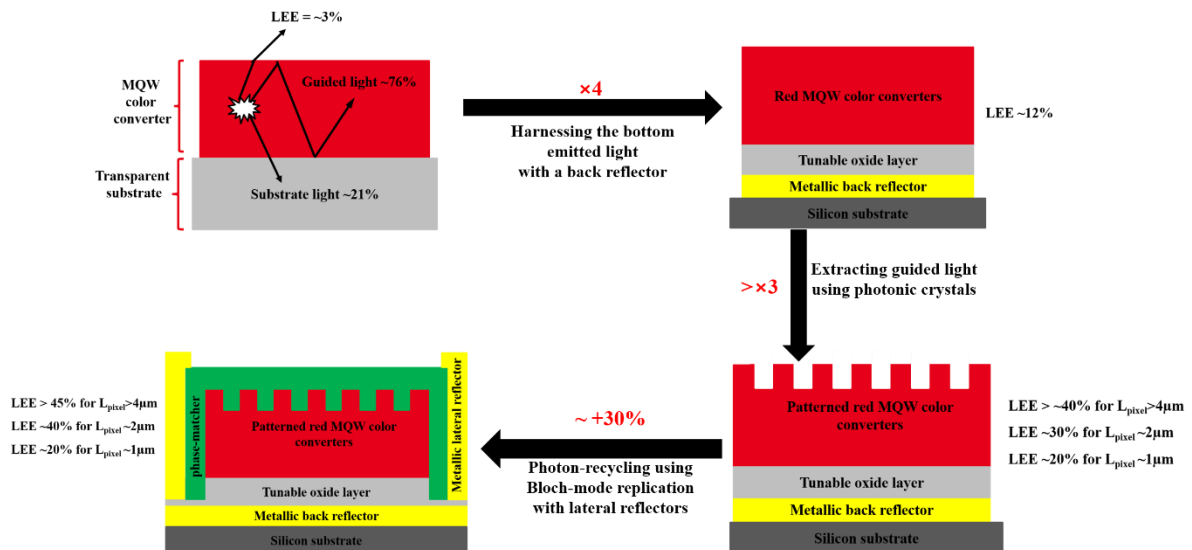


**Figure V-1:** Summary of the light extraction efficiency improvements made during this PhD work starting from the bare MQW color converters on transparent substrate, while keeping directional emission and short extraction lengths.

All these results are currently being used on ongoing projects to develop the first RGB AR microdisplays based on MQW color converters, which could pave the way for monolithic integration of full-color displays.

## V.2 Perspectives towards the integration of MQW CCL on blue $\mu$ -LED arrays

Let us recall that the overall efficiency of the color-conversion process is often assessed by the external photoluminescence quantum yield (EPLQY) which is the ratio between the number of down-converted photons extracted out of the CCL and the number of blue incoming pumping-photons. It reads as:

$$EPLQY = \eta_{abs} \times IQE \times LEE. \quad (V-1)$$

Here  $\eta_{abs}$ ,  $IQE$  and  $LEE$  account for absorption efficiency, internal quantum efficiency and light extraction efficiency, respectively.

As explained throughout this manuscript, the main efficiency bottleneck of red MQW CCL was their low  $LEE$ , which has been extensively investigated in this work.  $IQE$  decrease due to photonic-crystal patterning and pixelization have also been examined, highlighting the need for efficient passivation techniques for pixels with very short lateral sizes. Thus, the aim of this last section is to address briefly additional steps towards the integration of MQW CCL on blue  $\mu$ -LED arrays and further improvement their performances, particularly regarding their absorption efficiency.

### V.2.1 **Near-field coupling between the color converters and the blue pump for mode-to-mode absorption: proof of concept**

While the subject was not directly dealt with in this manuscript, it has been pointed out that a 600nm-thick red InGaP/AlGaInP MQW CCL is enough to observe no transmission of the blue incoming light during a single pass. Thus, the overall absorption efficiency of the system blue pump / MQW CCL will be limited by the extraction efficiency of the GaN blue pump. Let us consider the simplified case of a single-mode GaN waveguide ( $n=2.47$ ) operating in TE polarization at 460nm. FDTD simulations (see **Figure V-2**) of centered dipole emitter shows that only 6% of the emitted light is extracted in air upwards and downwards, which limits the amount of blue light that could be absorbed by the red CCL to ~12% at most.

A straightforward route to overcome this limit could be to pattern the blue  $\mu$ -LEDs with photonic crystals as we did with the MQW CCL. In the following, we propose a second and more compact way to do so without patterning based on the same operating principle as hybrid III-V lasers on silicon for integrated photonics [4].

**Figure V-3** depicts the two possible coupling regime between the single-mode blue pump and the red MQW CCL. When the two epilayers are far from each other (farfield regime), only blue light extracted out of the pump can be absorbed by the CCL. This limits the overall EPLQY of the CCL to ~12%. However, when the two epilayers are brought close enough together that the two guided modes start

overlapping, one could benefit from a strong mode-to-mode coupling leading to direct energy exchange between those two. This could significantly enhance the absorption efficiency of the CCL.

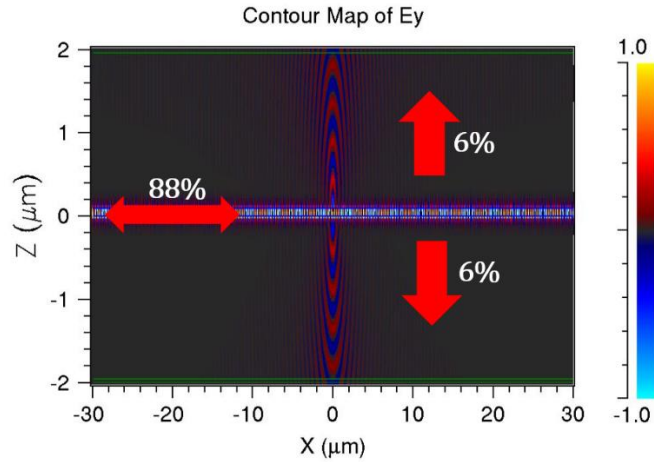


**Figure V-2:** FDTD simulation of a dipole centered in a single-mode blue GaN slab emitting at  $\lambda=460\text{nm}$ . Contour map of the electric field ( $E_y$ ) in the stationary regime.

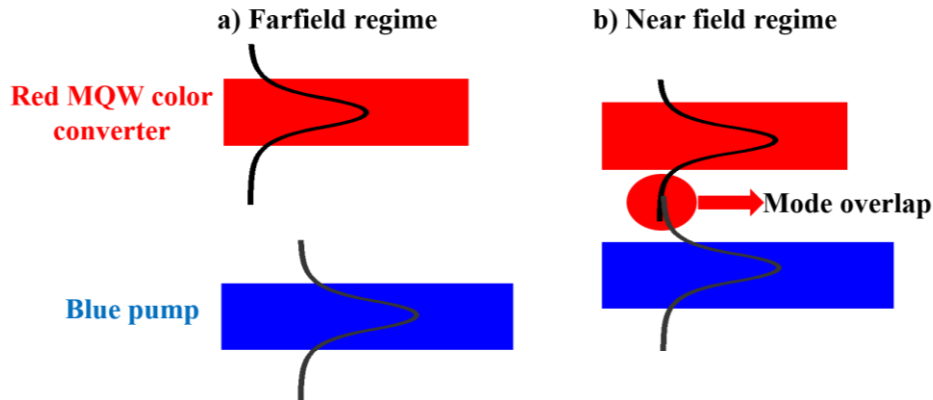


**Figure V-3:** Possible coupling regime between the GaN blue pump and the red AlGaInP color converter. a) Farfield regime where only light extracted out the blue pump can be absorbed by the red MQW color converter. b) Near field regime where direct mode-to-mode absorption occurs.

To confirm this latter strategy, we perform additional FDTD simulations on the system described in **Figure V-3**. We placed a TE polarized dipole emitter in the middle of a single-mode GaN ( $n=2.27$ ) emitting at  $\lambda=460\text{nm}$ . A red absorbing AlGaInP epilayer ( $n=3.4$ ,  $k=0.36$ ) is placed on top of the former blue pump at a distance we will refer to as *gap*. The former imaginary index accounts for the absorption of AlGaInP in the blue spectral range. Then, we vary the gap between the two epilayers and measure the absorption efficiency inside the red epilayer using an absorption monitor (see **Appendix A.1** for more details about the FDTD method). The results are shown in **Figure V-4**.

As we can see, when the MQW CCL is far away from the pump ( $n_{\text{gap}}d_{\text{gap}} > \lambda/4$ ), the absorption efficiency is limited to  $\sim 4\%$ , which corresponds to the 6% extracted out of the blue pump multiplied by the transmission of the air-CCL interface ( $\sim 70\%$ ). However, in the near field regime, the absorption efficiency rapidly increases until it reaches values over 90% because of a direct energy-exchange between the two guided modes supported by the pump and the CCL. This emphasizes the paramount importance of the near-field regime for an overall efficient microdisplay.

In the case of real-life devices, the blue  $\mu$ -LEDs and MQW CCL are separated with oxide-like bonding layers. For instance, for a  $\text{SiO}_2$  gap layer, the previous analyzes would mean that the  $\text{SiO}_2$  thickness should be kept below  $0.3 \lambda/n_{\text{gap}} \approx 95\text{nm}$ , which is technologically feasible.

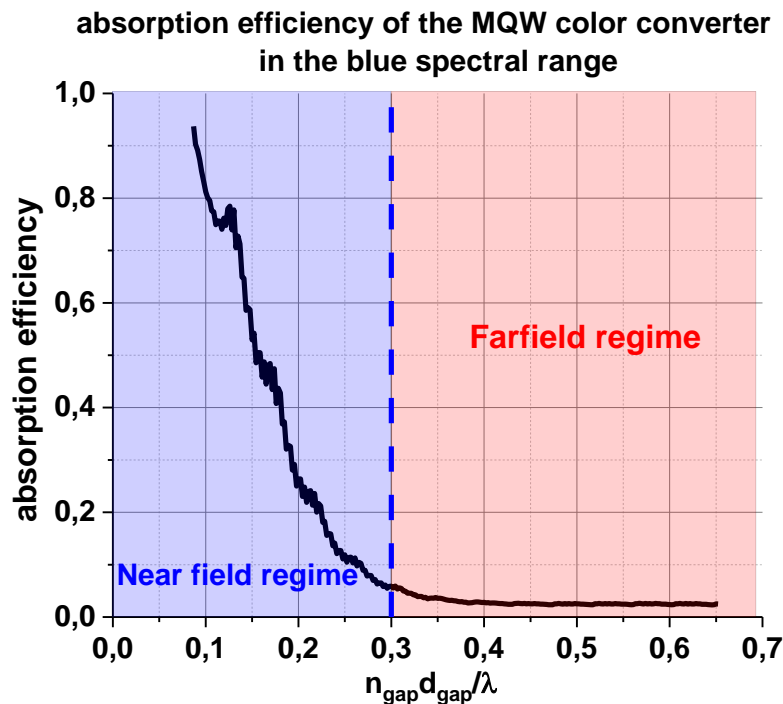


**Figure V-4:** FDTD simulation results. Absorption efficiency of the red MQW color converter in the blue spectral range as a function of the optical thickness of the gap between said color converter and the blue pump.

### V.2.2 Does further thinning the MQW epilayer help?

Although it has only been briefly addressed in this manuscript, we have emphasized that epitaxial design is of key interest in the performances of the final devices. Indeed, it sets the number of guided modes as well as their coupling to spontaneous emission (important for the directionality of the emission) and to the PhC patterns (which sets the grating strength). Different design rules have been highlighted in this work regarding the epilayer and the main ones are as follows:

- The red MQW color converters need to be thick enough to absorb all the incoming blue light during a single pass.
- The PhC patterns must be etched at around the third of the total epilayer thickness to keep reasonable values of grating strength.
- To avoid IQE decrease, carrier generation should not happen in etched regions. Thus, the epilayer thickness before the PhC needs to be enough for complete blue light absorption.

The initial red epilayer used in this PhD work and labeled as “Design 1” is depicted in **Figure V-5**. As already discussed, it is a multimode membrane supporting more than 6 guided modes. Although high directionality values have been achieved as well as high LEE, thinning this epilayer towards a single-mode color-converter could provide a further increased directionality and LEE control [5].

In **Figure V-5**, we propose different possible designs meeting the requirements cited before. The design corresponds to  $1.5\lambda$ -cavity with still no transmission of the blue light as a PhC etch depth that needs to be  $\sim 100\text{nm}$  to have good coupling strength. In that framework, the CCL would support less guided modes as the directionality could be better controlled. As for LEE, 3D-FDTD simulations (not shown here) help us found that when patterned “Design 1” and “Design 2” achieve the same LEE. “Design 2” could thus be interesting in terms of controlling the emission pattern.

As for “Design 2”, “Design 3” is a  $1\lambda$ -cavity supporting thus less guided modes ( $\sim 2$ ). With a PhC etched at around  $\sim 66\text{nm}$ , one reaches the same LEE and has a better control of the directionality, while not affecting IQE.

For the “Design 4” on the other hand, there is not enough room for the PhC to be etched while not affecting IQE. This corresponds to the single-mode case, which could be interesting in terms of directionality but could be detrimental for the overall efficiency of the color converter, since carrier generation could happen in etched regions.

With this quick analysis, thinning the MQW color converter could be envisioned up to a  $1\lambda$ -cavity, which could improve the directionality while keeping similar LEE. Thinner cavities do not leave enough room for PhC patterning without decreasing the IQE.

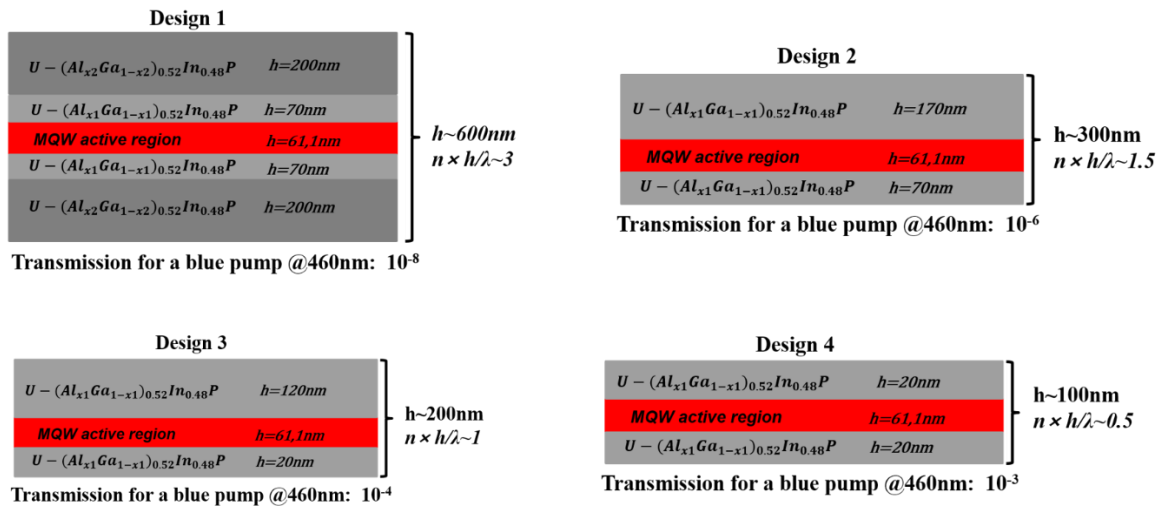


**Figure V-5:** Possible epitaxial designs for an AlGaInP/InGaP blue-to-red MQW color converters. The different values of the transmission efficiency at 460nm are provided below each design. They were evaluated using RCWA simulations.

All the levers for improvements defined above along with the present work in this manuscript could help integrate MQW CCL on blue  $\mu$ -LED arrays.

### V.3 References

1. E. Quesnel, A. Lagrange, M. Vigier, M. Consonni, M. Tournaire, V. Le Marchand, A. Suhm, P. Demars, J.-C. Pillet, B. Ben Bakir, N. Olivier, E. Feltin, J. M. Lamy, M. D’Amico, E. Cao, G. Haas, L. Charrier, and P. Coni, "Dimensioning a full color LED microdisplay for augmented reality headset in a very bright environment," J. Soc. Inf. Disp. **29**, 3–16 (2021).
2. H. Benisty, R. Stanley, and M. Mayer, "Method of source terms for dipole emission modification in modes of arbitrary planar structures," JOSA A **15**, 1192–1201 (1998).

3. J. Flemish, Z. Ren, W. Soer, R. Armitage, H. Lofti, R. Pathak, H. J. Kim, S. Banna, W. Sillevs-Smitt, J. C. Tan, Y. M. Tio, R. Distor, S. Lim, and K. B. Lim, "MicroLED architectures for low power wearable displays," in *Light-Emitting Devices, Materials, and Applications XXVI* (SPIE, 2022), Vol. 12022, pp. 5–10.
4. B. B. Bakir, A. Descos, N. Olivier, D. Bordel, P. Grosse, E. Augendre, L. Fulbert, and J. M. Fedeli, "Electrically driven hybrid Si/III-V Fabry-Pérot lasers based on adiabatic mode transformers," *Opt. Express* **19**, 10317–10325 (2011).
5. K. Bergenek, Ch. Wiesmann, H. Zull, R. Wirth, P. Sundgren, N. Linder, K. Streubel, and T. F. Krauss, "Directional light extraction from thin-film resonant cavity light-emitting diodes with a photonic crystal," *Appl. Phys. Lett.* **93**, 231109 (2008).

## **Appendix A**

*Description of the rigorous electromagnetic simulation techniques utilized in this work.*

## A.1 Incoherent light emission with the Finite-Difference Time-Domain technique

In the manuscript, we employ 2D- and 3D-FDTD from commercially available software: LED Utility from the Rsoft Design Suite. The underlying coherent simulation performed by the LED Utility is Rsoft's FullWAVE simulation tool, which uses the well-known Finite-Difference Time-Domain (FDTD) technique. The FDTD method is a rigorous solution to Maxwell's equations and does not have any approximations or theoretical restrictions. Since FDTD is a direct solution of Maxwell's curl equations, it can be used to model arbitrarily complex LED structures. Moreover, the LED utility can utilize the clustering feature of FullWAVE to distribute the simulation workload over several cores and computers on a network resulting in faster and larger simulations.

### Incoherent and isotropic light emission

Numerical simulation of a light emitting diode (LED) is tedious since LEDs are inherently incoherent and unpolarized light-emitters. The cost of including incoherence in a FDTD simulation is very high because the time-scale for a dipole's phase variation is much larger than the optical period ( $T = 2\pi/\omega$ ) and would require prohibitively long simulations (nanoseconds vs. few ten femtoseconds).

In addition, a simulation model of this type of source requires a group of dipole sources with:

- **Temporal Incoherence:** The phase of each dipole varies over time
- **Spatial Incoherence:** The phase variation of a specific dipole is independent from the phase variation of any other dipoles
- **Random Polarization:** A large number of dipoles with random polarization are required to achieve unpolarized radiation, typically 50/200 dipoles for 2D/3D simulations.

The active region within a LED is then modelled as a series of incoherent dipole sources. This type of source can be created by separately simulating a series of 'unpolarized' light sources within the source plane and then incoherently combining the results.

### Creating a single 'unpolarized' light dipole with FDTD

An 'unpolarized' dipole source can be created by incoherently combining the simulation results from three orthogonal dipoles. **Figure A-1** shows the radiation patterns from three orthogonal dipole sources radiating in free space along X, Y and Z directions, respectively. We can see that the radiation patterns are strongly dependent on the dipole orientation.

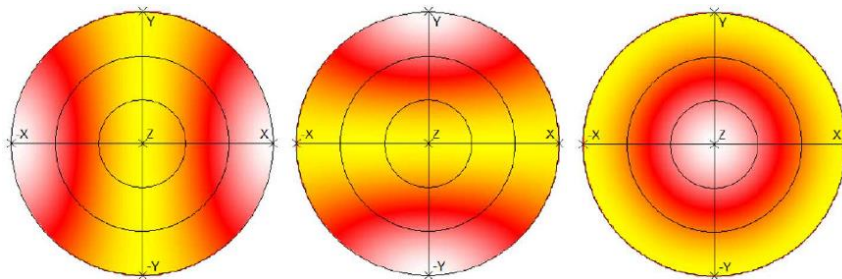


**Figure A-1:** Farfield patterns of a radiating dipole along X, Y and Z directions.

The radiation pattern from an unpolarized light source can be obtained by combining incoherently the individual results from the three orthogonal dipoles, as shown in **Figure A-2**. As expected, for an unpolarized dipole the resulting radiation pattern is spatially uniform.

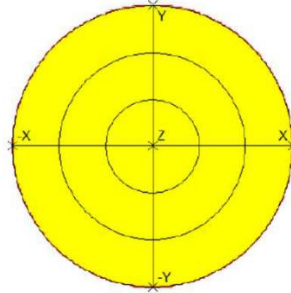


**Figure A-2:** Farfield pattern obtained by incoherently combining three orthogonal results.

Indeed, light is generated in the active layer of a LED as the electrons and holes recombine to create photons. The photons are created by a process called spontaneous emission and each photon has a random direction, phase and polarization. While in principle, the exact description of this process must involve quantum mechanics, in practice, it is possible to describe the generated light classically using electromagnetic point dipole (or current) sources. The latter approach is easier to model and simulate. Therefore, the average electromagnetic field intensity of an ensemble of incoherent, isotropic dipole emitters in a small spatial volume can be calculated by:

$$\langle |\vec{E}|^2 \rangle = \frac{1}{3} [ |E_x|^2 + |E_y|^2 + |E_z|^2 ] \quad (\text{A-1})$$

Here  $E_x$ ,  $E_y$  and  $E_z$  are the electromagnetic fields generated by a single dipole along the x, y and z-axes.

### Creating a spatially incoherent unpolarized LED

The spatially incoherent nature of the light generated by LEDs is handled as follows: the source in the active region is treated as a collection of single ‘unpolarized’ point current sources as shown in **Figure A-3**. Spatial incoherence of these multiple sources is created by simulating each of these sources separately (coherently) using FDTD, and then combining the individual results incoherently.

It should be noticed that for quantum-well based LEDs, since the confinement is in the z direction, the dipoles are oriented in the 2D epi-growth plane so that only x & y dipoles are considered in the simulations. In addition, for photonic-crystal structures, one only needs to distribute dipoles within a lattice period.

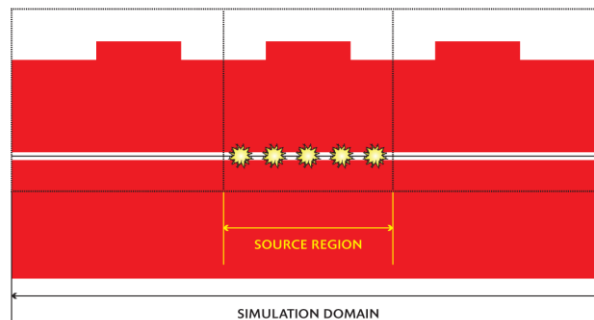


**Figure A-3:** Point current source scan for an incoherent LED simulation.

## Decay rates

FDTD based simulations of LED devices often involve measuring enhancements to the radiative decay rate of the emitter. The following definitions are generally used:

- $\gamma_{\text{rad}}$ : The decay rate of excitations to photons that can be collected and used in the device. For a LED structure, this would be the decay rate of excitations to photons that propagate from the LED structure into the air within a useful range of angles. **Calculations involving the radiative decay rate are within the scope of an FDTD simulation.**
- $\gamma_{\text{loss}}$ : The decay rate of excitations to photons that are absorbed or otherwise lost in the device. Photons absorbed in lossy material, trapped by TIR (total internal reflection) in high index layers, or radiate outside a desired range of angles are included in this category. **Calculations involving the loss decay rate are within the scope of an FDTD simulation.**
- $\gamma_{\text{em}} = \gamma_{\text{rad}} + \gamma_{\text{loss}}$ : the total electromagnetic decay rate. This is simply the sum of  $\gamma_{\text{rad}}$  and  $\gamma_{\text{loss}}$ . **This is within the scope of an FDTD simulation.**
- $\gamma_{\text{nr}}$ : the decay rate of excitations to non-radiative processes (SRH, Auger, etc.). **Calculations involving the non-radiative decay rate of an emitter are beyond the scope of an FDTD simulation.**
- $\Gamma_{\text{excitation}}$ : The excitation rate of the emitter. The emitter is typically excited electrically. **Calculations involving the excitation rate are beyond the scope of an FDTD simulation.**

## Light extraction efficiency and farfields

The light extraction efficiency ( $LEE$ ) for a LED is defined as the fraction of optical power generated in the active layer of the LED that escapes into the air above the LED within a ‘desired’ range of angles:

$$LEE = \frac{\gamma_{\text{rad}}}{\gamma_{\text{rad}} + \gamma_{\text{loss}}} = \frac{\gamma_{\text{rad}}}{\gamma_{\text{em}}} \quad (\text{A-2})$$

We can also define the *light extraction efficiency enhancement* ( $\eta_{LEE}$ ) as the ratio of the light extraction efficiency for two different designs, such as a patterned vs un-patterned LED structure:

$$\eta_{LEE} = \frac{LEE_{\text{pattern}}}{LEE_{\text{wo/pattern}}} \quad (\text{A-3})$$

When calculating the light extraction efficiency, we measure the fraction of useful power emitted from the LED device relative to the total power emitted from the active layer. We may consider the fraction of useful power to be the light that escapes to the air (or to the substrate), or we may consider the light escaping to the air within a particular solid angle.

The following are the steps for analyzing the light extraction efficiency, once the simulations have completed:

- Simulate three (or two / in the case of the quantum-well based emitters) polarizations separately
- Scan position of point source
- Each simulation contains one point source

- Sum up far-field and extraction ratio, incoherently, for each wavelength
- Sum up far-fields and extraction ratios weighted by radiation spectrum, for combined results.

## **Appendix B**

*Photonic crystals for light extraction from  
MQW III-V membrane on transparent  
substrate: additional information.*

### B.1 Excitation-power dependent photoluminescence measurements

Until the transparency regime, quantum wells also act as saturable absorbers, which means that QW re-absorption process depends on the pumping levels. In particular, it should be greatly reduced at high excitation intensity. However, due to the short extraction lengths of our structures (between  $\sim 1.6\mu\text{m}$  and  $13\mu\text{m}$  at high acceptance angles, far shorter than typical re-absorption lengths in said devices), light extraction plays the preponderant role. Therefore, DLEE enhancement factors should be independent on the excitation levels for a given PhC structure.

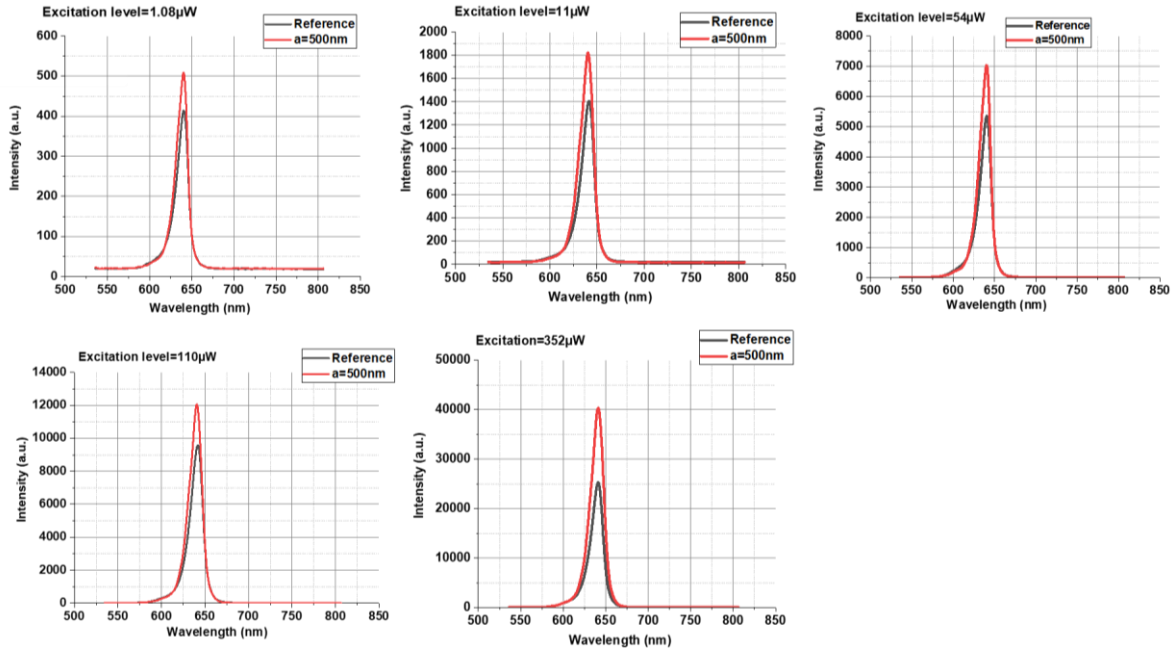


**Figure B-1:** Photoluminescence spectra from a laser excitation at 514nm with different excitation levels ( $1.08\mu\text{W}$ ,  $11\mu\text{W}$ ,  $54\mu\text{W}$ ,  $110\mu\text{W}$  and  $352\mu\text{W}$ ) for holes with a lateral extent of 25 periods and a lattice period of 500nm.  $\text{NA}=0.25$ .

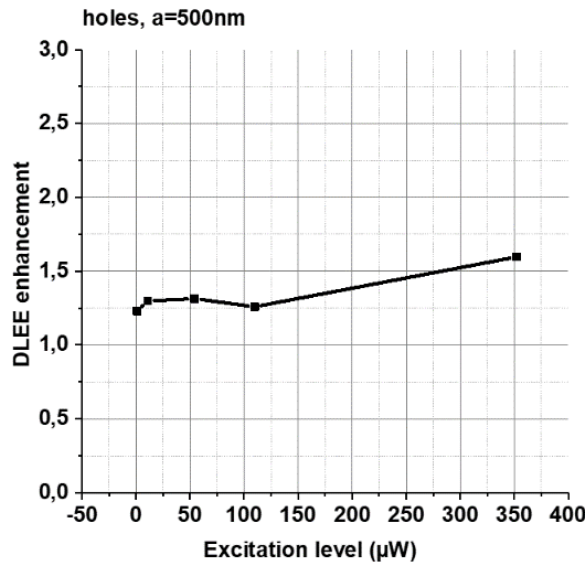


**Figure B-2:** Measured DLEE enhancement as a function of the excitation levels for holes with a lattice constant of 500nm and a lateral extent of 25 periods.

To investigate that last conclusion, we performed excitation-power dependent photoluminescence (PL). We chose the PhC structure with the lowest DLEE enhancement factors (square lattice of air holes with a lattice period of 500nm and a FF~20%) and the microscope objective with the lowest collection angle (NA=0.25) to avoid saturating the detector. The experimental setup is the micro-PL setup described in **Chapter III**. The excitation levels were increased from  $1.08\mu\text{W}$  to  $352\mu\text{W}$  and the measured spectra are displayed in **Figure B-1**.

We evaluated DLEE enhancement factors with the formulas provided in **Chapter III** and the results are displayed in **Figure B-2**. It shows that DLEE enhancement factors are quasi-independent on the excitation levels (quasi-constant as a function of the excitation levels) which supports our conclusion that light extraction plays the preponderant role in this our structure.

## B.2 Measured vs simulated azimuthal farfield emission patterns

We have performed additional incoherent 3D-FDTD simulations for comparing some of the emission patterns measured for the devices of **Chapter III** to the calculated ones.

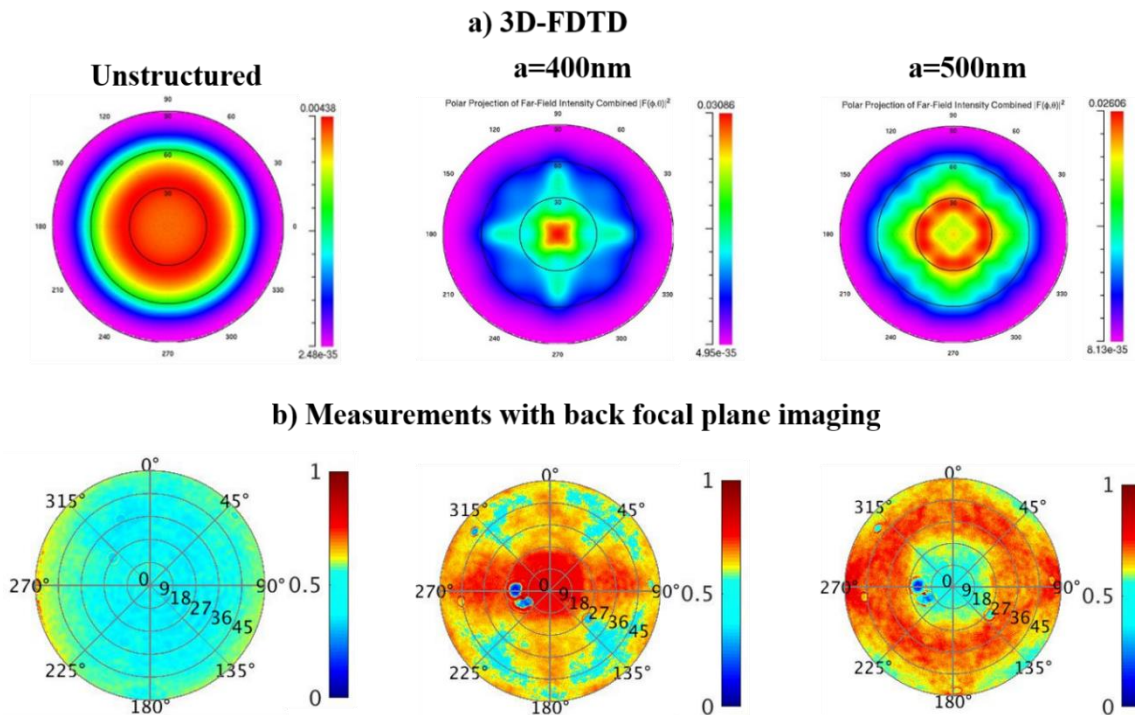


**Figure B-3:** Simulated and measured azimuthal farfield emission patterns for square lattice of air holes with a FF~20% and lateral extents of 10-period (simulation) and 100periods (measurements).

The lateral dimensions of the computational domain were fixed at 10 lattice periods for computing time issues and surrounded by perfectly matched layers (PML). The input spectrum is Gaussian-shaped with a center wavelength at 640nm and a FWHM of 20nm as in our PL measurements. The MQW region was represented by a source plane of 50 transverse electric (TE)-polarized dipoles in the middle of the CCL. We only consider devices with a FF~20% and an etch depth ~180nm. Let us recall that on the contrary to measured farfield patterns (with NA=0.75), the simulated ones are collected in the complete half-sphere ( $2\pi$  sr) with an equivalent NA=1.

The results are displayed in **Figure B-3** showing that the shapes of both measured and simulated farfield patterns are in very close agreement. In addition, using the simulated farfield patterns, we evaluate the directionality values at all angles. We found that more than 85% of the emitted light is comprised into a  $\pm 50^\circ$  cone ( $D(50^\circ) > 85\%$ ), which confirms that a numerical aperture (NA) of 0.75 is enough to collect most of the emitted light and validates the use of an objective with NA=0.75 for back focal-plane imaging.

### B.3 Vertical vs tapered profiles of the PhC patterns: simulation study

In this section, we wish to visualize briefly the impact of the non-vertical sidewalls of the PhC patterns on the farfield emission shapes. To do so, we performed incoherent 3D-FDTD simulations on some of the devices of **Chapter III** with the same parameters used in the previous subsection. We compare the emission for devices patterned with PhC having vertical sidewalls to the ones having tapered ones. A tapered angle of  $18^\circ$  is chosen to be consistent with FIB measurements performed in **Chapter IV**. The results are displayed in **Figure B-4** showing the emission patterns are impacted because of local changes of air filling factors due to non-vertical sidewalls.

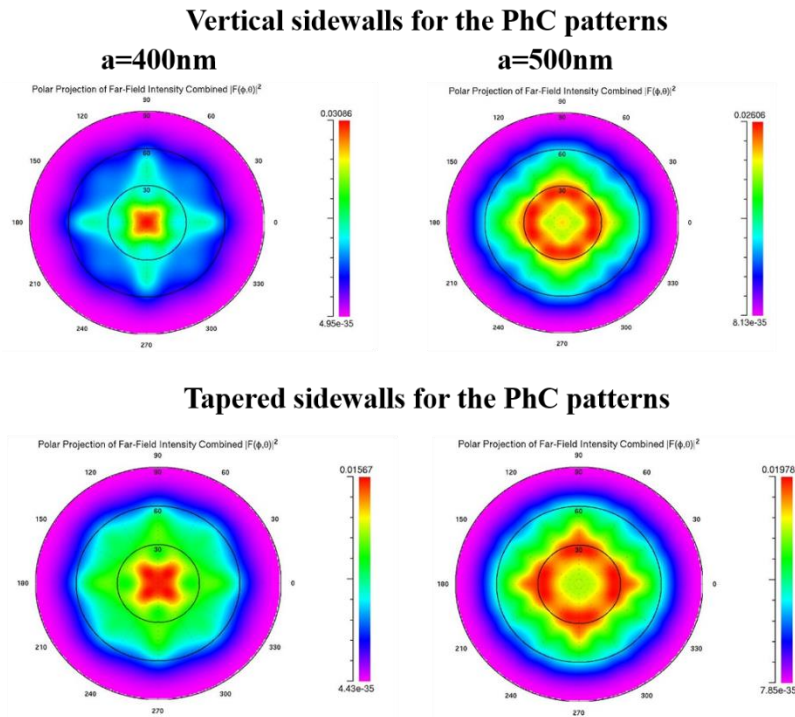


**Figure B-4:** 3D-FDTD simulation results for square lattice of air holes with a FF~20% and an etch depth ~180nm. Vertical and  $18^\circ$  tapered sidewalls for the PhC patterns are implemented.

However, an evaluation of the directionality close to normal incidence and at  $\pm 30^\circ$  shows that these impacts are slight for a tapered angle  $18^\circ$ . In any case, the etching parameters should be controlled during fabrication not to have large tapered angles, which could create discrepancies between the designed PhC and the fabricated ones.

#### B.4 Impact of the PhC patterns on the absorption efficiency: simulation study

In this section, we wish to assess the impact of the PhC patterns on the absorption efficiency of the final patterned devices as compared to unpatterned structures. To do so, we performed 3D-RCWA simulations using a commercially available software (DiffractMOD from the Rsoft Design Suite). The absorbed light is deducted from the reflected and transmitted light. The refractive indices and extinction coefficients used for the simulations are provided in **Table B-1**.

**Table B-1:** Refractive indices (n) and extinction coefficients (k) used for the RCWA simulations.

Layer	Thickness	$\lambda=405\text{nm}$	$\lambda=514\text{nm}$
Cladding	200 nm	n=3.86, k=1.098	n=3.66, k=0.08
MQW barrier	70 nm	n=3.9, k=1.83	n=3.7, k=0.22
MQW region	4.4 nm (QW) / 8.7 nm (Barrier)	$n_{\text{average}}=3.49$ , k=1.23	$n_{\text{average}}=3.38$ , k=0.051
MQW barrier	70 nm	n=3.9, k=1.83	n=3.47, k=0.22
Cladding	200 nm	n=3.86, k=1.098	n=3.66, k=0.08

Structural parameters of the PhC patterns (lattice periods, etch depth  $\sim 188\text{nm}$  and filling factors  $\sim 20\%$ ) are the ones measured in the fabricated devices of **Chapter III**. For the sake of simplicity, only square lattices are considered. As a reference, we also performed calculations for flat structures to evaluate absorption ratios between PhC and unpatterned structures. Results for both blue and green excitation wavelengths are displayed in **Figure B-5**.

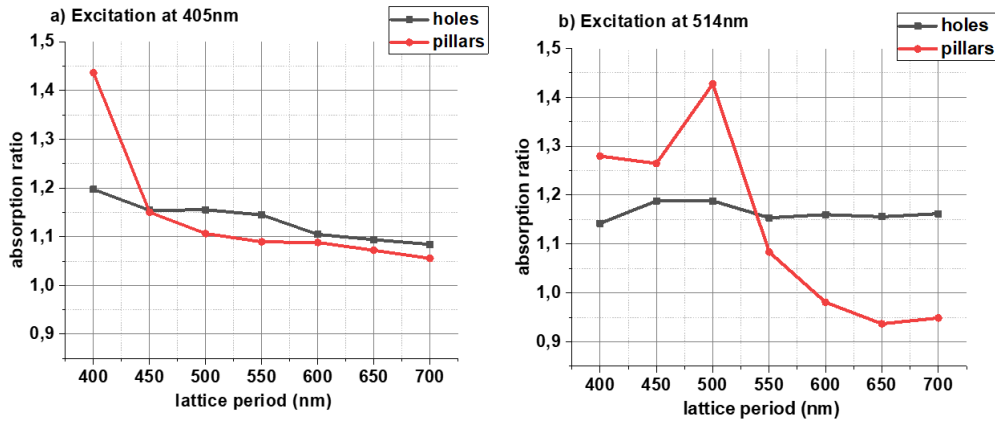


**Figure B-5:** Absorption ratios between PhC and unpatterned structures for excitation wavelengths of a) 405nm and b) 514nm.

In terms of light absorption efficiency, pillars and holes do not behave the same way. For hole-type PhC, light absorption efficiency increases by less than 20% compared to the unpatterned structures for both excitation wavelengths.

For nanopillar-type PhC, the tendencies are slightly different. For an excitation at 405nm, light absorption variations are similar to those of holes except for an increase of light absorption efficiency by  $\sim 40\%$  for a lattice constant of 400nm. For an excitation at 514nm, we observe an increase by less than 30% for a lattice period of 400nm and 450nm, by  $\sim 40\%$  for lattice period of 500nm and by less than 10% for higher lattice periods.

Roughly speaking, for both lattices and both excitation wavelengths, PhCs tend to enhance light absorption by factors between  $\sim 1$  and  $\sim 1.4$ . Therefore, IQE decrease is mostly responsible of the discrepancies between measured and simulated LEE enhancement factors in **Figure III-25** of **Chapter III**.

### B.5 LEE and farfield emission patterns vs etch depth: simulation study

In this last and final section of Appendix B, we wish to study briefly the impact of the PhC etch depth on LEE and farfield shapes using incoherent 3D-FDTD simulations as in the previous subsections. We consider devices of **Chapter III** on transparent substrates comprising SLAH with  $a=450\text{nm}$ ,  $\text{FF}=50\%$  and a lateral extent of 10 periods for computing-time issues. The PhC etch depth is varied from 0 (unpatterned surfaces) to 250nm (20nm away from the MQW). As explained in **Chapter III**, etching deeper will lead to a rapid decrease of IQE and therefore of the overall conversion efficiency due to non-radiative recombinations.

**Figure B-6** reports on LEE as a function etch depth. As we can see, LEE increases for increasing etch depths starting from  $\sim 1\%$  for unpatterned structures before saturating at  $\sim 10\%$  after 150nm.

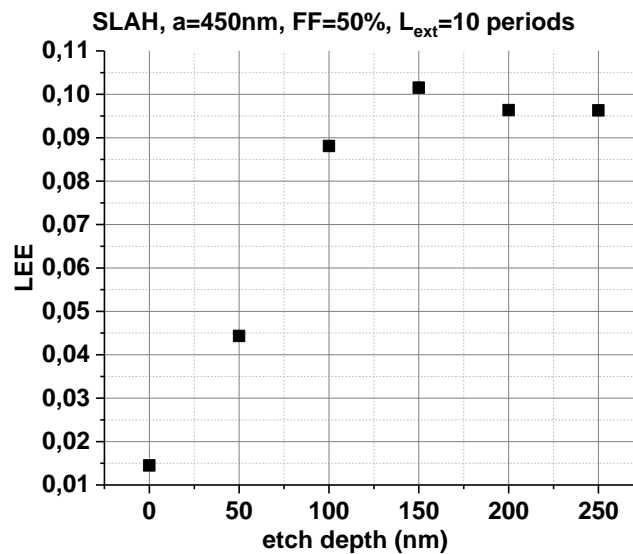


**Figure B-6:** 3D-FDTD simulation study of the impact of the etch depth on the light extraction efficiency of devices on transparent substrates. Structural parameters are in the inset.

This can be easily understood by considering the model derived from coupled-mode theory proposed in **Eq. (III-2)** of **Chapter III**. Indeed, a deeper etching implies a better interaction between the guided Bloch-modes and the PhC patterns as explained in **Section III.4** of **Chapter III**. This increases the coupling strength and thus the LEE until it saturates (see also Ref. 8 of the third chapter for a more detailed discussion on this topic). In our devices, we have shown that a deeper etching ( $>200\text{nm}$ ) becomes detrimental to the overall conversion. We can conclude that the etch depth should be kept between 150nm and 200nm (around the third of the total epilayer thickness).

Furthermore, as explained in **Chapter III**, increasing the etch depth will also change the effective index distribution inside the color converter and thus affect the azimuthal farfield patterns.

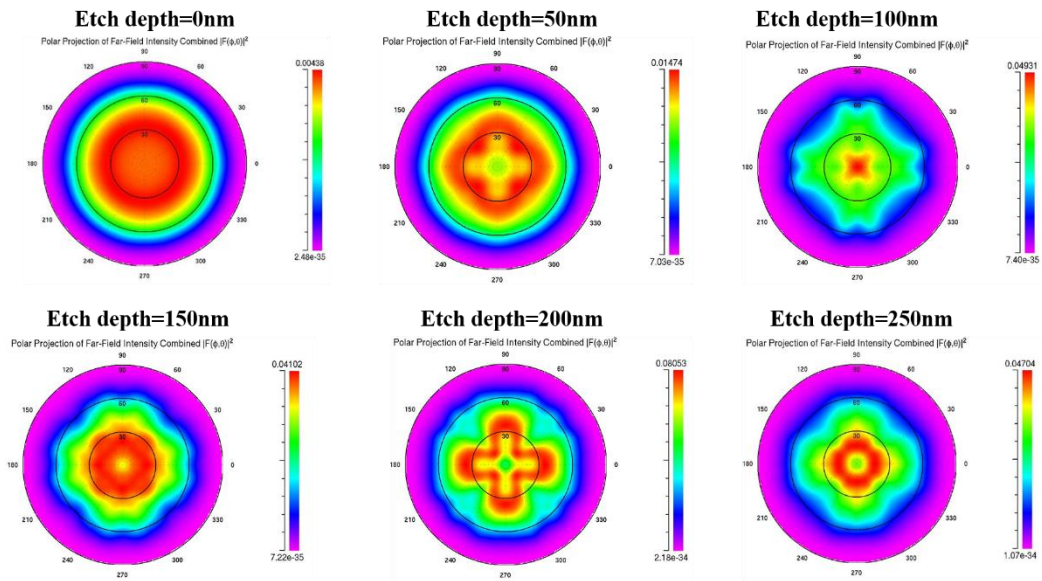


**Figure B-7:** 3D-FDTD simulations of the impact of the PhC etch depth on the azimuthal farfield patterns for devices on transparent substrates. SLAH are considered with  $a=450\text{nm}$ ,  $\text{FF}=50\%$  and a lateral extent of 10 periods.

As displayed in **Figure B-7**, increasing the etch depths can heavily reshape the farfield radiation patterns. This shows that this parameter also needs to be properly controlled during fabrication in order to obtain farfield patterns corresponding to the designs.

## **Appendix C**

*Pixelated photonic-crystal MQW III-V  
membrane with back- and lateral reflectors:  
supplemental information.*

### C.1 Reflectance measurements for the back- and lateral reflectors

Figure C-1 shows reflectance measurements for the back-and lateral mirrors as well as bare Ti and Cu reflectors.

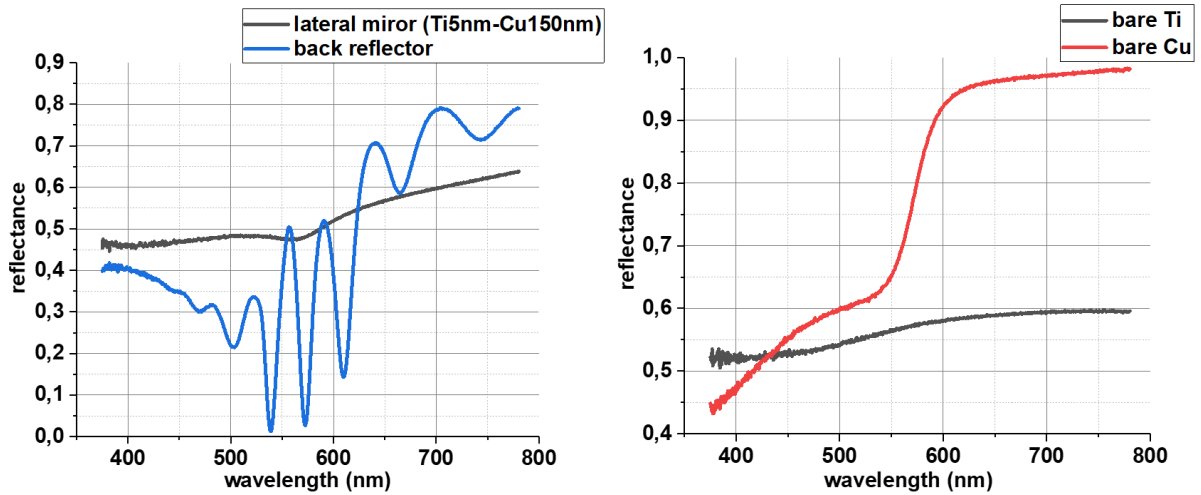


**Figure C-1:** Measured reflectance spectra for the lateral- and back reflectors (left plot) as well as for the bare Ti and Cu mirrors (right plot).

As we can see, the back reflector has a reflectance of ~65% at 640nm while the reflectance values for the lateral mirrors amount to ~50%.

The right plot shows that without the thin Ti layer the lateral mirror (bare Cu) reflectance values could amount to ~95%, which would definitely better the effects of the Bloch-mode replication and enhance light extraction efficiency for pixel with short lateral sizes.

*The end...*



## AUTORISATION DE SOUTENANCE

Vu les dispositions de l'arrêté du 25 mai 2016 modifié par l'arrêté du 26 août 2022,

Vu la demande du directeur de thèse

**Monsieur C. SEASSAL**

et les rapports de

**M. H. BENISTY**

Professeur - Laboratoire Charles Fabry - Institut d'Optique Graduate School - Paris Saclay  
2 avenue Augustin Fresnel - 91127 Palaiseau cedex

et de

**M. D. VAN THOURHOUT**

Professeur - Ghent University - IMEC - Department of Information Technology  
Technologiepark-Zwinjnaarde 128 - 9052 Gent - Belgique

**Monsieur NDIAYE Amade**

est autorisé à soutenir une thèse pour l'obtention du grade de DOCTEUR

**Ecole doctorale ELECTRONIQUE, ELECTROTECHNIQUE, AUTOMATIQUE**

Fait à Ecully, le 5 janvier 2023

Pour le directeur de l'Ecole centrale de Lyon  
Le directeur des Formations

Grégory VIAL

